Detection of a Transverse Crack in a Rotating Shaft using Wavelet Transform

by

Surajudeen Adedotun Adewusi

A Thesis Presented to the

FACULTY OF THE COLLEGE OF GRADUATE STUDIES

KING FAHD UNIVERSITY OF PETROLEUM & MINERALS

DHAHRAN, SAUDI ARABIA

In Partial Fulfillment of the
Requirements for the Degree of

MASTER OF SCIENCE

In

MECHANICAL ENGINEERING

May, 2000

DETECTION OF A TRANSVERSE CRACK IN A ROTATING SHAFT USING WAVELET TRANSFORM

BY

SURAJUDEEN ADEDOTUN ADEWUSI

A Thesis Presented to the
DEANSHIP OF GRADUATE STUDIES

KING FAHD UNIVERSITY OF PETROLEUM & MINERALS
DHAHRAN, SAUDI ARABIA

In Partial Fulfillment of the
Requirements for the Degree of

MASTER OF SCIENCE

In

MECHANICAL ENGINEERING

May, 2000

UMI Number: 1399742

UMI®

UMI Microform 1399742

Bell & Howell Information and Learning Company
300 North Zeeb Road
P.O. Box 1346
Ann Arbor, MI 48106-1346

KING FAHD UNIVERSITY OF PETROLEUM AND MINERALS

DHAHAN 31261, SAUDI ARABIA

DEANSHIP OF GRADUATE STUDIES

This thesis, written by **SURAJUDEEN ADEDOTUN ADEWUSI** under the direction of his Thesis Advisor and approved by his Committee, has been presented to and accepted by the Dean of Graduate Studies, in partial fulfillment of the requirements for the degree of **MASTER OF SCIENCE**.

Thesis Committee

22 May 2000
Dr. B.O. Al-Bedoor (Thesis Advisor)

May 22, 2000
Dr. Mohammad N. Hamdan (Member)

22/5/2000
Dr. Moustafa Elshafei (Member)

٢٢/٥/٢٠٠٠
Dr. Yagoub Al-Nassar (Member)

19/2/1421
Department Chairman

Dean of Graduate Studies

27/5/2000
Date

DEDICATION

This thesis is dedicated to my wife (Fatima), my son (Abdullah) and members of my family

ACKNOWLEDGEMENT

Praise and thanks are due to Allah, the Exalted, for His guidance, provisions, mercy and blessings on my family and myself. I thank Allah for making it possible for me to complete this M.S. program.

I acknowledge the financial support of King Fahd University of Petroleum and Minerals. The cooperation and assistance of the chairman, entire faculty members and staff of Mechanical Engineering Department is also appreciated.

I wish to express my sincere appreciation to my Thesis Committee members. I am very grateful to my Thesis Advisor, Dr. Bassem Odeh Al-Bedoor for his efforts and contributions towards the success of this thesis work. I also wish to thank my Thesis Committee members, Dr. Mohammad N. Hamdan, Dr. Moustafa Elshafei and Dr. Yagoub Al-Nassar for their contributions, assistance and cooperation. May Allah reward them most abundantly.

I also appreciate the contributions and assistance of Dr. C. A. Loto, Dr. Mehmet Sunar, Dr. Kamar Chakravarthy, Dr. M. Kalyon, Dr. L. Cheded and Mr. Lahouri Ghouti I thank members of my family for their moral support, patience and perseverance while I was away from home. In particular, I thank my uncle, Mr. Ismail Sanni, my in-laws, Mr and Mrs. Owolobi, for taking good care of my wife and son during my absence.

The support and assistance of friends and colleagues who made my study at King Fahd University of Petroleum and Minerals and stay in Saudi Arabia worthwhile is also acknowledged and appreciated. I thank Dr. Qamorudeen Abidogun, Dr. Yahya Oloriegbe, Abdul Hakeem Adeleke, Hussain Al-Gathani, Faisal Mahmud, Bashir Adamu, Abdul Kareem Melaiye, Taofiq Ayinde, Babalola Abdul Hammed, Muhammad

Shazali, Abdul Kareem Adinoyi, Sulaiman Edah, Taofiq Abiola, Sulayman Iyanda, Sulayman Oloriegbe, Jimoh Tijani, Umar Yunus, Danjuma Ikwenti, Abdul Bassit Shaibu, Abu idris and many others.

CONTENTS

LIST OF TABLES

LIST OF FIGURES

THESIS ABSRTACT

NAME: Surajudeen Adedotun Adewusi

TITLE: "Detection Of A Transverse Crack In A Rotating Shaft Using Wavelet Transform"

MAJOR FIELD: Mechanical Engineering

DATE: May, 2000.

This is an experimental study on the dynamic response of a rotor with a transverse surface crack. The influences of a non-propagating and propagating transverse crack, and side load on the dynamic response of rotors were investigated in order to get some clues that can be used to detect the presence of a crack in rotating shafts. Startup and steady state vibration signatures were analyzed using the Wavelet Transform, a Joint Time-Frequency Analysis technique. Vibration signals were also analyzed with the conventional methods in which the results presented in the form of Frequency Spectrum Cascades and Waterfalls, Bode plots and orbits for comparison. Two experimental setups, simply supported and overhang shaft arrangements, were used; the response of the two experimental arrangements under the influence of crack and side load was different. The results showed that crack introduces additional features in the wavelet transform of the startup signals and produces changes in amplitude of 1X and 2X vibration harmonics at steady state. The results of the conventional analysis showed that crack increases the resonance bandwidth and may or may not excite 2X harmonics during startup depending on the location of the crack. Also, crack produces changes in amplitudes of 1X and 2X harmonics and produces two-loop orbit in the steady state signals.

MASTER OF SCIENCE DEGREE

KING FAHD UNIVERSITY OF PETROLEUM AND MINERALS

Dhahran, Saudi Arabia.

May, 2000.

خلاصة الرسالة

إسم الطالب الكامل : **سراج الدين إديدوتون أديوسي**

عنوان الدراسة : **التعرف على الشق العرضي في محور دوار باستخدام طريقة التحويل الموجوي**

التخصص الرئيسي : **الهندسة الميكانيكية**

تاريخ الشهادة : **مايو ٢٠٠٠ م**

تقدم هذه الرسالة دراسة تدريبية على التجاوب الديناميكي لمحور عليه شق عرضي ولقد درس تأثير الشق الثابت والمتغير تحت تأثير أحمال جانبية . ودرست اهتزازات المحور الدوار في مرحلتي بداية التشغيل والعمل المستمر باستخدام طريقة التحول الموجي كطريقة تجمع بين الذبذبة والوقت وقوة الاهتزاز . و كذلك حللت النتائج باستخدام رسمات بودي ومدارات الحركة وطرق تحليل الذبذبات المتلاصقة . ولهذه الغاية قام الباحث باستخدام نموذجين تجريبيين أحدهما يمثل المحاور المعلقة من الطرفين ويقع الشق في المنتصف آما الثاني فيمثل المحور المعلق من جهة ويقع الشق في الجهة الخارجية المعلقة . أوضحت النتائج أن الشق يؤدي إلى ظهور سمات إضافية مع ظهور اهتزازات على سرعة الدوران (١X) واهتزازات على اثنين سرعة الدوران ٢X ولقد أوضحت النتائج وجود زيادة في عرض منحنى التجاوب عند وجود شق وكذلك وجود مدارين منفصلين .

درجة الماجستير في العلوم

جامعة الملك فهد للبترول والمعادن

الظهران — المملكة العربية السعودية

مايو ٢٠٠٠ م

CHAPTER 1

INTRODUCTION

1.1 MACHINE CONDITION MONITORING

A shaft is the backbone machine component that is used for power transmission and to support machinery elements like disks, blades, vanes, etc. Competition in industries has promoted the need for more reliable and efficient machines that are running at high operating speeds and loads. One way of increasing the reliability, availability and performance of a machine is by adequately monitoring its operation conditions by a Machinery Condition Monitoring System (MCMS). In the past, machines were shutdown for inspection for faults; this method is grossly uneconomical and could lead to crack magnification during shutdown and start-up of the machine if there is a crack in the shaft. An important operation parameter of machine that is monitored is its vibrations. The causes of vibrations in a machine include imbalance, misalignment of shafts, looseness of bolts and nuts, rubbing, bearing problems, shaft cracks and others. A crack in a rotating shaft can lead to catastrophic breakdown of the machine if it is not detected at an early stage.

Advancement in science and technology particularly in the fields of System Monitoring and Control, and Signal Measurement and Analysis has contributed to machinery diagnosis by enhancing vibration measurement and analysis. Signal monitoring and control devices that can automatically shutdown a machine when its vibrations exceed a safe value are already in use. Signal analysis methods, like Frequency Spectral Analysis and Short-Time Fourier Transform (STFT) have been used to analyze vibration signals to identify machinery problems; applications of these techniques are developed for machine health monitoring. However, the problem is still complicated and extensive research is still needed particularly for crack detection and assessment.

1.2 EFFECT OF A CRACK ON A ROTATING SHAFT

Although rotors are carefully designed for fatigue loading and high level of safety by using high quality materials and precise manufacturing techniques, catastrophic failures of rotors as a result of cracks may still occur. A crack is an undesirable opening in a material and it is a sign of deterioration of the material, which is caused by factors such as fatigue loading. Continuous operation of a cracked rotor results in crack propagation, which will ultimately result in a sudden breakdown of the machine or one of its elements. Important features of a cracked shaft are variation in stiffness and damping with the rotation angle of the shaft, production of forced vibration [1] and [2], and continuous changes in natural frequencies. A crack on a rotating shaft also introduces transient components into the vibration signals. Consequently, the

overall dynamic behavior of the shaft is altered; this produces high varying amplitudes particularly in the second harmonic component but other failures like misalignment, asymmetry, gravity and side loads may also produce the same effect [2].

1.3 PROBLEM DEFINITION

The dynamic behavior of rotors is affected by many problems such as imbalance, misalignment, rubbing, fluid-induced instabilities, cracks and others. The problem of monitoring and evaluating the health of rotors depends mainly on the correct diagnostics and identification of the cause. The problem of identifying cracks in rotors through vibration measurements has attracted many researchers due to its importance. Researchers have presented their findings in form of orbits, frequency spectral analysis and time-waves; some reported 1X and 2X harmonics as main factor for crack identification; sub-harmonics were reported by others, while few reported the presence of transient signals as a crack identification factor. Therefore, more research is still needed towards better understanding of crack presence, propagation and identification. Due to the anticipated frequency and amplitude variation, attention is directed towards the use of wavelet transform analysis, a Joint Time-Frequency Analysis, of the cracked and un-cracked shaft vibration signals.

1.4 OBJECTIVE OF THE THESIS

The work in this thesis is an experimental study of the vibration of rotors with a transverse surface crack using the FFT-based conventional signal analysis and wavelet

analysis, a Joint Time-Frequency Analysis technique. The theory of wavelet transformation and wavelet analysis presentations and interpretations in vibration analysis are presented. The Power Spectra Density, frequency cascades, orbits, bode plots of vibration signals of cracked and un-cracked rotors are studied towards finding unique features that can be used to characterize the presence of crack as well as monitoring crack propagation in rotating shafts. The effect of side load and crack on the dynamic response of a rotor is also investigated.

1.5 THESIS OUTLINE

The first three sections of Chapter 2 describe the effect of crack on the dynamic response of rotating shaft, crack identification methods and different crack models. The fourth section presents research works on the study of cracked shafts and crack identification while research works on application of wavelet transform and other Joint Time-Frequency Analysis methods in vibration analysis are presented in section five.

Chapter 3 discusses different signal processing techniques, wavelet transform theory, wavelet bases, wavelet coefficient determination, and wavelet transform results presentations and interpretations. The relationship between frequency and scale is also investigated. Experimental methodology is described in Chapter 4 and results are presented and discussed in Chapter 5. Chapter 6 presents the drawn conclusions and recommendations for future extension of this work.

CHAPTER 2

LITERATURE REVIEW

2.1 INTRODUCTION

The study of dynamic behavior of a rotating shaft with a transverse surface crack started in early 1960s by Dimarogonas and his colleagues when they attempted to identify a crack on a large steam turbine. They were able to develop a supervisory instrument, which could give an early crack warning in middle of 1970s. Dimarogonas [3] observed the local flexibility of a cracked shaft and developed an analytical expression for the crack local flexibility in relation to the crack depth by using Paris displacement equation for a cracked structure; he also showed the influence of the crack upon the dynamic response of the rotor. Figure 2.1 shows the geometric section of a shaft with a transverse crack and graphs of dimensionless flexibility verses the ratio of crack length to the shaft radius; a represents crack depth, R is shaft radius, E is Young's modulus, ν is Poisson's ratio and c is flexibility influence coefficient.

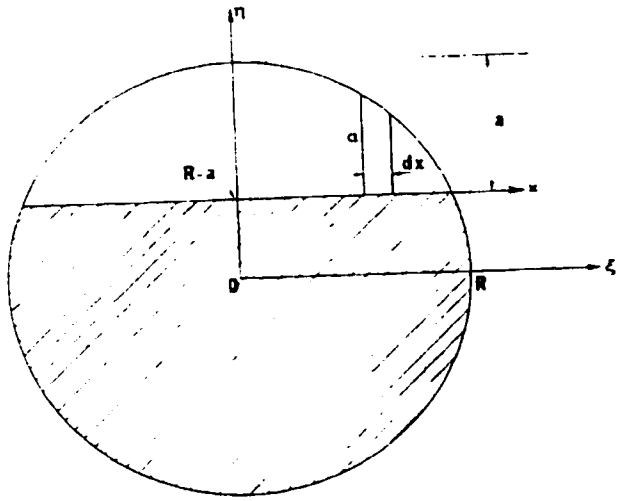

(a)

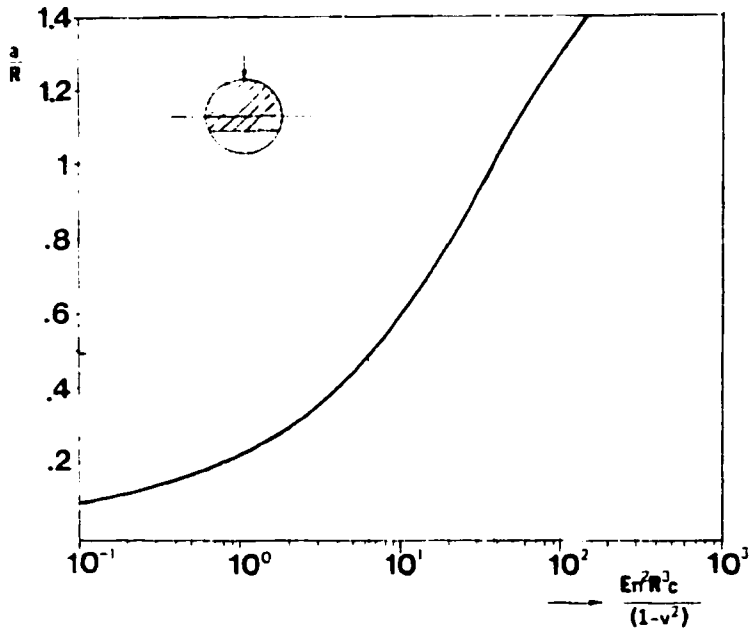

(b)

Fig. 2.1. (a) Geometric section of a cracked shaft, (b) Dimensionless flexibility variation with load normal to crack edge

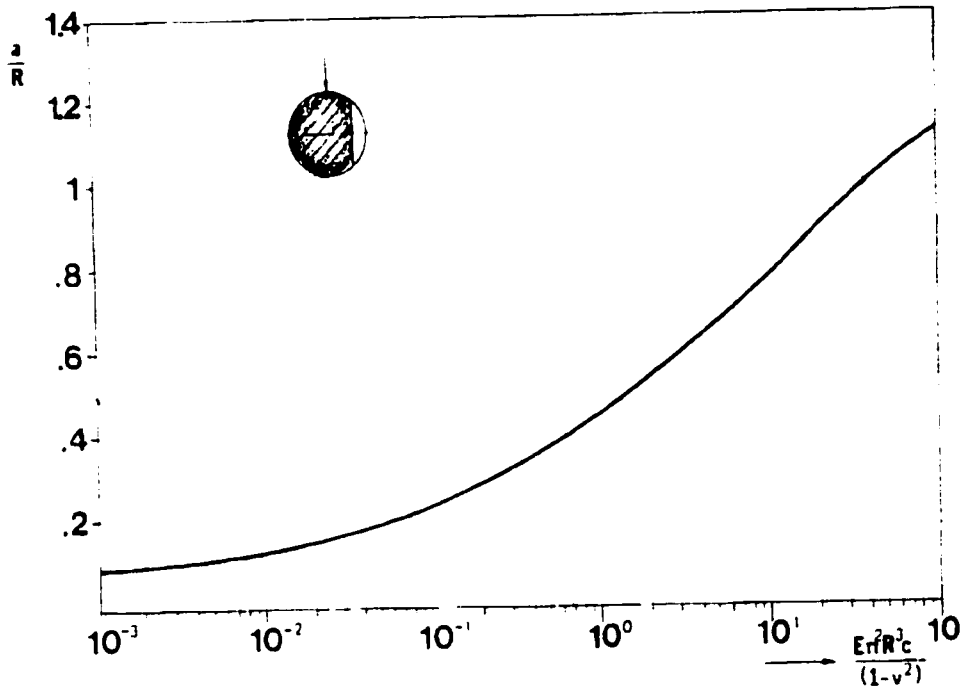

(c) Dimensionless flexibility with load parallel to cracked edge

Figure 2.1 Local flexibility variations with crack depth [3]

2.2 CRACK DETECTION METHODS

In the past, two main techniques, Coast-Down or Shutdown Method and Temperature-Transient Method, were used to detect crack in rotating machinery. The Central Electricity Generating Board of Britain developed the first method. Shutdown or startup vibration signals can detect a reduction in the natural frequency of a system as a result of changes in its stiffness. This information has been used to detect the presence of crack depth of about 25% or higher of the shaft diameter [4]. Shutdown and startup could lead to crack magnification and in some cases, shutdown leads to loss of production.

The Temperature-Transient Method, as the name implies, is used to detect crack in machines that use high temperature working fluids, like steam turbines. A rapid change in steam temperature induces thermal shock that forces the crack, if present, to open. This creates an asymmetry in shaft stiffness and results in high vibration. The increased vibration decays slowly as the temperature stabilizes. This technique cannot detect cracks located at regions that are not in contact with the working fluid [4].

Presently, attention has been focused on on-line crack identification. Researchers have studied the theory of crack initiation and propagation and how these affect the dynamic response of shafts. The next section of this chapter presents the common models that have been used in the study of cracks in shafts. This is followed by literature review of the published work on the analysis and identification of cracks in rotors and the last section reviews published papers on the engineering applications of wavelet transform (WT) in signal processing and vibration signals analysis.

2.3 CRACK MODELS

The dynamic equation for a Laval shaft shown in Figure 2.2 without any crack but with an unbalance weight can be represented by the linear equation in the vertical and horizontal directions as

$$\begin{aligned} My^{\cdot\cdot} + C_y y^{\cdot} + K_y y &= me\omega^2 \sin(\omega t) \\ Mx^{\cdot\cdot} + C_x x^{\cdot} + K_x x &= me\omega^2 \cos(\omega t) \end{aligned} \tag{2.1}$$

The amplitudes of the steady state response of the system are respectively

$$\begin{aligned} Y &= \frac{me\omega^2}{M\sqrt{\left(1-\left(\frac{\omega}{\omega_{ny}}\right)^2\right)^2 + \left(2\xi_y\left(\frac{\omega}{\omega_{ny}}\right)\right)^2}} \\ X &= \frac{me\omega^2}{M\sqrt{\left(1-\left(\frac{\omega}{\omega_{nx}}\right)^2\right)^2 + \left(2\xi_x\left(\frac{\omega}{\omega_{nx}}\right)\right)^2}} \end{aligned} \tag{2.2}$$

$$\omega_n = \sqrt{\frac{K}{M}}, \quad \xi = \frac{C}{2M\omega_n} = \frac{C}{2\sqrt{KM}}$$

Where M is the modal mass of the system, m is the unbalance mass, e is the radial distance of m from the axis of rotation, ω is the running speed of the shaft; ω_{ny} and ω_{nx} are critical speeds of the system in the vertical and horizontal directions of the inertia coordinate system, respectively; C_y and C_x are damping of the system in the vertical and horizontal directions; ξ_y and ξ_x are damping factor in the vertical and horizontal directions, respectively. K_y and K_x are the stiffness of the system in the vertical and horizontal directions, respectively.

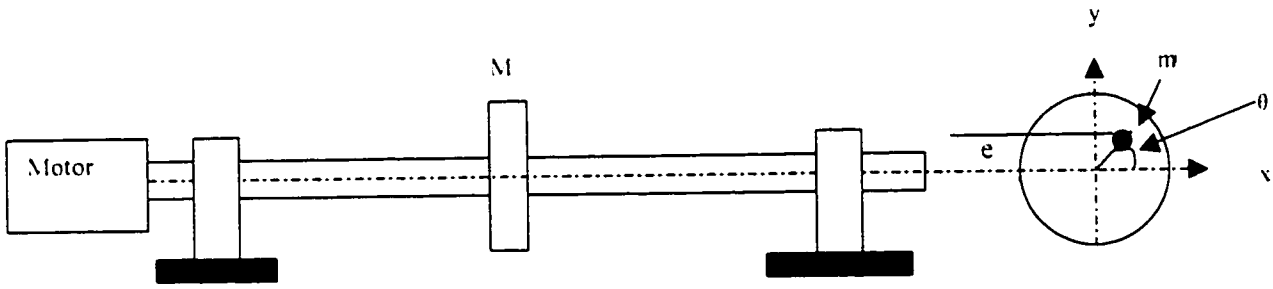

Figure 2.2. A De-Laval rotor with unbalance weight

The presence of a crack will produce asymmetry in shaft stiffness, unbalance since mass distribution is altered, and will produce stiffness that depends on angle of rotation, speed and crack depth; these will introduce non-linearity into the dynamic equation. Some researchers [1, 2, 5, 6] have introduced these changes in the dynamic equation of a cracked shaft by using different crack models. Gash [1] defined the equation of motion for a cracked shaft as

$$M\ddot{z} + C\dot{z} + [K_o + \Delta K(z,t)]z = P_o + P_m \qquad (2.2)$$

$\boldsymbol{M}$ is mass matrix, z is displacement vector, $\boldsymbol{C}$ is damping matrix, $\boldsymbol{K_o}$ is the stiffness matrix of un-cracked shaft, ΔK is change in stiffness matrix due to crack, $\boldsymbol{P_o}$ is static force vector and $\boldsymbol{P_m}$ is force vector due to imbalance. There are two types of crack models that can be used: these are the open crack and the closing or breathing crack. Figure 2.3 shows a shaft with a transverse crack under load with the cracked region subjected to compressive and tensile stresses. It illustrates the phenomenon of a breathing crack.

2.3.1. The Open Crack

Open crack model assumes that the crack is always open whether the cracked region is in compression or tension; this introduces dissimilar moment of inertia that results in dissimilar shaft stiffness along the rotor-fixed coordinate [1, 2]. The dissimilar moment of inertia along coordinate axes does not vary with time and angle of rotation as the crack is assumed to be permanently open at all time. Open crack can be assumed for small vibration amplitudes and static deflections that are substantial. Also, a transverse surface notch with big angle will produce an open crack.

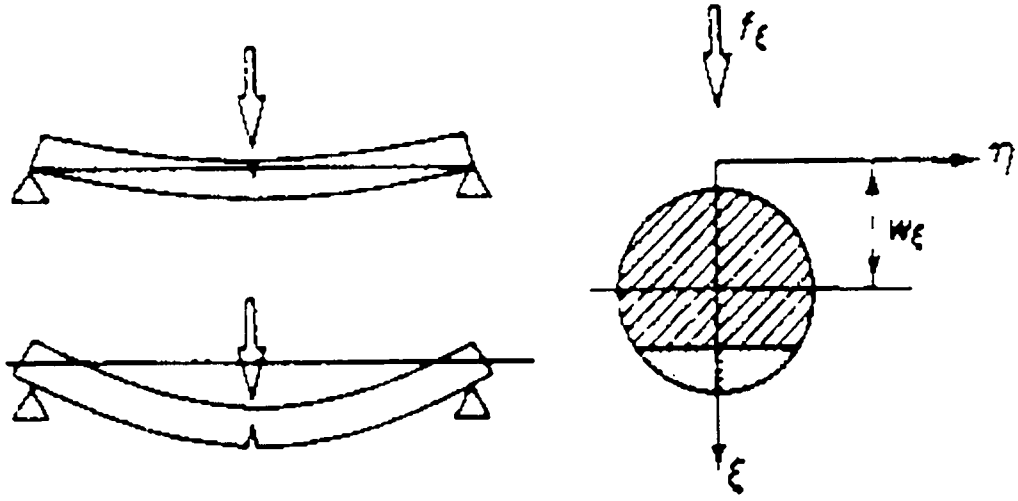

Figure 2.3. Crack Region in Compression and Tension [1].

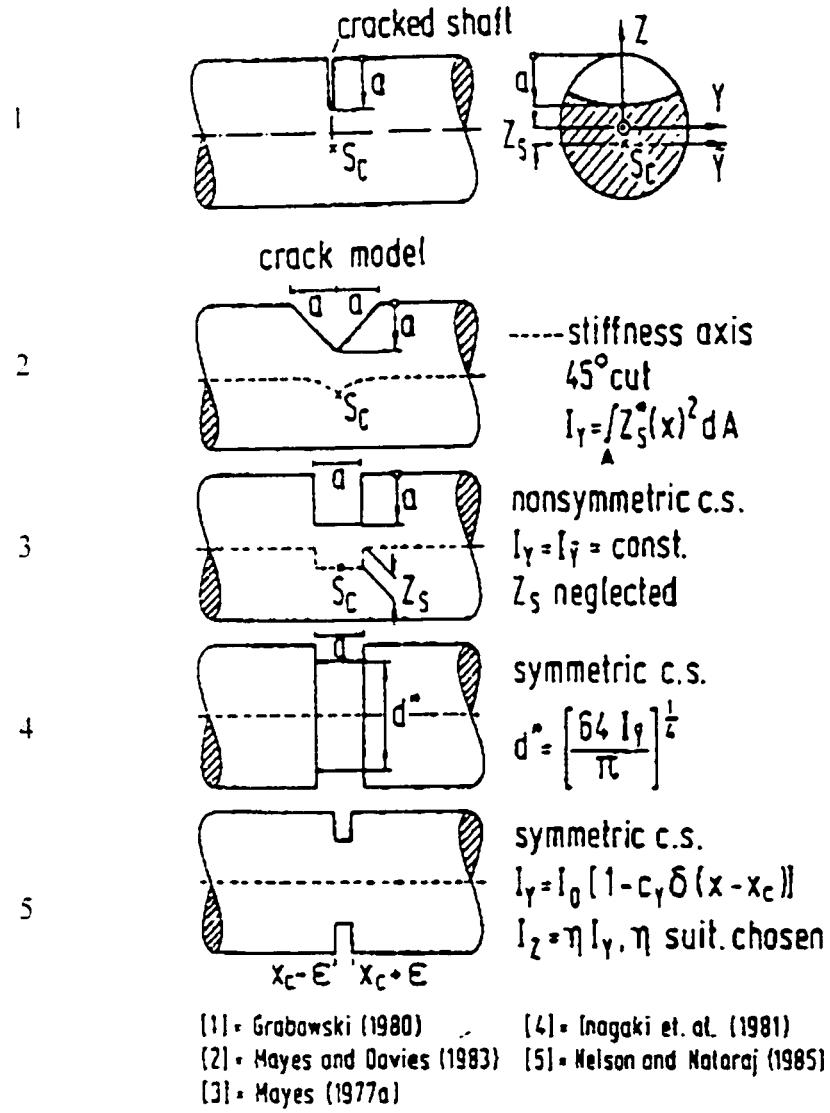

Figure 2.4 Models of Cracked Shaft [6]

2.3.2. The Closing or Breathing Crack

If a cracked shaft rotates slowly under an external load or the load of its own weight, the crack will close at position where compressive stresses occur at the location of the crack and will open at position where tensile stresses occur at the location of the crack, see Fig. 2.3. This introduces time varying stiffness into the equation of motion of the cracked shaft. This model is also known as switching crack model.

2.3.3 Types of Surface Transverse Crack

The different types of surface transverse cracks that have been used by researchers are shown in Figure 2.4. This figure shows that the center of gravity and the rotation axis for the first three models are non-coincident and this produces imbalance. Furthermore, the second moment of inertia about the vertical and horizontal axes is different leading to different stiffness along these axes as indicated in Fig. 2.1. Moreover, Figure 2.4 shows the models and the following parameters: a is crack depth, S_c is the center of cracked section, Z_c represents the coordinate of cracked section, c.s. means cracked section, X_c represents crack location, ε is increment in length, η is a constant and $\delta(x)$ is dirac delta function.

2.4 DYNAMICS OF CRACKED ROTORS

Most of the published research on detection of cracks in rotors involved mathematical modeling and formulation of equations of motion, analytical, numerical

and modal solutions of the equations. However, some researchers supported their findings with experimental results.

Gasch [1] studied the stability behavior of the Laval rotor with a crack, and the forced vibration due to both imbalance and crack. The results showed that the recognition of cracks is very difficult because the significant double and triple frequency vibrations are only very slightly involved in the crack response. Moreover, in contrast to imbalance effect, a crack may excite a strong backward whirl component, which cannot be balanced out.

Grabowski [2] used modal analysis to study the vibration behavior of a turbine rotor containing a transverse crack. His numerical results showed that a crack causes important changes in shaft vibration. He reported that the crack excites 1X and 2X vibrations, which are independent of the out-of-balance but depend on the crack locations. Imam, et al [4] used a 3-D finite element method and a nonlinear rotor dynamics to model a cracked rotor system and developed an on-line rotor crack detection and monitoring system. The analysis combined rotor dynamics, fracture mechanics, vibration signature analysis techniques, and heuristics. They established that it is very difficult to differentiate vibration signals of a cracked and un-cracked shafts using the convectional FFT when the crack is about 2% of shaft diameter, hence he used histogram signature analysis, which is the FFT of the difference between the averaged vibration signals of cracked and un-cracked shafts. Experiment results showed 1X and 2X vibration peaks.

Inagaki, et al [5] utilized the iterative numerical calculation (transfer matrix) method to analyze transverse vibrations of a general cracked-rotor bearing system and an experiment was used to validate the results. The results showed 1X and 2X vibration

responses under mutual influences between gravity, imbalance and their phase relations. and vibration mode characteristics at the rotating speed. The work of Dirr and Schmalhorst [6] was comprehensive. They used vibration measurement method and potential difference method of fatigue crack measurement to study the shape of cracks at different depth during crack propagation in a rotating shaft. Crack depths measured by potential difference method were related to crack shape by numerically solving Laplace differential equations for three-dimensional potential field. The FFT of experimental vibration signals showed 1X and 2X. 3D Finite Element crack model was also used to study the bending stress distribution near a crack tip.

Mayes and Davies [7] analyzed the response of a multi-rotor-bearing system with a transverse crack using a linear rotor dynamic computer program. The change in rotor stiffness was modeled by a reduction in the shaft diameter. The results were supported by experimental work using a test rig to study the effect of dynamic bending moments and rotor running speed on crack depth. The results of the theoretical analysis were presented in form of graphs of once and twice/revolution amplitude versus running speed and compliance function versus crack depth, there is fair agreement between theoretical and experimental results.

Bently and Bosmans [8] of Bently Nevada Corporation used experimental set-up to study a cracked rotor model of a Reactor Coolant Pump. The results showed a variation in the amplitude of the 2X vibration and an orbit with two loops due to crack propagation. Wauer [9,10] carried out a comprehensive literature survey on the state-of-the-art of the dynamics of cracked rotors, none of the researchers used wavelet transform to analyze vibration signals of a cracked rotor. He also modeled and formulated the governing dynamic equations of a cracked Timoshenko rotor, which is flexible in

extension and torsion. He used the Galerkin's method to reduce the equations of motion wherein the torsional vibrations of a circular shaft with a circumferential crack was studied.

Collins, et al [11] studied a cracked Timoshenko rotor by solving the six coupled equations obtained by Wauer [9,10]. The frequency spectrum of the rotor response to a periodic axial impulse was also studied. The results showed an increase in the coupling between axial, torsional and transverse vibration contrary to the results of Gabowski [1] peaks in the spectrum which are not multiples of the forcing frequency are reported and this was attributed to coupling rather than nonlinearity.

Theoretical and experimental study of the on-line crack detection for turbo-generator rotors was presented by Diana et al [12]. The effects of thermal gradient were accounted for in the diagnostic program, using probability evaluation. In this work, when the crack is propagating, the change in 1X and 2X vibration amplitudes is monitored. The vector difference between the current vibration and the previous vibration vector, in this algorithm, is used as input to an optimization rotor model. The program calculates the vibration forces and compares them with the measured ones, wherein the ratio is called the residual vector. The comparison can give some indication of crack existence, but again the procedure can mix other rotor problem signatures with that of the crack.

Dimarogonas and Papadopoulas [13] studied the stability of cracked rotors in the coupled vibration mode. The study showed that a surface crack on a rotating shaft can yield a variety of unstable region of operation due to the coupled lateral and axial vibration. The frequency spectra of the vibration signal of a 300 MW steam turbine

showed high 2X, $\frac{1}{2}X$ and $\frac{1}{4}X$ vibration components that suggested the existence of deep crack. The same frequency spectra showed high harmonics that were suggested to be due to torsional or longitudinal natural frequencies.

Meng and Hahn [14] analyzed a cracked Jeffcott rotor theoretically and numerically. The same results as that of Gasch [1] were reported but with additional information on the effect of a crack on orbits and the cross-stiffness change ratio. WU and Huang [15] studied the dynamic response of a rotor with a transverse crack by numerically solving dynamic equations obtained by Huang. FFT of the response at various speeds, crack depths and crack locations showed 1X and 2X harmonics. Floquent theory and multiple scales methods were also used to study the stability of the cracked shaft system. Zheng [16] studied numerically the vibration of rotor system with a switching crack. He suggested the use of features other than 1X and 2X harmonics for crack detection. The Gabor analysis of the vibration signals, after 1X and 2X has been removed, showed the presence of transient signals. He highlighted that Gabor transform does not have simultaneous high frequency resolution in both time and frequency domains.

2.5 WAVELET TRANSFORM (WT) AND JOINT TIME-FREQUENCY ANALYSIS (JTFA) APPLICATIONS

An appropriate signal processing method is very important in crack detection [16]. The newly developed wavelet transform is increasingly becoming useful in vibration signals analysis. Some of its unique characteristics are that it can handle both stationary and non-stationary signals, and can transform any signal directly into

time/space and frequency/scale domains, which can provide detailed information about signal evolution. Wavelet transform can be used for discontinuity and breakdown point detection, signal suppression, signal de-noisinig, signal compression and image processing [17].

Doubrava [18] demonstrated the superiority of JTFA over the frequency spectral analysis in terms of resolution in both time and frequency domains. Newland [19, 20] discussed the theory of wavelets and their applications in signal analysis. Onsay and Haddow [21] used wavelet transform to analyze transient wave propagating in a dispersive medium. Experimental vibration data of the transient flexural vibrations of an impact excited uniform beam were measured and analyzed. The results showed the efficacy of WT in detecting transient waves in a dispersive medium. Kishimoto, et al [22] used Wavelet Transform to analyze dispersive waves in a beam. The results showed that wavelet could decompose strain response into time and frequency components. Hamdan, et al [23] carried out the comparison of various basic wavelets for the analysis of flow induced vibration of a cylinder in a cross-flow. The result showed that the modulated Gaussian wavelet gave better results. This agrees with the criterion given by Doubrava [18] that the best JTFA resolution is obtained when the basic wavelet is optimally localized in both time and frequency domains. Newland [24] demonstrated the application of harmonic wavelets in Time-Frequency mapping of transient signals. The advantage of WT over Short-Time Fourier Transform and Wigner-Ville frequency decomposition methods is that its bandwidth can be chosen arbitrarily hence it offers a variable Q transform. Aretakis and Mathioudakis [25] applied wavelet analysis to gas turbine fault diagnosis and compared the results with Fourier analysis. The results

showed that wavelet amplitude provide information about signal characteristics in frequency.

2.6. CURRENT STATUS

Majority of the researchers that studied on-line crack detection used frequency spectral analysis to analyze the vibration signals. They reported an increase in 1X and 2X harmonics as crack identification criterion. Few reported a decrease in 1X amplitude and an increase in 2X amplitude as the crack propagates. Others reported, in addition to 1X and 2X harmonics, sub-harmonics, higher harmonics and elliptical orbits with double loops. Only Zheng [16] reported the presence of transient and chaotic vibration and he used Gabor transform, a Joint Time-Frequency Analysis.

However, other machine faults like misalignment, looseness, gravity, side load, coupled lateral-torsional vibration and shaft stiffness asymmetry can produce similar results. Therefore, further research is necessary in order to arrive at a more reliable method to distinguish vibration signal of a cracked shaft. Wavelet analysis has some characteristics that can reveal more features of vibration signals and may be a useful tool for an on-line crack detection. Wavelet analysis has not been used before in crack detection in rotors. This work uses wavelet transform to analyze the vibration signals of un-cracked shaft and shafts with non-propagating and propagating transverse cracks. Two experimental setups namely the simply supported and overhang shaft arrangements will be used.

Finally, a lot of research has been done on fatigue crack growth, detection, monitoring and measurement in different materials [26, 27 and 28] from the Fracture Mechanics point of view. However, none of the methodology is applicable to on-line

crack monitoring and detection in rotors since almost all the methods use devices that have to be in contact with the material that contains the crack. Similarly, analytical study of crack, stress distribution near cracks and related issues are fully developed in Fracture Mechanics. The two important approaches of Linear Elastic Fracture Mechanics (LEFM) that describe the behavior of cracks are the Stress Intensity Approach and Energy Release Rate Approach developed by Inglis and Griffith respectively [26]. However, Elastic-Plastic Fracture Mechanics (EPFM) is used for time-independent, nonlinear behavior (i.e., plastic deformation). Parameters of interest in EPFM are Crack Tip Opening Displacement (CTOP) and the J Contour Integral.

CHAPTER 3

THE JOINT TIME –FREQUENCY ANALYSIS

3.1 INTRODUCTION

Signal processing is derived from the mathematical principles of series expansion. Equation (3.1). by which any given function *x(t)* can be expressed as the summation of other functions whose properties are known. The concept of inner product is usually used if *g(t)* is an orthonormal function. A signal is transformed or processed in order to extract useful information for diagnosis purposes. The signal is presented in a graphical form that shows salient features of the signal that may not be visible when the signal is represented in the traditional magnitude-time form.

$$x(t) = \sum_{-\infty}^{\infty} a_i g(t) \tag{3.1}$$

where a_i is the expansion coefficient and $g(t)$ is an orthogonal transformation function of known properties.

Fourier transform (FT) gives frequency information of signals. Experience has however shown that FT is suitable only for signals whose frequency contents do not change with time known as stationary signals. But most of the signals encountered in real life are non-stationary, their frequency contents change with time. In order to

efficiently analyze non-stationary or transient signals, the Joint Time-Frequency Analysis (JTFA) was developed. It gives information on how the frequency contents of signals evolve with time. Various techniques for JTFA include Short Time-Fourier Transform (STFT), Gabor Transform (GT), Wigner-Ville Distribution (WVD) and Wavelet Transform (WT) [29].

JTFA representation is classified into two types namely: linear representation and non-linear or bilinear representation [29]. Examples of linear representation techniques are STFT, GT and WT. These do not suffer cross-term interference defect and are particularly interesting and important because the signal can be regenerated or reconstructed. However, the frequency-time resolution of linear representation, with the exception of WT, may be poor. Examples of bilinear representation include WVD, Choi-Williams Distribution and Cone-Shape Distribution. These have a very good frequency-time resolution but suffer from cross-term interference; also the decomposed signal may be difficult to reconstruct. WT is used in this work therefore; the linear JTFA family will be briefly discussed in the following sections.

3.2 THE SHORT TIME FOURIER TRANSFORM (STFT)

This is the widely used traditional signal processing technique. Fourier transform (FT), Equation (3.2), gives the frequency contents of signals and it is represented as power spectrum plot, which is a graph of square of FT versus frequency, Figure 3.1(a).

$$X(\omega) = \int_{-\infty}^{\infty} x(t)e^{-i\omega t}\,dt \tag{3.2}$$

$$X(\omega, t) = \int_{-\infty}^{\infty} x(t)g(\tau - t)e^{-i\omega t}\,dt \tag{3.3}$$

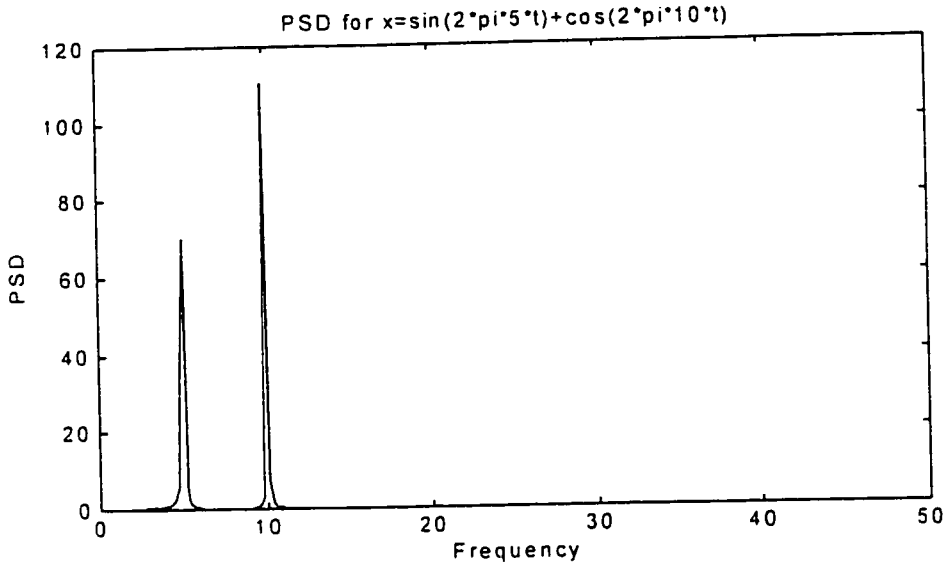

(a)

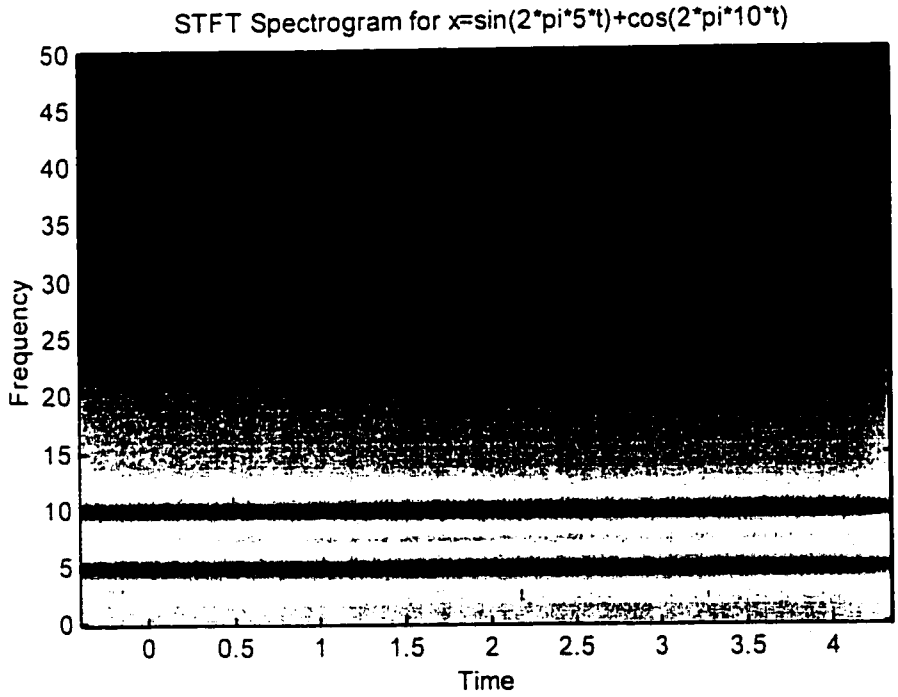

(b)

Figure 3.1 FFT analysis of $\sin(2\pi 5t) + \cos(2\pi 10t)$

(a) Spectral analysis. (b) Short Time Fourier Transform

Where $x(t)$ signal is the signal to be analyzed and $g(t-\tau)$ is a window function. The signal used in this Chapter is x(t) = sin(10π t) + cos(20π t) with a time step of 0.01 or sampling frequency of 100 Hz. In order to overcome the deficiency of FT that gives no information of the frequency time history, STFT was developed. STFT compares the signal with an elementary window function that is localized in both time and frequency. Figure 3.1(b) represents the STFT Spectrogram for sin(10π t) + cos(20π t).

Power spectrum density (PSD) is the square of Equation (3.2) and it represents the energy content of the signal at each frequency. STFT spectrogram is obtained from Equation (3.3). The window function g(t-τ) has short time duration therefore the FT of x(t)g(t-τ) reflects the local frequency properties of x(t). By moving g(t-τ) over the entire signal and repeating the same process, information on how the signal frequency changes with time is obtained. However, time-frequency behavior of a signal is not independent, frequency is inversely proportional to time. A small window time gives high frequency resolution, vice-versa. Therefore, the choice of the window function and an appropriate time interval are very important in STFT analysis and this is one of the shortcomings of the technique, there is time-frequency trade-off otherwise known as bandwidth-localization trade-off. Other shortcomings include aliasing and time window effect. Usually, Equations (3.2) and (3.3) are written in discrete forms as shown in Equations (3.4) and (3.5), respectively to facilitate the use of computer programs.

$$X(k) = \sum_{n=0}^{N-1} x(n) e^{-i2\pi kn/N} \qquad , k = 0, 1, \ldots, N \tag{3.4}$$

$$X(k,n) = \sum_{n=0}^{N-1} x(n) g(n-k) e^{-i2\pi kn/N} \qquad , k = 0, 1, \ldots, N \tag{3.5}$$

3.3 GABOR TRANSFORM (GT)

Gabor transform (GT) is an improved STFT to overcome some of the shortcomings associated with it. In 1946, Gabor represented a signal in two dimensions with time and frequency as coordinate [29]. The elementary function of GT is sampled in both time and frequency hence it gives a better time-frequency resolution and solves the problem of bandwidth-localization trade-off. GT is given by

$$x(t) = \sum_{m=-\infty}^{\infty} \sum_{n=-\infty}^{\infty} C_{m,n} h_{m,n}(t - mT) e^{jn\Omega t} \tag{3.6}$$

where $C_{m,n}$ is Gabor coefficients, $h(t)$ is Gabor elementary function [29], T and Ω denote the time and frequency sampling steps, respectively. Figure 3.2(a) represents Gabor sampling grid. The necessary condition for the existence of GT is that the sampling cell $T\Omega$ must be small enough to satisfy

$$T\Omega \leq 2\pi \tag{3.7}$$

If $T\Omega$ is too large, it may be very difficult to completely recover the original signal. On the other hand, if $T\Omega$ is too small, the representation will be redundant. Critical sampling occurs when $T\Omega = 2\pi$ and oversampling occurs when $T\Omega < 2\pi$. GT is a useful tool in computing the inverse of discrete STFT, which may be non-invertible, when window function and time are imprudently chosen [29]. GT spectrogram is similar to STFT spectrogram but with better time-frequency resolution. Unlike harmonically related orthonormal sinusoidal functions used in the Fourier series, Gabor elementary functions, in general, do not constitute an orthogonal basis. At critical sampling, GT elementary functions are linearly independent and unique; these are not true at oversampling. The

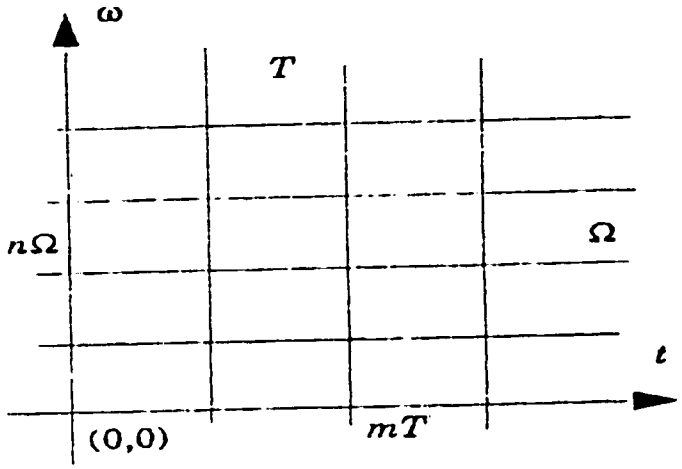

(a) Gabor sampling lattice or grid

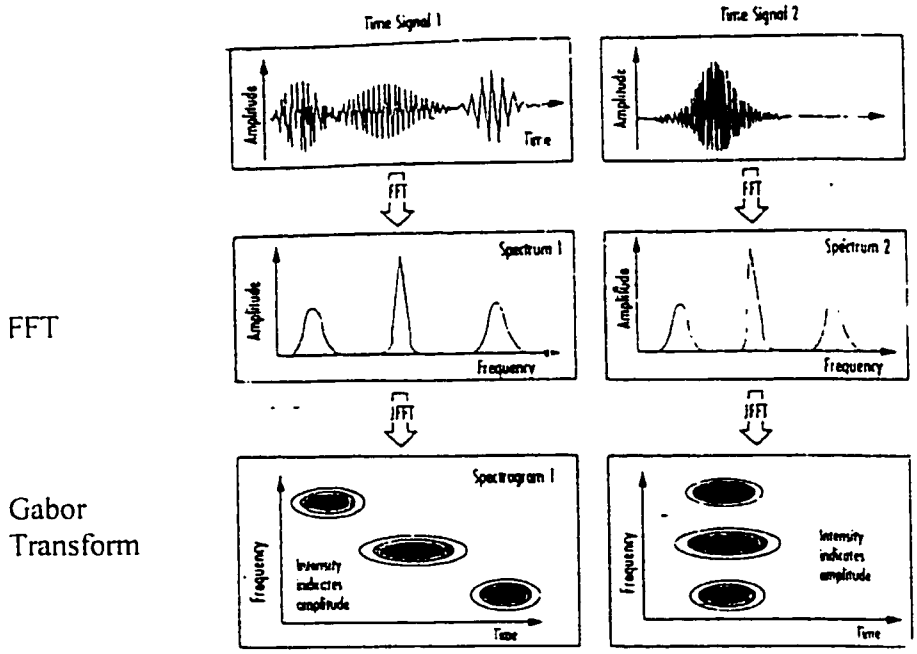

(b) Power Spectral Analysis and Gabor Spectrogram comparison graph [18]

Figure 3.2 Gabor Sampling lattice and Spectrogram

issues that deserve attention in GT include completeness, linear independence and orthogonality of the elementary functions or bases. Extensive research has been done to solve these problems; this resulted in complicated algorithms that need high level of computation. However, improvement in the computing power of computers has made this no problem. Figure 3.2(b) is a comparison between the Power Spectral Density or FFT Analysis and Gabor Analysis.

3.4 WAVELET TRANSFORM (WT)

The major shortcoming of FT and other related transforms is due to the fact that FT decomposes signals into sine and cosine waveforms that have infinite duration (Figure 3.3a). Sine and cosine waveforms are not localized in time but are highly localized in frequency and their energy content is infinitely distributed. A wavelet is a small waveform of limited duration with an average value of zero, and has its energy content concentrated in time as indicated in Figure 3.3(b). Wavelets are localized in both time and frequency domains, they are therefore a good tool for JTFA for the analysis of transient, non-stationary or time-varying phenomena. [29,30]. WT is free from the shortcomings of STFT and GT; it decomposes signals into different frequency or scale components, and studies each component with a resolution matched to its scale as shown in Figure 3.3 (c).

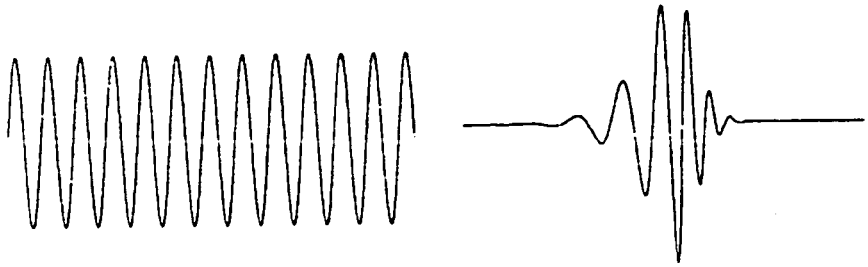

(a) Sine wave. (b) Wavelet basis.

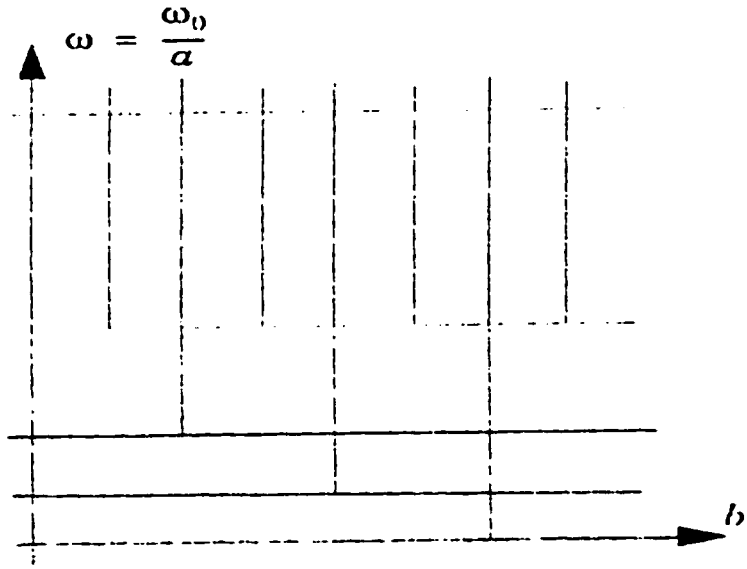

(c) Wavelet lattice

Figure 3.3.Waveform and wavelet [30]

Like FT, STFT and GT, WT can be depicted as a continuous transform (CWT) or discrete transform (DWT). Mathematically,

$$W(a,b) = \frac{1}{\sqrt{a}} \int x(t)\psi\left(\frac{t-b}{a}\right)dt \tag{3.8}$$

$$W(a,b) = \frac{1}{\sqrt{a}} \sum_{n} x(n)\psi\left(\frac{n-b}{a}\right) \tag{3.9}$$

where W(a, b) is wavelet expansion coefficients, ψ(t) is the mother wavelet or wavelet basis, a is called the dyadic scale defined, for discrete transformation, as

$$a = 2^{j}\ ,\ j \in \mathbf{Z} \tag{3.10}$$

j represents scale level, which is related to frequency, and b is the dyadic translation defined as

$$b = \mathrm{k}a\ ,\ \mathrm{k} \in \mathbf{Z} \tag{3.11}$$

Where k represents time or space location.

WT is the multiplication of a signal $x(t)$ with an analyzing window $\psi(t)$ called the mother wavelet shifted in time by parameter b and dilated by the scale parameter, a. The scale, a, is related to the frequency, it is inversely proportional to frequency ($f \alpha\ 1/a$) according to Equation (3.8). Hence, WT can be represented as either frequency-time or scale-time representation. Unlike STFT and GT that use a window of constant width, WT uses an analyzing function (mother wavelet) scaled in time and magnitude to

have a fixed number of oscillations inside the envelope. Therefore, the mother wavelet is compressed for high frequencies and dilated for low frequencies. The mathematical theories of WT are rigorous but well established in the literature [30]. Many wavelet bases are orthonormal bases on $L^2(R)$ space. $L^2(R)$ is Hilbert space of square integrable functions, this makes WT appropriate for multiresolution analysis.

3.4.1 CHARACTERISTICS OF WAVELET

The characteristics of wavelet that make it a useful tool in signal processing are as follows:

1. It is a two-dimensional (frequency/scale and time) expansion set

$$x(t) = \sum_k \sum_l W_{l,k}(a,b)\psi_{l,k} \tag{3.12}$$

$x(t)$ is the signal, $W_{l,k}$ is the expansion coefficient and $\psi_{l,k}(t)$ is the wavelet basis or set. The 2-D expansion set is achieved from the definition of the mother wavelet or the wavelet basis

$$\psi_{l,k}(a,b) = \frac{1}{\sqrt{a}}\psi\left(\frac{n-b}{a}\right) \tag{3.13}$$

a and b are as defined in Equations (3.10) and (3.11).

2. It gives a frequency-time or scale-time localization.

3. Discrete wavelet expansion can be calculated with order N $O(N)$ operations. This means the number of floating-point multiplication and addition increase linearly with the

length of the signal, N. Continuous wavelet transform requires $O(NlogN)$ operations like the FFT

4. Most wavelet expansions are from a single scaling function by simple scaling and translation. A scaling function is a basic function from which wavelet bases are derived.

5. Almost all wavelet expansion satisfy multiresolution conditions. A signal can be decomposed into many levels each of which represents a resolution at a particular frequency.

6. The lower resolution coefficients can be calculated from the higher resolution coefficients by a tree-structured algorithm called a filter bank. The coefficients can also be obtained by numerically solving equations of the properties of the coefficients.

7. It can represent sharp corner or discontinuity in signals better than any other transform.

8. The original signal can be completely reconstructed or recomposed.

3.4.2 WAVELET BASES

The choice of a wavelet basis is very important in the application of wavelet transform in signal analysis since this affects the results. A good wavelet basis should be highly localized in time and frequency [18, 23]. Wavelet basis can be expressed in either time/space domain or frequency domain, however, some wavelet do not have explicit expression [17]. It should be noted that while wavelets are compact in the sense that they have a definite beginning and ending in the time/space domain; they may not be

compact in the frequency domain since Fourier transform extends over an infinite frequency range. While wavelet in time/space domain are real and their coefficients can be determined by filter bank, wavelets in frequency domain are usually complex having both the real and imaginary parts, this facilitates the calculation of an additional parameter, the phase (arctan (imaginary part/real part)), that can detect singularity in signals and is less affected by the type of wavelet basis used [31]. The following are the most common wavelet bases.

3.4.2.1 The Modulated Gaussian Wavelet

This is highly localized in both time and frequency [23, 31]. It is does not have scaling function and hence does not form orthogonal wavelets.

$$\psi(t) = \pi^{-1/4}(e^{-i\omega_o t} - e^{-\omega_o^2})e^{-t^2/2} \tag{3.14}$$

$$\psi(\omega) = \pi^{-1/4}(e^{-(\omega-\omega_o)^2/2} - e^{-\omega^2}e^{-\omega_o^2}) \tag{3.15}$$

$$\omega_o = \pi(2/\ln 2)^{1/2} \tag{3.16}$$

Figure 3.4 represents the Gaussian mother wavelet or wavelet basis.

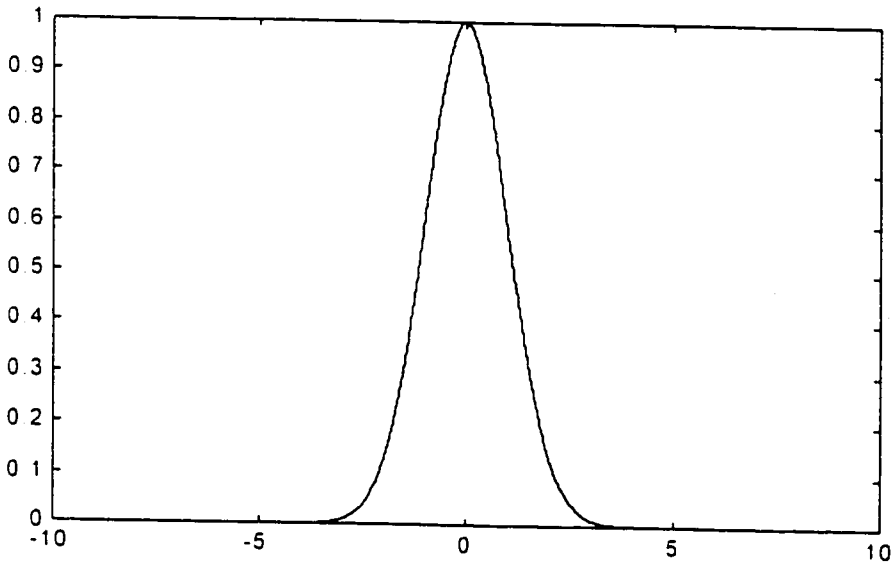

Figure 3.4 Gaussian wavelet

3.4.2.2 The Daubechies Wavelet (dbN)

This is an orthogonal wavelet that has found wide applications. N represents the order of the wavelet and can only take integer values. The regularity of the wavelet increases with N. dbN is not a symmetric wavelet. When N is 1, the simplest wavelet known as Haar wavelet is formed [17, 23]. Figure 3.5 represents the graph of Daubechies scaling and wavelet functions for N = 20.

$$\psi_{j,k}(t) = 2^{j/2}\psi(2^j t - k),\ j,k \in \mathbf{Z} \tag{3.17}$$

$$\psi(\omega) = (\log a)^{-1/2}\begin{cases} 0, \omega < l \\ \sin\left[\frac{\pi}{2}v\left(\frac{\omega - l}{l(a-l)}\right)\right], l \le \omega \le al \\ \cos\left[\frac{\pi}{2}v\left(\frac{\omega - l}{al(a-l)}\right)\right], al \le a^2 l \\ 0, \omega < a^2 l \end{cases} \tag{3.18}$$

$$l = \frac{2\pi}{ba^2 - 1} \tag{3.19}$$

v is a C^k (or C^∞) function and satisfies

$$v(x) = \begin{cases} 0, x \le 0 \\ 1, x \ge 1 \end{cases} \tag{3.20}$$

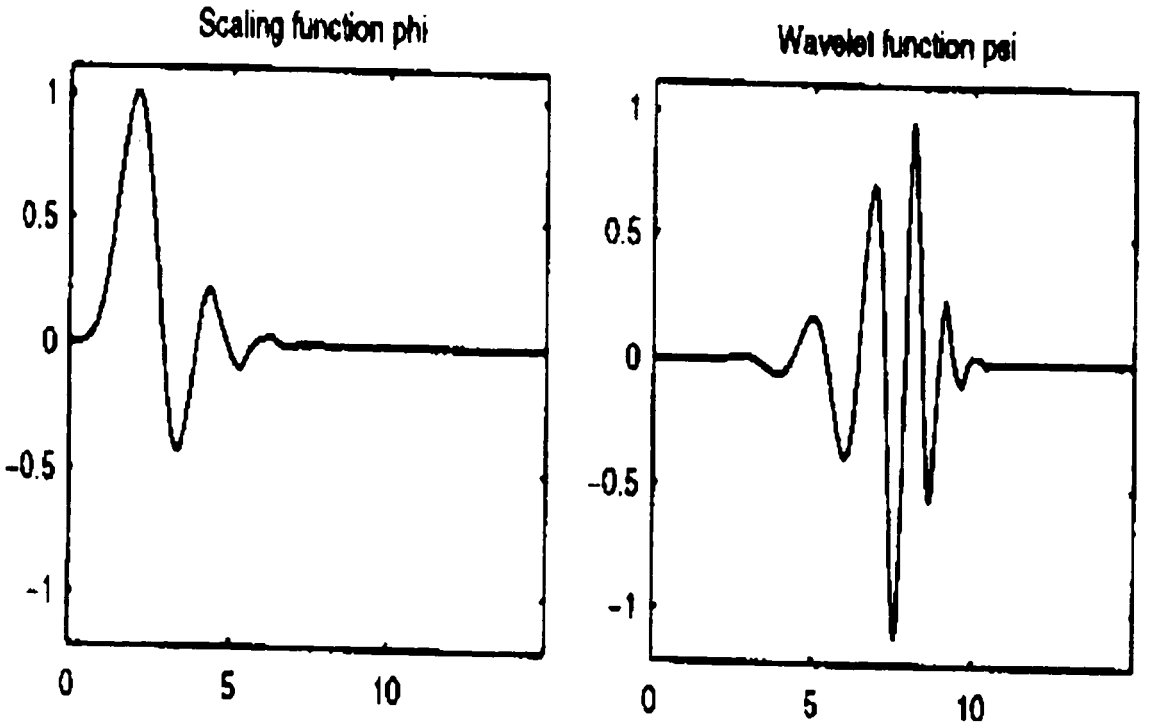

Figure 3.5 Daubachies (db20) wavelets [17]

3.4.2.3 Meyer Wavelet

This is derived from the Daubechies (dbN) wavelet basis. The Daubechies wavelet is orthogonal but not symmetric. Meyer wavelet is both orthogonal and symmetric [17, 23]. Figure 3.6 shows the graph of Meyer scaling and wavelet functions. Meyer wavelet is expressed in the frequency domain as

$$\psi(\omega) = \frac{1}{\sqrt{2\pi}} e^{i\omega/2} (\psi(\omega) + \psi(-\omega)) \tag{3.21}$$

$\psi(\omega)$ represents Daubechies wavelet

3.4.2.4 Mexican-Hat Wavelet

The function of this wavelet is proportional to the second derivative function of the Gaussian probability density function. It is not an orthogonal function since its scaling function does not exist [17,23]. If the function is plotted and rotated about a symmetric axis, a shape similar to a Mexican hat is obtained. Figure 3.7 represents the graph of the Mexican-Hat wavelet

$$\psi(t) = \frac{2}{\sqrt{3}} \pi^{-1/4} (1 - t^2) e^{-t^2/2} \tag{3.22}$$

$$\psi(\omega) = \frac{2}{\sqrt{3}} \pi^{-1/4} \omega^2 e^{-\omega^2/2} \tag{3.23}$$

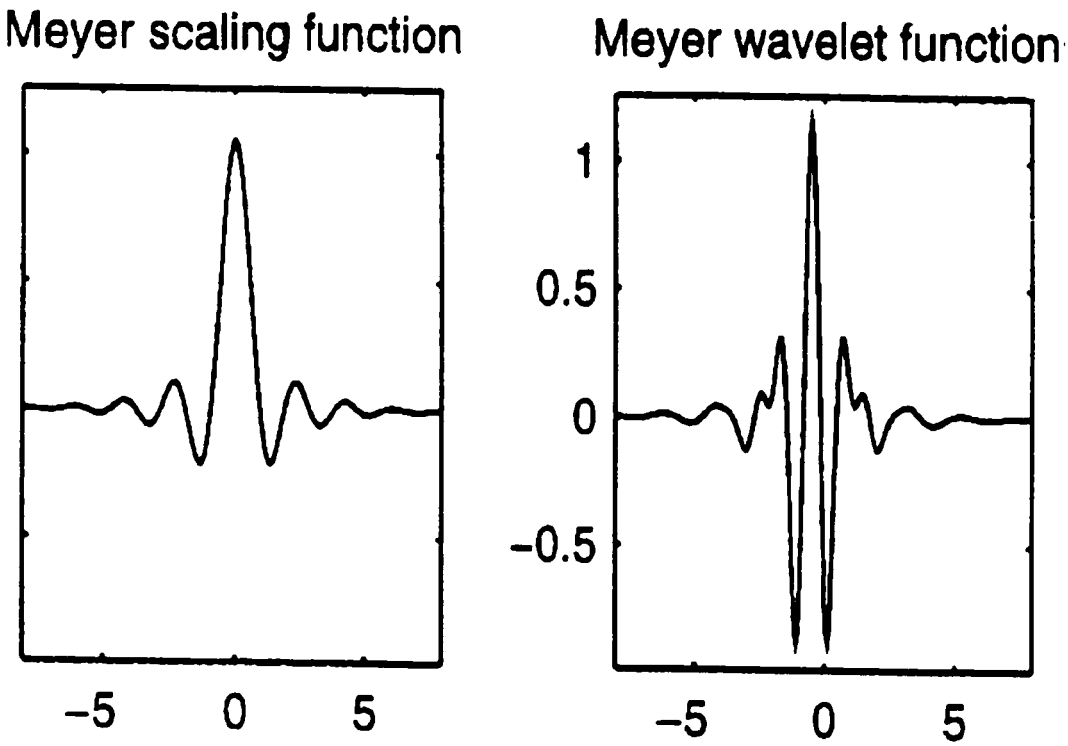

Figure 3.6 Meyer wavelet [17]

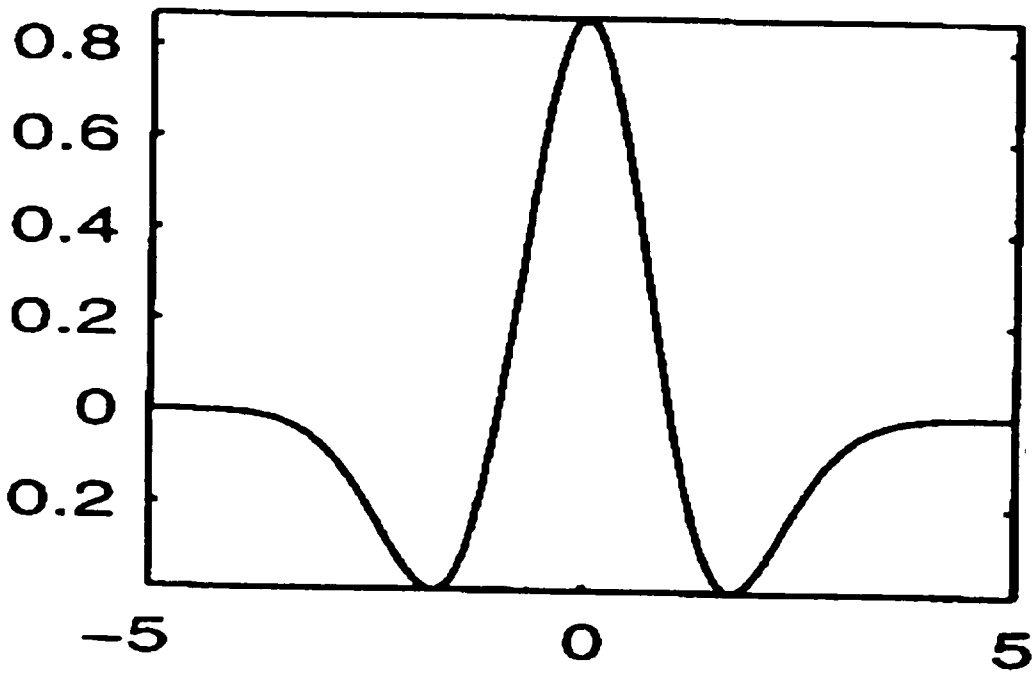

Figure 3.7. Mexican-Hat wavelet [17]

3.4.2.5 Morlet Wavelet

This is a non-orthogonal symmetrical function without a scaling function [17]. It is expressed as

$$\psi(t) = Ce^{-t^2/2}\cos(5t) \tag{3.24}$$

C is the normalizing factor. Figure 3.8 shows the graph of Morlet wavelet

3.4.2.6 Harmonic Wavelet

This is the only known wavelet that is compact in frequency domain and also orthogonal without a scaling function. Newland [24, 32] recently developed it. It can be considered as a Daubechies (DbN) wavelet with an infinitely large N.

The wavelet is a complex function and both its magnitude and phase can be used in signal analysis.

$$\psi(t) = \frac{e^{i4\pi t} - e^{i2\pi t}}{i2\pi t} \tag{3.25}$$

$$\psi(\omega) = \begin{cases} 1/2\pi, 2\pi \le \omega \le 4\pi \\ 0, elsewhere \end{cases} \tag{3.26}$$

Figure 3.9 shows the graph of harmonic wavelet; the upper graph represents the real part of Equation (3.25) while the lower graph represents its imaginary part.

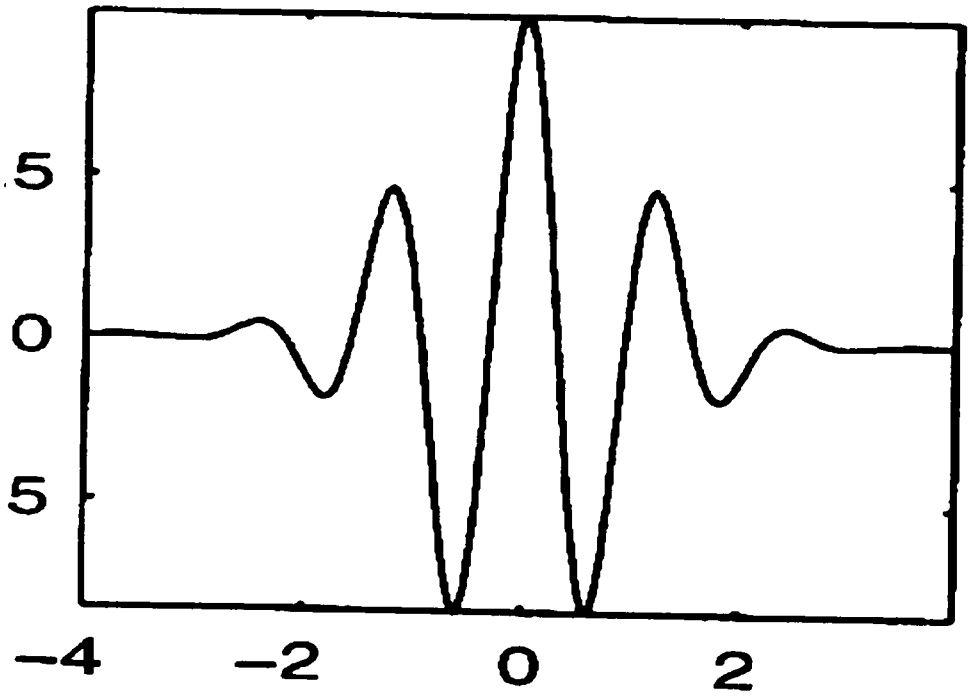

Figure 3.8 Morlet wavelet [17]

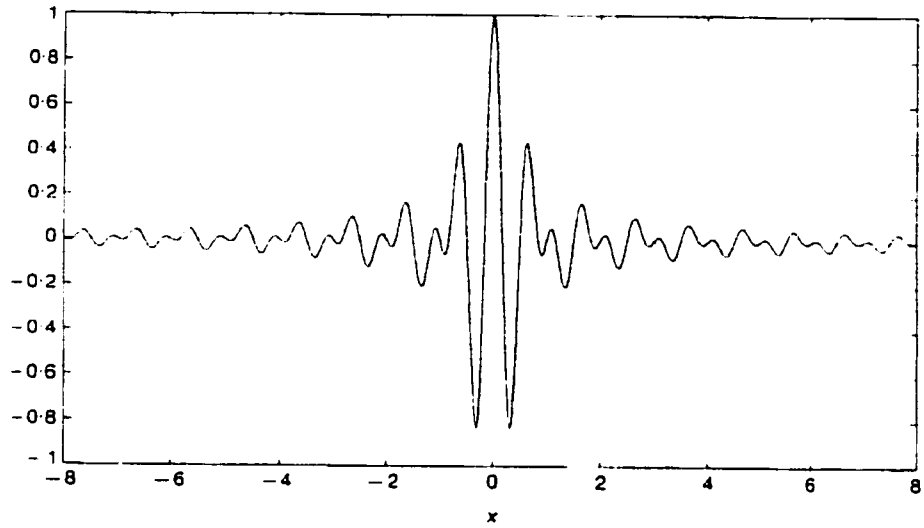

(a) Real part

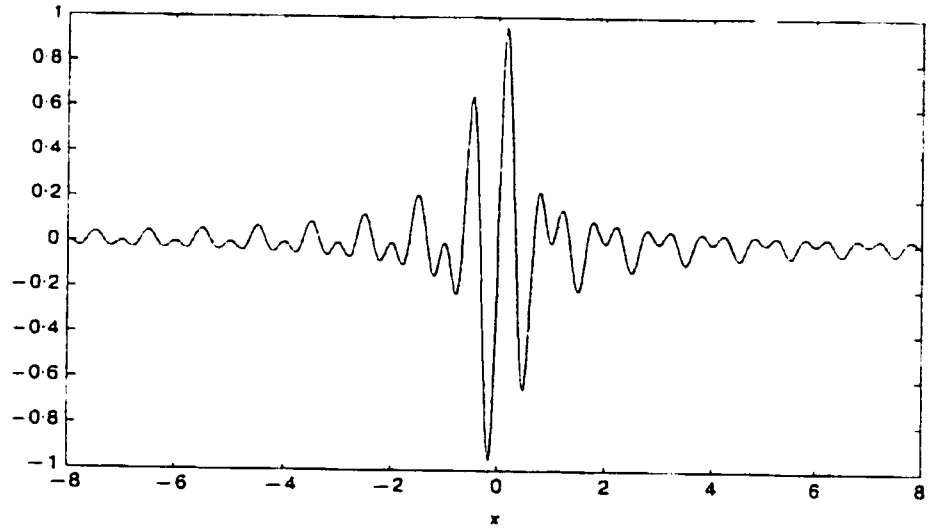

(b) Imaginary part

Figure 3.9. Harmonic wavelet [32]

3.4.3 DETERMINATION OF EXPANSION COEFFICIENT

Wavelet transform (WT) involves the determination of expansion coefficients, $W(a, b)$, of Equations (3.8) and (3.9) by the multiplication of the signal $x(t)$ or $x(\omega)$ and a mother wavelet $\psi(t)$ or $\psi(\omega)$, respectively. The signal can be reconstructed by the convolution of $W(a, b)$ and $\psi(t)$ or $\psi(\omega)$, Equation (3.12). $W(a, b)$ or $W(j,k)$ for j, k $\in$ **Z** gives frequency-time information when $x(\omega)$ and $\psi(\omega)$ are used. This can be written, in general, as

$$W(j,k) = \sum_{j}\sum_{k} 2^{j} \int_{\omega} e^{j\omega k 2^{j}} \psi(\omega).X(\omega)d\omega \qquad (3.27)$$

where $\psi(\omega)$ and $X(\omega)$ are the Fourier transforms of the wavelet basis and the signal. Figure 3.10 shows a simple algorithm that can be used to calculate wavelet coefficients [24, 33]. On the other hand, $W(a, b)$ or $W(j,k)$ from the convolution of $x(t)$ and $\psi(t)$ gives scale-time information. This can be achieved by numerically solving the simultaneous equations obtained from the properties of the coefficients [32] or by using Mallat tree algorithm that uses Finite Impulse Response (FIR) filters [17] as shown in Figure 3.11.

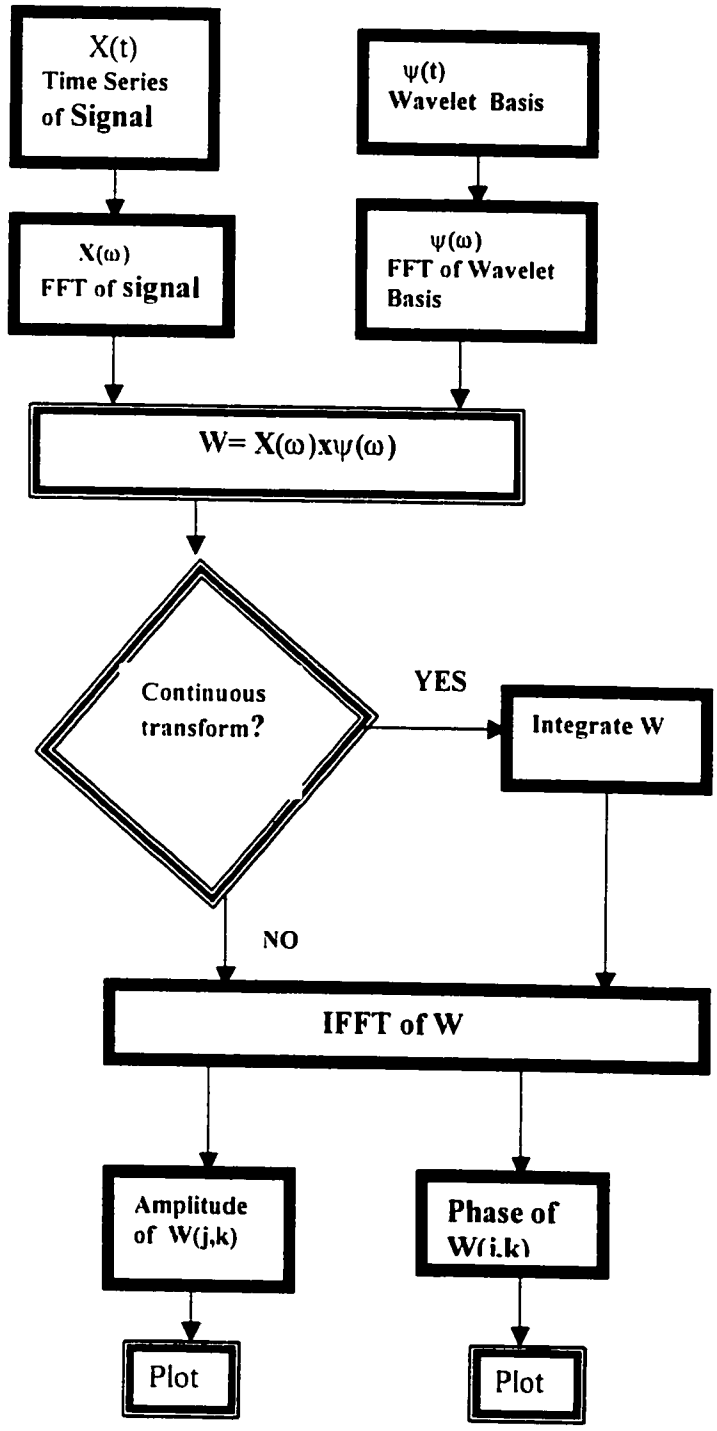

Figure 3.10 WT Algorithm in frequency domain.

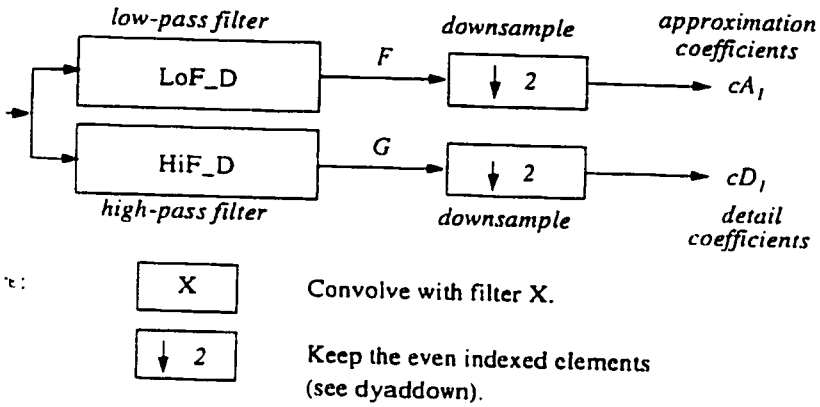

(a) FIR filter single level decomposition [17]

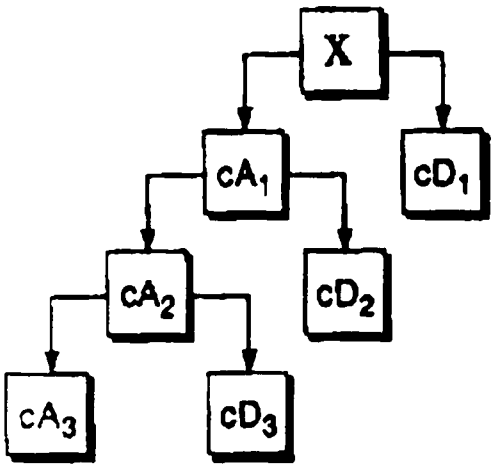

(b) Multi-level decomposition [17]

Figure 3.11 FIR filter decomposition

Wavelet transform via FIR filter involves passing the signal through lowpass and highpass filters then dowmsampling to give approximate coefficients (cA) and detailed coefficients (cD) respectively [17, 29, 30]. Dowmsampling means neglecting all coefficients that occupy odd position in the series, the result is a signal with half the original sampling points. FIR filters are invertible to reconstruct the signal. This is done by upsampling cA and cD before passing them through lowpass and highpass filters respectively, the resulting signals are then added together, Figure 3.12. Upsampling means inserting zeros in-between the coefficients to double the sample points. Whatever wavelet transform method is employed, the resulting coefficients, $W(j,k)$, is a 2-D array that can be represented in a number of ways that are discussed in the next section.

3.4.4 GRAPHICAL PRESENTATION OF WAVELET TRANSFORM

The goal of any signal processing method is to explicitly express certain characteristics, usually, frequency related features, of a signal in a way to deduce useful information that are helpful in problem diagnostics. An informative display or visualization of W(j,k) is very important for effective interpretation and presentation of results. There are three ways of presenting W(j,k) graphically namely: level presentation, scalogram or intensity plot and 3-D plot. The following graphs are obtained by using the Daubachies wavelet (DbN) of the Matlab Wavelet toolbox, which uses FIR filter. Different values of N (6 and 12) were used and the same results were obtained as shown in Figures 3.13-2.15. Increase in N only increases the regularity of the Daubachies wavelet.

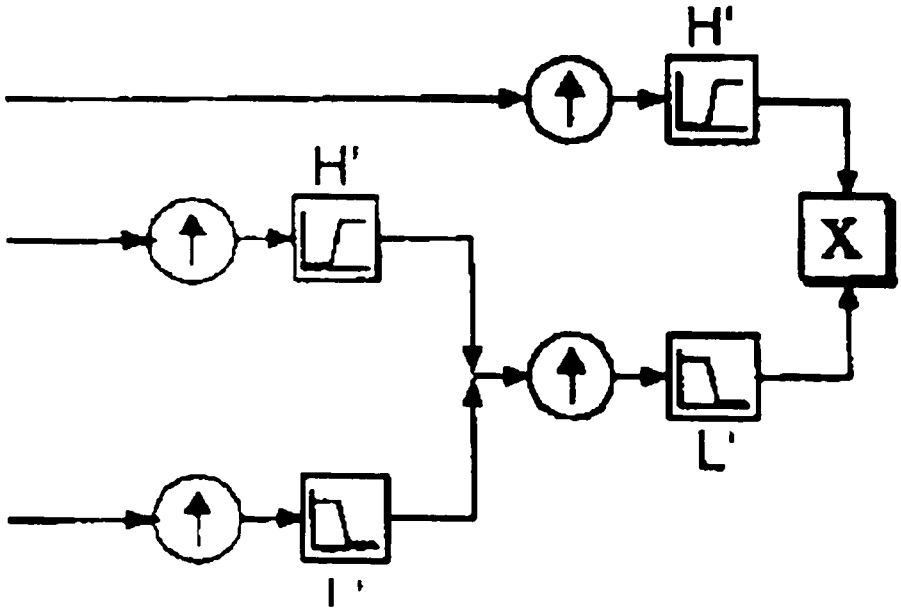

Figure 3.12 FIR Reconstruction [17]

3.4.4.1 Level Presentation

Wavelet transform decomposes any signal into components, each component is called a level and the levels are numbered from 1 upward [17]. The scale ($a = 2^j$) depends on the level and the total number of levels depends on the length, N, of the signal to be analyzed. Usually, $N = 2^n$ meaning that there are n levels. However, n can be chosen arbitrarily and may not be restricted by N. The magnitude versus space (or time) graph of each level can be plotted. Figure 3.13 shows the level representation of $x = \sin(10\pi t) + \cos(20\pi t)$ with sampling frequency of 950 Hz using db6 and db12 wavelet. It can be observed that level 6 and level 7 are more prominent than other levels since their magnitudes are high compared with others, this suggests the presence of two frequency components.

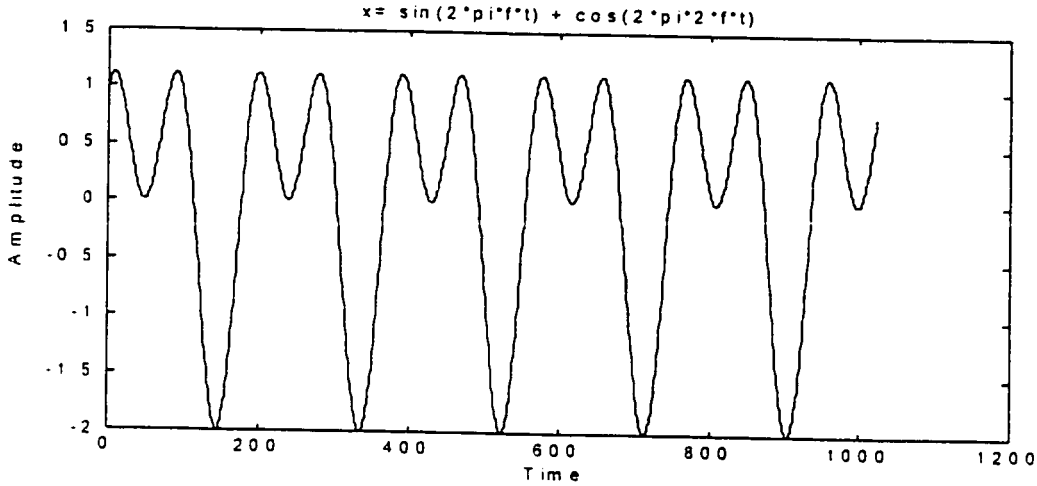

Fig.3.13 (a) Graph of $\sin(10\pi t)+\cos(20\pi t)$

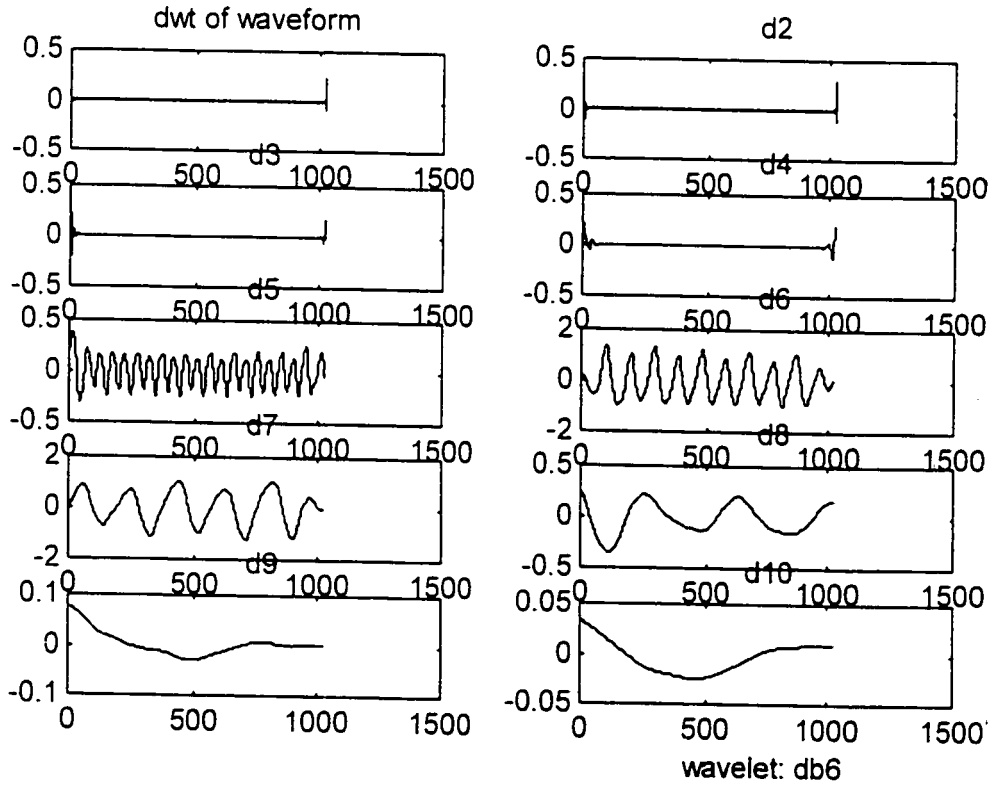

Fig.3.13 (b) DWT (Db6) of $\sin(10\pi t)+\cos(20\pi t)$

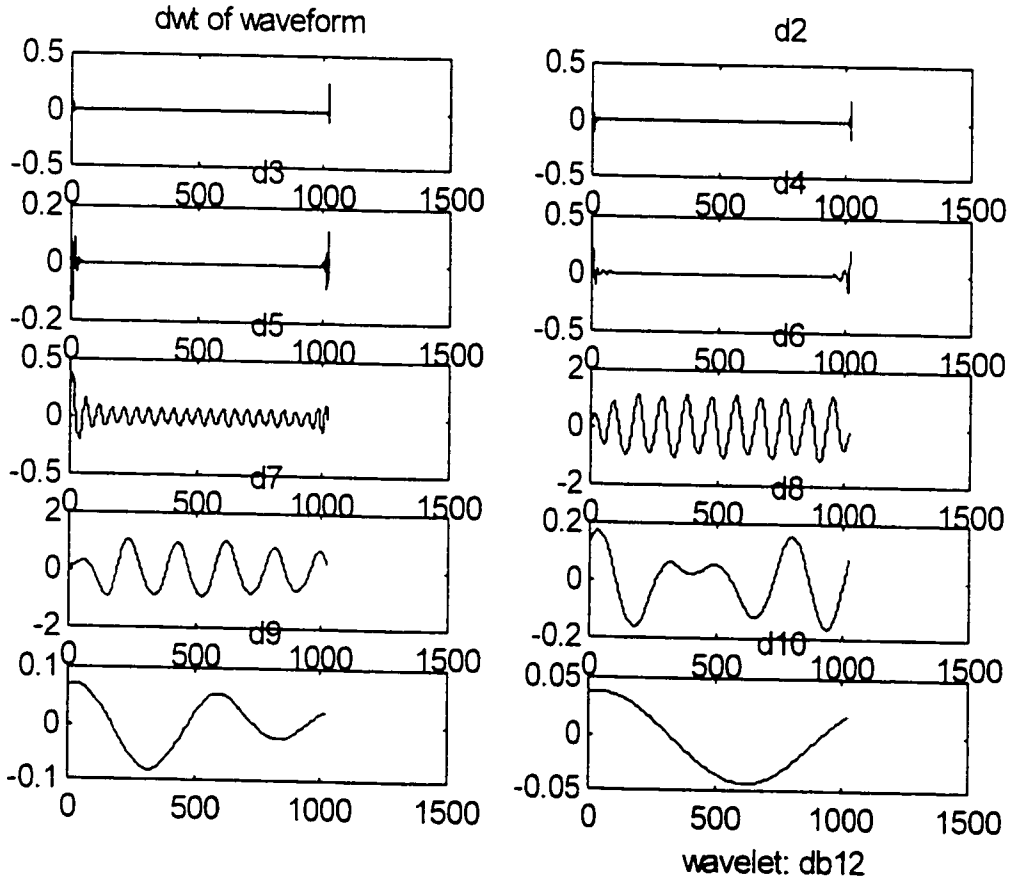

Fig.3.13 (c) DWT (Db12) of $\sin(10\pi t) + \cos(20\pi t)$

Figure 3.13 Wavelet Level Representation of x = Sin(10πt) + Cos(20πt)

3.4.4.2 Scalogram

This is similar to the STFT spectrogram. Newland [20] called it wavelet map. It is either a 2-D contour plot of the mean-square value of *W(a,b)* [20, 31] or an intensity (or image) plot of the mean-square value of *W(a,b)*. Figure 3.14 shows the scalogram of the same signal represented in Figure 3.13.

3.3.4.3 3-D Presentation

This is a 3-D graph of the square of magnitude (energy) or phase of W (m, n) plotted vertically on plane containing the plot of scale versus time. Newland [20] referred to it as mesh of wavelet map. It is also known as space (or time)-scale energy distribution graph [36]. Figure 3.15 shows the 3-D for DWT of signal $x = \mathrm{Sin}(10\pi t) + \mathrm{Cos}(20\pi t)$.

Db6 Db12

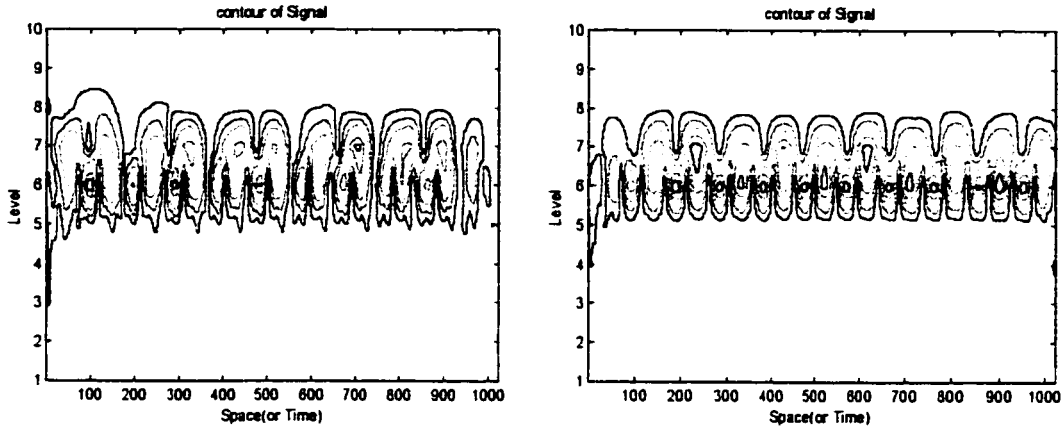

Fig 3.14 (a). Contour plot for DWT of $\sin(10\pi t)+\cos(20\pi t)$

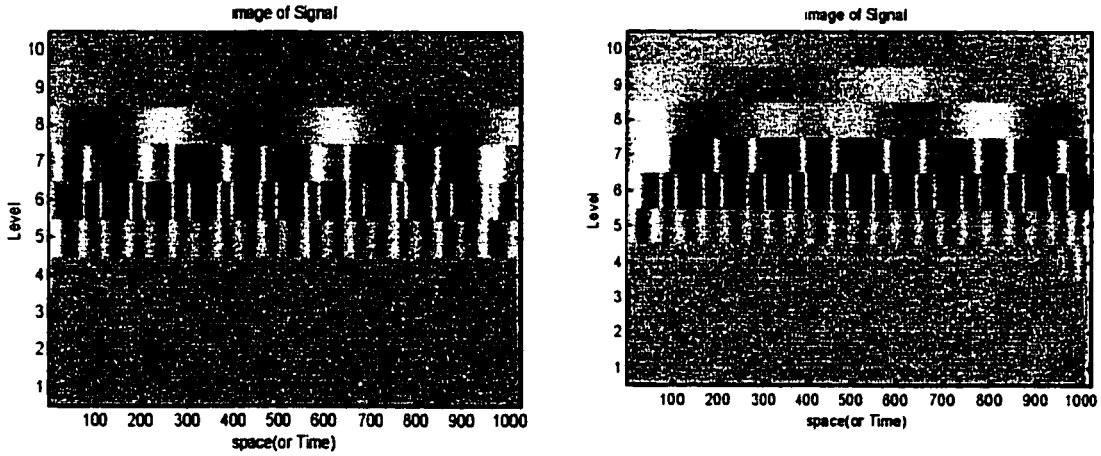

Fig 3.14 (b). Intensity/image plot for DWT of $\sin(10\pi t)+\cos(20\pi t)$

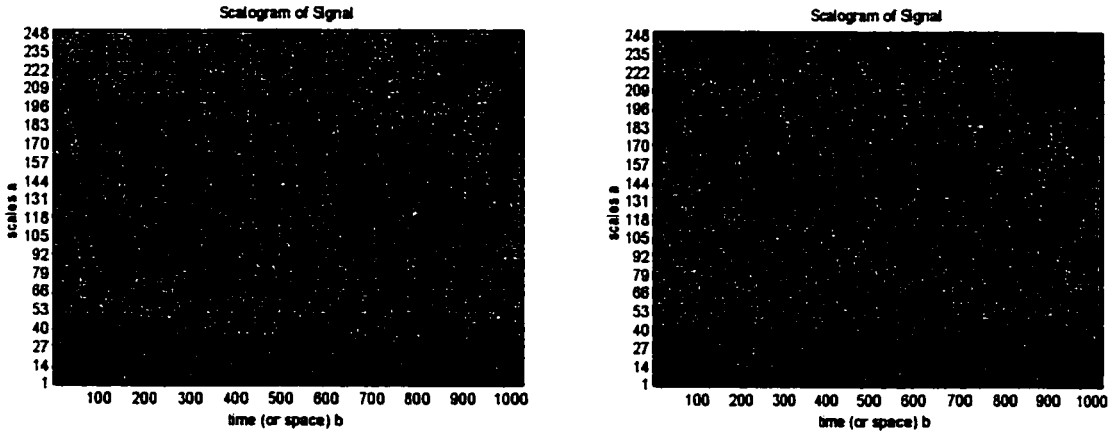

Fig. 3.14 (c). Scalogram for CWT of $\sin(10\pi t)+\cos(20\pi t)$

Figure 3.14. 2-D Representation or Scalogram of Sin(10πt) + Cos(20πt)

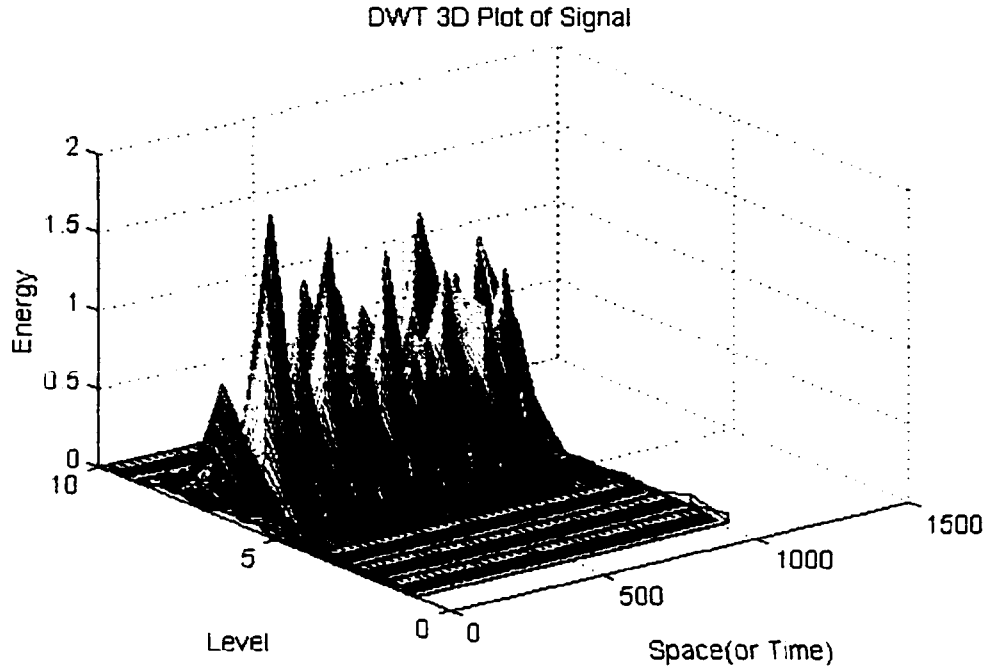

Fig. 3.15 (a) DWT (Db6) of $\sin(10\pi t)+\cos(20\pi t)$

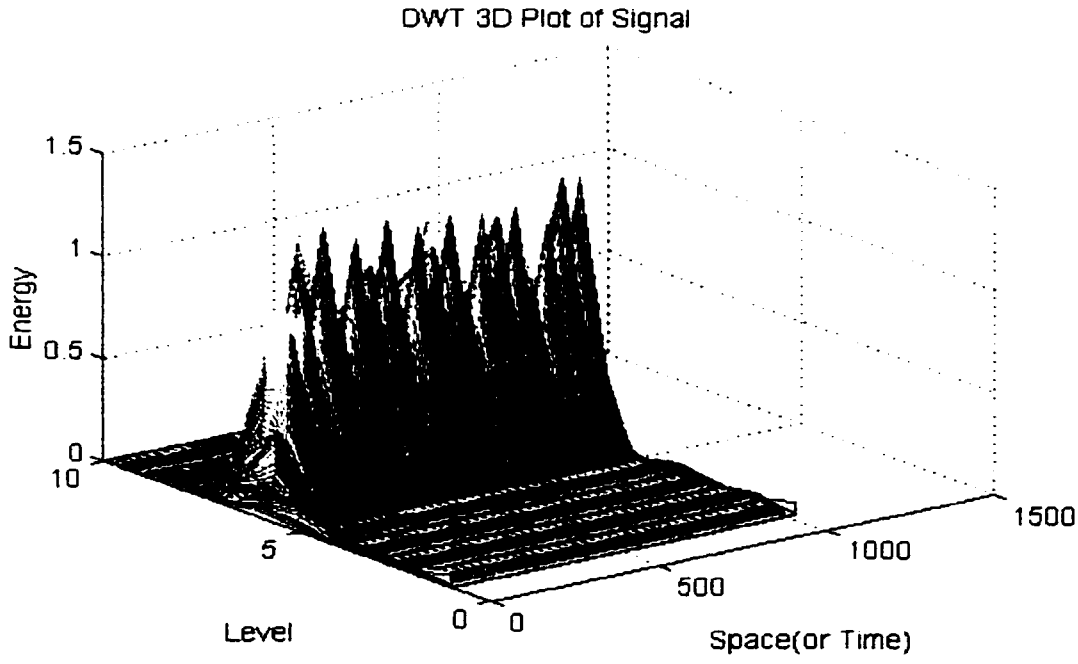

Fig. 3.15 (b). DWT (Db12) of $\sin(10\pi t)+\cos(20\pi t)$

Figure 3.15. Scale-time energy distribution for DWT of $\sin(10\pi t)+\cos(20\pi t)$

3.4.5. WAVELET TRANSFORM OF A TRANSIENT SIGNAL

Wavelet transform is suitable for analyzing both transient and stationary signals. Graphical representations of WT of a stationary signal were presented above. It is a good idea to know how graphical representations of WT of a transient signal will look like. Figure 3.16 shows the graphical representation of a chirp signal with frequencies range of 0 to 150 Hertz. which is defined as

```
t=0:1/1000:3
y = chirp(t,0,1,150)
```

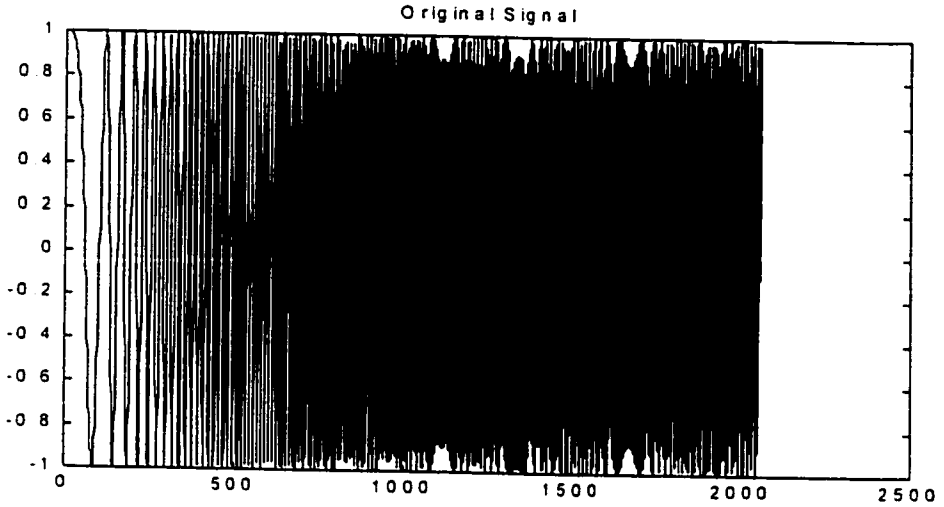

(a)

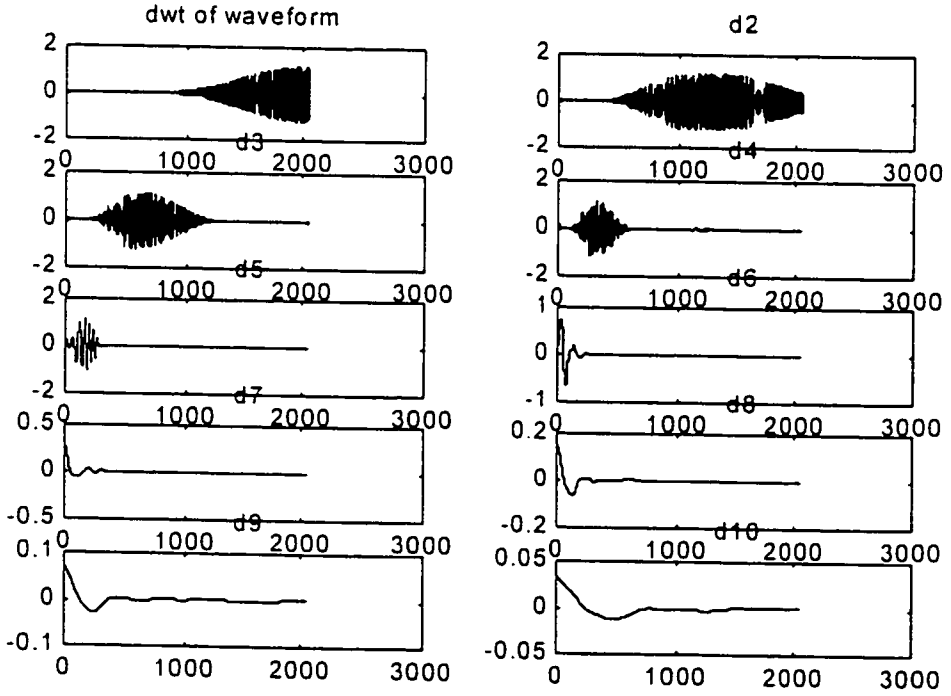

(b)

Fig. 3.16. (a) Chirp signal. (b) Level representation of DWT Db12

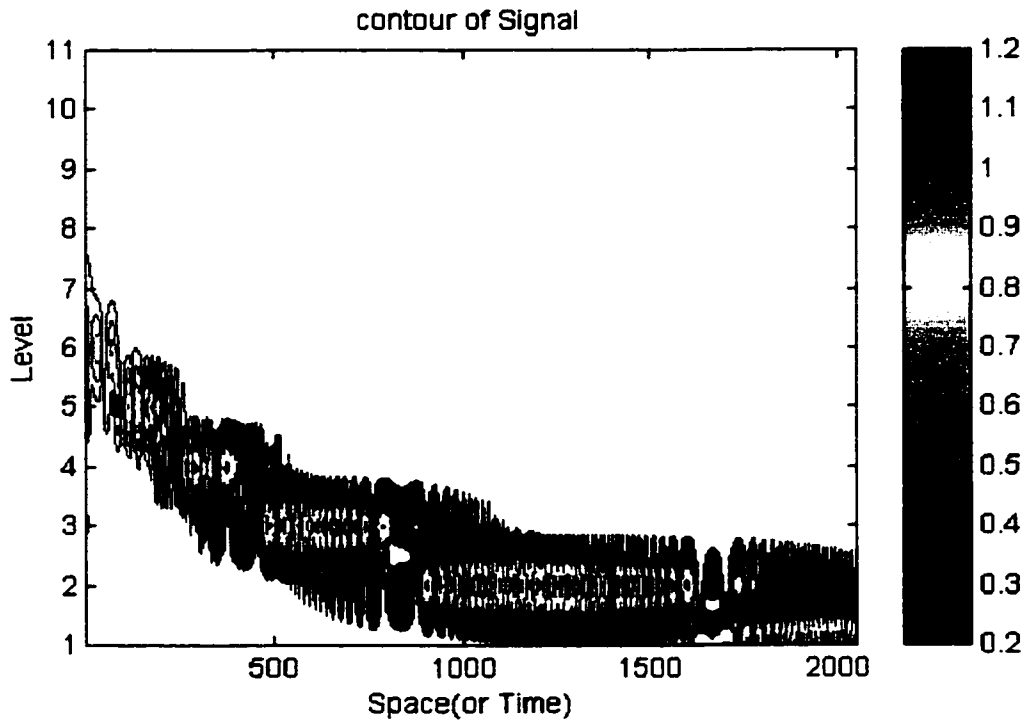

(c)

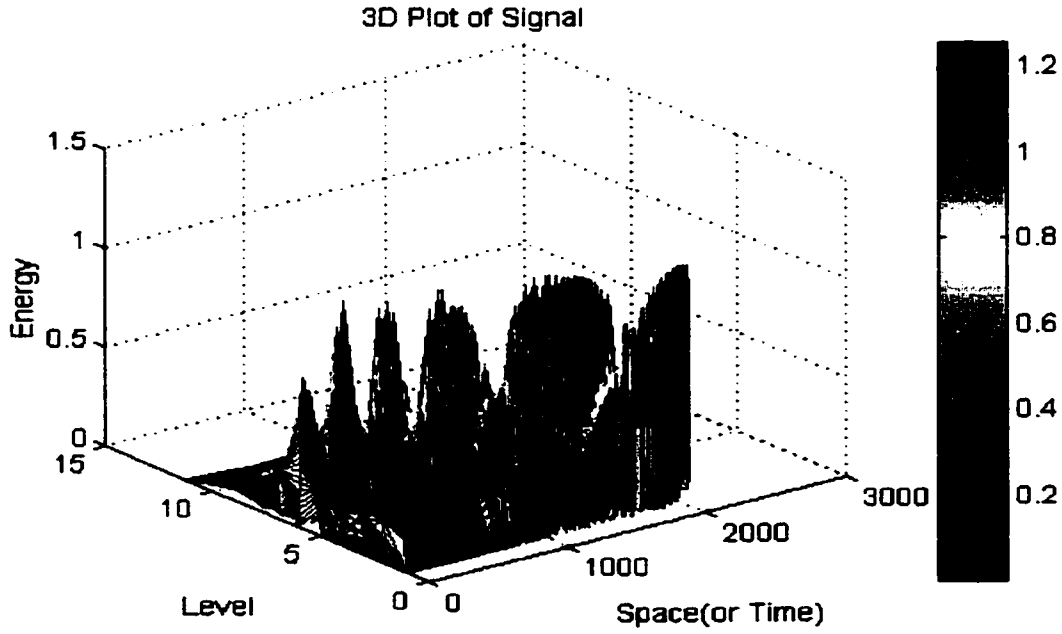

(d)

Fig. 3.16 Contd. (c) Db12 DWT Scalogram. (d) Db12 DWT 3-D plot

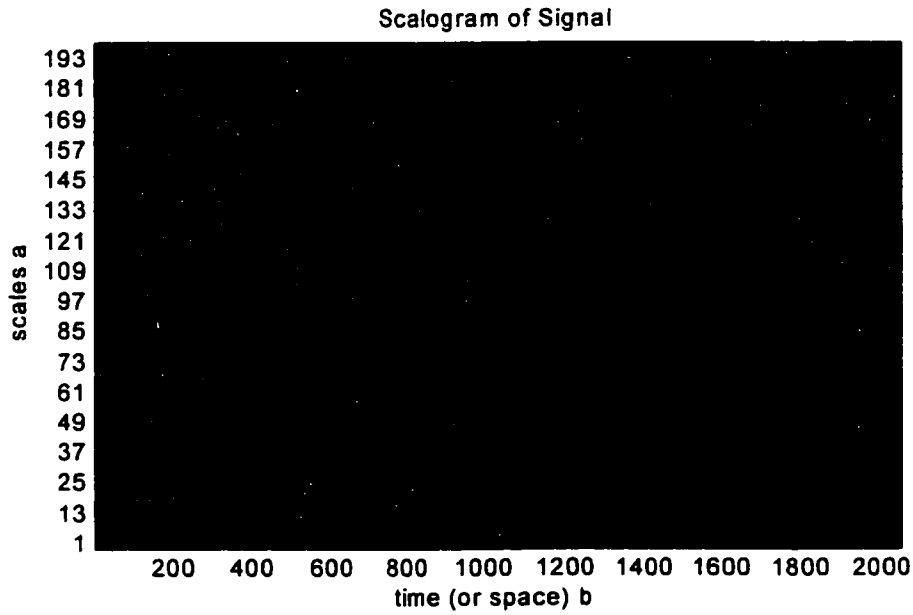

(e) Db12 CWT Scalogram

Figure 3.16 DWT and CWT of a chirp signal

3.5 INTERPRETATION OF WAVELET TRANSFORM (WT) GRAPHS

In machine vibration diagnosis, the frequency contents and their evolution with time are very important. Unlike FT and STFT that give frequency information directly, WT gives scale and space information. However, scale and space can be converted to frequency and time, respectively. This section examines works that have been done on proper interpretation of WT graphs and presents a new method of converting scale to frequency.

Misiti et al [17] defined the relationship between frequency and scale as an inverse relationship, i.e. $f \alpha \, 1/a$. This is the relationship used by most authors that expressed wavelet equation according to Equation (3.13). Newland defined wavelet function as

$$\psi_{j,k} = \psi(2^j t - k) = \psi(at - k) \tag{3.28}$$

$$j, k \in \mathbf{Z}$$

The reason for the difference in the relationship between frequency and scale according to Misiti et al [17] and Newland [20] is obvious when Equations (3.13) and (3.28) are compared. Equation (3.13) is $\psi_{j,k} = \frac{1}{\sqrt{a}}\psi\left(\frac{t-b}{a}\right) = \frac{1}{\sqrt{a}}\psi\left(\frac{t}{a} - k\right)$

For dyadic discrete wavelet, Newland [20] stated that if a signal has a length of record duration T and 2^n sample points, then the space or time variable can be replace by t/T and the sampling interval is $1/2^n$. The period of identical wavelets at level j is $1/2^j$ and their fundamental frequency is 2^j cycles/unit time. He reported that the DWT (Db20) a signal of time span of 1.2 second with sample points of 2048 and sampling frequency

of 1.66KHz at level 8 has frequency range centered about 208Hz. And at level 5 has 26Hz but he did not give any expression for the relationship between f and a. However, from the statement of relationship between fundamental frequency and scale stated above, the following relationship can be deduced

$$f = Ca;\ a = 2^l \text{ and } C = 0.8125 \tag{3.29}$$

Sabaneh [33] defined wavelet function according to Equation (3.13) but he gave a different relationship between f and a. The relationship is

$$a = \sqrt{\frac{f_s}{f}} \tag{3.30}$$

where f_s is an arbitrary constant that depends on the type of wavelet used. For Daubechies wavelet, he used $f_s = 4.188$. In the results he presented, all levels were negative, which means that the actual relationship is

$$\frac{1}{a} = \sqrt{\frac{f_s}{f}} \tag{3.31}$$

Either Equation (3.30) or (3.31) does not conform to the definition of wavelet function he gave. However, $a = 2^l$ only for dyadic wavelet. Any other value, apart from 2 may be used to get another family of wavelet known as M-band wavelet packet. M can take any value [17, 30, 36] this might be what he intended.

Graham-Hansen and Dorize [34] also expressed wavelet function as depicted by Equation (3.13) and described the relationship between f and a for continuous Morlet wavelet as

$$a = \frac{\omega_0 f_s}{2\pi f} = \frac{0.796 f_s}{f} \tag{3.32}$$

where f_s is the sampling frequency, $\omega_o = 5$ and f is the frequency that corresponds to a.

The algorithm according to Misiti et al [17] in MATLAB Wavelet Toolbox was used and attempt was made to establish the relationship between f, f_s and a for Daubachies wavelet that will be used to analyze experimental vibration data. The results are presented in Table 3.1 and Figure 3.17. Table 3.1 is a summary of the results that were obtained when Discrete and Continuous Daubachies (Db12) Wavelet Transforms were applied on sine signals of varying frequency for three different sampling frequencies (100 Hz, 200 Hz and 1000 Hz). Figure 3.17 represents the graph of frequency against Scale for DWT and CWT at different sampling frequencies. The curves confirm the inverse relationship between frequency and scale; the equations on the graphs represent this relationship. R^2 measures the correlation between the points, the closer the value of R^2 to one the better.

Table 3.1 Sampling frequency, frequency and scale from DWT and CWT of $\sin(2\pi ft)$

Sin(2*pi*f*t)					
	DWT			CWT	
		Level	Scale	Scale	loga/log2
F_s	f(Hz)	j	$a = 2^j$	a-avrg	j (Level)
100	5	4	16	17.5	4.13
	10	3	8	9.93	3.31
	20	2	4	4.5	2.17
	40	1	2	2	1.00
200	2	6	64	86	6.43
	4	5	32	42	5.39
	8	4	16	22	4.46
	16	3	8	10.5	3.39
	32	2	4	4.5	2.17
	64	1	2	3	1.58
1000	10	6	64	84	6.39
	20	5	32	41	5.36
	30	5&4	32&16	27	4.75
	40	4	16	20	4.32
	50	4	16	16.5	4.04
	60	4&3	16&8	14	3.81
	80	3	8	10	3.32
	160	2	4	5	2.32

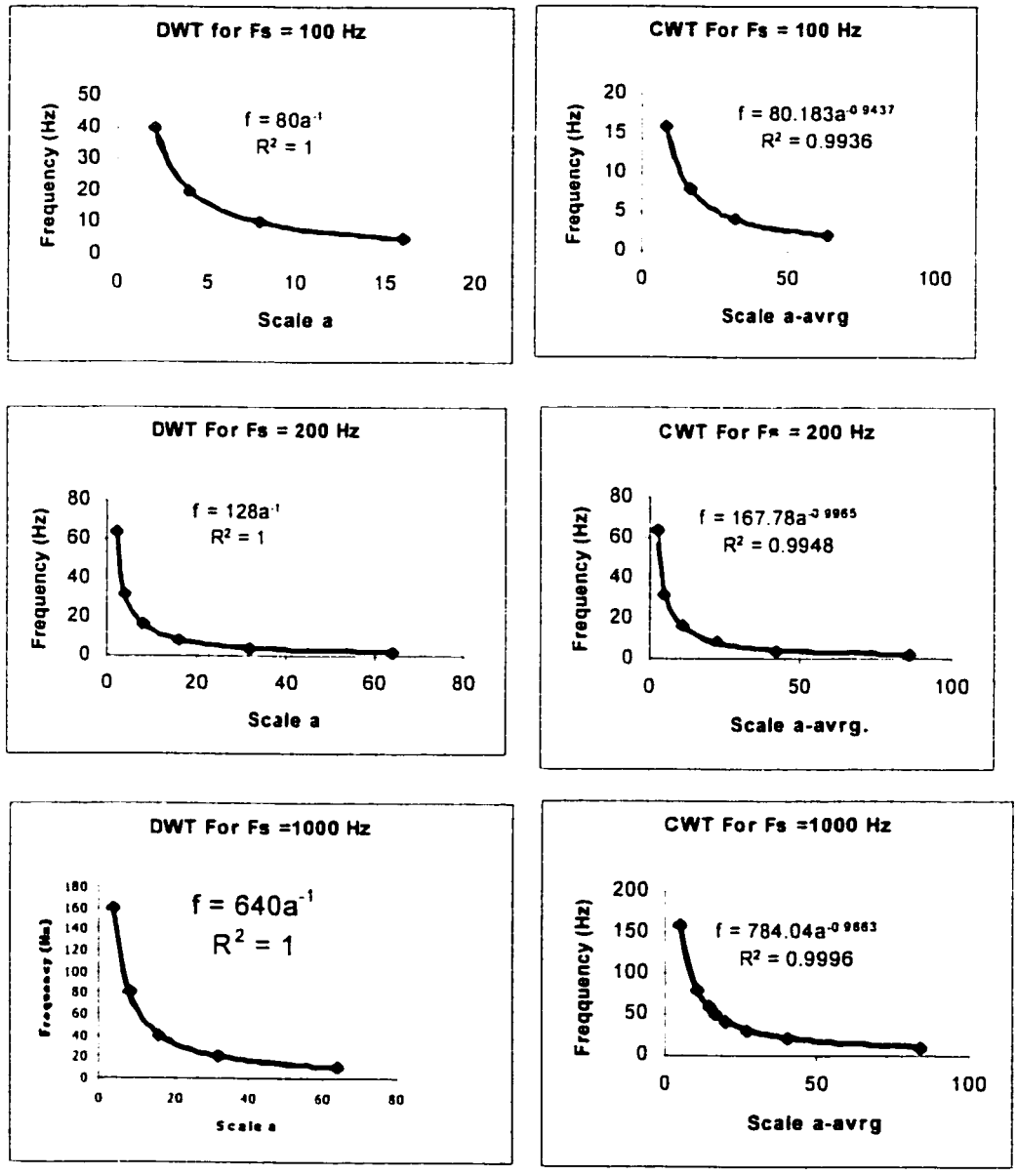

Figure 3.17 Graphs of frequency versus scale for Db6 of $\sin(2\pi ft)$

Table 3.2 Constants of proportionality for DWT and CWT of $\sin(2\pi ft)$

	DWT			CWT		
F_s	K	$C = K/F_s$	Index	K	$C = K/F_s$	Index
100	80	0.8	1	80.185	0.802	0.9437
200	128	0.64	1	167.78	0.834	0.9965
1000	640	0.64	1	784.04	0.784	0.9863
AVRG		**0.693**	**1**		**0.807**	**0.9755**

3.5.1 Discrete Wavelet Transform (DWT) Graphs Interpretations

To interpret DWT, one needs to consider all its graphical representations. The level presentation is interpreted by considering the level with highest coefficient value as representing the dominant frequency content of the analyzed signal. The contour plot, the intensity or image plot and 3-D plot are read in a similar manner, a level with the highest value will be the brightest. In Figures 3.13-15, two levels are prominent; this suggests the presence of two different frequencies in the signal. The analyzed signal indeed contains two frequencies 5Hz and 10Hz. It was however observed that more than one level may be obtained in some cases when a signal with only one frequency is analyzed, see Figure 3.18.

Unlike Figures 3.13-15, the two prominent levels in Figure 3.18 do not resemble the analyzed signal in any way. Furthermore, the intensity/image plot has the same pixel width at both levels; however, the pixel width should be different at different level since a level represents a unique frequency. Also, two distinct levels are not obvious in the

3-D graph, Figure 3.18(d). All these are indicators that the actual level of the signal is neither of the two prominent levels in Figure 3.18 but somewhere in-between the two levels.

Figure 3.18 is the DWT results of $\sin(2\pi 60t)$ with a sampling frequency of 1000 Hz as shown in Table 3.1. In Table 3.1, two levels were obtained for frequencies 30 Hz and 60 Hz, which are not dyadic multiples of 10 Hz. From this, one of the shortcomings of the dyadic DWT is established, i.e., it cannot accurately analyze signals whose frequency contents are not multiples of two. CWT does not have this shortcoming. Figure 3.18 and Table 3.2 are closely studied in order to find the constant of proportionality, C, between f and a $\left(f\alpha \, {}^{1}\!/_{a}, f = {}^{Cf_s}\!/_{a}\right)$. The constant values of the equations of the graphs were divided by their corresponding sampling frequency to obtain the dimensionless constant, C as summarized in Table 3.2. It is observed that C is approximately the same for CWT while C for DWT for $f_s = 100Hz$ is significantly different from others. The reason for this was investigated by using f_s between 80 and 160 Hz. The same results as shown in Table 3.1 were obtained for f_s between 100 and 130 Hz. For other values of f_s, results similar to those of Figure 3.18 were obtained. The range of f_s that gave good results were related to the maximum frequency obtainable (frequency corresponding to j=1 or a = 2) the result is

$$f_{s,min} = 2.5 f_{max}$$
$$f_{s,max} = 3.25 f_{max} \qquad (3.33a)$$

The average of Equation (3.33a) gives,

$$f_s \geq 2.875 f_{max} \qquad (3.33b)$$

Equation (3.3) can be related to Nyquist frequency, $f_s \geq 2f_{max}$. For dyadic DWT $f_s \geq 2.875 f_{max}$; f_s is used to get C as presented in Table 3.3

Table 3.3 Constant of proportionality for DWT of $\sin(2\pi ft)$

	DWT		
F_s	$F_{s,avrg}$	K	$C = K/F_{s,avrg}$
100	115	80	0.696
200	184	128	0.696
1000	920	640	0.696

Therefore, for Daubachies DWT, the relationship between f_s, f and a is

$$f = \frac{0.696 f_s}{a} \tag{3.34}$$

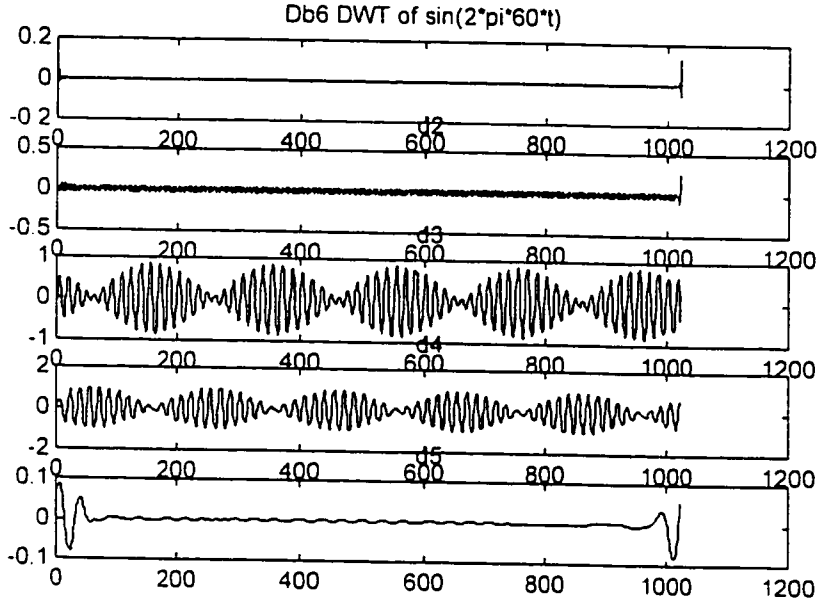

(a)

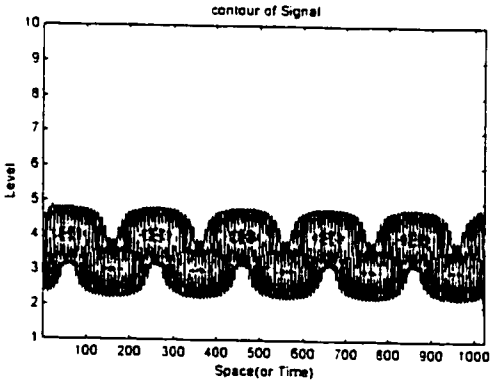

(i) Contour plot of $\sin(2\pi ft)$

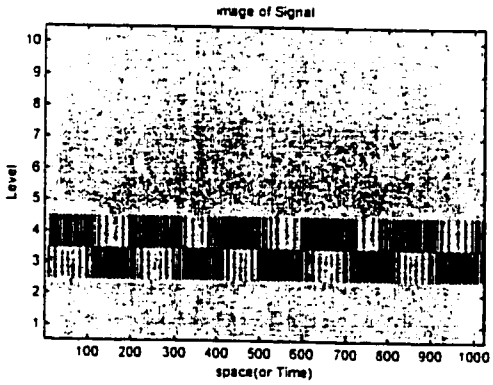

(ii) Intensity plot of $\sin(2\pi ft)$

(b)

Figure 3.18. (a) Level representation of $\sin(2\pi 60t)$. (b) DWT scalogram of $\sin(2\pi 60t)$

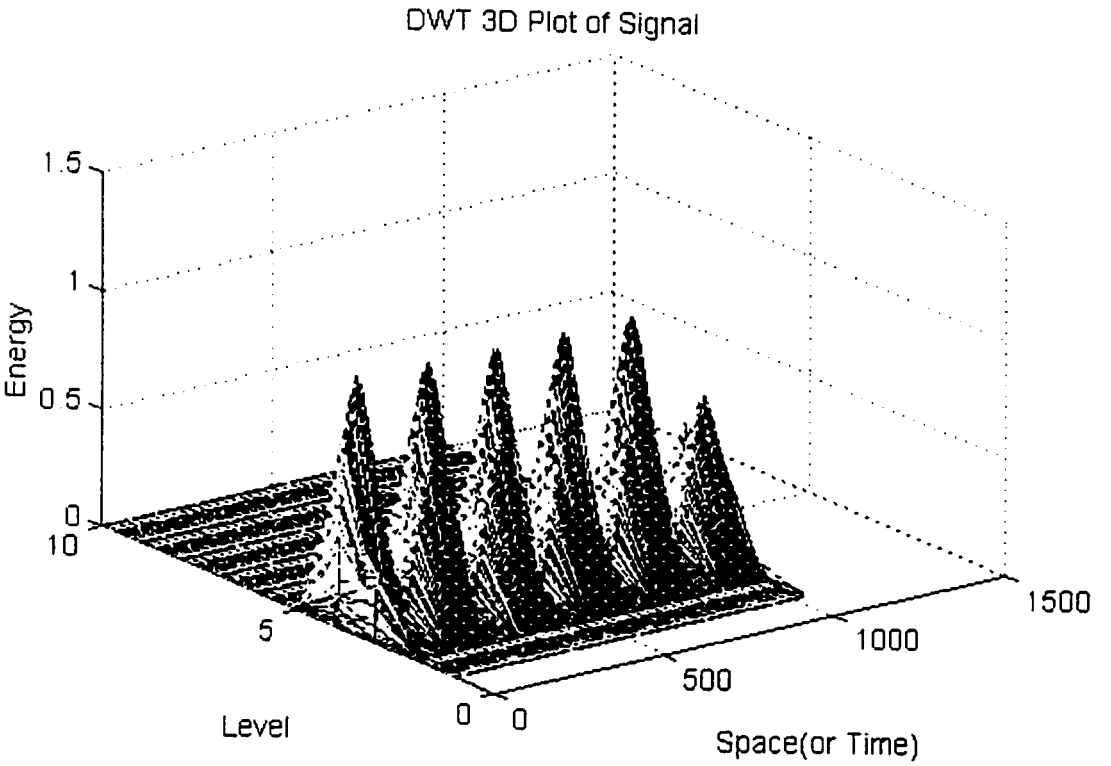

(c) 3-D plot for $\sin(2\pi 60t)$

Figure 3.18 Graphical Representation of DWT of $\sin(2\pi 60t)$

3.5.2 Continuous Wavelet Transform (cwt) Graph Interpretation

The scalogram of CWT can give any frequency content and their evolution with time since all discrete values of the scale are considered. However, the intensity spot does not occur at a single scale but occupies range of scales as shown in Figures 3.14(c) and 3.19. The usual thing is to consider the scale at the middle of the intensity spot [20], which is represented as a-avrg in Table 3.1 and Figure 3.17.

By taking the average value of C and index for CWT in Table 3.2, we get

$$f = \frac{0.807 f_s}{a^{.9755}}$$

$$or \qquad (3.35)$$

$$f = \frac{0.866 f_s}{a}$$

The shortcoming of CWT is related to the difficulty of getting accurate scale from CWT Scalogram, error may be introduced by wrong reading.

Equations (3.34) and (3.35) are validated by applying them to the results obtained for $x = \sin(2\pi 5t) + \cos(2\pi 10t)$ as presented in section 3.4.4, Figures 3.13-15. The sampling frequency was 950 Hz; the prominent levels for DWT are 6 and 7 hence,

$$f = \frac{0.696 * 950}{2^7} = 5.166 \text{ Hz}$$

$$f = \frac{0.696 * 950}{2^6} = 10.331 \text{ Hz}$$

For the CWT, there are two distinct regions and their scales are

$$a_1 = \frac{42 + 102}{2} = 72$$

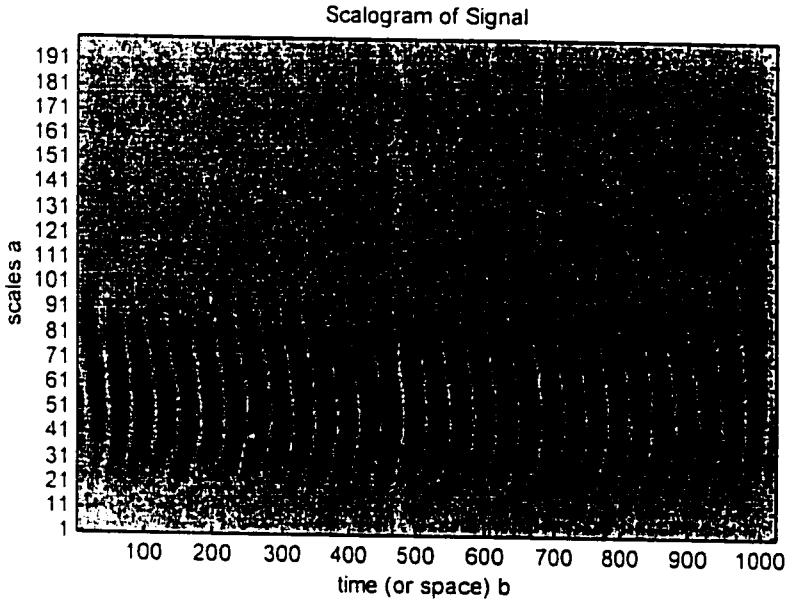

Figure 3.19 Graphical Representation for CWT of $\sin(2\pi 60t)$

$$a_2 = \frac{42 + 248}{2} = 145$$

Therefore,

$$f = \frac{0.866 * 950}{72} = 11.426 \text{ Hz}$$

$$f = \frac{0.866 * 950}{145} = 5.674 \text{ Hz}$$

Also, wavelet analysis of a vibration signal of an unbalanced rotor system was carried out to check the validity of Equations (3.34) and (3.35). 1024 samples were taken with a sampling frequency of 3200 Hz. Figure 3.20 shows graphs of the signal, its Power Spectra Density, Contour and intensity plots of DWT results, and scalogram of CWT results. The DWT gave only one level, 7, this gives

$$f = \frac{0.696 * 3200}{2^7} = 17.4 \text{ Hz}$$

For the CWT, a =(63+155)/2 = 109

$$f = \frac{0.866 * 3200}{109} = 25.4 \text{ Hz}$$

However, the actual frequency, as indicated by the Power Spectrum Density is 25Hz.

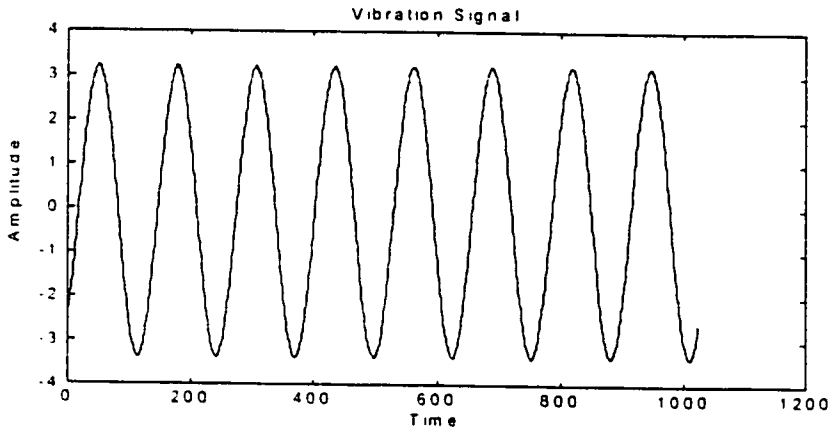

(a)

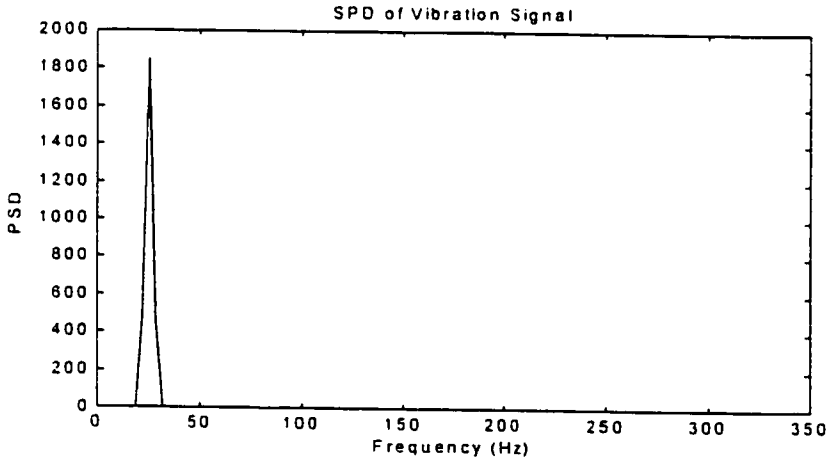

(b)

Fig. 3.20. (a) Vibration signal waveform. (b) Frequency Spectral Analysis

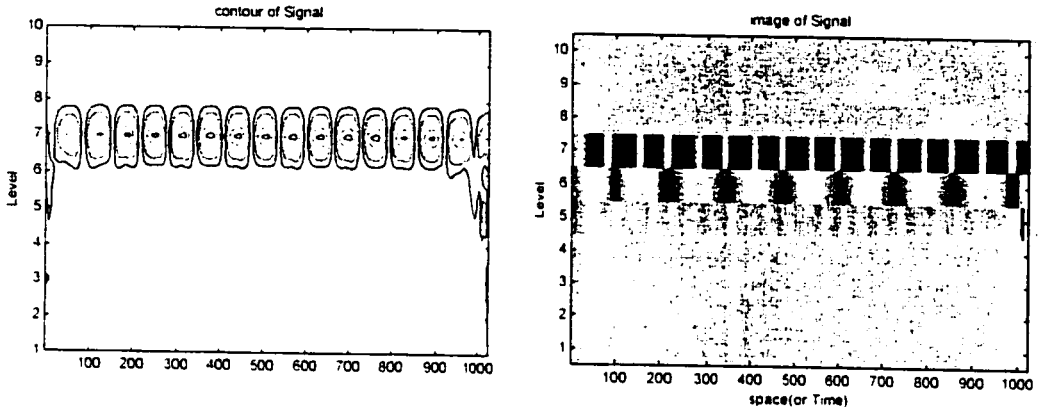

(c) Scalogram of DWT

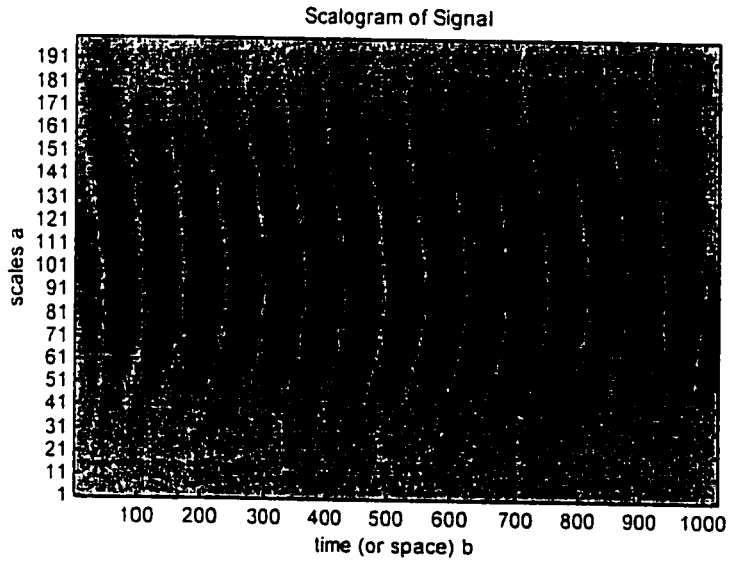

(d) Scalogram of CWT

Figure 3.20. Graphs of DWT and CWT of vibration signals for an unbalanced rotor with sampling frequency of 3200 Hz.

It can be seen from the above calculations that Equations (3.34) and (3.35) fairly estimate the frequencies of the simulated signal but only Equation (3.35) for CWT fairly estimates the frequency of the vibration signal of an unbalanced rotor. Another experimental data of an unbalanced rotor was taken at 6400 Hz sampling frequency, the results are presented in Figure 3.21.

$$f = \frac{0.696 * 6400}{2^7} = 34.8 \text{ Hz}$$

For CWT, a =(65+155)/2 = 110

$$f = \frac{0.866 * 6400}{110} = 50.4\text{Hz}$$

From the validation results presented above, Equation (3.34) for DWT cannot be used to estimate frequency from experiment data. Equation (3.35) for CWT produced fairly accurate results for both simulated and experimental signals, hence it is more reliable. However, if we take the frequency at level 7 of the DWT scalogram as the minimum, the maximum frequency at a sampling frequency of 6400 Hz that can be detected is 3200 Hz. This condition satisfies the Nyquist frequency inequality but does not satisfy the frequency limit established for DWT in Equation (3.33), i.e., that sampling frequency should be 2.875*3200, which is 9200 Hz. If this value is used, the result becomes:

$$f = \frac{0.696 * 9200}{2^7} = 50.025 \text{ Hz}$$

Alternatively, it is observed that if C is set to one in Equation (3.34), this gives accurate results for the DWT of the experimental data as shown below.

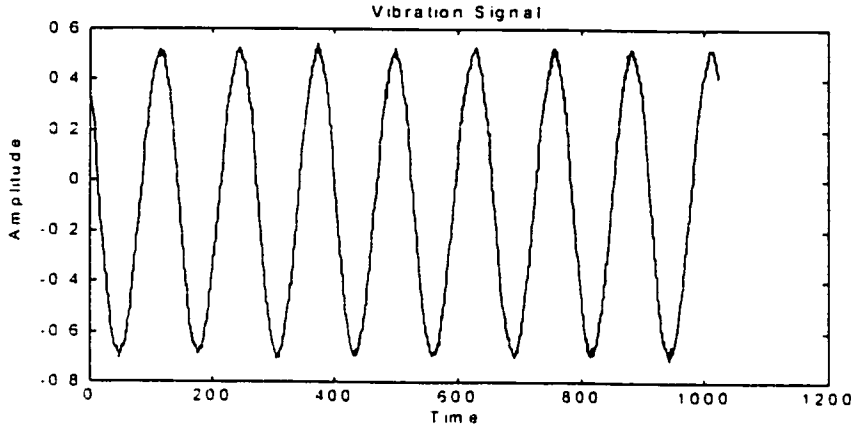

(a)

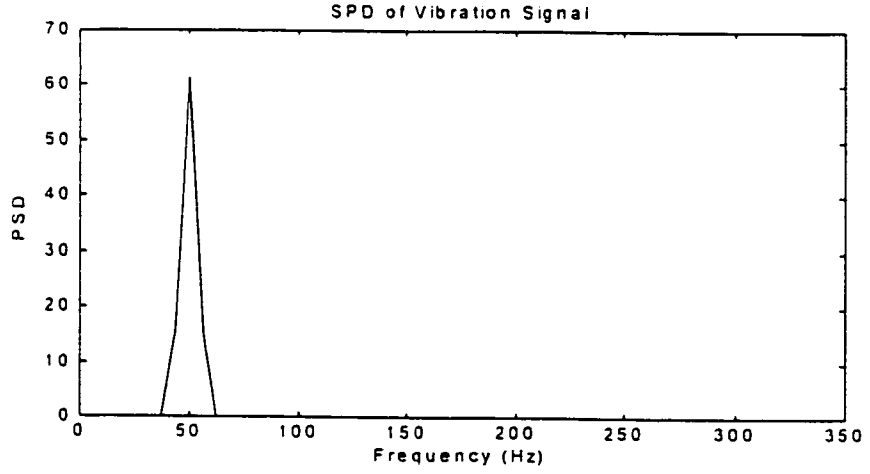

(b)

Fig. 3.21. (a) Vibration signal waveform. (b) Frequency Spectral Analysis

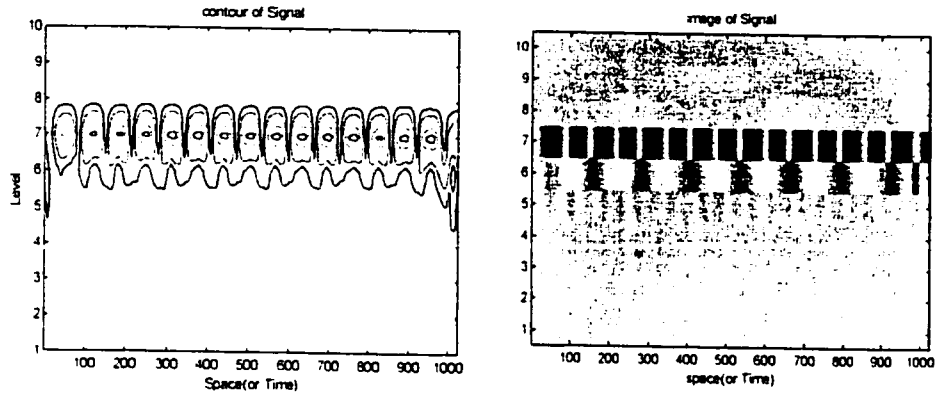

(c) Scalogram of DWT

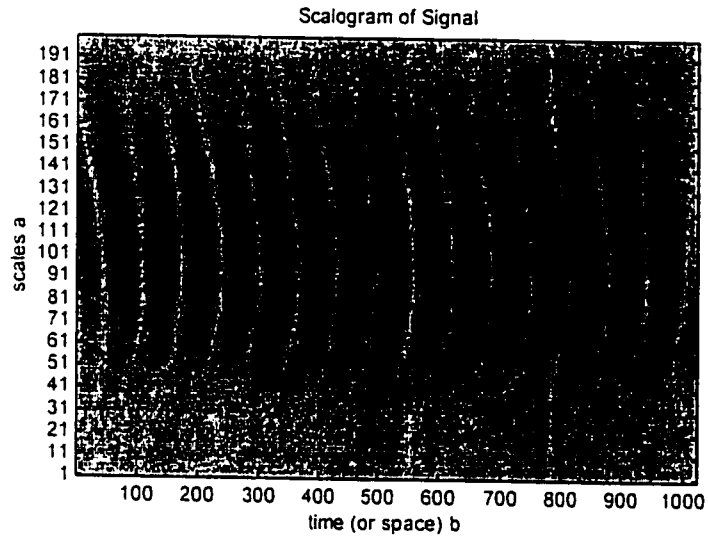

(d) Scalogram of CWT

Figure 3.21. Graphs of DWT and CWT of vibration signal of an unbalanced rotor with sampling frequency of 6400 Hz.

For results shown in Figure 3.20,

$$f = \frac{3200}{2^7} = 25 \text{ Hz}$$

For the results presented in Figure 3.21,

$$f = \frac{6400}{2^7} = 50 \text{ Hz}$$

From the results presented in Figures 3.18 and 3.19, and the results of Equations (3.34) and (3.35) applied to simulated and experimental signals, the following summary is obtained. Continuous wavelet transform (CWT) should be used if one is interested in getting values of frequency contents of a signal. The accuracy of the estimation of frequency from CWT scalogram is limited by the reading of the scale, a, from the scalogram. Also, CWT requires longer computation time than the dyadic discrete wavelet transform (DWT) and the computation results are so much that they can only be represented graphically as a 2-D plot known as CWT scalogram (Figure 3.21(d)).

The DWT has low computation time and can be represented graphically as level plot, scalogram and 3-D plot. However, DWT cannot accurately analyze signal whose frequency contents are not multiples of 2, see Figure 3.18. Estimation of values of frequency contents of experimental signals using dyadic DWT is difficult; what is certain is that a level of DWT corresponds to a particular frequency.

The steady state vibration response of any system contains harmonics of the excitation frequency. Therefore, dyadic DWT can be used to analyze vibration signals since $\frac{1}{2}X$, 1X, 2X, 4X, 8X, etc can be accurately detected by DWT. In the application of wavelet transform to crack detection in this thesis, attention will be focused on

comparing wavelet graphs of cracked and un-cracked shafts rather than calculating frequency values.

CHAPTER 4

METHODOLOGY

4.1 INTRODUCTION

This is an experimental work that involves the use of Rotor Kit, Rotor Kit Motor Speed Control, 208-P Data Acquisition Interface Unit (DAIU), Automated Diagnostics for Rotating Equipment (ADRE) Software, Oscilloscopes and other accessories. It also involves the design of shafts with transverse cracks with different depth, shape and location. The collected vibration signals from the cracked and uncracked shafts were analyzed using Power Spectra Density Analysis and wavelet transform, a JTFA. The proximity probes are expensive and needed to be protected from damage. To ensure this, it was ascertained that the static deflection of shafts under load is less than the required distance between the probe and shaft surface, this will prevent rubbing. The probes were located close to the bearing supports, a place where the deflection is not as much as at the center of the shaft. Figure 4.1 represents the experimental setup of the test rig.

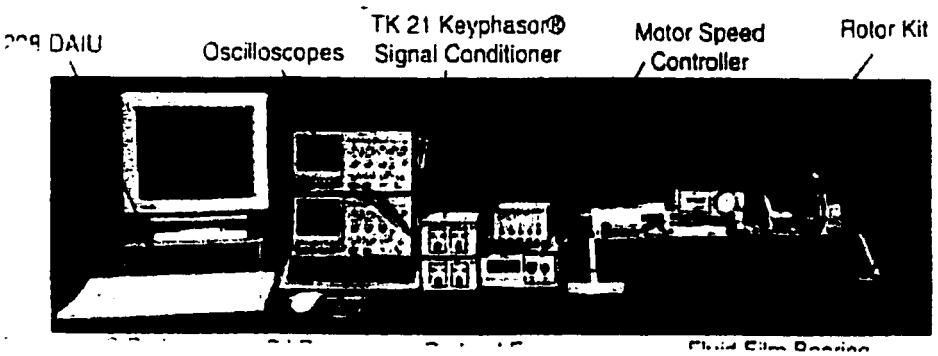

(a) Equipment arrangement

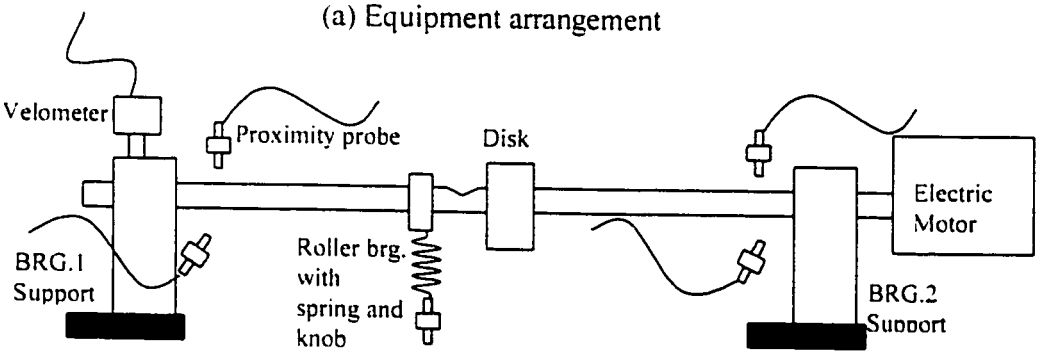

(b) Schematic diagram for the first experimental set-up (Simply Supported).

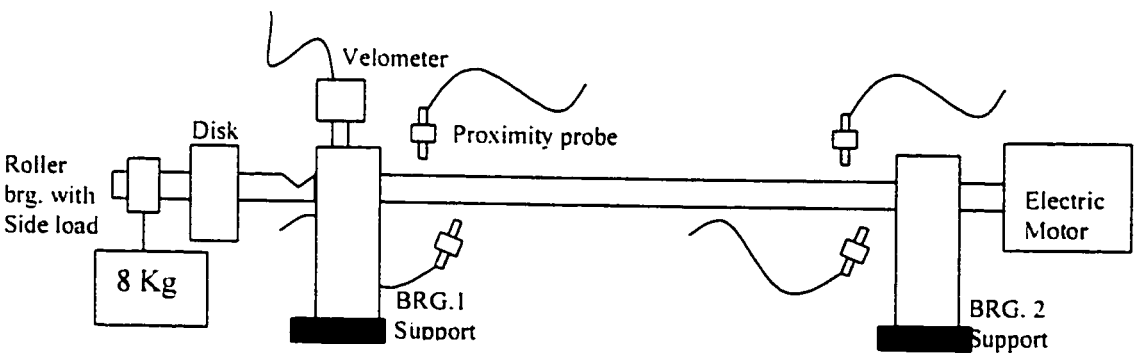

(c) Schematic diagram for the second experimental set-up (Overhang).

Figure 4.1 Experiment rig

4.2 EXPERIMENTAL SET-UP

The instrument used for the experiment include a Rotor Kit, Rotor Kit Motor Speed Control. Data Acquisition Interface Unit (DAIU) with accessories, Oscilloscopes. Personal Computer (PC). Eddy Current Displacement/proximity Probes. Velometer. Automated Diagnostics for Rotating Equipment (ADRE) for Windows Software and shafts. The experiment is set up as shown in Figure 4.1. The proximity probes were connected via auxiliary components to Oscilloscopes to observe the amplitude-time waveforms and orbits of the vibration signals. The probes and the velometer were also connected to the DAIU. which is in turn connected to the PC. The DAIU operation is controlled by the ADRE for Window Software to collect, store and analyze vibration data to obtain orbits. spectra analysis. bode and polar plots. frequency analysis waterfall. time trend. etc. The collected vibration data were then retrieved for further analysis using wavelet transform.

In the arrangement of Figure 4.1 (b), un-cracked and cracked shafts with different surface transverse crack shapes. and disks located at the middle of the shaft span are fitted on the rotor-kit in turn. The shafts rested on sleeve bearing fitted in the bearing supports. This arrangement limited the maximum side load that can be applied from the spring to about 4.3 Kg. which is small compared with 12 Kg applied by Bently and Bosmans [21] for crack propagation. The vibration data at startup and steady state at a speed of 3500 rpm (above the first critical speed of the arrangement) for the un-crack shaft without and with spring side load of 4.3 Kg were taken. The procedure was repeated for shafts with notch and slot transverse cracks of 4mm depth. The cracked

shafts with the side load were left to run for more that 18 hours but no change was observed in the vibration signatures.

The arrangement of Figure 4.1 (c) made it possible for side load greater than 4.3Kg to be applied for crack propagation. The startup and steady state data at different speeds (below the critical speed of the setup) for un-crack shaft without and with 8 Kg side load were obtained. The same procedure was repeated for a shaft with a surface transverse notch of depths of 3mm and 4mm. After some hours, less than 18 hours, of continuous operation at a steady speed with side load of 8 kg, the crack started to propagate and sharp increase in vibration amplitude was observed till the shaft fractured.

4.3 DESIGN OF CRACKED SHAFTS

Basic design procedures were used to ascertain that the static deflection of shaft is less than the required proximity probe gap. Shafts were made of ductile steel bar AISI 4140 and were designed according to known parameters of the Rotor Kit on which they were mounted. The parameters are as follows:

Diameter of Shaft, D	=	10 mm
Span of Shaft, L	=	540 mm
Mass of disk, M	=	0.8 Kg
Mass of shaft, m	=	0.72Kg/m
Proximity probe gap, δ	=	$0.762mm \leq \delta \leq 3mm$
Young Modulus of shaft material, E	=	200Gpa

The second moment of Inertia, I, of section of the cracked shaft in Fig. 4.2(a) can be estimated as shown in Figure 4.2(b). It is sufficient to consider only the shaft with 4

mm crack depth. The second moment of Inertia will vary with the shaft angle of rotation due to the presence of the transverse crack.

$$H = D/2 - a \tag{4.1}$$

H = 5 - 4 = 1 mm

$$B = 2\sqrt{D^2/4 - H^2} \tag{4.2}$$

= 9.8 mm

$$\bar{y} = \frac{\frac{\pi D^2}{8} * \frac{4r}{3\pi} + \frac{H}{2} * BH}{\frac{\pi D^2}{8} + BH} \tag{4.3}$$

= 1.798 mm

$$I_{xx} = \left(\frac{\pi D^4}{128} + \frac{\pi D^2}{8} * \left(\frac{4r}{3\pi} - \bar{y}\right)^2\right) + \left(\frac{BH^3}{12} + BH * \left(\bar{y} - \frac{H}{2}\right)^2\right) \tag{4.4}$$

= 498.68 mm^4

The static deflection due to the disk and the weight of the rotor can be calculated. its value should be between acceptable ranges of probe gap to prevent rubbing. The total load, P, acting on the rotor system is

P = (2*0.8 + .56*0.72)*9.81 = 21.61 N

$$\frac{PL^3}{48EI} = \delta \tag{4.5}$$

$$\delta = \frac{21.61 * 540^3}{48 * 498.68 * 200 * 10^3} = 0.71 \text{ mm}$$

Two types of transverse crack shapes were used namely surface notch and surface slot of depth, a, varying from 1mm to 4 mm. The cracks were produced at

different locations on shafts as shown in Figure 4.3. However, it was observed that crack of depth less than 3 mm produced very little change in the dynamic response of the rotor system. Therefore, attention was focused on the shaft with 3mm and 4mm cracks. The crack leading edge cannot be sharp; it was measured with optical microscope and found to be 0.1168 mm.

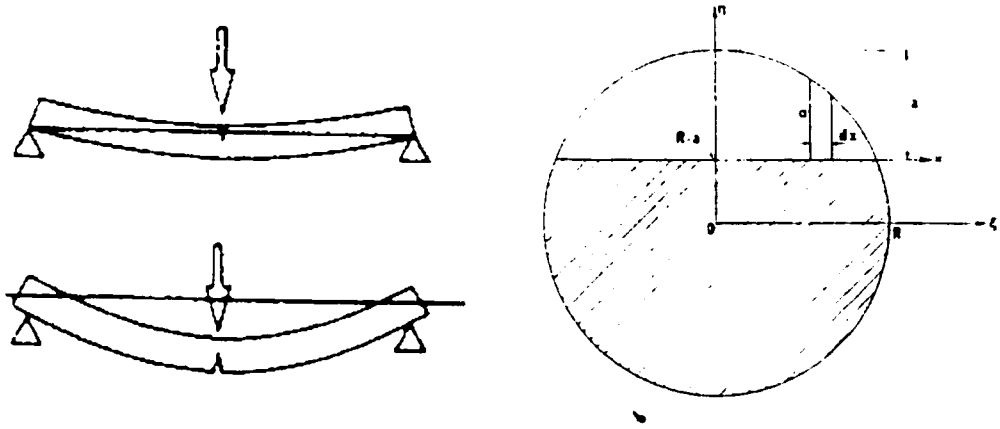

(a) Cross-section of the cracked shaft

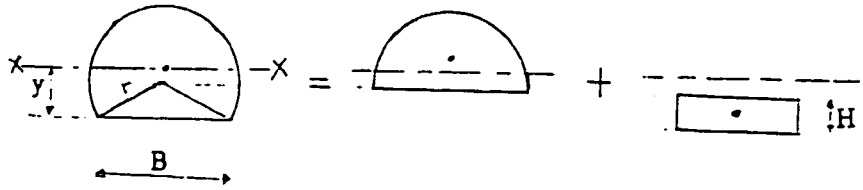

(b) Diagram for estimation of I

Figure 4.2. Cracked shaft geometry

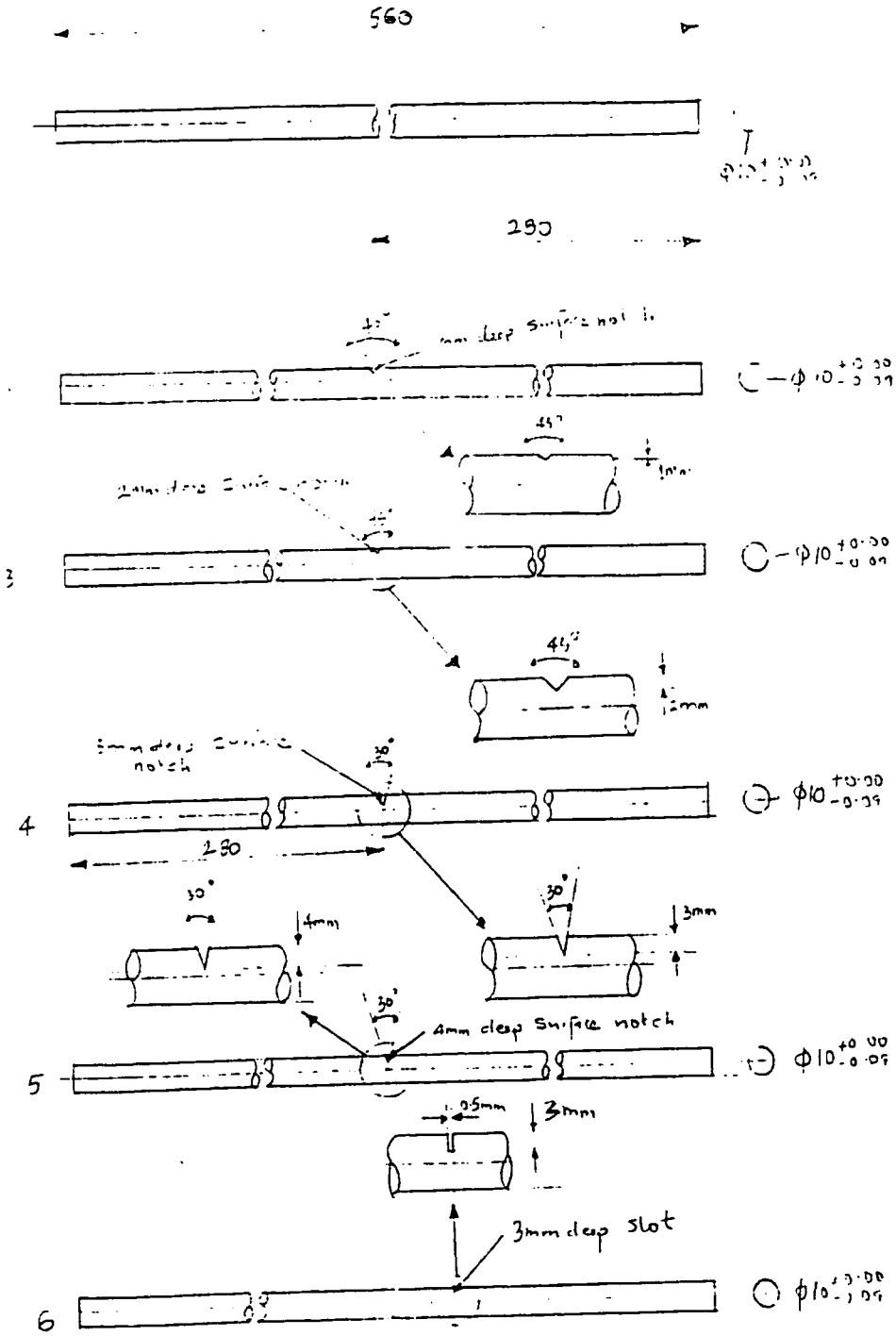

Figure 4.3 Shafts with transverse surface notches and slots

CHAPTER 5

RESULTS AND DISCUSSION

5.1 INTRODUCTION

The results of bode plot of startup data, conventional spectral analysis waterfall and orbit of steady state data are presented in section 5.2 for the two experimental setups, i.e. the simply supported and the overhang shaft experiments, described in the previous Chapter. Also, the discrete and continuous wavelet analysis of startup and steady state data for the two experimental setups are presented in section 5.3.

5.2 CONVENTIONAL ANALYSIS RESULTS.

The Automated Diagnosis for Rotating Equipment (ADRE) software and the Data Acquisition Interface Unit (DAIU) sample rate at the speed ranges used is 128 samples per revolution and the window buffer can accommodate a maximum of eight revolutions; this means that the window buffer has a length of 1024 and this forms a waveform. The DAIU can accommodate a maximum of 128 waveforms. The sampling is done at an equal interval of preset time interval for a steady state data acquisition or equal interval of preset speed interval for startup data acquisition. Each waveform is analyzed to get the frequency spectrum and all the spectra are put together to get the frequency waterfall.

5.2.1 First Experimental Setup (Simply Supported Shaft)

The vibration signals at startup and steady state conditions measured by vertical and horizontal probes for un-cracked and cracked shafts with and without side vertical tension are presented in this section

5.2.1.1 Un-cracked shaft

Figures 5.1 and 5.2 show the vibration response of the un-cracked rotating shaft without and with 4.3kg side spring load, respectively. Each Figure consists of Bode plot and the frequency cascade of the startup data, the frequency waterfall and orbit of the steady state data. The Bode plots, Figures 5.1(a) and 5.2(a), and the orbits, Figures 5.1(d) and 5.2(d), show that the critical speed of the shaft is different in the vertical and horizontal directions; the shaft is stiffer in the horizontal direction. Application of vertical side tension increased the critical speeds in both directions without affecting the asymmetry of shaft stiffness. This and the presence of split resonance in the Bode plots are indication of anisotropy in shaft material. The critical speeds in the vertical and horizontal directions for a low-pressure turbine coupled with a generator reported by Grabowski [2] showed similar trend, i.e., critical speed in X-direction is greater than critical speed in the vertical direction. The application of 4.3 kg side tension excites 2X vibration in the startup frequency cascade, Figure 5.2(b). 1X, 2X, 3X and 4X harmonics are present in varying magnitude in the signals of un-cracked shaft with and without side tension as shown in Figures 5.1(c) and 5.2(c).

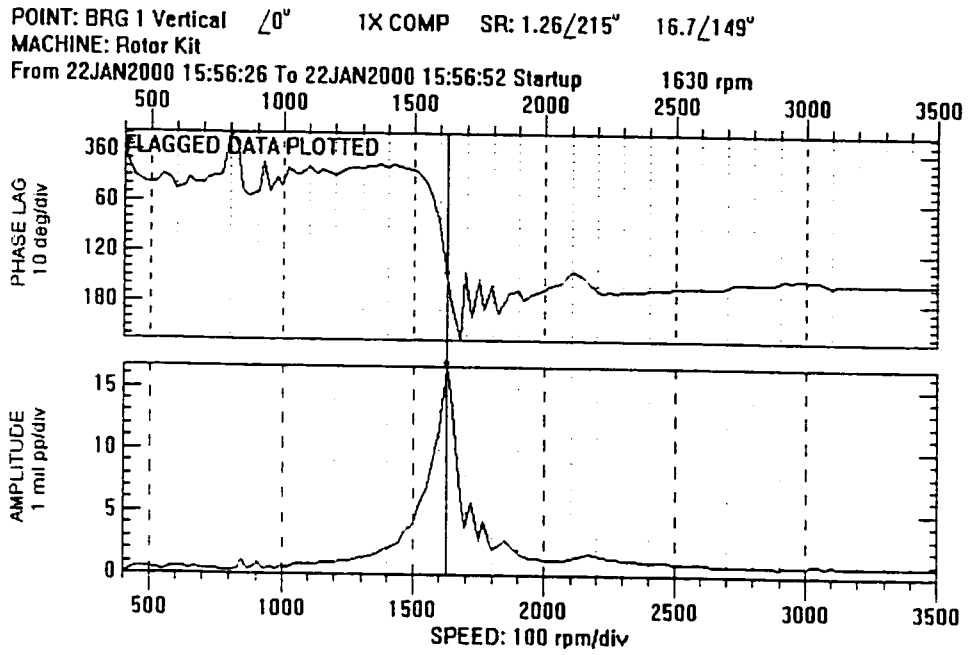

(i) Vertical

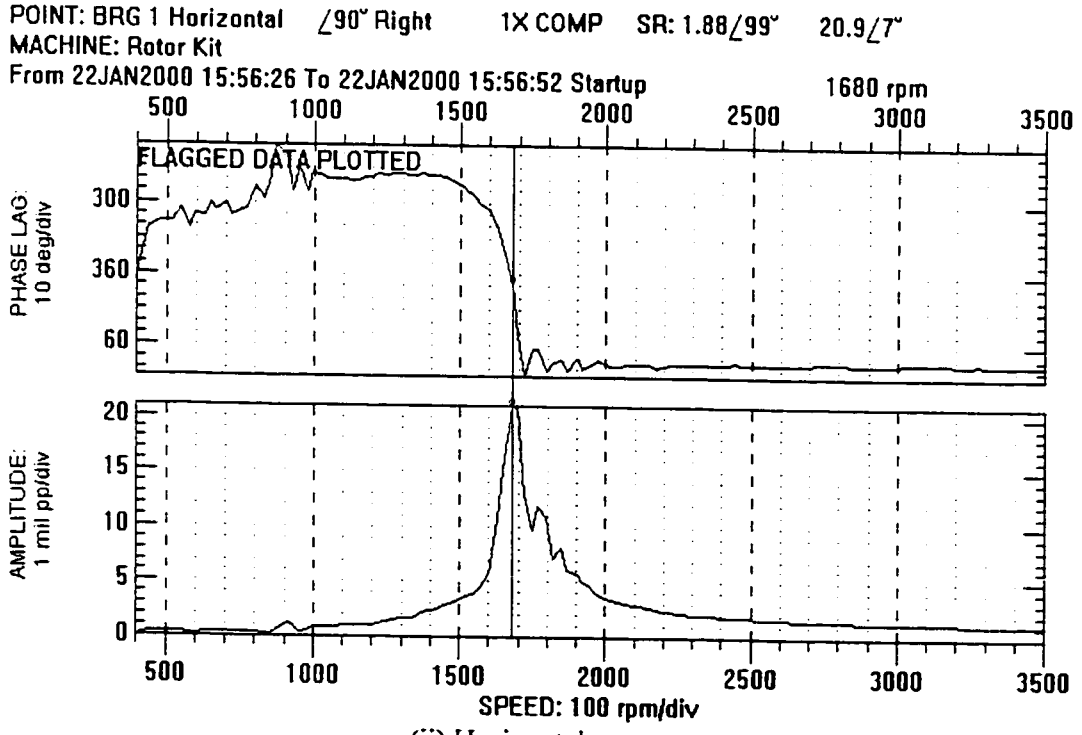

(ii) Horizontal

Fig. 5.1 (a) Bode plot of the startup data for un-cracked shaft

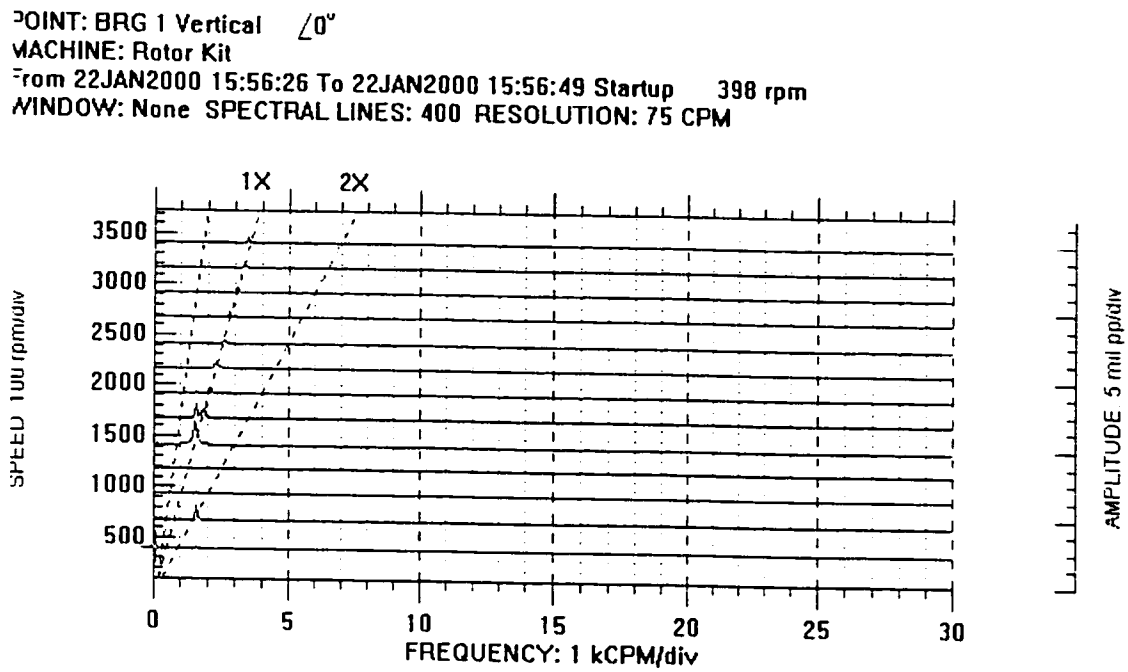

(i) Vertical direction

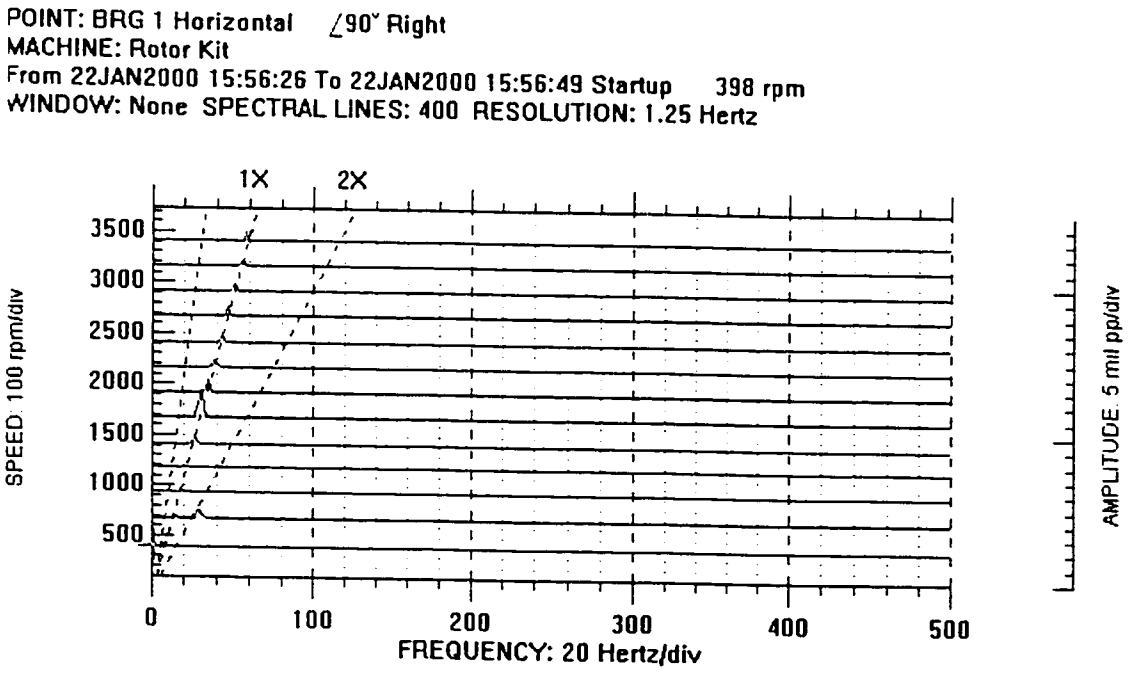

(ii) Horizontal direction

Fig. 5.1 (b) Frequency Cascade of the startup data for un-cracked shaft

POINT: BRG 1 Vertical ∠0°
MACHINE: Rotor Kit
From 22JAN2000 15:59:41 To 22JAN2000 16:04:41 Steady State 16:04:41
WINDOW: Hanning SPECTRAL LINES: 400 RESOLUTION: 1.25 Hertz

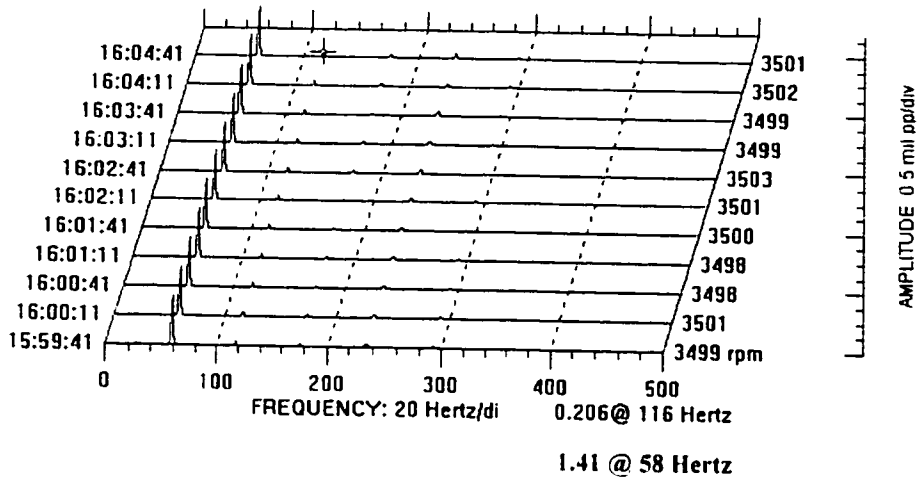

(i) Vertical direction

POINT: BRG 1 Horizontal ∠90° Right
MACHINE: Rotor Kit
From 22JAN2000 15:59:41 To 22JAN2000 16:04:41 Steady State 16:04:41
WINDOW: Hanning SPECTRAL LINES: 400 RESOLUTION: 1.25 Hertz

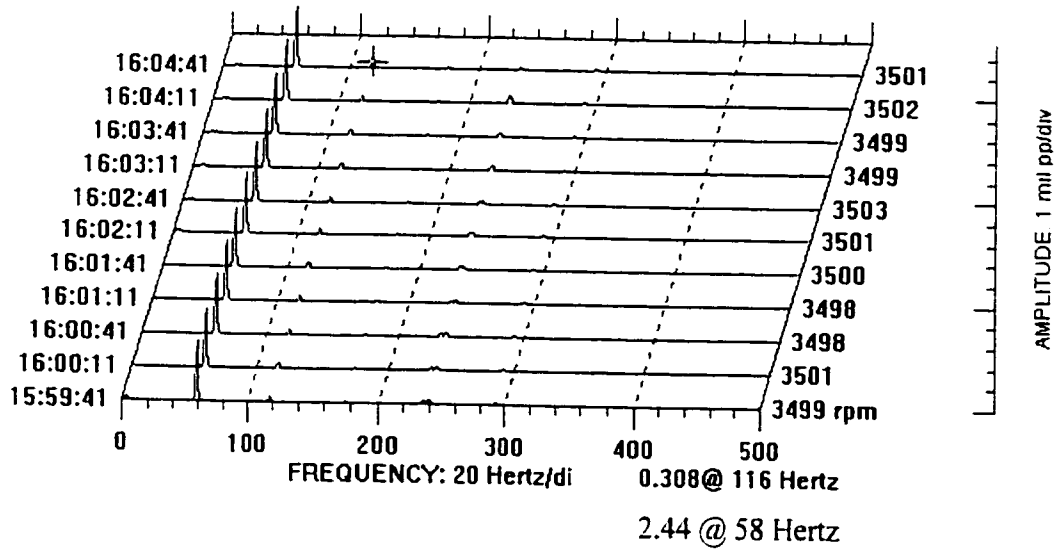

(ii) Horizontal direction

Fig. 5.1(c). Frequency waterfall for steady state data at 3500rpm for un-cracked shaft

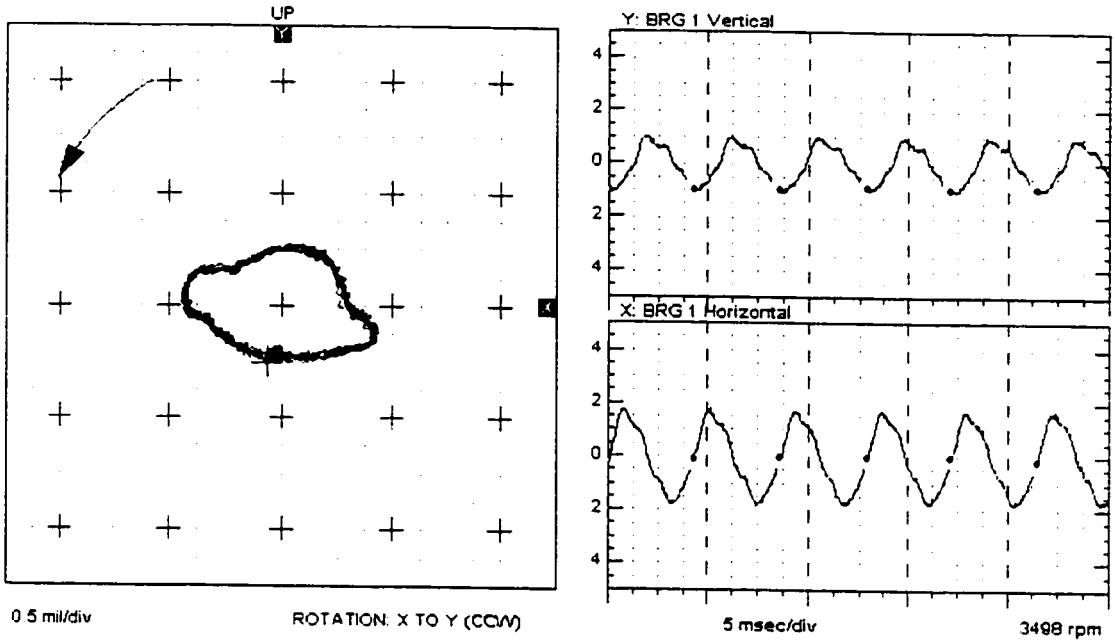

Fig. 5.1 (d). Orbit of un-cracked shaft at a steady state speed of 3500 rpm.

Figure 5.1 Startup and steady state analysis results for un-cracked shaft

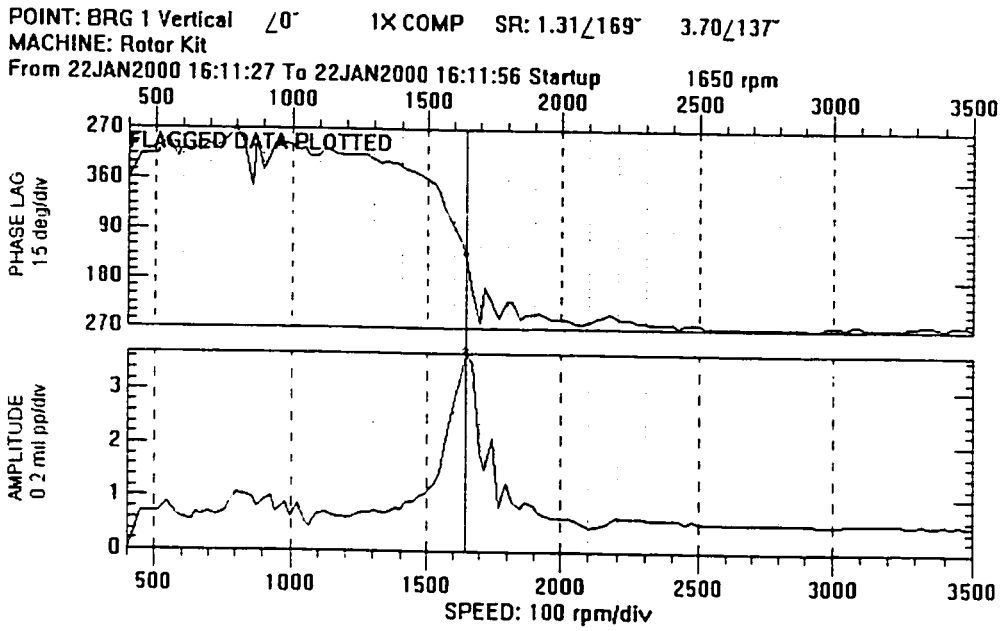

(i) Vertical direction

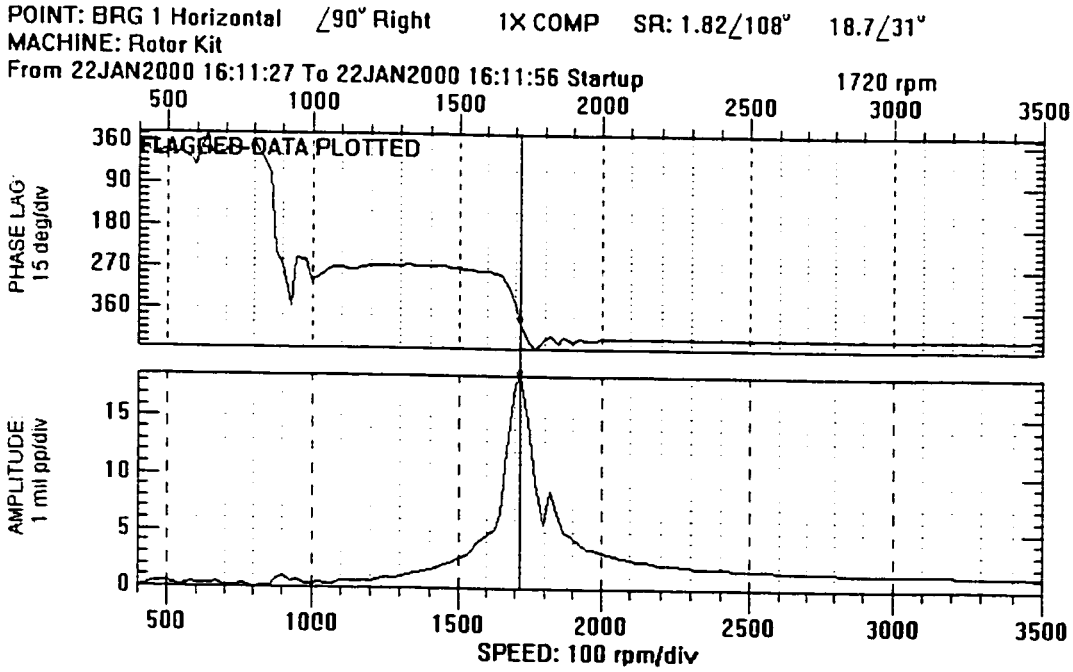

(ii) Horizontal direction

Fig. 5.2 (a). Bode plot of startup data for un-cracked shaft with a vertical tension load of 4.3 kg

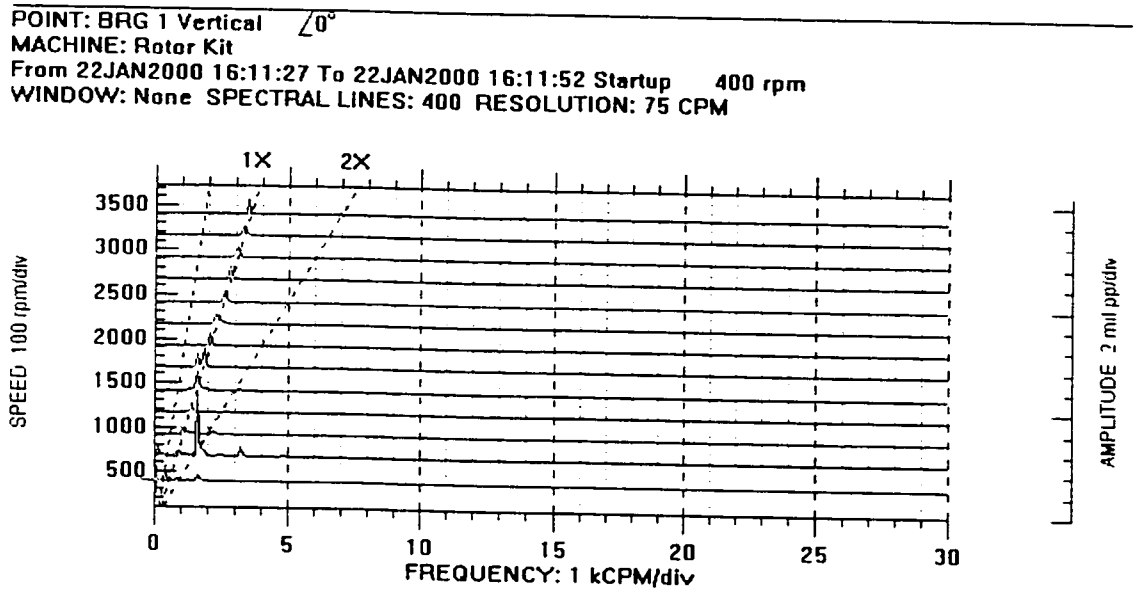

(i) Vertical direction

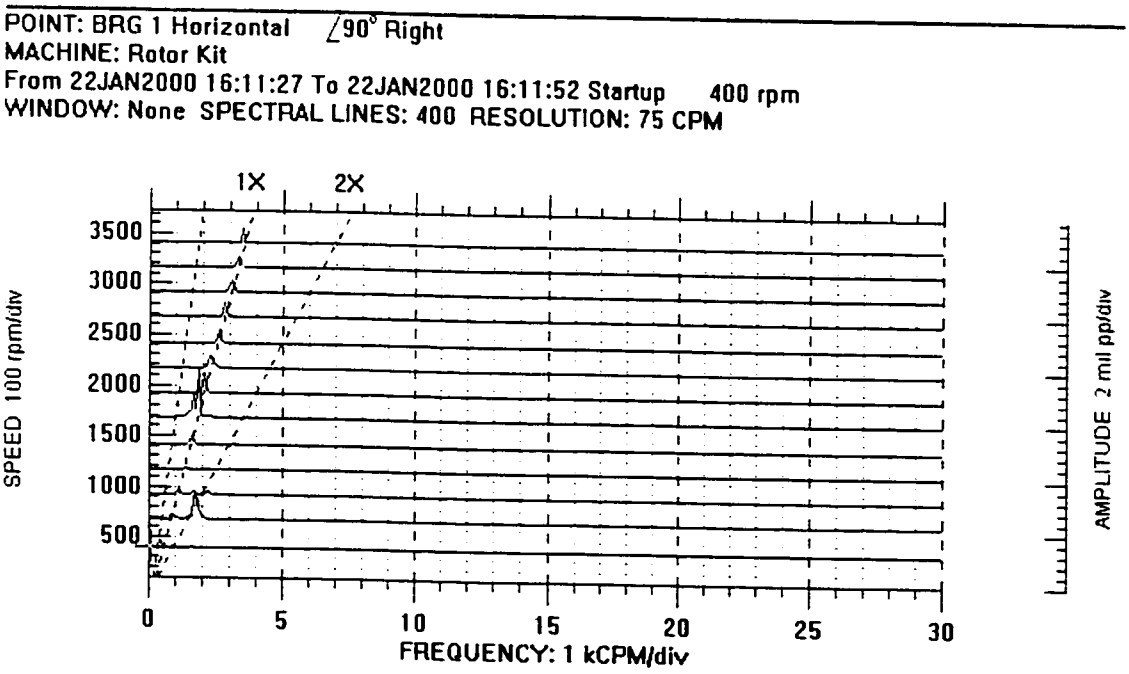

(ii) Horizontal direction

Fig. 5.2 (b) Frequency Cascade of the startup data for un-cracked shaft with a vertical tension load of 4.3 kg

POINT: BRG 1 Vertical ∠0°
MACHINE: Rotor Kit
From 22JAN2000 16:13:24 To 22JAN2000 16:19:24 Steady State 16:19:24
WINDOW: Hanning SPECTRAL LINES: 400 RESOLUTION: 1.25 Hertz

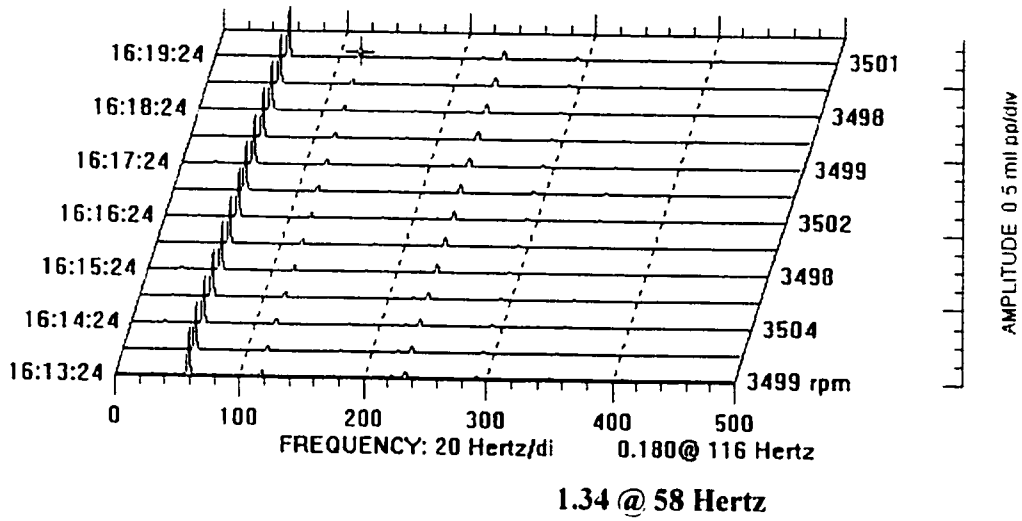

(i) Vertical direction

POINT: BRG 1 Horizontal ∠90° Right
MACHINE: Rotor Kit
From 22JAN2000 16:13:24 To 22JAN2000 16:19:24 Steady State 16:19:24
WINDOW: Hanning SPECTRAL LINES: 400 RESOLUTION: 1.25 Hertz

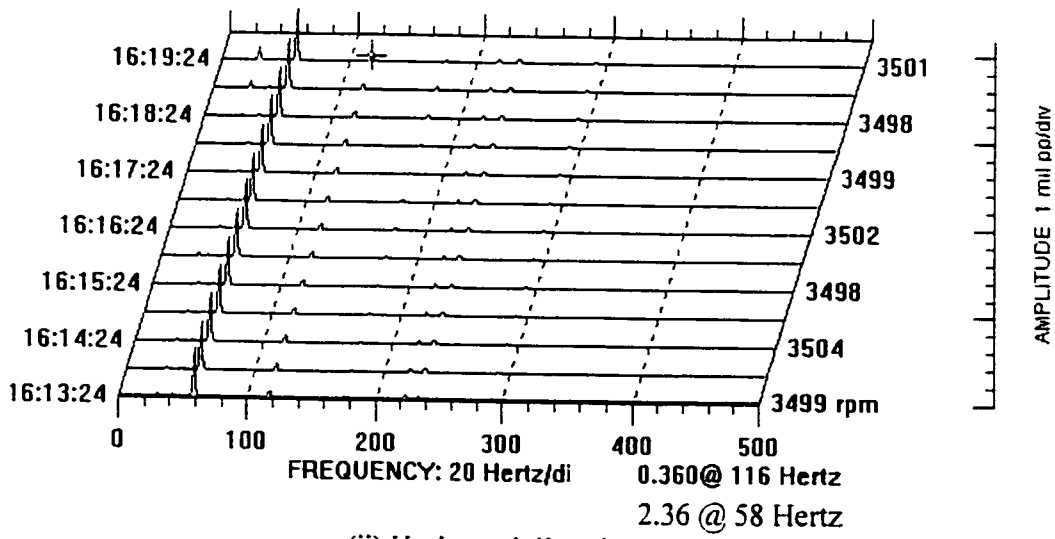

(ii) Horizontal direction

Fig. 5.2(c). Frequency waterfall for steady state data at 3500rpm for un-cracked shaft with a vertical tension load of 4.3 kg

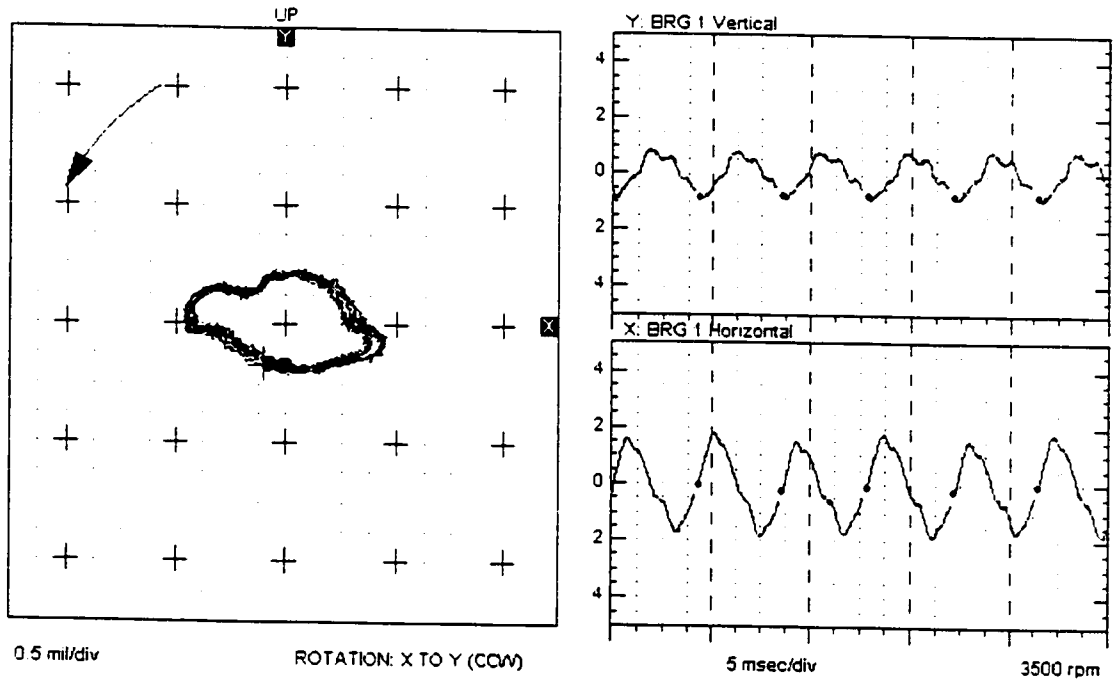

Fig. 5.2(d). Orbit of un-cracked shaft at a steady state speed of 3500 rpm with a vertical tension load of 4.3kg.

Figure 5.2 Startup and steady state analysis results for un-cracked shaft with a vertical tension load of 4.3 kg

5.2.1.2 Shaft with Surface Transverse Crack

Figure 5.3 shows the vibration response of the rotating shaft with 4mm surface transverse notch without the side spring load while Figure 5.4 shows the vibration response of the same shaft with 4.3kg side spring load. Each Figure consists of bode plot and frequency cascade of the startup data, frequency waterfall and orbit of the steady state data. The experimental arrangement with side tension load was left to run for about 18 hours but no significant change was observed in the vibration signals since the crack could not propagate.

The Bode plots show that critical speed of the cracked shaft decreased and there is an increase in the resonance bandwidth, Figure 5.3(a). The frequency waterfalls of the cracked shaft without and with the side tension, Figures 5.3(c) and 5.4(c) are different from those for un-cracked shaft, Figures 5.1(c) and 5.2(c). For the cracked shaft, Fig.5.3(c)(i), only 1X and 2X harmonics appeared in the vertical signal while additional transient signal about the same magnitude as 2X and of frequency ranges from 220 – 250 Hertz appeared in the horizontal direction. Zeng [16] reported that crack introduces transient signal into the vibration signal of cracked shaft systems. Application of side load tension altered the magnitude of 1X and 2X and introduced higher harmonic in the vertical direction, Fig.5.4(c)(i). The magnitude of 1X and 2X also changed and the transient signal disappeared in the horizontal direction, Fig.5.4(c)(ii), due to side tension application.

The shape of orbits, Figures 5.3(d) and 5.4(d), became nearly circular unlike the orbits of Figures 5.1(d) and 5.2(d) for the un-cracked shaft. This means that the crack has contributed in making a circular orbit. This is an indication of changes in stiffness distribution.

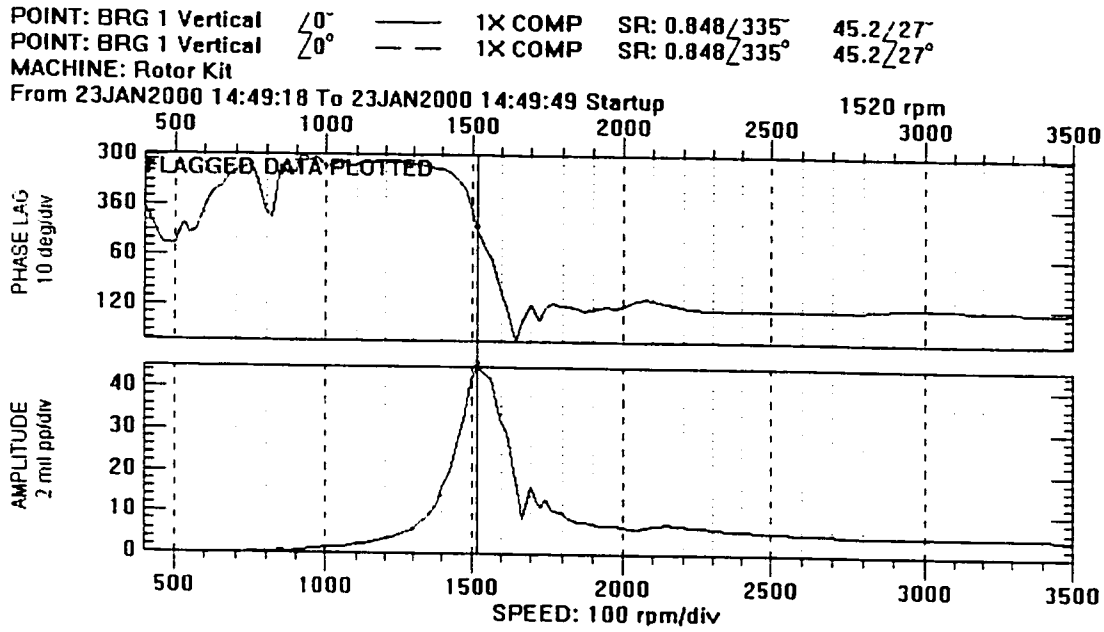

(i) Vertical direction

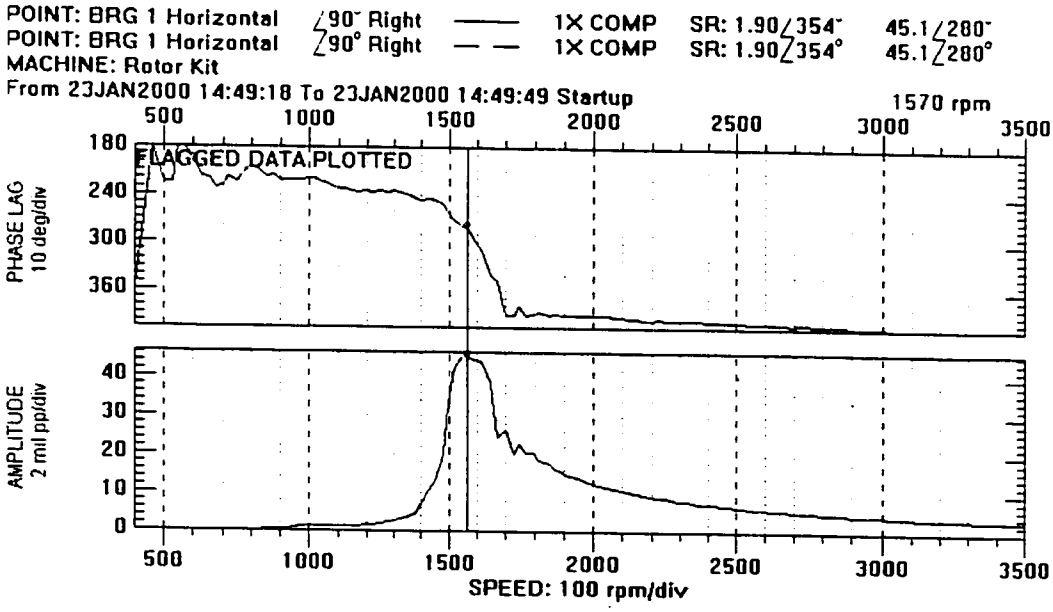

(ii) Horizontal direction

Fig.5.3 (a). Bode plot of startup data for shaft with 4mm notch crack

POINT: BRG 1 Vertical ∠0°
MACHINE: Rotor Kit
From 23JAN2000 14:49:18 To 23JAN2000 14:49:46 Startup 401 rpm
WINDOW: None SPECTRAL LINES: 400 RESOLUTION: 1.25 Hertz

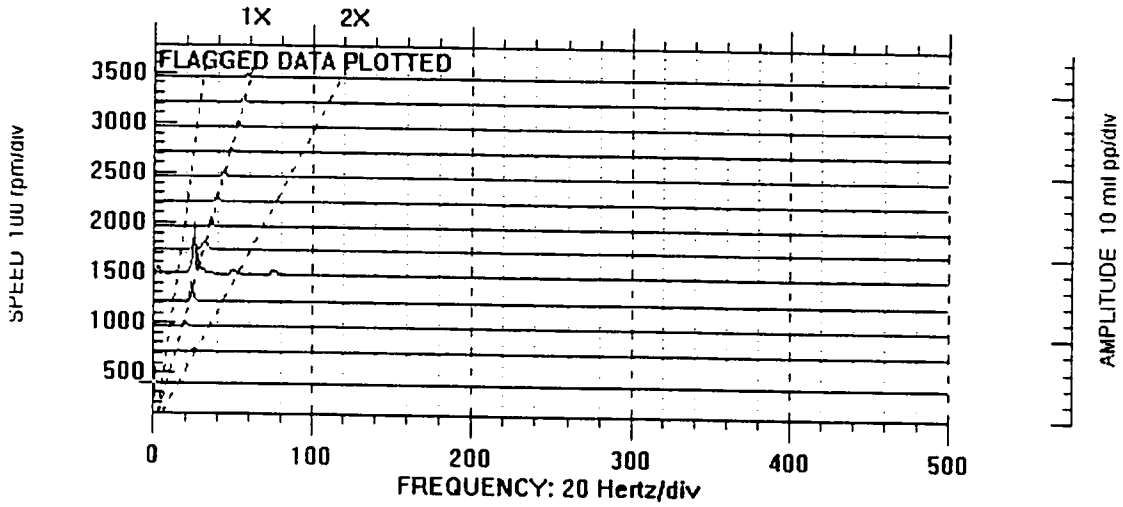

(i) Vertical direction

POINT: BRG 1 Horizontal ∠90° Right
MACHINE: Rotor Kit
From 23JAN2000 14:49:18 To 23JAN2000 14:49:46 Startup 401 rpm
WINDOW: None SPECTRAL LINES: 400 RESOLUTION: 1.25 Hertz

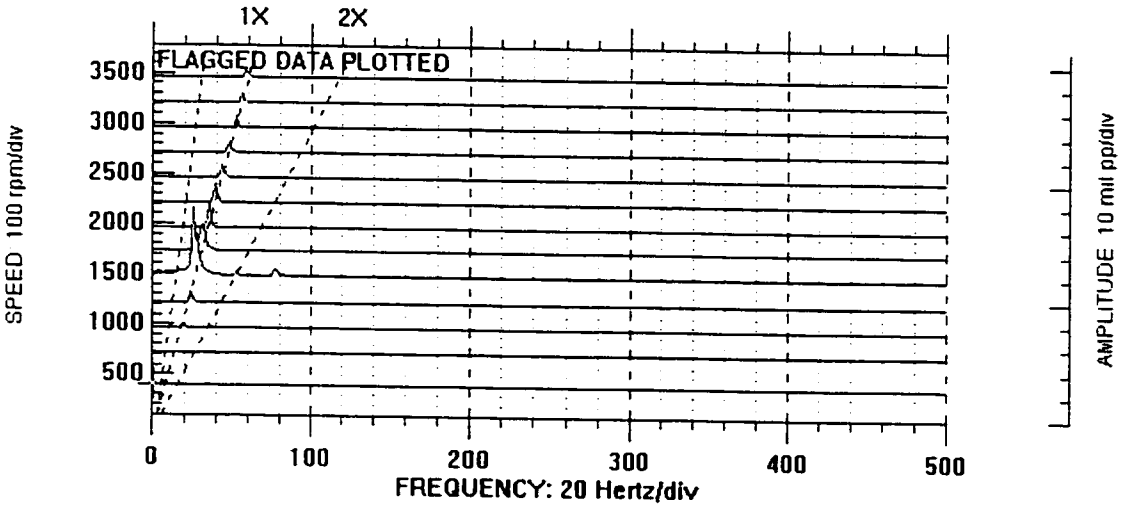

(ii) Horizontal direction

Fig.5.3 (b). Frequency cascade for steady state data at 3500rpm for shaft with 4mm notch crack.

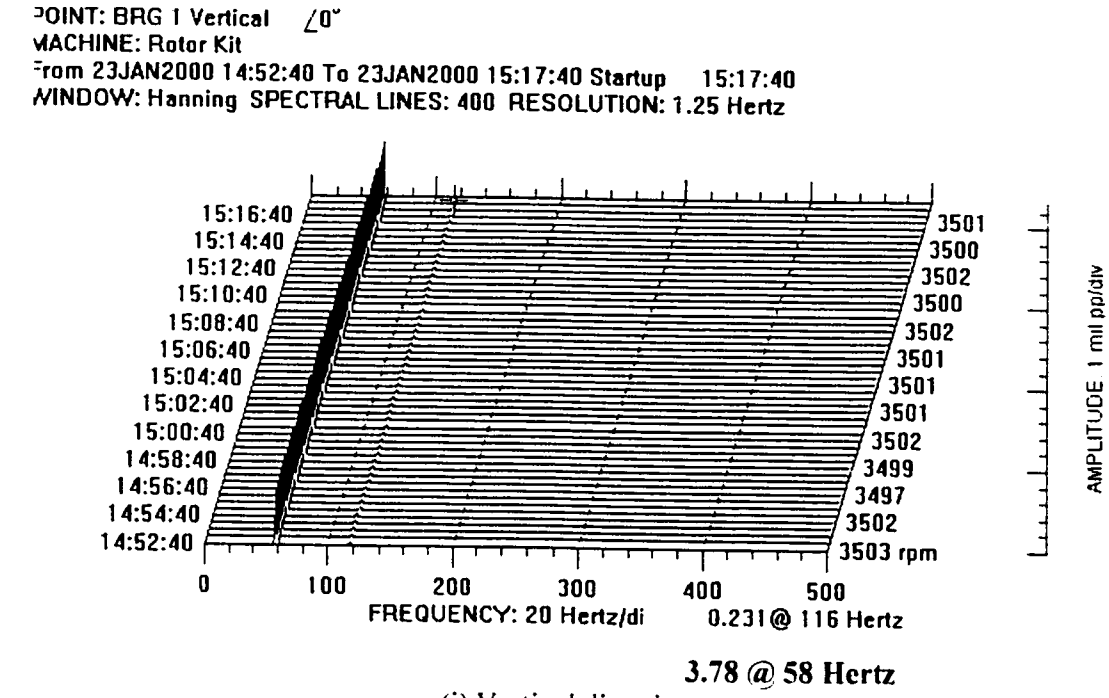

3.78 @ 58 Hertz

(i) Vertical direction

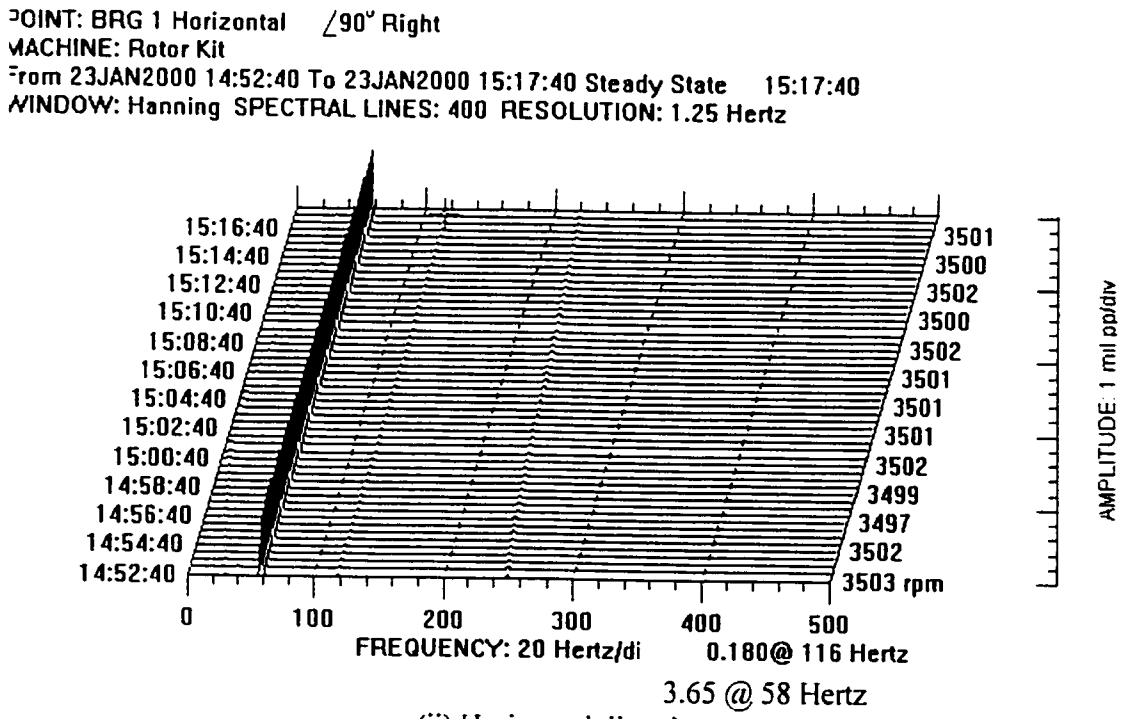

3.65 @ 58 Hertz

(ii) Horizontal direction

Fig.5.3 (c). Frequency waterfall for steady state data at 3500rpm for shaft with 4mm notch crack

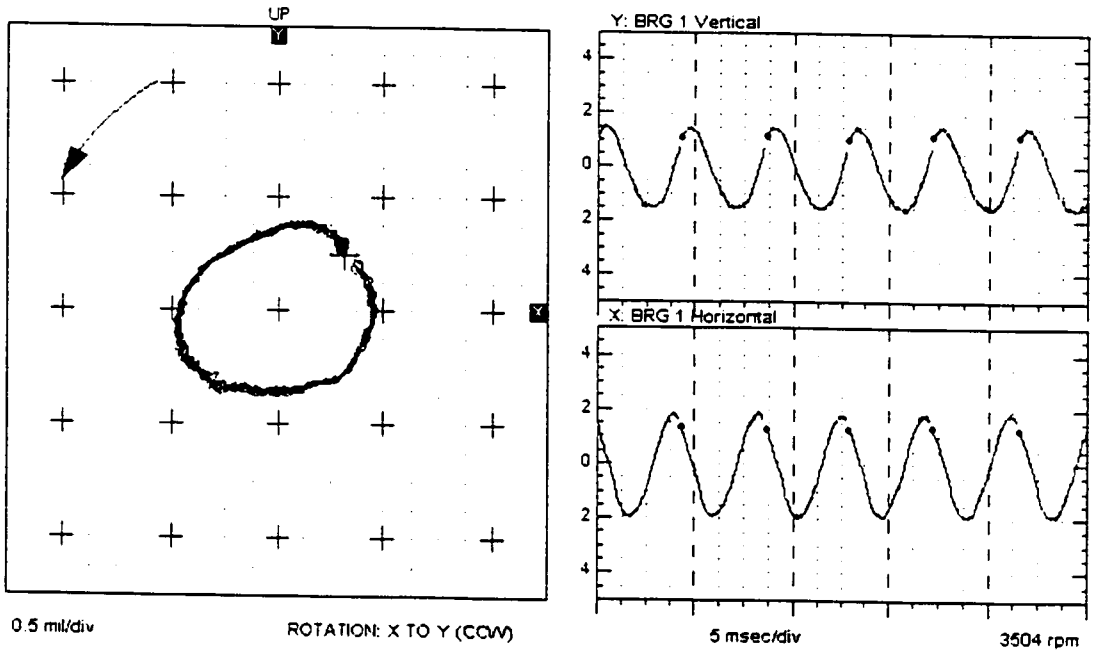

Fig. 5.3 (d) Orbit of shaft with 4mm notch crack at a steady state speed of 3500 rpm

Figure 5.3 Startup and steady state results for shaft with 4mm notch crack

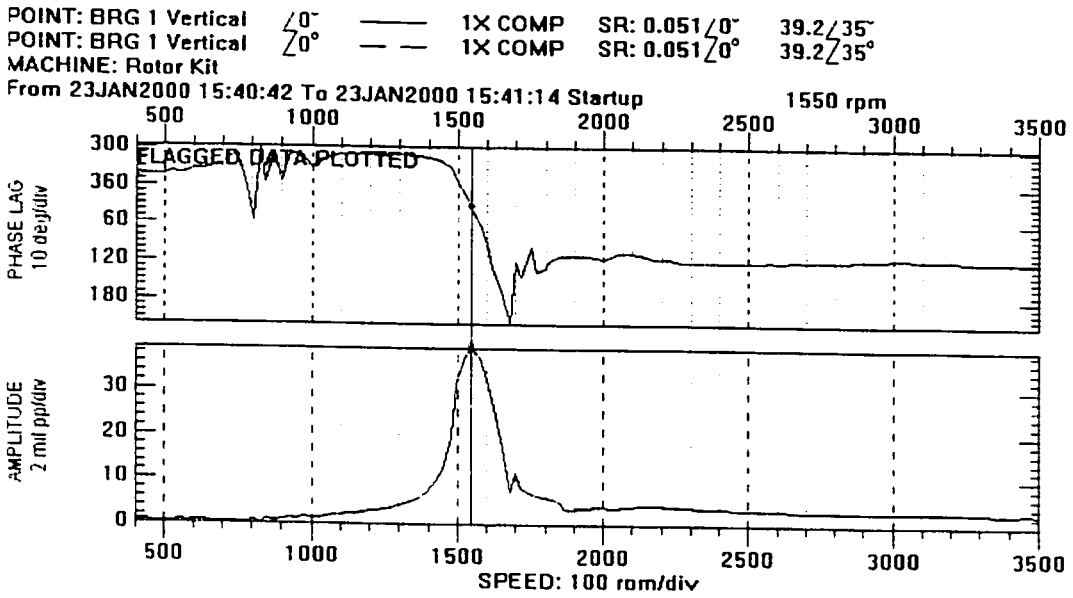

(i) Vertical direction

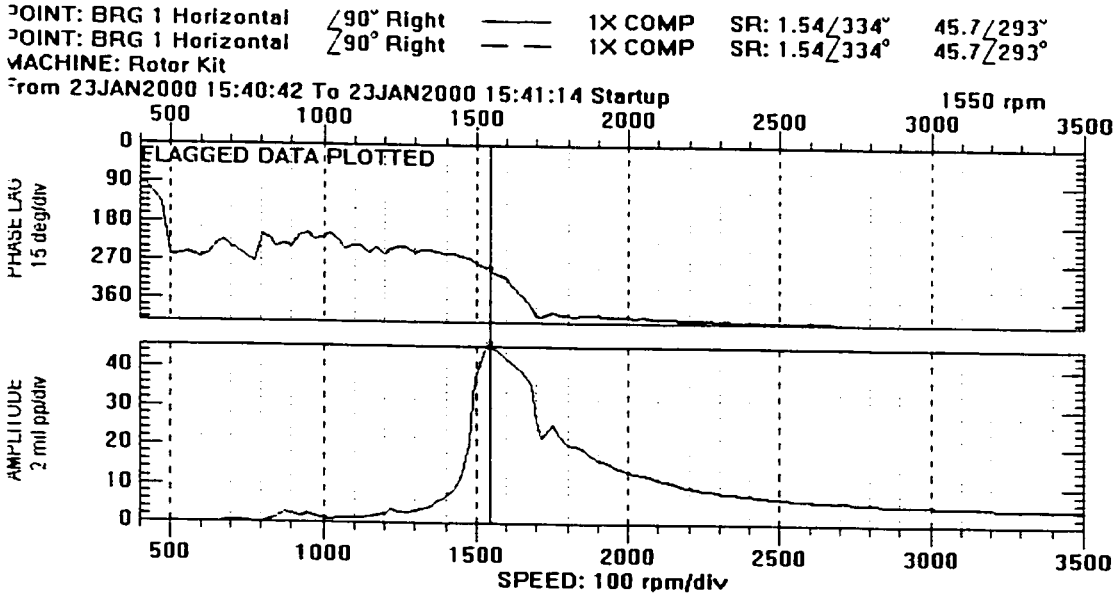

(ii) Horizontal direction

Fig. 5.4 (a) Bode plot of startup data for shaft with 4mm notch crack and vertical tension load of 4.3 kg

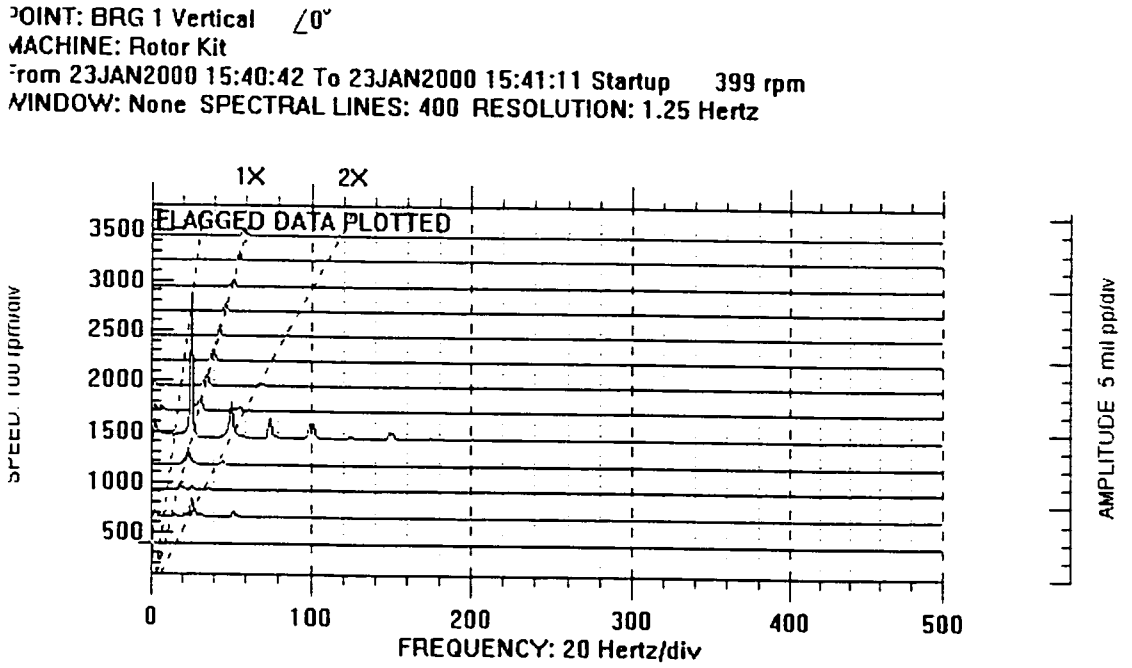

(i) Vertical direction

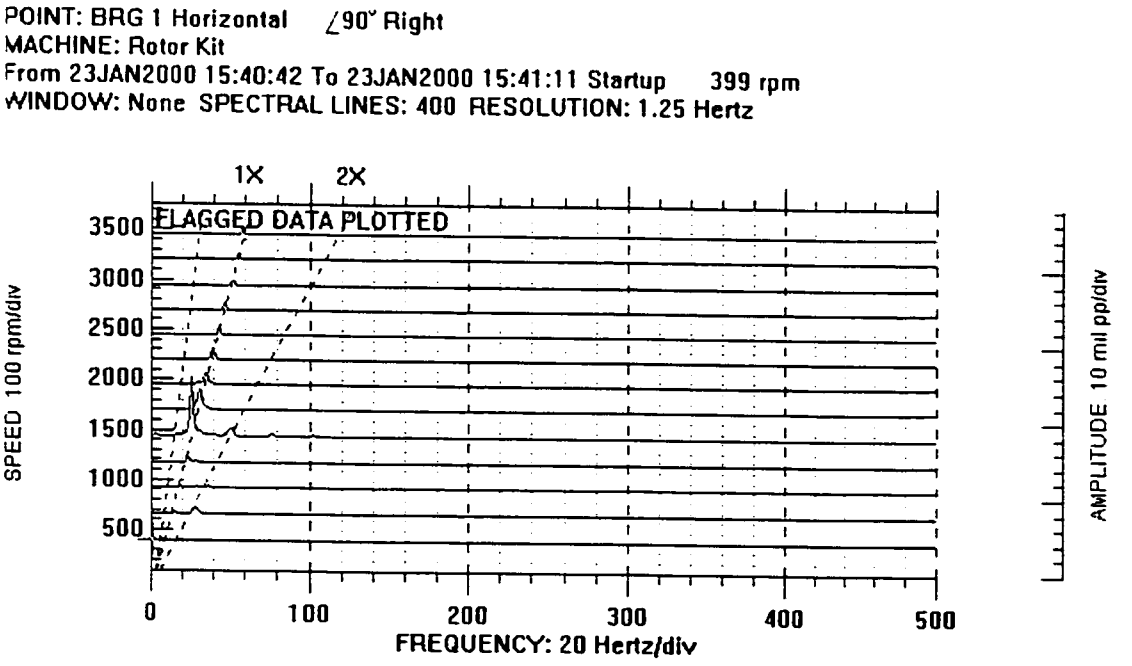

(ii) Horizontal direction

Fig.5.4 (b). Frequency cascade for steady state data at 3500rpm for shaft with 4mm notch crack and vertical tension load of 4.3 kg

POINT: BRG 1 Vertical ∠0°
MACHINE: Rotor Kit
From 23JAN2000 15:43:23 To 23JAN2000 16:05:53 Steady State 16:05:53
WINDOW: Hanning SPECTRAL LINES: 400 RESOLUTION: 1.25 Hertz

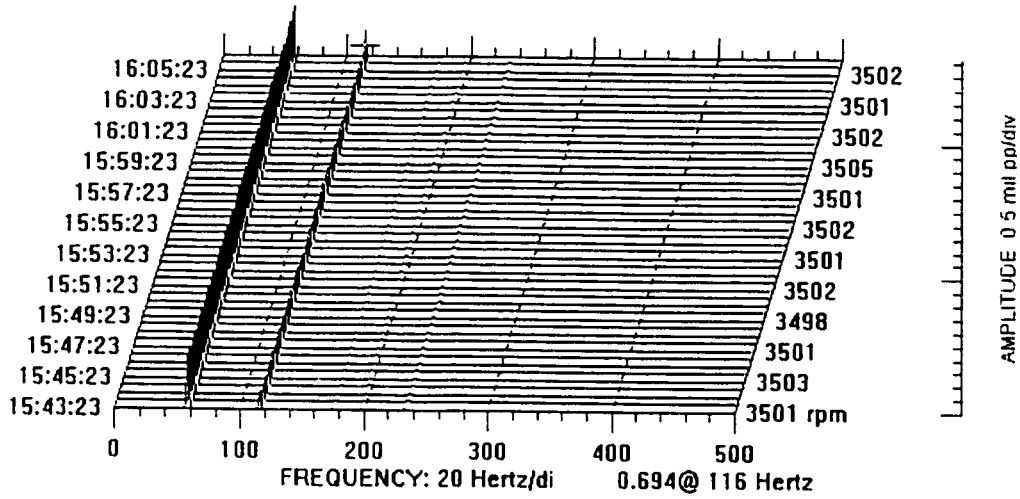

2.29 @ 58 Hertz

(i) Vertical direction

POINT: BRG 1 Horizontal ∠90° Right
MACHINE: Rotor Kit
From 23JAN2000 15:43:23 To 23JAN2000 16:05:53 Steady State 16:05:53
WINDOW: Hanning SPECTRAL LINES: 400 RESOLUTION: 1.25 Hertz

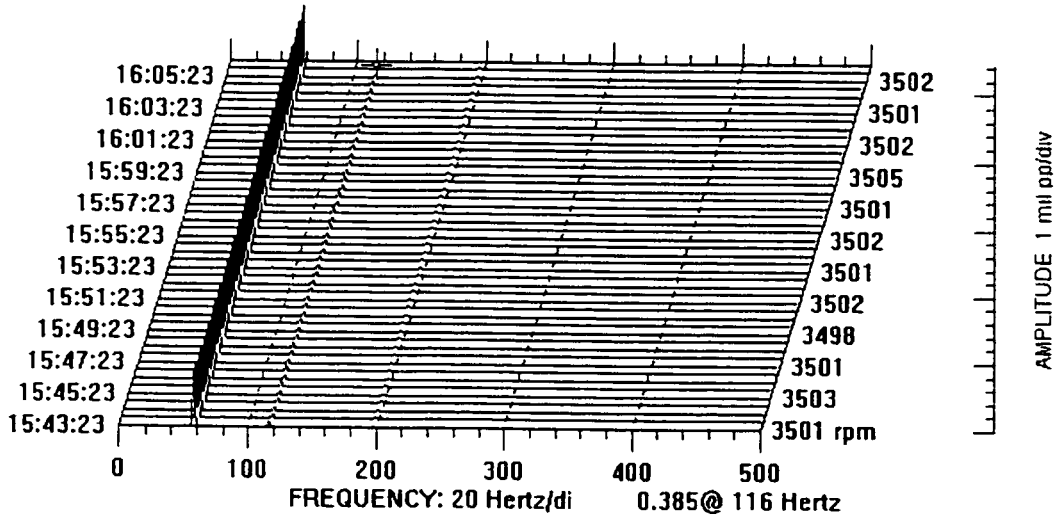

3.73 @ 58 Hertz

(ii) Horizontal direction

Fig. 5.4 (c) Frequency waterfall for steady state data at 3500rpm for shaft with 4mm notch and vertical load tension of 4.3 kg

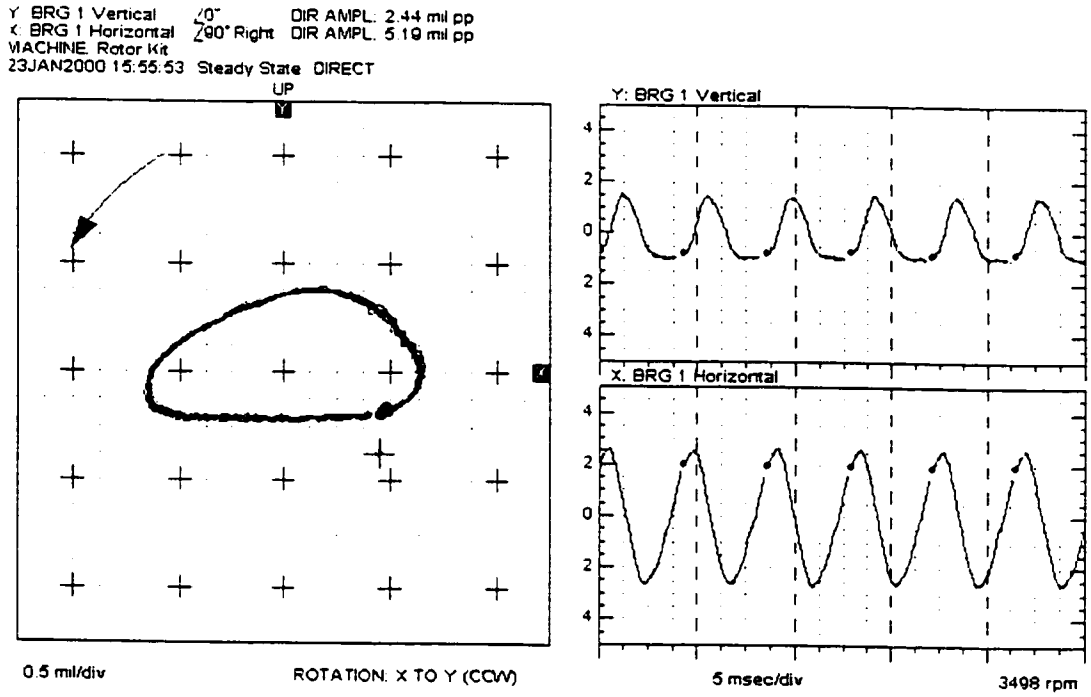

Fig. 5.4 (d) Orbit of shaft with 4mm notch crack and side tension at a steady state speed of 3500 rpm

Figure 5.4 Startup and steady state analysis results for shaft with 4mm notch crack and vertical tension load of 4.3 kg

The experiment was repeated for a shaft with 4mm surface slot crack and the trend of the results obtained are similar to that reported for the shaft with 4mm surface notch crack. Table 5.1 summarizes the changes in the critical speed of different shafts as presented in the Bode plots. Figures 5.1(a), 5.2(a) 5.3(a) and 5.4(a) of the startup data. The experiment was also performed latter to ascertain the reproducibility of the results and study the effect of horizontal side tension on the vibration response of cracked and un-cracked shafts. Data for each experiment were taken at least three times (see Appendix A1) and the average results are presented in Tables 5.2 and 5.4.

The presence of a crack decreased the first critical speed of the system since crack reduces the stiffness of a shaft. It should be noted that the change in stiffness in the vertical direction is a function of the crack depth (Table 5.1). The observed difference, although small, between critical speed in the vertical and horizontal directions may be due to stiffness asymmetry of the shaft rotor system.

Application of vertical side tension increased the first critical speed of both cracked and un-cracked shafts (Tables 5.1 and 5.2) in the vertical and horizontal directions. However, application of horizontal side tension decreased the critical speed of the un-cracked shaft in the horizontal direction and does not affect the critical speed in the vertical direction. For the cracked shaft, horizontal side tension increased the critical speed in both directions.

Imam et al. [4] reported that it is difficult to distinguish between the spectral analysis results for un-cracked and cracked shafts, particularly for a very small crack, since 1X, 2X and other higher harmonics are always present although in varying

Table 5.1 Critical speeds for simply supported un-cracked and cracked shafts

Critical Speed (rpm)				
Shaft Description	**Without Spring Tension**		**With Vertical Spring Tension (4.3kg)**	
	Y	**X**	**Y**	**X**
Un-cracked	1630	1680	1650	1720
4 mm notch	1520	1570	1550	1550
4 mm slot	1520	1650	1550	1700

Table 5.2 Averaged critical speeds for simply supported un-cracked and cracked shafts

DESCRIPTION	**CRITICAL SPEED (rpm)**	
	Y	**X**
Un-cracked shaft	1626	1694
Un-cracked Shaft with Vertical tension of 4.3Kg	1680	1717
Un-cracked Shaft with Horizontal tension of 4.3Kg	1627	1680
Cracked Shaft with 4mm notch	1567	1627
Cracked Shaft with 4mm notch and 4.3 Kg Vertical Tension	1637	1650
Cracked Shaft with 4mm notch and 4.3 Kg Horizontal Tension	1603	1670

Table 5.3. Change in 1X and 2X amplitudes due to side load and crack

	Vertical Probe		Horizontal Probe	
SHAFT DESCRIPTION	**1X (mil)**	**2X (mil)**	**1X (mil)**	**2X (mil)**
Un-cracked Shaft	1.41	0.206	2.44	0.308
Un-cracked shaft with 4.3kg side spring load	1.08 (-23.4%)	0.18 (-12.6%)	2.36 (-3.3%)	0.36 (+16.7%)
Shaft with 4mm surface notch	3.03 (+114.9%)	0.231 (+12.1%)	3.65 (+49.5%)	0.18 (-41.6%)
Shaft with 4mm surface notch and 4.3kg sid	1.67 (+18.4%)	0.694 (+236.8%)	3.73 (+52.9%)	0.385 (+25%)

Table 5.4. Averaged changes in 1X and 2X amplitudes due to side load and crack

	Y PROBE		X PROBE	
DESCRIPTION	**1X**	**2X**	**1X**	**2X**
Un-cracked shaft	1.470	0.206	2.295	0.334
Un-cracked Shaft with Vertical Side tension of 4.3Kg	1.235 (-16.0%)	0.154 (-25.2%)	2.250 (-2.0%)	0.347 (+3.9%)
Un-cracked Shaft with Horizontal Side tension of 4.3Kg	1.600 (+8.8%)	0.189 (-8.3%)	1.977 (-13.9%)	0.257 (-23.1%)
Cracked Shaft with 4mm notch	2.477 (+68.5%)	0.240 (+16.5%)	3.147 (+37.1%)	0.223 (-33.2%)
Cracked Shaft with 4mm notch and 4.3 Kg Vertical Tension	1.943 (+32.2%)	0.385 (+86.9%)	3.413 (+48.7%)	0.411 (+23.1%)
Cracked Shaft with 4mm notch and 4.3 Kg Horizontal Tension	2.570 (+74.8%)	0.325 (+57.8%)	2.417 (+5.3%)	0.377 (+12.9%)

proportion. He therefore subtracted the vibration signal of un-cracked shaft from signal of cracked shaft before performing spectral analysis to study changes in 1X and 2X amplitudes; this analysis was termed histogram. Furthermore, some researchers [4, 6, 8 and 35] that experimentally studied the dynamic behavior of cracked shaft applied side load by different mechanisms to aid crack propagation, side load or tension is known to cause asymmetry in shaft stiffness but no one, according to the author's knowledge, has reported the effect of side load on 1X and 2X amplitudes.

Table 5.3 summarizes the changes in 1X and 2X amplitudes due to application of side load, the presence of crack and the presence of both side load and crack. The values in brackets represent the percentage change in amplitude with respect to the un-cracked shaft. Figures 5.1(c), 5.2(c), 5.3(c) and 5.4(c) are the frequency spectral waterfalls showing values of amplitudes for 1X and 2X harmonics. The results of this experimental study for the simply supported shaft show that vertical side tension excites 2X vibration during startup, and during steady state, it decreased the amplitudes of 1X and 2X harmonics in the vertical direction but in the horizontal direction, 1X is decreased while 2X is increased but the change is small compared with the change in vertical direction, see Tables 5.3 and 5.4. Similarly, horizontal side tension decreased 1X and 2X harmonics in the horizontal direction but in the vertical direction, 1X is increased while 2X is decreased but the change is small compared with changes in horizontal direction.

The effect of a 4mm deep surface notch crack increased the startup resonance bandwidth. During steady state, it increased 1X and 2X harmonics with the percentage increase in 1X greater than 2X in the vertical direction. But 1X is increased while 2X is decreased in the horizontal direction (Tables 5.3 and 5.4). This means that the presence

of crack changed the stiffness, damping and mass distribution of the system, excites mainly 1X and 2X harmonics with a small transient signal as shown in Figure 5. 3(c).

The combined effect of a transverse crack and vertical or horizontal side tension increased 1X and 2X harmonics in both directions with the appearance of 3X and 4X harmonics of very small amplitude compared with 1X and 2X amplitudes, see Figure 5.4(c). Tables 5.3 and 5.4 show that crack excites 1X and 2X harmonics and the changes in the amplitude of 1X and 2X harmonics can be used to detect the presence of a crack in a rotor. Many researchers [1, 2, 4, 5, 6, 8, 12 and 35] have reported that crack excites 1X and 2X in a rotating shaft. From Figures 5.1(d), 5.2(d), 5.3(d) and 5.4(d), it is observed that application of side tension in the vertical direction does not have any effect on the shape of the orbit of un-cracked shaft, the shape remained a distorted ellipse. However, vertical side tension applied to the cracked shaft changed the orbit shape considerably. This effect is due to the fact that the stiffness of the cracked shaft is less than that of the un-cracked shaft this made the cracked shaft respond more to the effect of side load.

5.2.2 Second Experimental Setup (Overhang Shaft)

The results of the effect of the presence of crack, crack propagation and side load on the dynamic response of a rotor system are presented in this section. The overhang shaft arrangement is important as it can be found in many industrial turbo-machines in which the compressor and turbine has a single shaft. Unlike the simply supported arrangement in which side load was applied via spring tension, a mass of 8 kg was attached at the end of overhang shaft with a thick string (Fig 4.1(c)). This arrangement

introduces an extra degree of freedom in the vertical direction and this is clearly shown in the Bode plots of the startup signals; there is the presence of another resonance at about 530 rpm in the vertical startup signals of all arrangements with side load. This resonance is ignored in the discussion of the results. The running speed at steady state was always kept below the first critical speed.

5.2.2.1 Un-cracked Shaft

Figure 5.5 presents the bode plot and the frequency cascade of the startup data, the frequency waterfall and the orbit of the steady state data from both the vertical and horizontal probes for the un-cracked shaft without 8kg overhanging side load. Figure 5.6 shows results for un-cracked shaft with 8kg overhang side load. Fig. 5.5(a) and Fig. 5.6(a) show that 8 kg hanging side load produced asymmetry in shaft response. The overhang disk that serves as the mass of the system excites 2X harmonic, which is more prominent in the horizontal direction as shown in Fig. 5.5(b)(ii) and Fig. 5.5(c)(ii). 3X harmonic and a transient signal are also present in the horizontal direction in addition to 1X and 2X harmonics that appeared in both the vertical and horizontal directions. The applied overhang side load increased the resonance bandwidth in the vertical direction: this suggests non-linearity and increased damping of the system due to increased rubbing of the shaft in the bearing in the vertical direction. This is different from the effect produced by crack in the simply supported mode that has increased bandwidth in both directions. Furthermore, unlike the simply supported arrangement, side load does not excites 2X vibration in the startup vibration. Side load also introduced more harmonics in the vertical direction but reduced 2X amplitude and contributed in

removing the transient signal in the horizontal direction, Fig. 5.6(c). The orbits, Fig. 5.5(d) and Fig. 5.6(d) show the present of asymmetry.

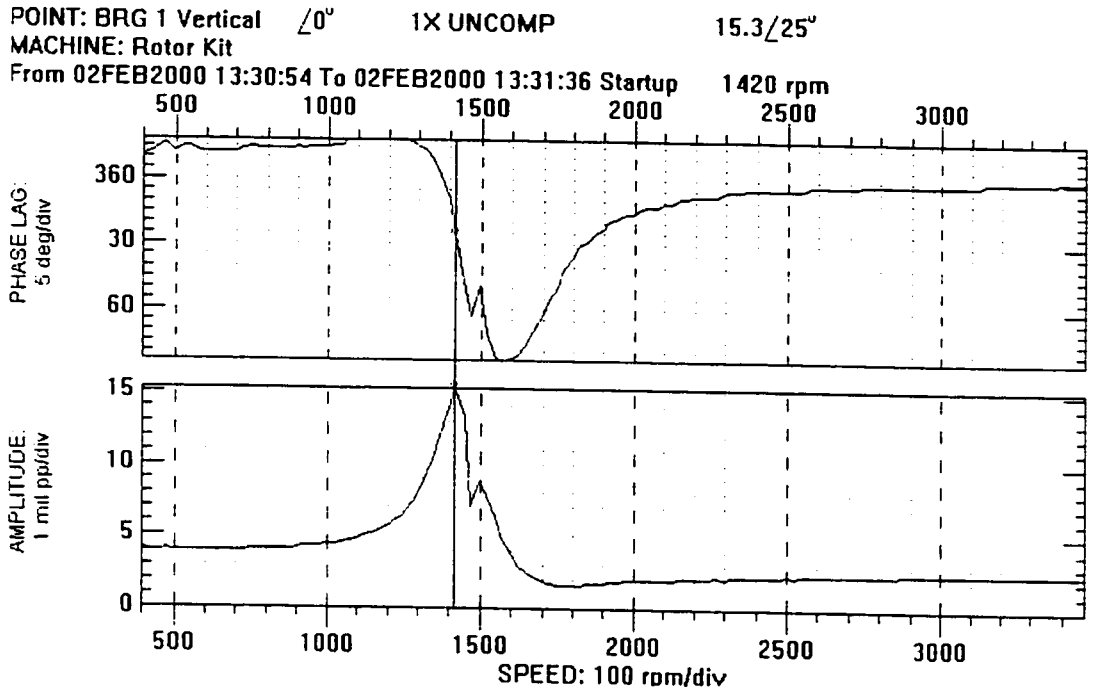

(i) Vertical direction

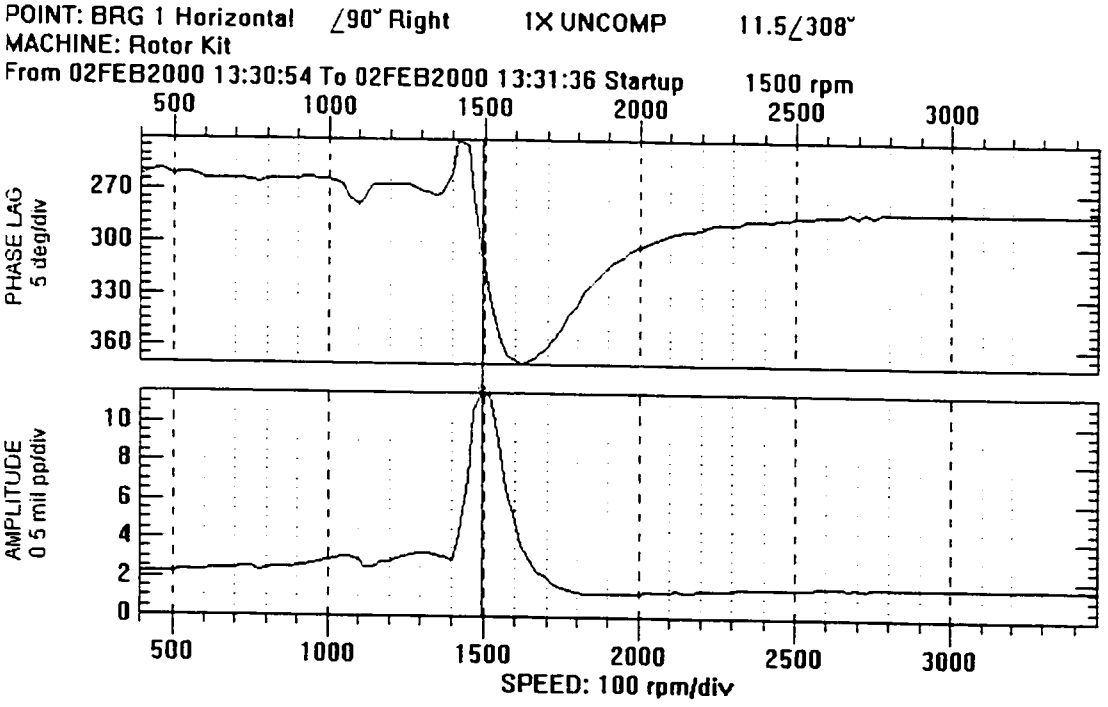

(ii) Horizontal direction

Fig. 5.5 (a). Bode plot of startup data for un-cracked shaft without the 8kg vertical hanging side load

POINT: BRG 1 Vertical ∠0°
MACHINE: Rotor Kit
From 02FEB2000 13:30:54 To 02FEB2000 13:31:34 Startup 399 rpm
WINDOW: None SPECTRAL LINES: 400 RESOLUTION: 1.25 Hertz

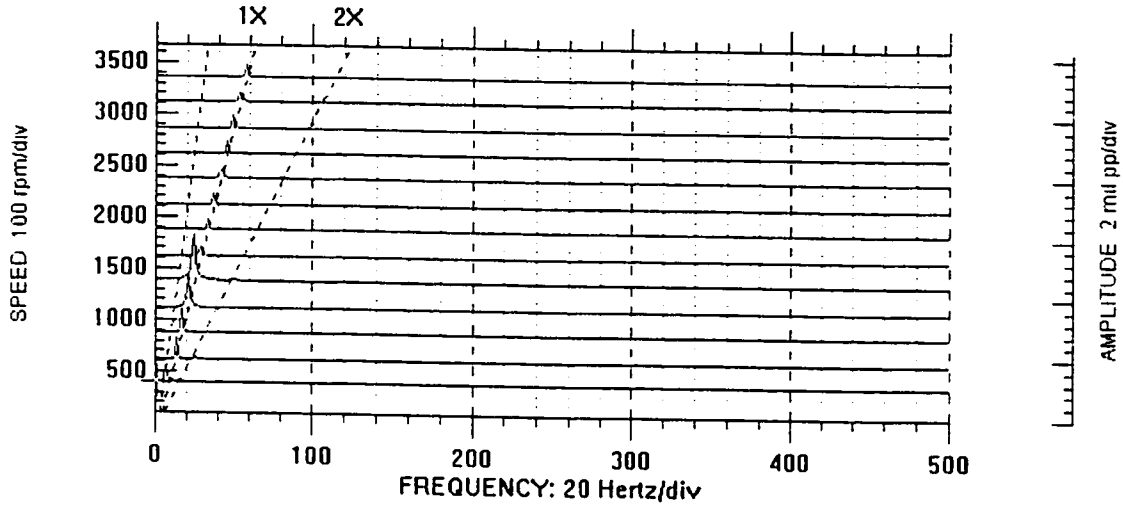

(i) Vertical direction

POINT: BRG 1 Horizontal ∠90° Right
MACHINE: Rotor Kit
From 02FEB2000 13:30:54 To 02FEB2000 13:31:34 Startup 399 rpm
WINDOW: None SPECTRAL LINES: 400 RESOLUTION: 1.25 Hertz

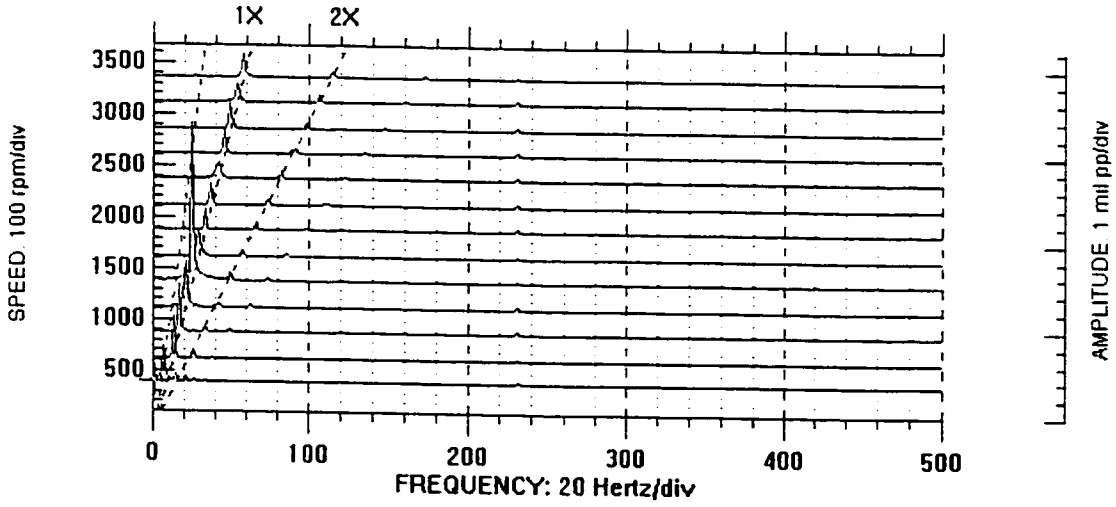

(ii) Horizontal direction

Fig. 5.5 (b). Frequency cascade of startup data for un-cracked shaft without the 8kg vertical hanging side load

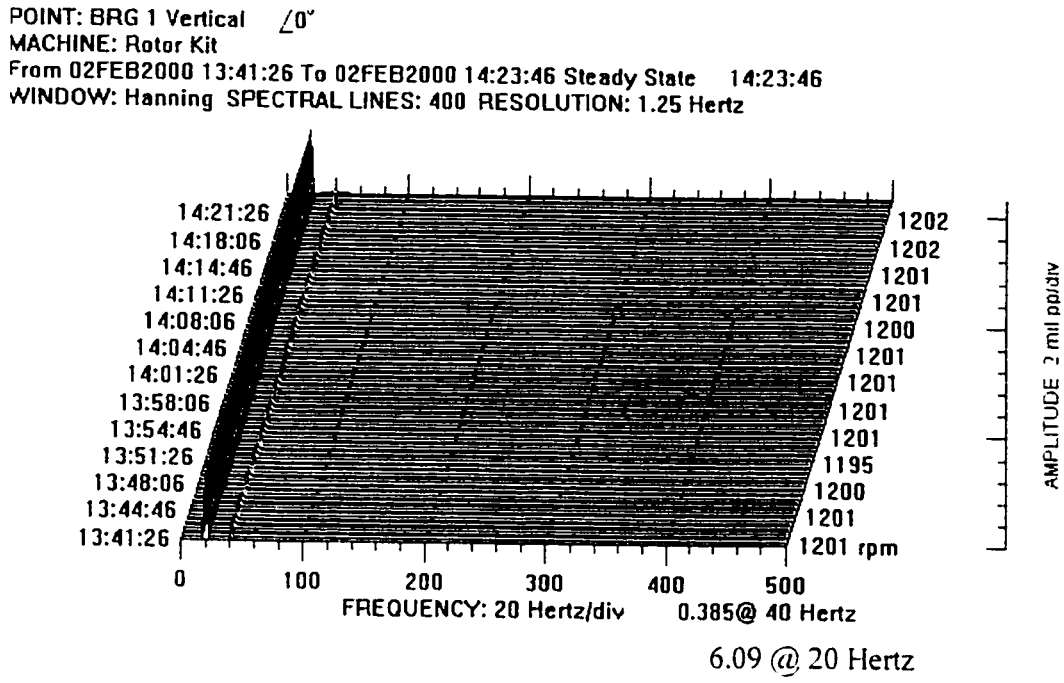

(i) Vertical direction

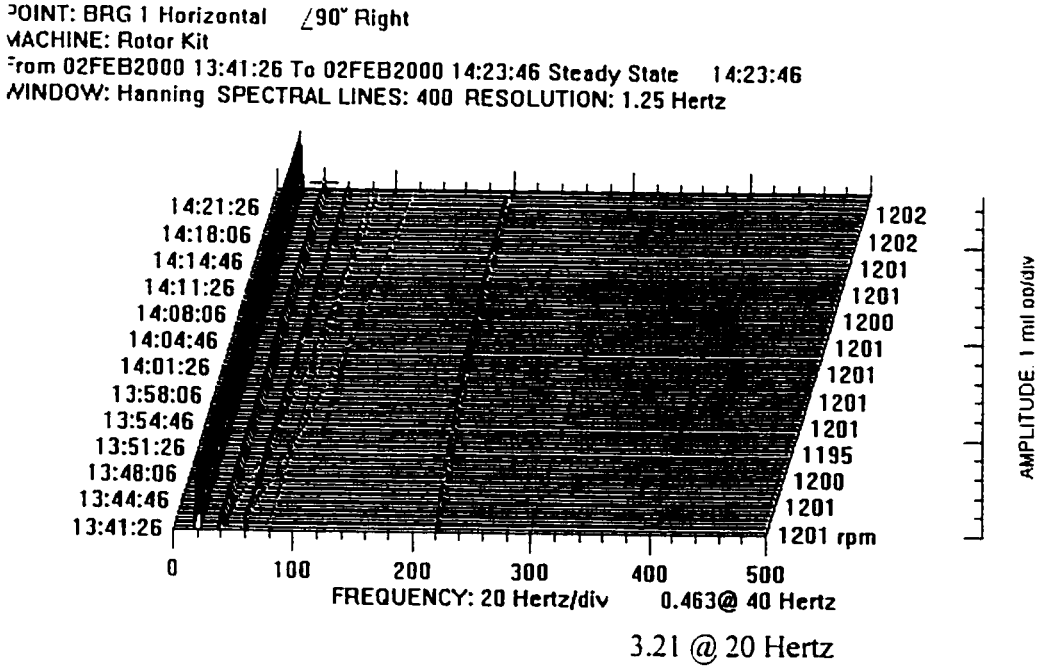

Fig. 5.5(c) Frequency waterfall of steady state data at 1200rpm for un-cracked shaft without the 8kg vertical hanging side load

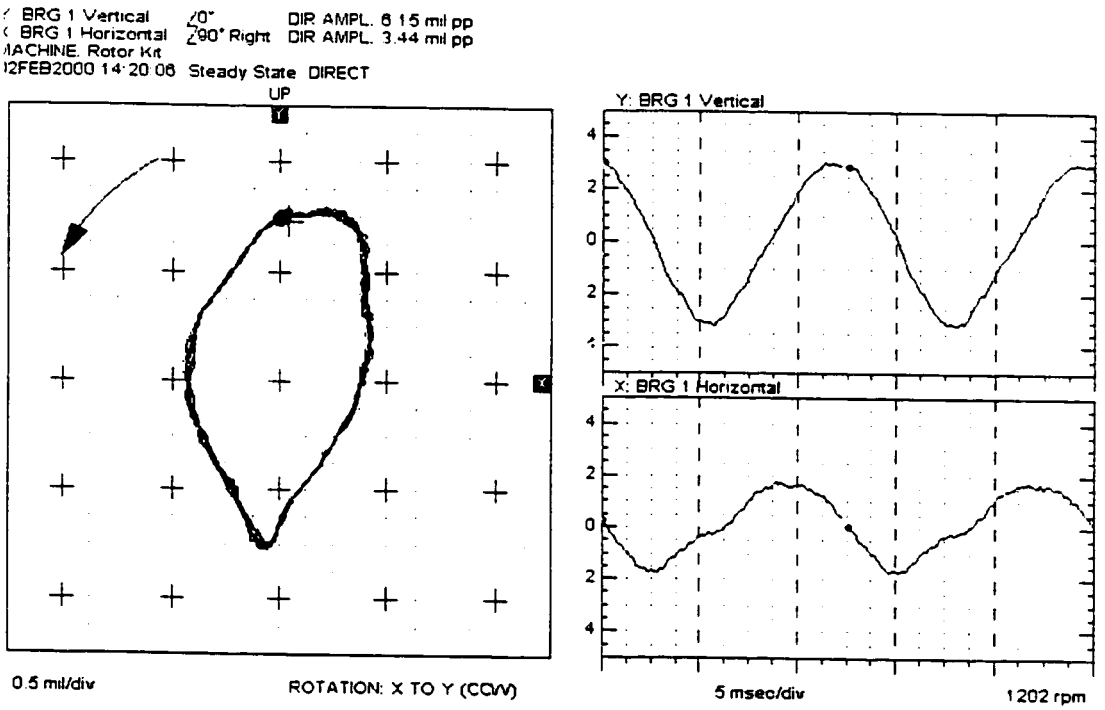

Fig. 5.5 (d). Orbit of steady state data at 1200rpm for un-cracked shaft without the 8kg vertical hanging side load

Figure. 5.5. Startup and steady state analysis results for un-cracked shaft without the 8kg vertical hanging side load

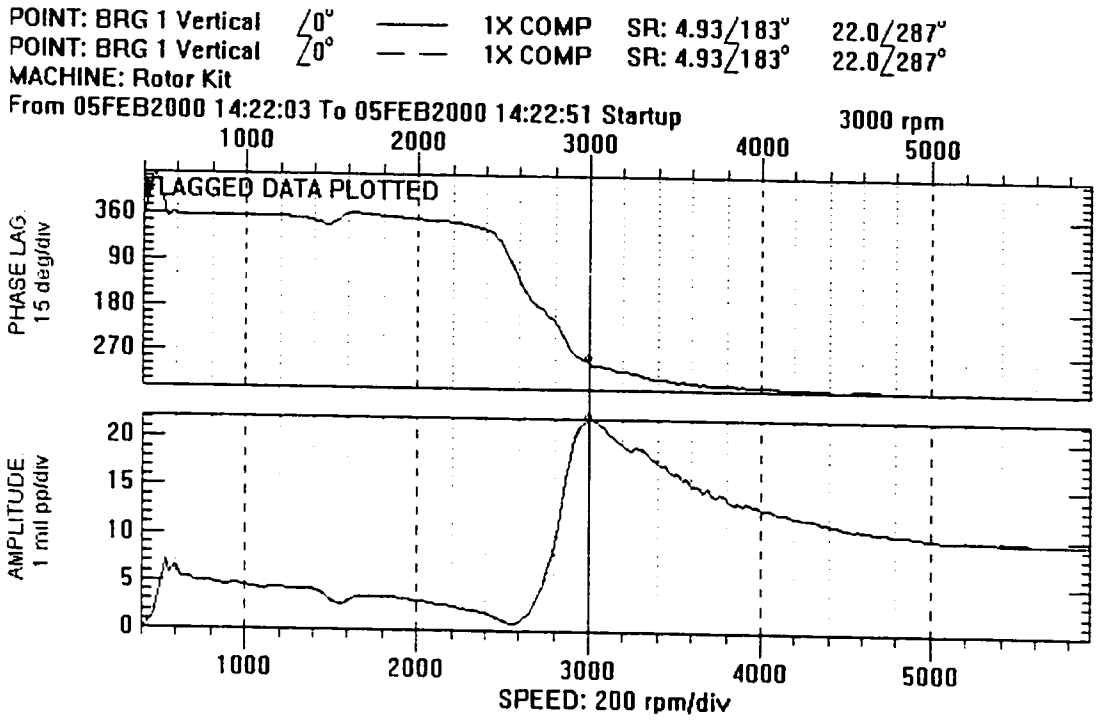

(i) Vertical direction

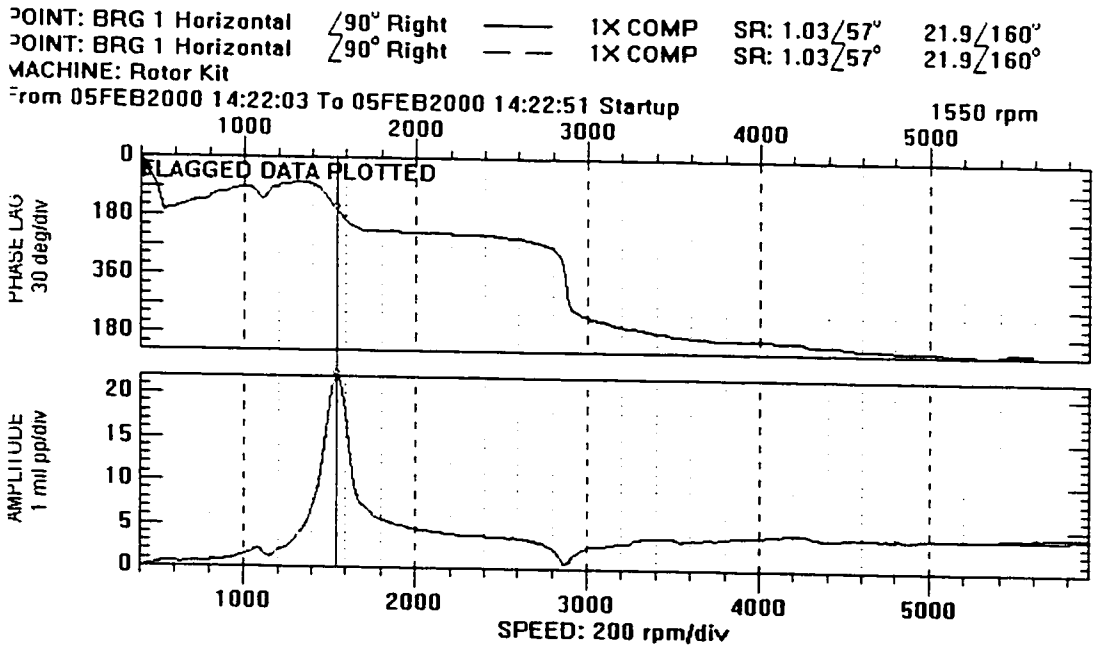

(ii) Horizontal direction

Fig. 5.6 (a). Bode plot of startup data for un-cracked shaft with 8 kg hanging side load.

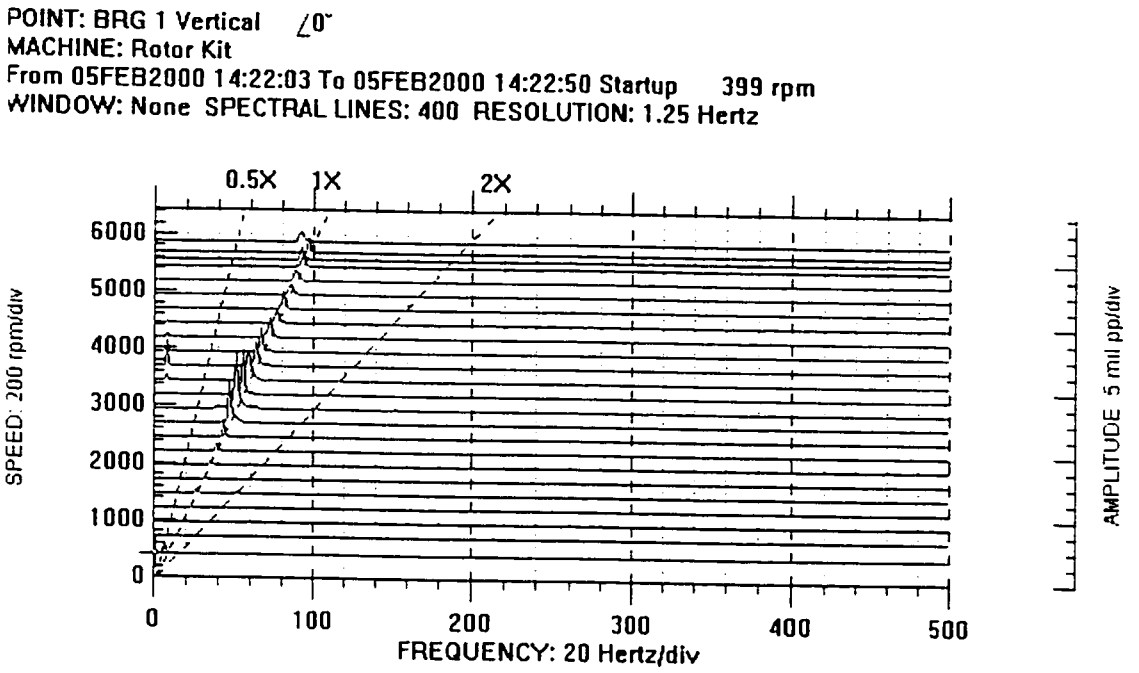

(i) Vertical direction

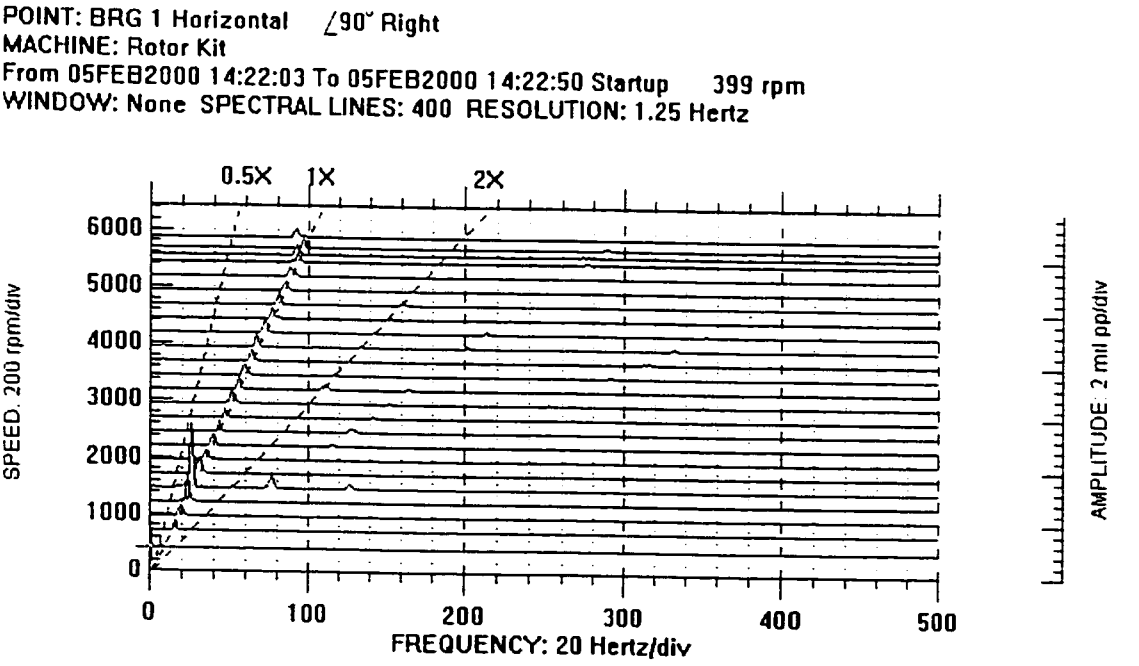

(ii) Horizontal direction

Fig. 5.6 (b). Frequency cascade of startup data for un-cracked shaft with the 8kg vertical hanging side load

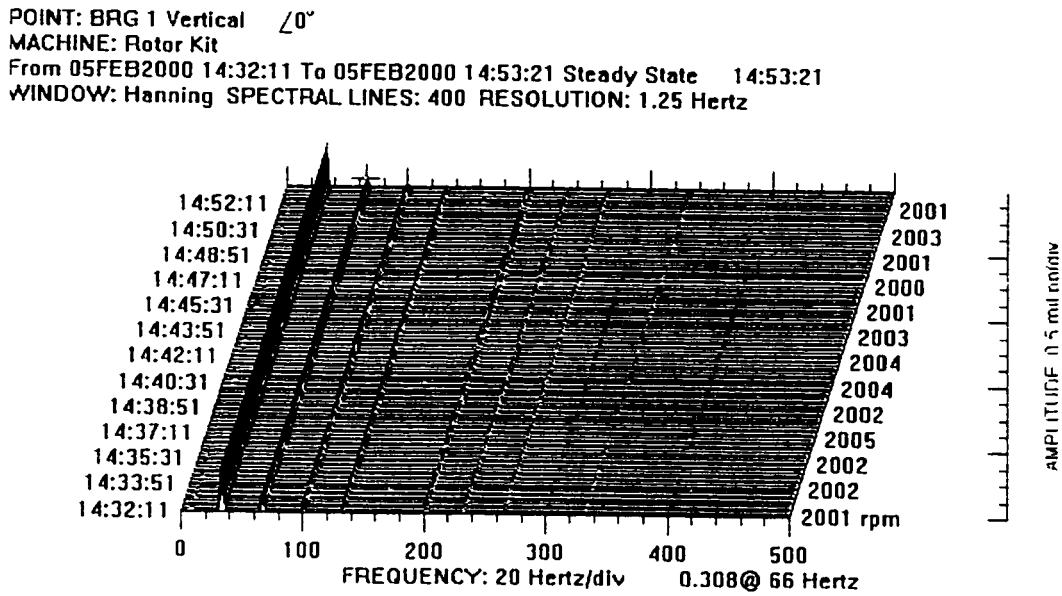

1.36 @ 33 Hertz

(i) Vertical direction

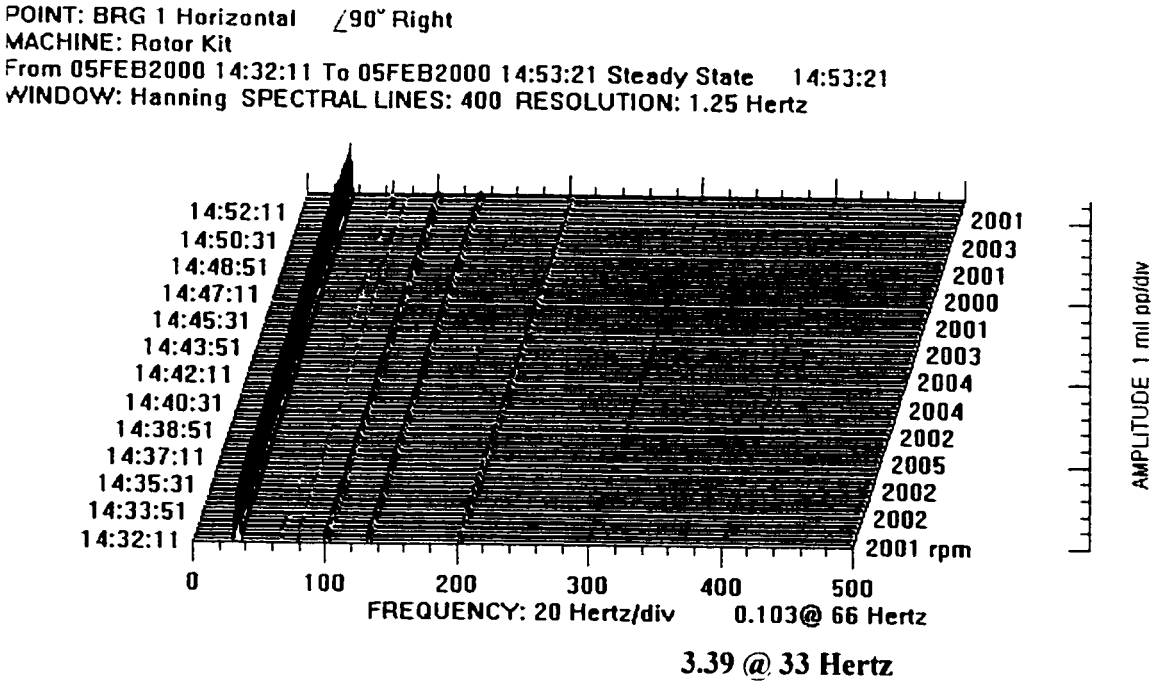

3.39 @ 33 Hertz

(ii) Horizontal direction

Fig. 5.6 (c). Frequency waterfall for the horizontal steady state data at 2000 rpm for un-cracked shaft with 8kg vertical hanging side load.

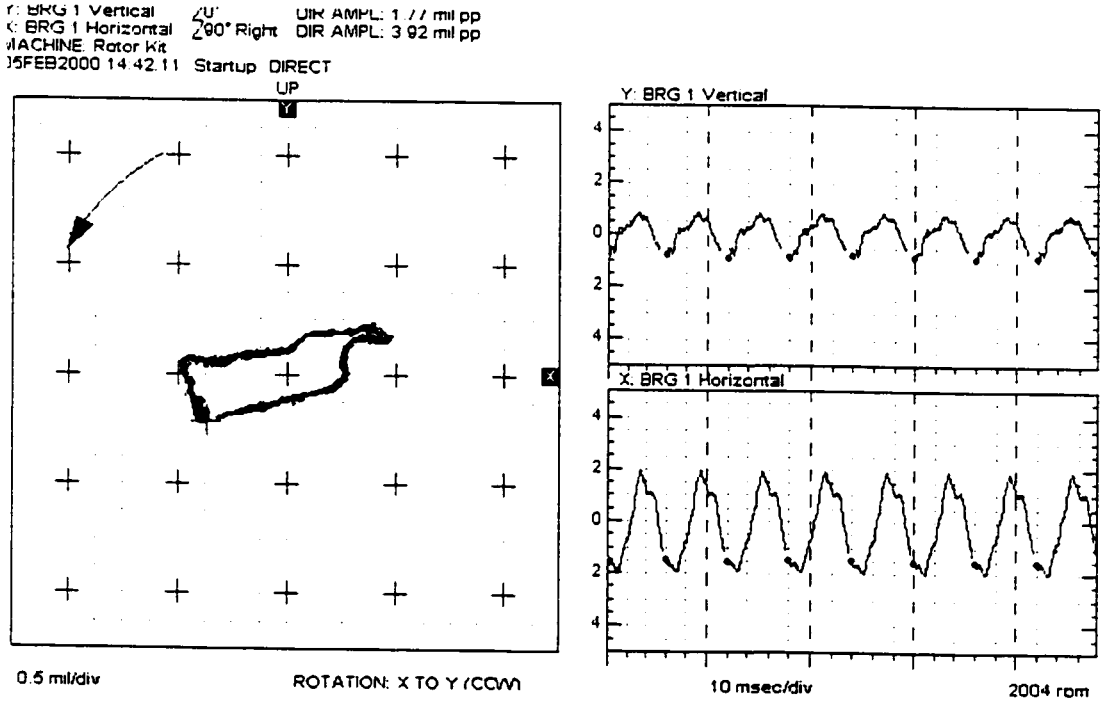

Fig. 5.6 (d) Orbit of un-cracked shaft with 8kg hanging side load at a steady state speed of 2000 rpm

Figure 5.6 Startup and steady state analysis results for un-cracked shaft with 8kg hanging side load

5.2.2.2 Shaft with Surface Crack

Figure 5.7 presents the bode plot and frequency cascade of the startup data, the frequency waterfall and the orbit of the steady state data from both the vertical and horizontal probes for a shaft with 3mm notch crack and without 8kg overhanging side load. Figure 5.8 presents the results for the same shaft with 8kg overhanging side load at the beginning of crack propagation. Figure 5.9 presents the results for the same cracked shaft with overhang side load just before the shaft fractured.

Fig. 5.7(a) compared with Fig. 5.5(a) shows that the presence of crack in the overhang shaft set-up increased the critical speed of the shaft in the vertical direction while critical speed in the horizontal direction remained unchanged, this is strange and contrary to the observation made with simply supported shaft further investigation is required to know the cause of this. Crack also introduced 2X vibration in the startup signal, Fig.5.7. Application of side load increased critical speeds of the cracked shaft in both directions as shown in Fig 5.8(a). Crack propagation produced an increase in the vertical critical speed and a decrease in the horizontal critical speed of the cracked rotor system see Figure 5.9(a). The combined effect of crack and overhang side load introduced 2X harmonic, which is more prominent in the horizontal direction in the startup signal of the shaft system as shown in Figures 5.8(b) and 5.9(b).

The amplitudes of 1X and 2X harmonics are reduced in both directions due to the presence of 3mm notch crack, Fig. 5.7(c) compared with Fig. 5.5(c): higher harmonics are present in the horizontal direction more than the vertical direction. The combined effect of crack and side load increased the amplitude of 1X and 2X harmonics in both directions, higher harmonics are present in the horizontal direction more than the vertical direction Fig. 5.8(c) and Fig.5.9(c). During crack propagation, 1X and 2X

amplitudes increased in the vertical direction while 1X amplitude decreased and 2X and 3X amplitudes increased in the horizontal direction as presented in Fig. 5.9(c).

The presence of crack and side load affects the shape of the orbit as shown in the Fig. 5.7(d). Fig.5.8(d) and Fig.5.9(d). The shape changed from an egg shape in Fig.5.5(d) to a distorted eclipse shape with additional very small loop at the bottom. Fig 5.7(d) then to a shape with three loops of different sizes, Fig.8(d) and finally to a shape that looks like a distorted letter 'Y' having more than one loop, Fig 5.9(d).

It is observed that the dynamic response of a simply supported shaft arrangement and overhang shaft arrangement is different under the influence of a transverse non-propagating crack and side load. This may be due to what has been reported in literature that the influence of crack on the stiffness and dynamic response of shaft depends on both the crack depth and its position [1, 4, 14].

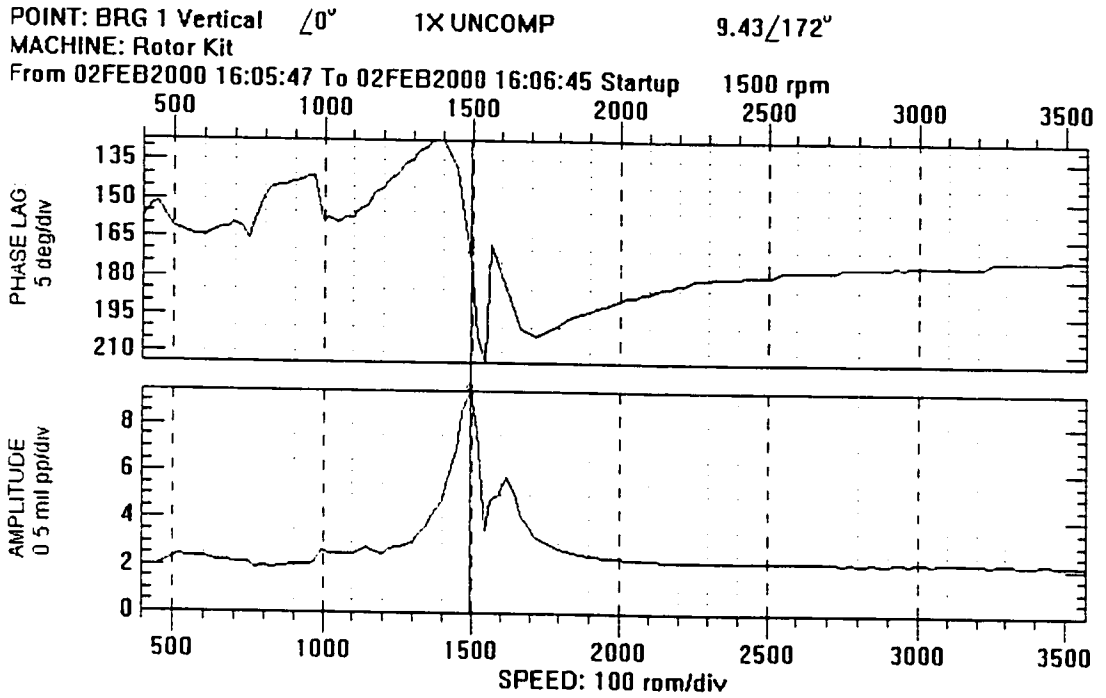

(i) Vertical direction

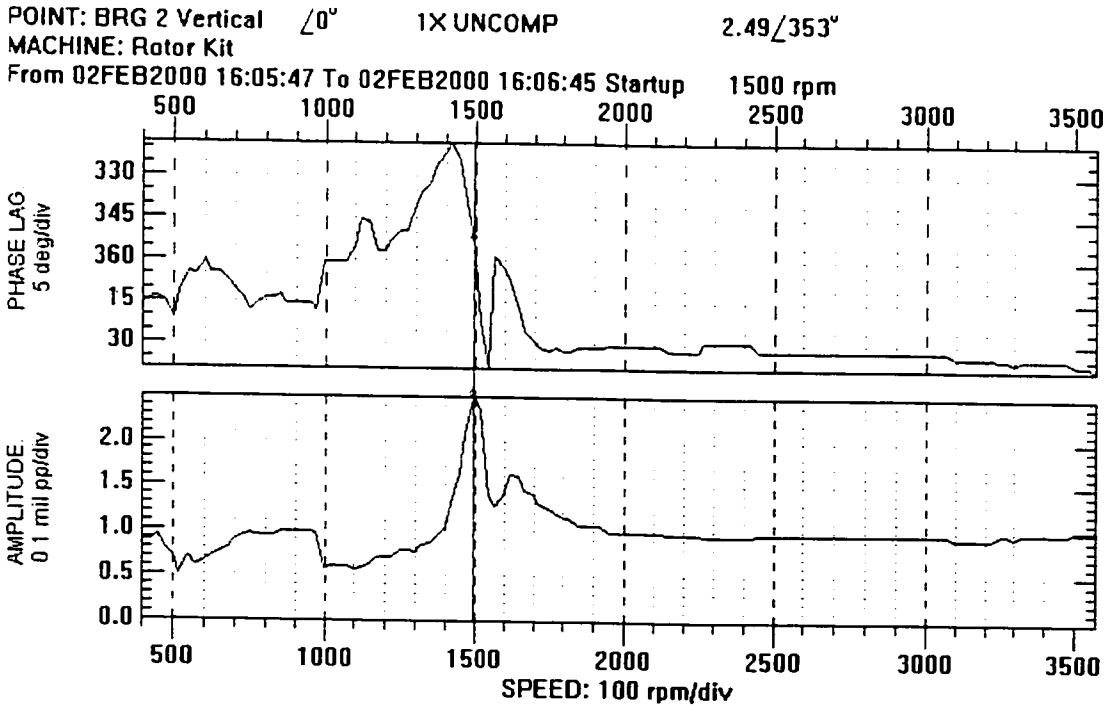

(iii) Horizontal direction

Fig. 5.7 (a) Bode plot of startup data for the shaft with 3mm notch crack without 8kg vertical hanging side load.

POINT: BRG 1 Vertical ∠0°
MACHINE: Rotor Kit
From 02FEB2000 16:05:47 To 02FEB2000 16:06:42 Startup 398 rpm
WINDOW: None SPECTRAL LINES: 400 RESOLUTION: 1.25 Hertz

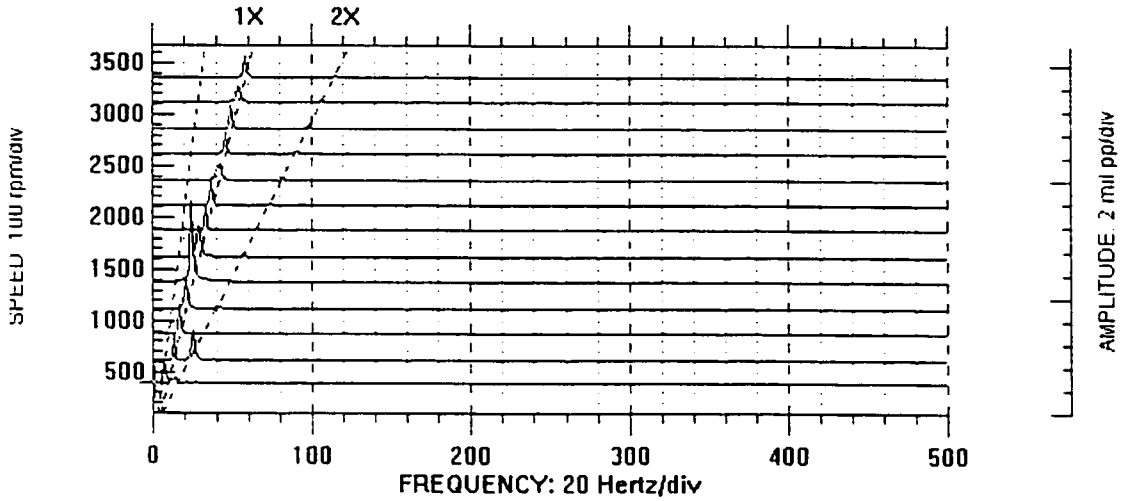

(i) Vertical direction

POINT: BRG 1 Horizontal ∠90° Right
MACHINE: Rotor Kit
From 02FEB2000 16:05:47 To 02FEB2000 16:06:42 Startup 398 rpm
WINDOW: None SPECTRAL LINES: 400 RESOLUTION: 1.25 Hertz

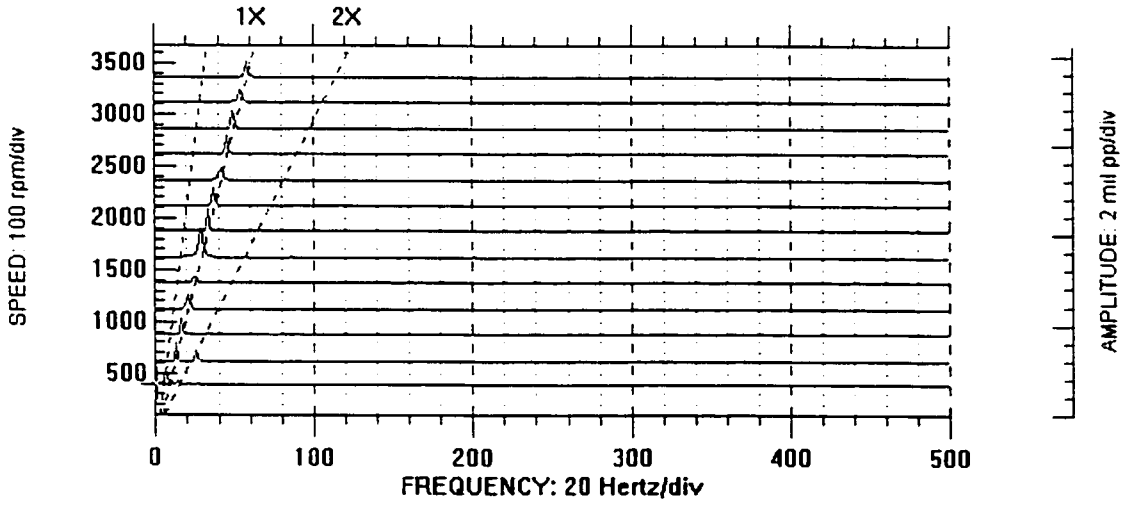

(ii) Horizontal direction

Fig. 5.7(b). Frequency cascade of startup data for the shaft with 3mm notch crack without 8kg vertical hanging side load.

POINT: BRG 1 Vertical ∠0°
MACHINE: Rotor Kit
From 02FEB2000 16:12:06 To 02FEB2000 16:54:06 Steady State 16:54:06
WINDOW: Hanning SPECTRAL LINES: 400 RESOLUTION: 1.25 Hertz

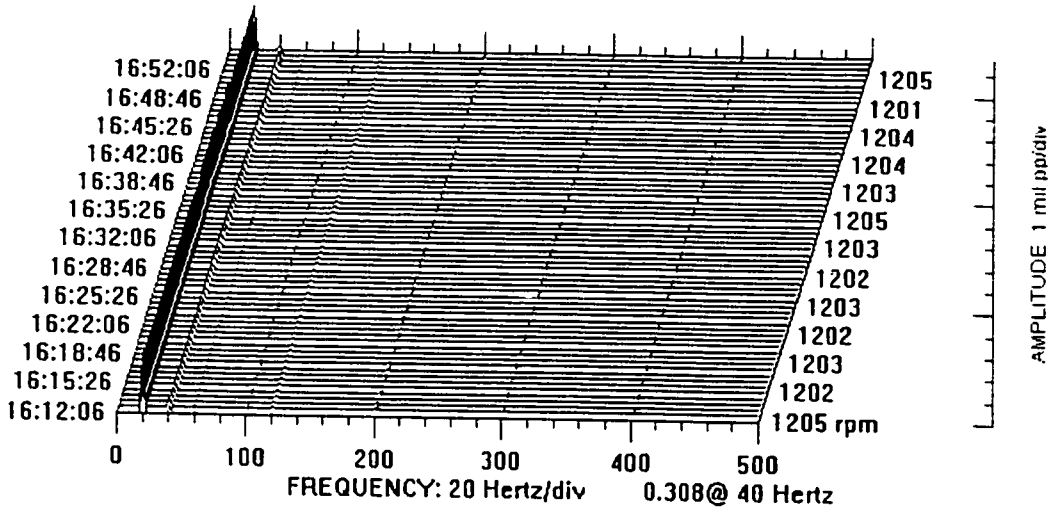

2.36 @ 20 Hertz

(i) Vertical direction

POINT: BRG 1 Horizontal ∠90° Right
MACHINE: Rotor Kit
From 02FEB2000 16:12:06 To 02FEB2000 16:54:06 Steady State 16:54:06
WINDOW: Hanning SPECTRAL LINES: 400 RESOLUTION: 1.25 Hertz

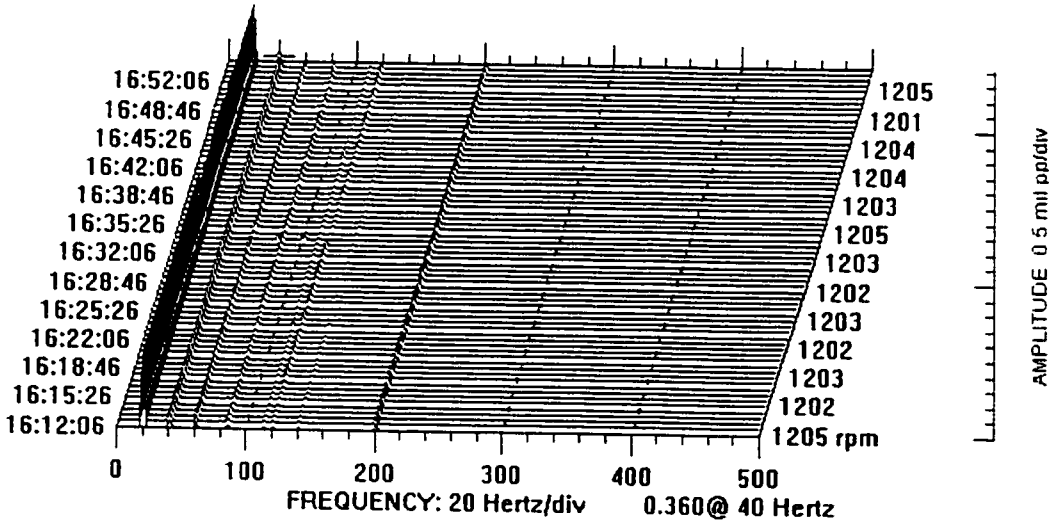

2.08 @ 20 Hertz

(ii) Horizontal direction

Fig. 5.7 (c). Frequency waterfall of steady state data at 1200 rpm for the shaft with 3mm notch crack without 8kg vertical hanging side load.

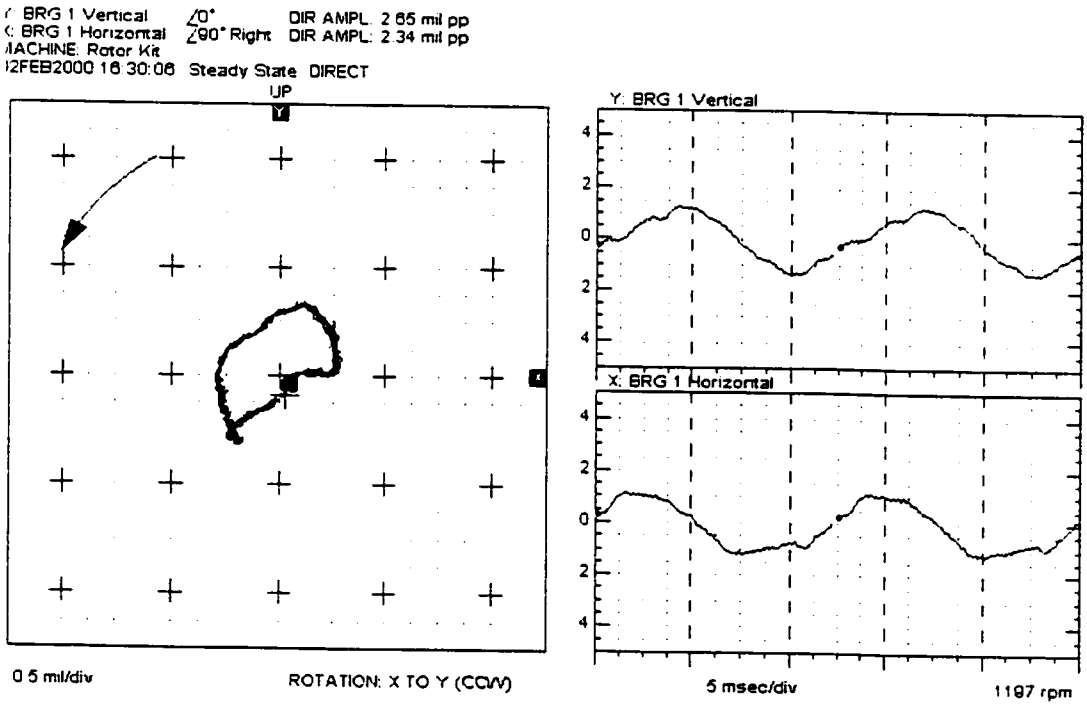

Fig. 5.7 (d). Orbit of steady state data at 1200 rpm for the shaft with 3mm notch crack without 8kg vertical hanging side load.

Figure. 5.7. Startup and steady state analysis results for the shaft with 3mm notch crack without 8kg vertical hanging side load.

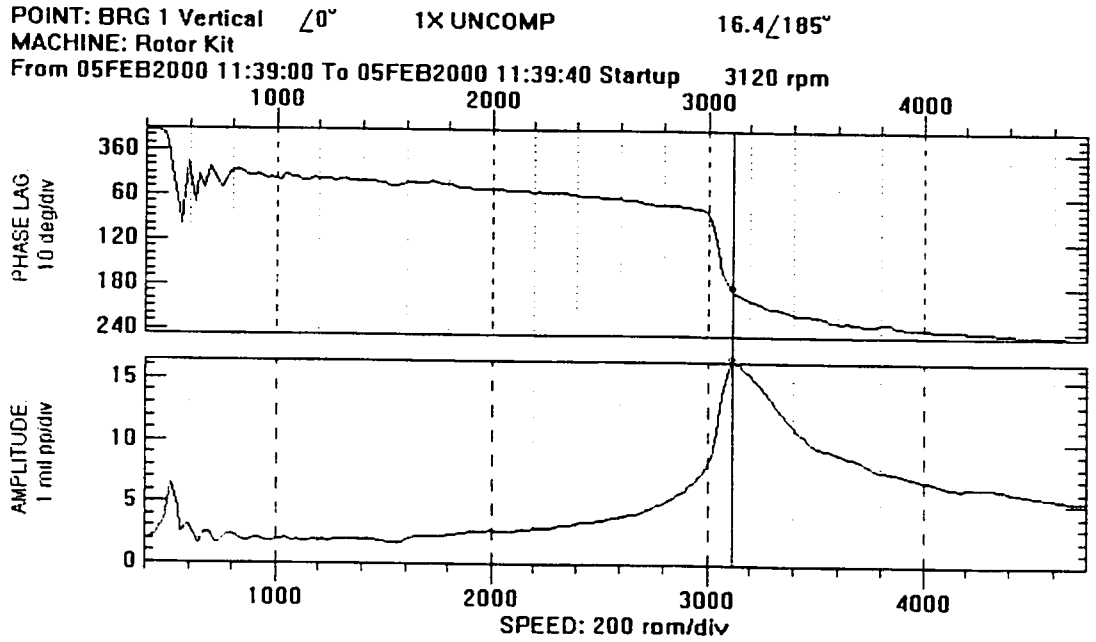

(i) Vertical direction

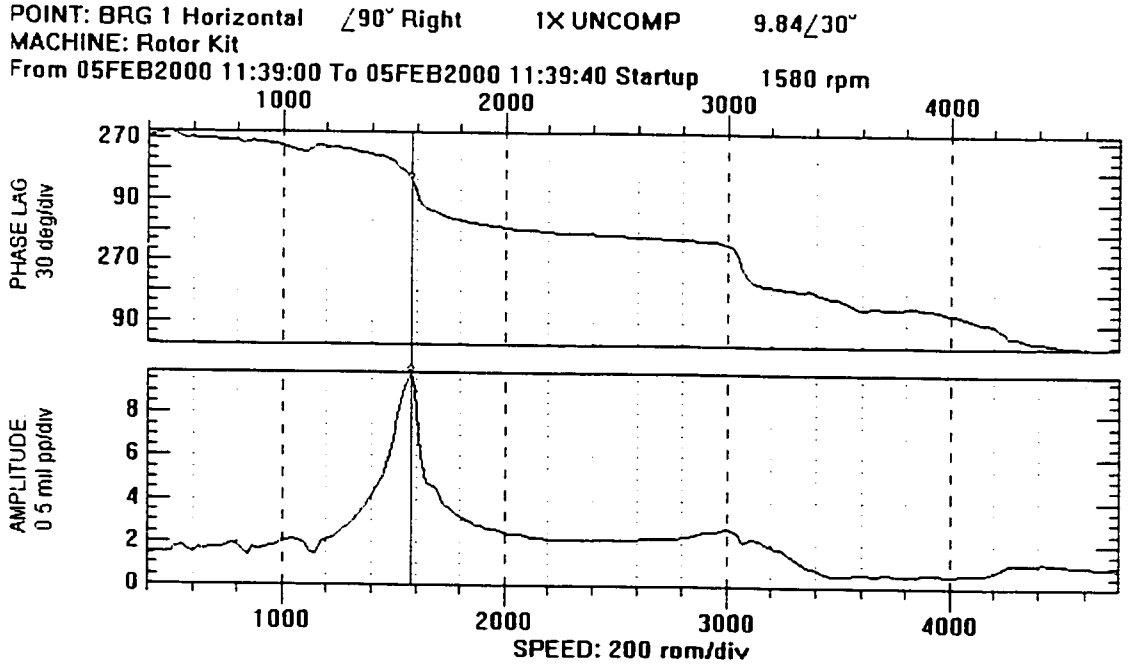

(ii) Horizontal direction

Fig. 5.8 (a). Bode plot of startup data for the shaft with 3mm notch crack with 8kg vertical hanging side load.

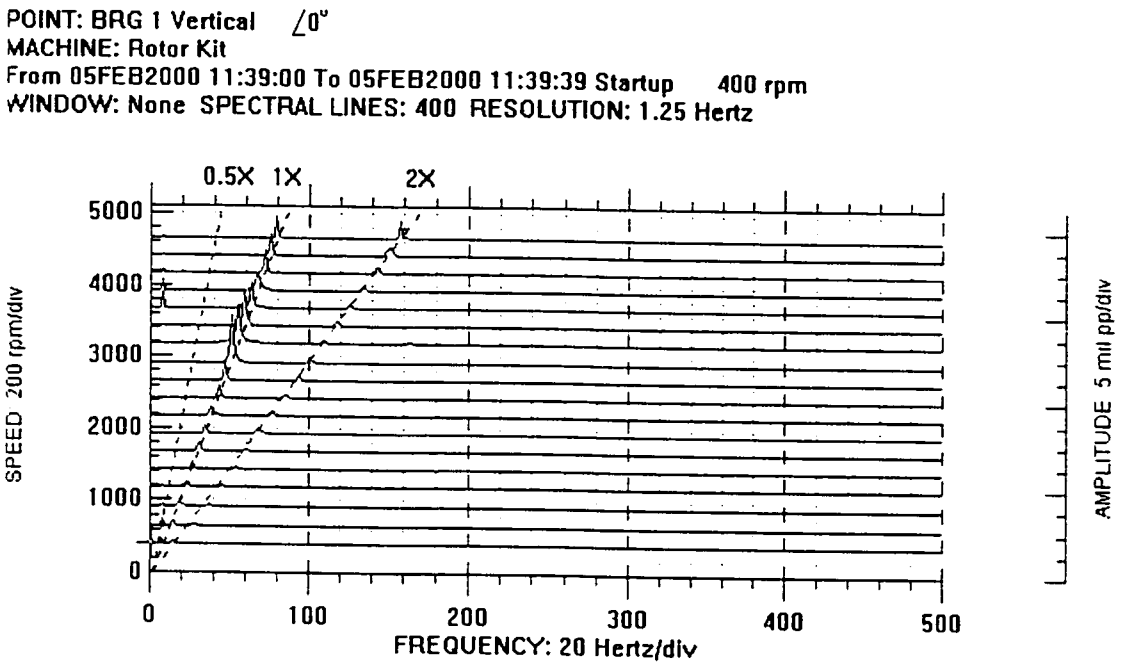

(i) Vertical direction

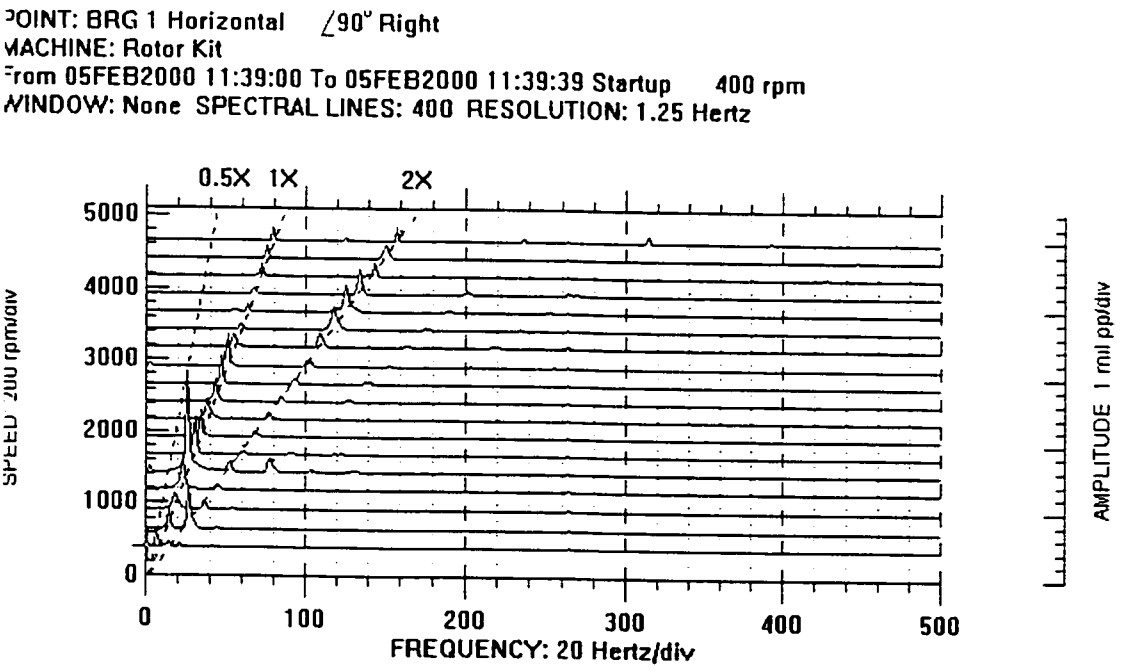

(ii) Horizontal direction

Fig. 5.8 (b). Frequency cascade of startup data for the shaft with 3mm notch crack with 8Kg vertical hanging side load.

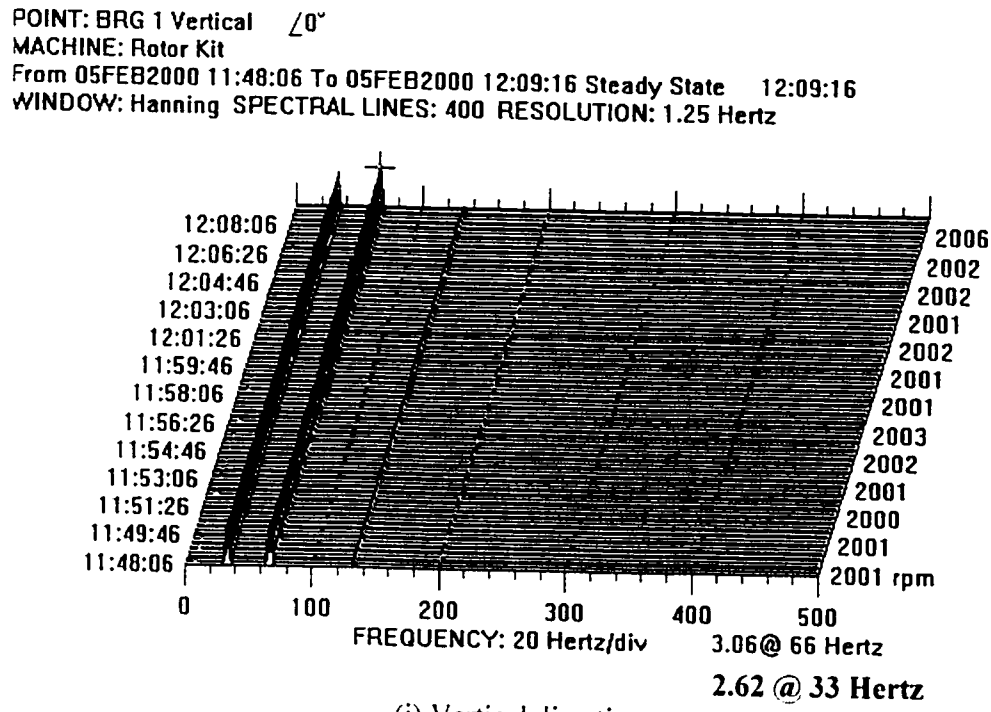

(i) Vertical direction

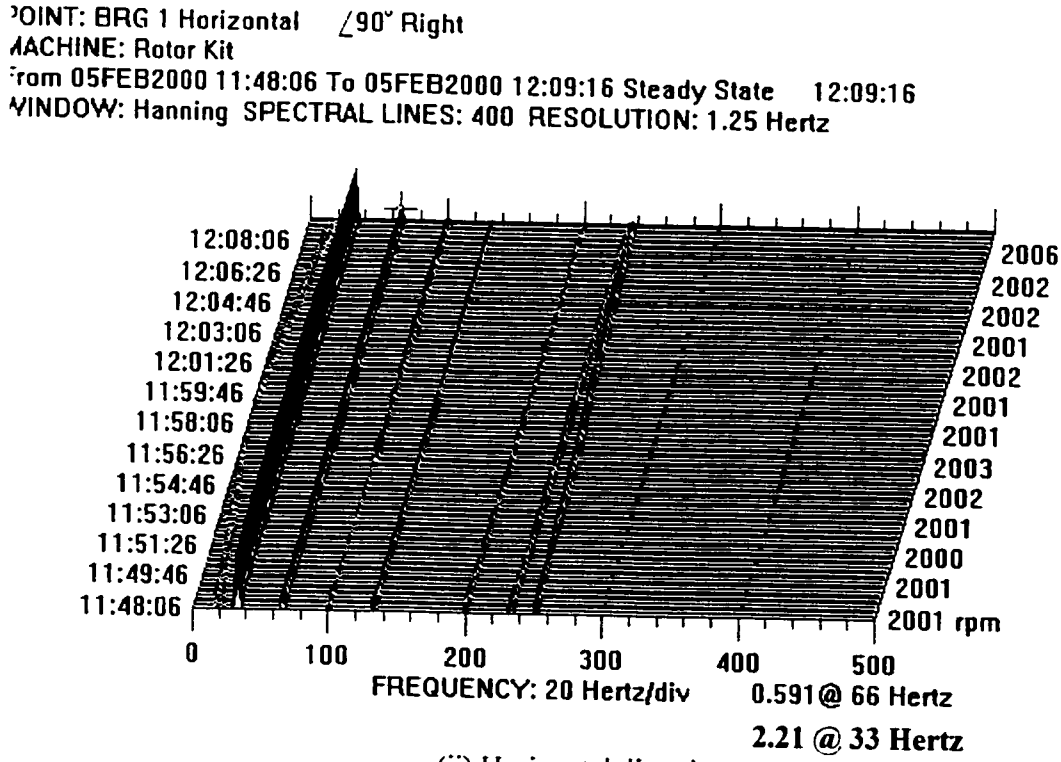

(ii) Horizontal direction

Fig. 5.8(c). Frequency waterfall of steady state data for the shaft with 3mm notch crack and 8kg vertical hanging side load

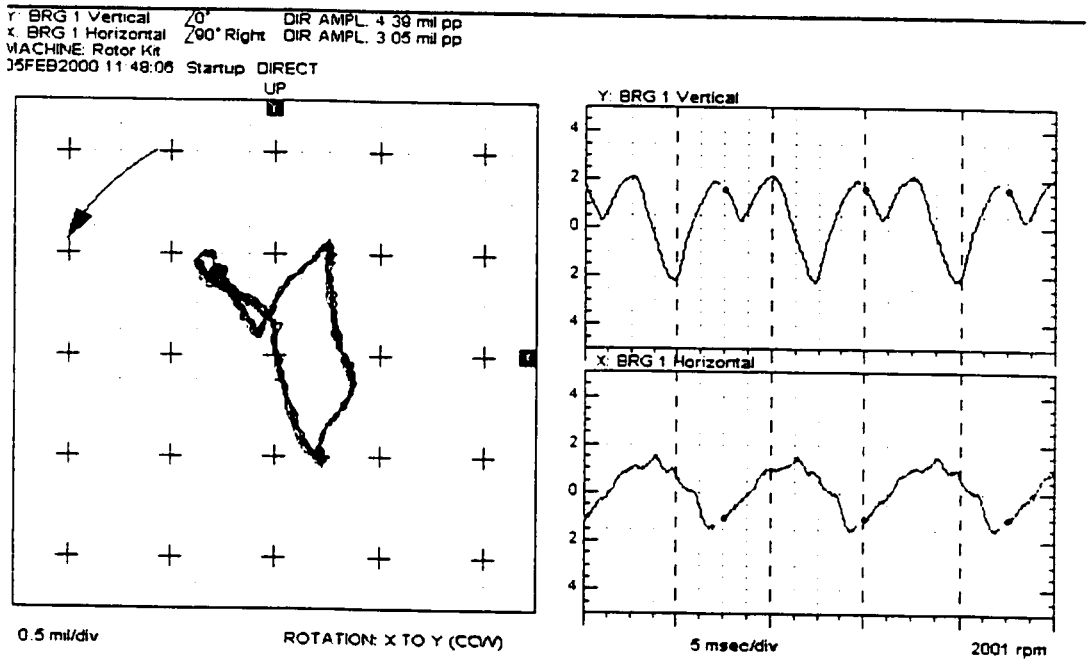

Fig. 5.8 (d). Orbit of steady state data for the shaft with 3mm notch crack and 8kg vertical hanging side load

Figure 5.8 Startup and steady state analysis results for the shaft with 3mm notch crack with 8 kg vertical hanging side load at the beginning of crack propagation

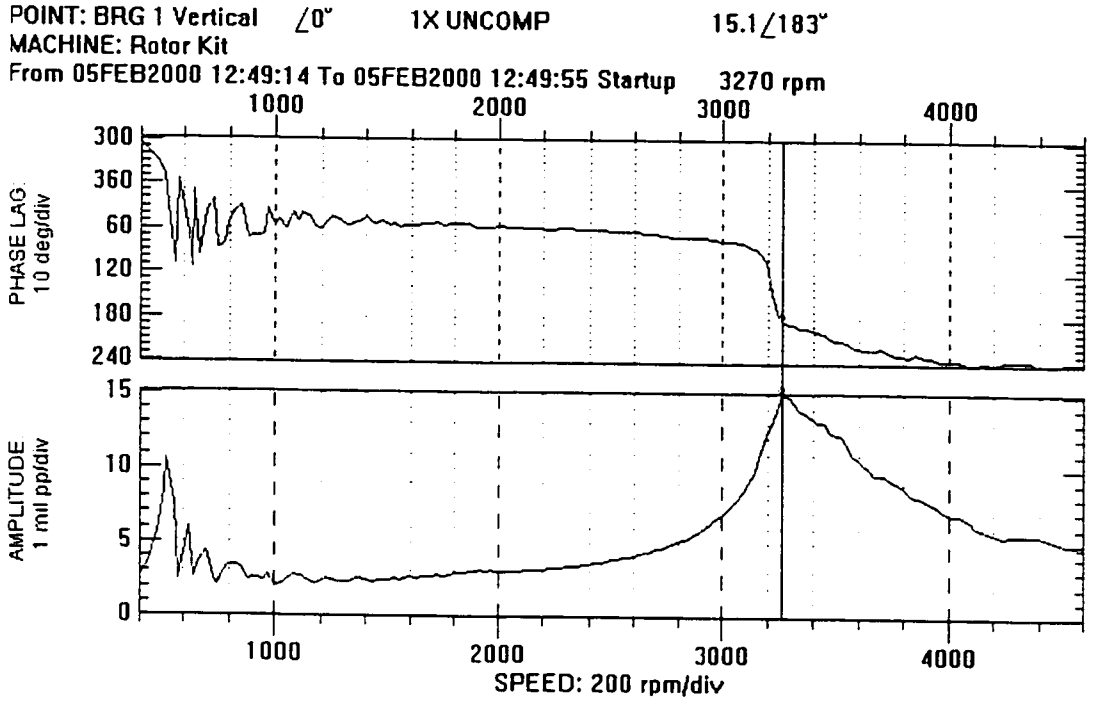

(i) Vertical direction

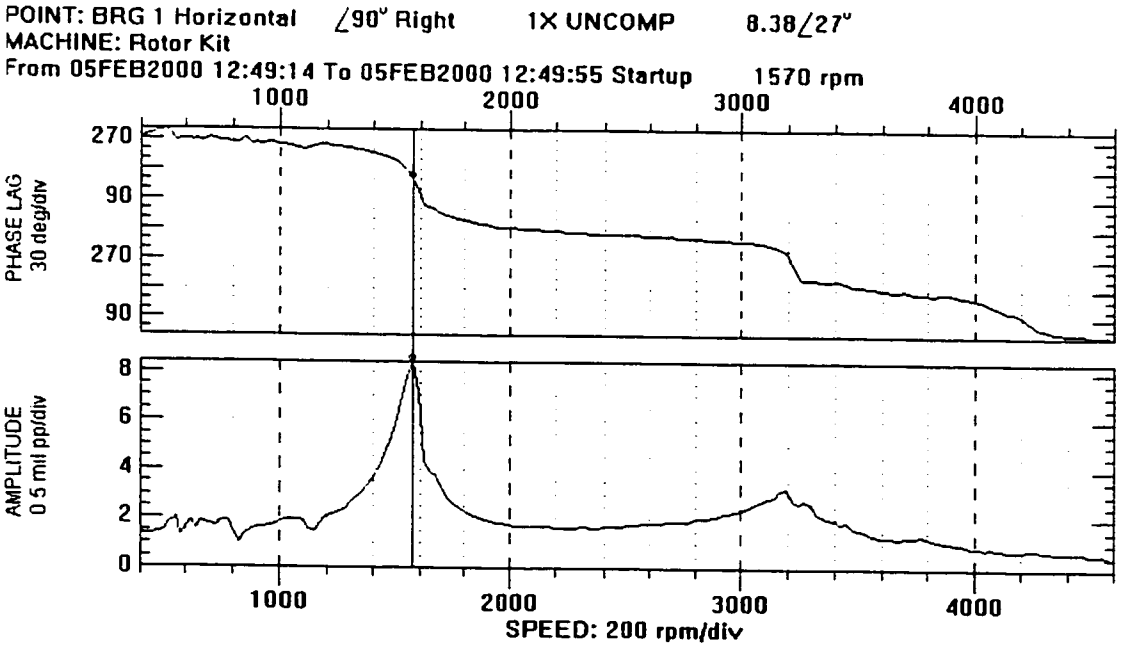

(ii) Horizontal direction

Fig. 5.9 (a). Bode plot of startup data for the shaft with 3mm notch crack with 8Kg hanging side load.

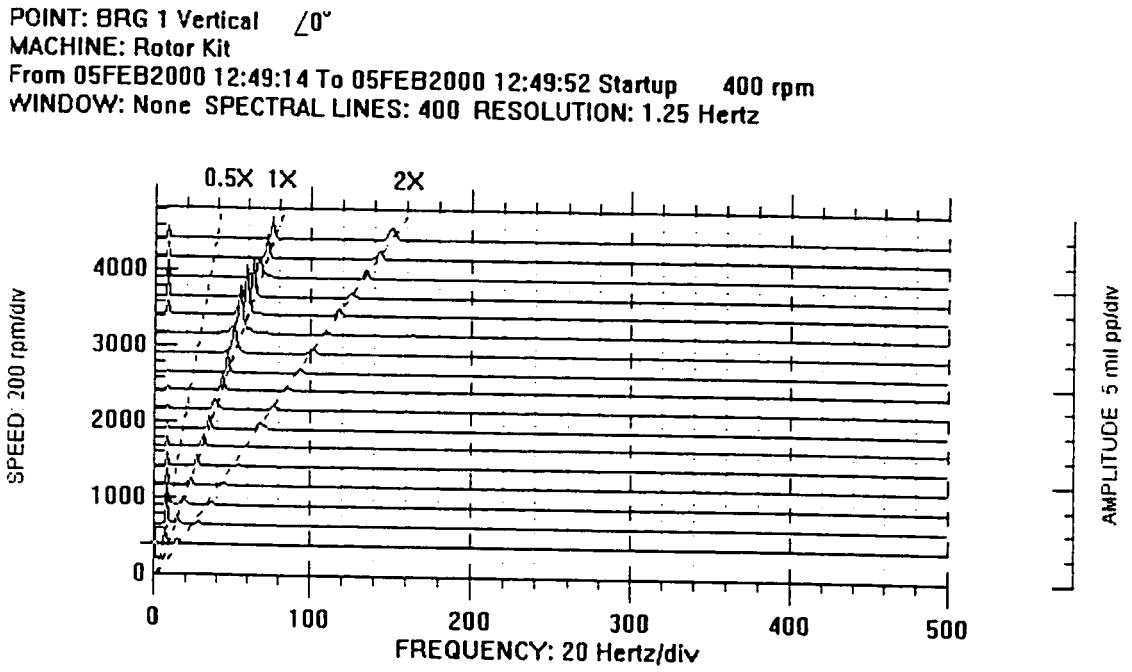

(i) Vertical direction

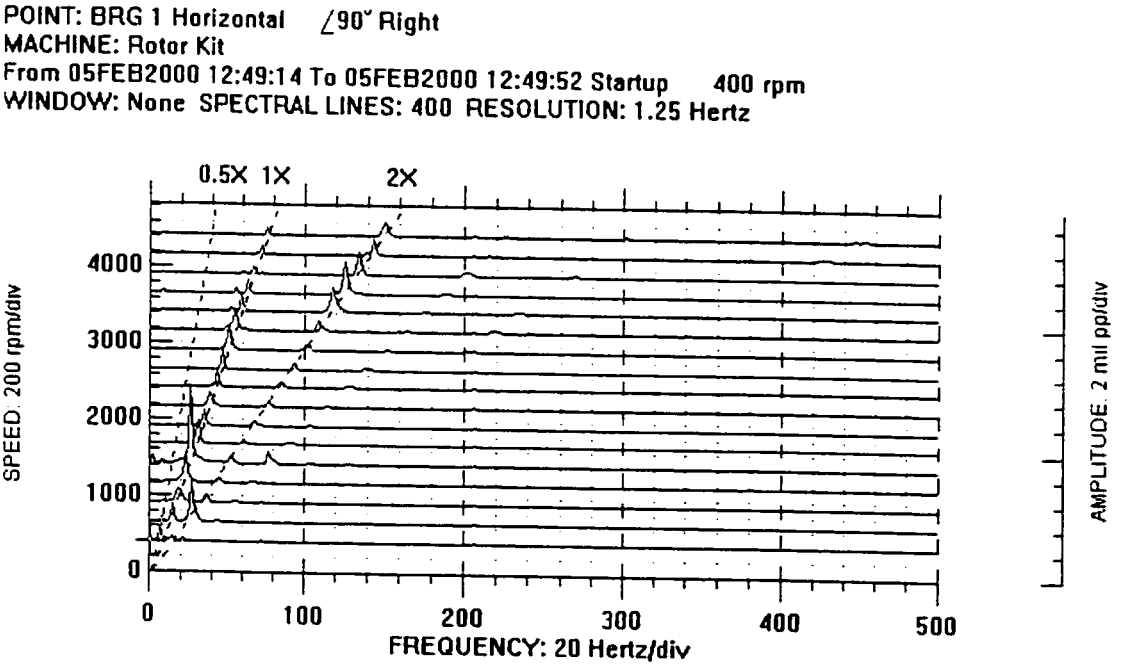

(ii) Horizontal direction

Fig. 5.9(b). Frequency cascade for steady state data at 2000rpm for shaft with 3mm notch crack and 8kg vertical hanging side load

POINT: BRG 1 Vertical ∠0°
MACHINE: Rotor Kit
From 05FEB2000 12:57:10 To 05FEB2000 13:37:30 Steady State 13:37:30
WINDOW: Hanning SPECTRAL LINES: 400 RESOLUTION: 1.25 Hertz

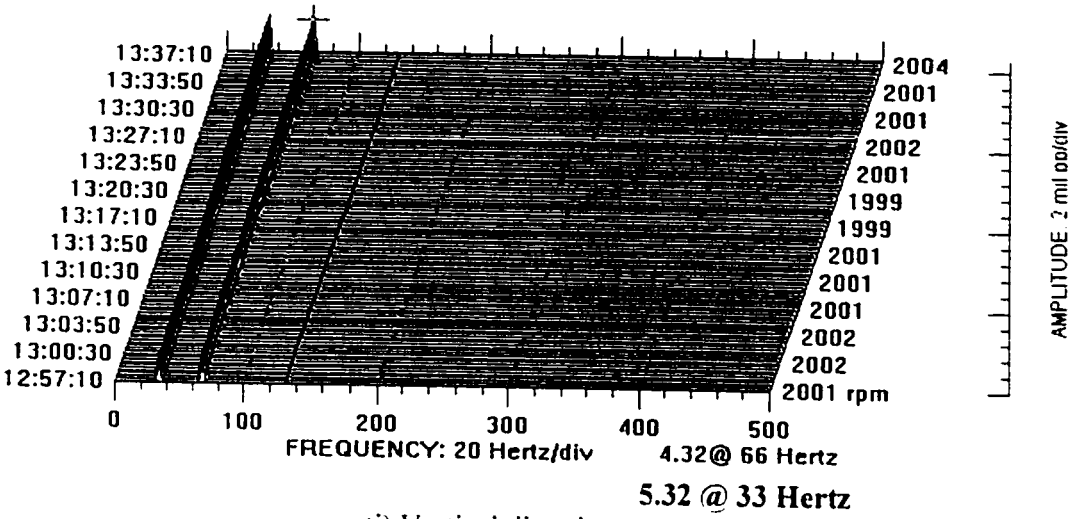

(i) Vertical direction

POINT: BRG 1 Horizontal ∠90° Right
MACHINE: Rotor Kit
From 05FEB2000 12:57:10 To 05FEB2000 13:37:30 Steady State 13:37:30
WINDOW: Hanning SPECTRAL LINES: 400 RESOLUTION: 1.25 Hertz

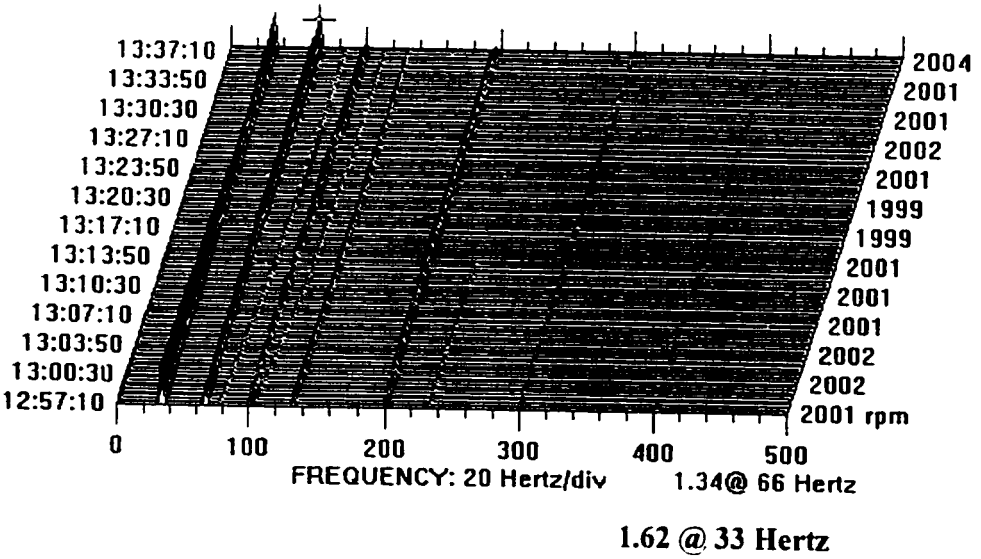

(ii) Horizontal direction

Fig. 5.9(c) Frequency waterfall for steady state data at 2000rpm for shaft with 3mm notch crack and 8kg vertical hanging side load.

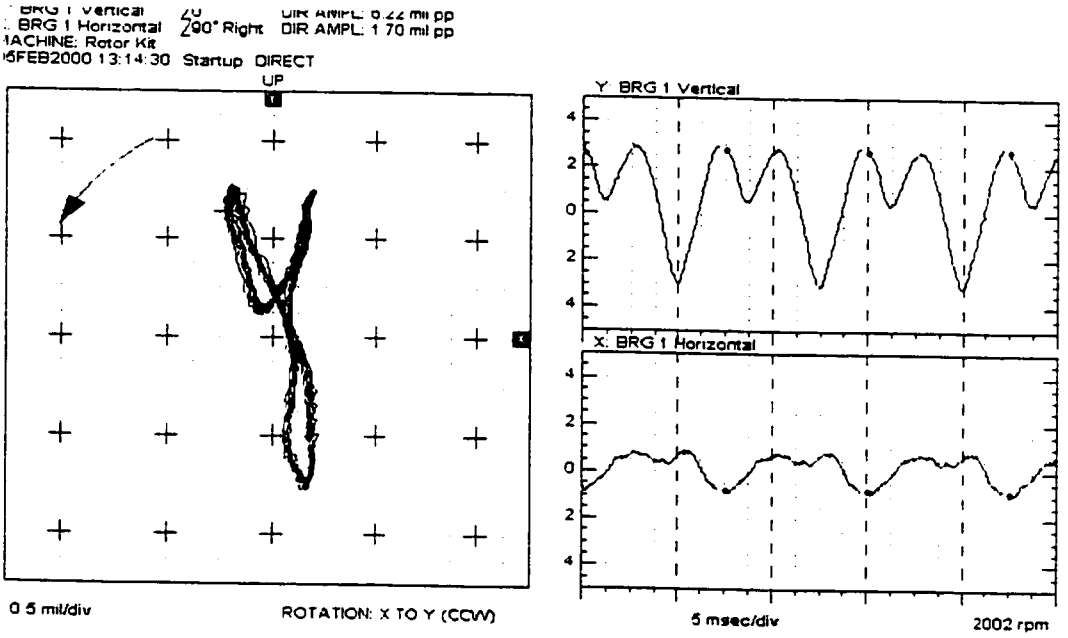

Fig. 5.9 (d) Orbit for shaft with 3mm notch crack and 8kg vertical hanging side load

Figure 5.9 Startup and steady state analysis results for the shaft with 3mm notch crack with 8Kg vertical hanging side load just before crack fracture.

The overhang shaft experiment was repeated with two additional shafts with 4mm notch crack to further study the effect of crack propagation on the dynamic response of the system. The results are presented in Figures 5.10, 5.11 and 5.12. Figure 5.10 represents the results for un-cracked shaft with 8 kg hanging side load. Figure 5.11 presents the results for the 1st cracked shaft with 4 mm notch and 8 kg hanging side load. The crack distance from the bearing support was 1.5 cm, the hanging side load was 13 cm from the bearing support and the distance between the two bearing supports was 39 cm. This is the same arrangement for the 3 mm notch crack whose results were presented in Figures 5.8 and 5.9. The startup data were taken more than one time (see Appendix A2) to study the observed increase in critical speed in the vertical direction due to the presence of a crack and side load. The repeated startup experiments caused cracked propagation and the shaft fractured very fast when left to run at steady state, Fig. 5.11(c). Figure 5.12 shows the results for the 2nd cracked shaft with 4mm notch crack and 8 kg hanging side load. The crack distance was 3.5 cm from the bearing support, the side load was placed 17 cm from the bearing support and the span between the bearing supports was 39 cm.

Table 5.5 summarizes the results of overhang shaft experiment. The presence of a transverse crack and side load at the middle of the shaft in the simply supported arrangement of shaft and bearing supports, first setup (Fig. 4.1(b)), reduced the critical speed of the shaft (Table 5.1). However, in the second setup, overhang shaft experiment, (Fig. 4.1 (c)) in which the crack and the side load are not within the shaft span, the critical speed of the system increased, see Figures 5.5(a) and 5.7(a). However, the results of the repeated experiments showed a decrease in critical speed of the 4mm depth cracked shaft, Figures 5.10(a), 5.11(a) and 5.12(a). More investigation is needed as the

Table 5.5 Summary of results for overhang shaft experiment

DESCRIPTION	Y PROBE		X PROBE		CRITICAL SPEEDS	
	1X	2X	1X	2X	Y	X
Un-cracked shaft (1200 rpm)	6.090	0.385	3.210	0.461	1420	1500
Cracked Shaft with 3mm notch (1200 rpm)	2.360 (-61.6%)	0.308 (-20.0%)	2.080 (-35.2%)	0.360 (-21.9%)	1550	1500
Un-cracked Shaft with hanging side load of 8 Kg (2000 rpm)	1.300	0.308	3.390	0.103	3000	1500
Cracked shaft with 3mm notch with hanging side load at the at the start of crack propagation (2000 rpm)	2.620 (+101.3%)	3.060 (+893.5%)	2.210 (-34.8%)	0.591 (+46.4%)	3120	1580
Cracked Shaft with 3mm notch with hanging side load of 8 kg before shaft fracture (2000 rpm)	5.320 (+309.2)	4.320 (+1302.3%)	1.620 (-52.2%)	1.340 (+1201.0%)	3270	1570
Repeated Experiment:		**1st Shaft**				
Un-cracked Shaft with hanging side load of 8 kg (3500 rpm)	2.080	0.025	0.694	0.231	4025	1785
Cracked Shaft with 4mm notch with hanging side load of 8 kg (3500 rpm)	0.617 (-70.3%)	2.130 (very high)	0.720 (+3.74%)	2.850 (high)	4010	1728
		2nd shaft				
Cracked Shaft with 4mm notch with hanging side load of 8 kg (3500 rpm)	4.990 (+139.9%)	1.820 (high)	3.140 (+244.6%)	5.860 (very high)	3750	1720

nature of crack propagation may affect changes in the stiffness; possible explanations are given in section 5.3.2.2. Gash [1] and Meng and Hahn [14] reported that the change in shaft stiffness and the synchronous response of a shaft-bearing system depends on both the crack depth and crack location.

Before crack propagation, the presence of 3mm notch crack without side load reduced vibration amplitudes of 1X and 2X in vertical and horizontal direction see Figures 5.5(c) and 5.6(c) with an increase in the critical speed in the vertical direction. Side load increased the stiffness of the system. The combined effect of crack and side load during crack propagation increased 1X and 2X in the vertical direction by 309.2% and 1302.6%, respectively. While 1X is decreased by 52.2% and 2X increased by 1201.6% in the horizontal direction.

For the first 4mm cracked shaft in the vertical direction, 1X amplitude decreased by 70.3% while 2X percentage increase is very high about 9000%. For the second 4 mm cracked shaft, 1X amplitude increased by 139.9% and 244.6% in the vertical and horizontal directions, respectively. The increase in 2X amplitude is very high in both directions. From Table 5.5, we see that the presence of crack increased 2X amplitude in both directions tremendously compared with 1X amplitude. In the simply supported experiment however, the increase in 1X amplitude is greater than 2X. Iman et al [4] reported that the increase in 2X amplitude is greater than 1X for crack located close to the bearing while 1X is greater than 2X for crack at the middle of the shaft.

During crack propagation, 1X amplitude increased continuously in the vertical direction till the shaft fractured, Figures 5.9 and 5.12 while it decreased continuously in the vertical direction in Fig. 5.11. Similarly, in the horizontal direction, 1X decreased in Fig. 5.9 but increased in Figures 5.11 and 5.12. Therefore, during crack propagation, 1X

amplitude may increase or decrease depending on the position of the crack and its depth. But 2X amplitude will always increase when there is crack propagation regardless of crack position. Nilson [46] also reported that crack reduces 1X amplitude and increases 2X amplitude. No significant change in the shape of orbit was observed when there was no crack propagation. However, the shape of the orbit changed during crack propagation to two-loop orbit, Fig. 5.11. The two-loop orbit may be distorted as shown in Figures 5.9 and 5.12. The presence of 2X vibration appeared clearly in the waveforms with the orbits.

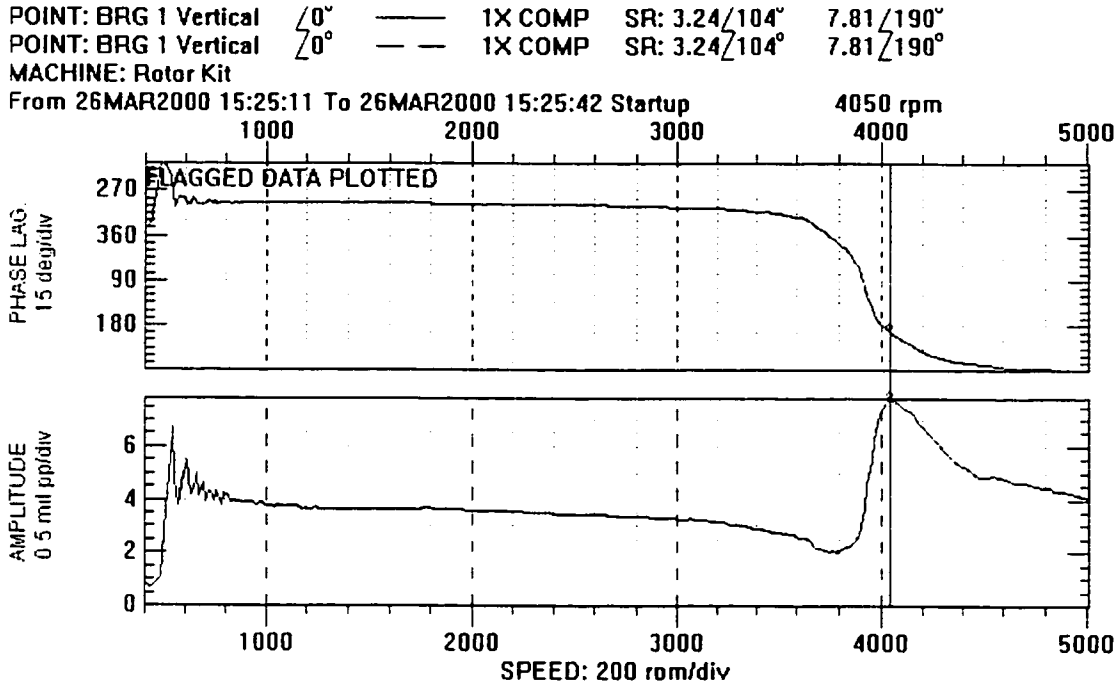

(i) Vertical direction

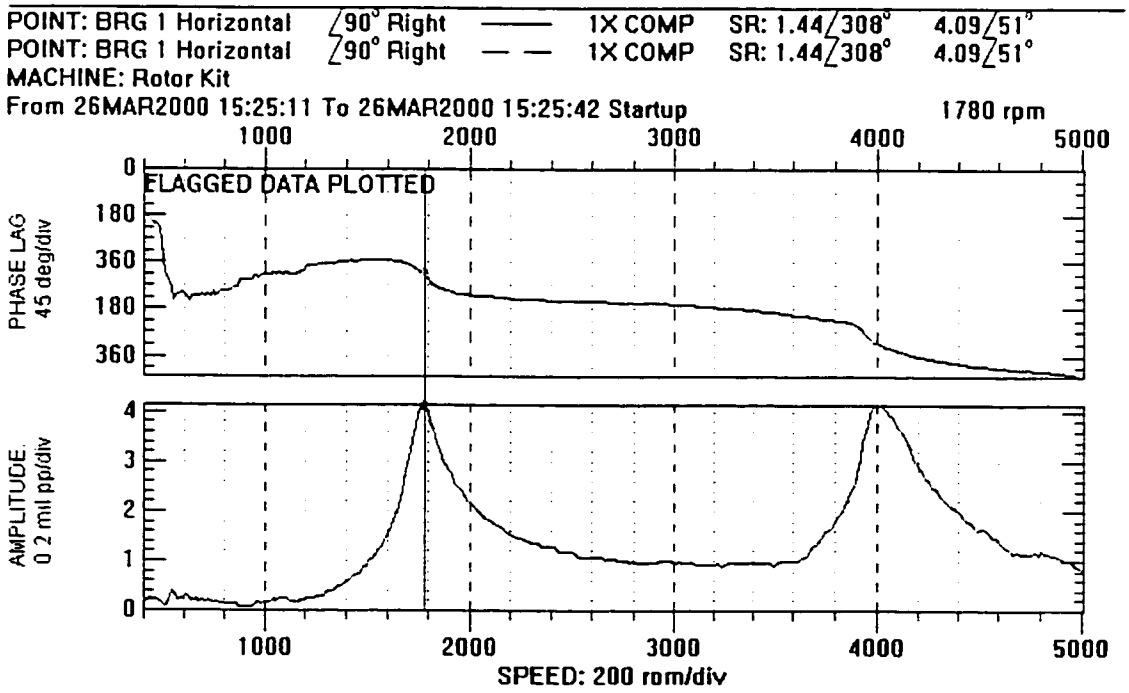

(ii) Horizontal direction

Fig. 5.10(a). Bode plot of startup data for un-cracked shaft with 8Kg hanging side load.

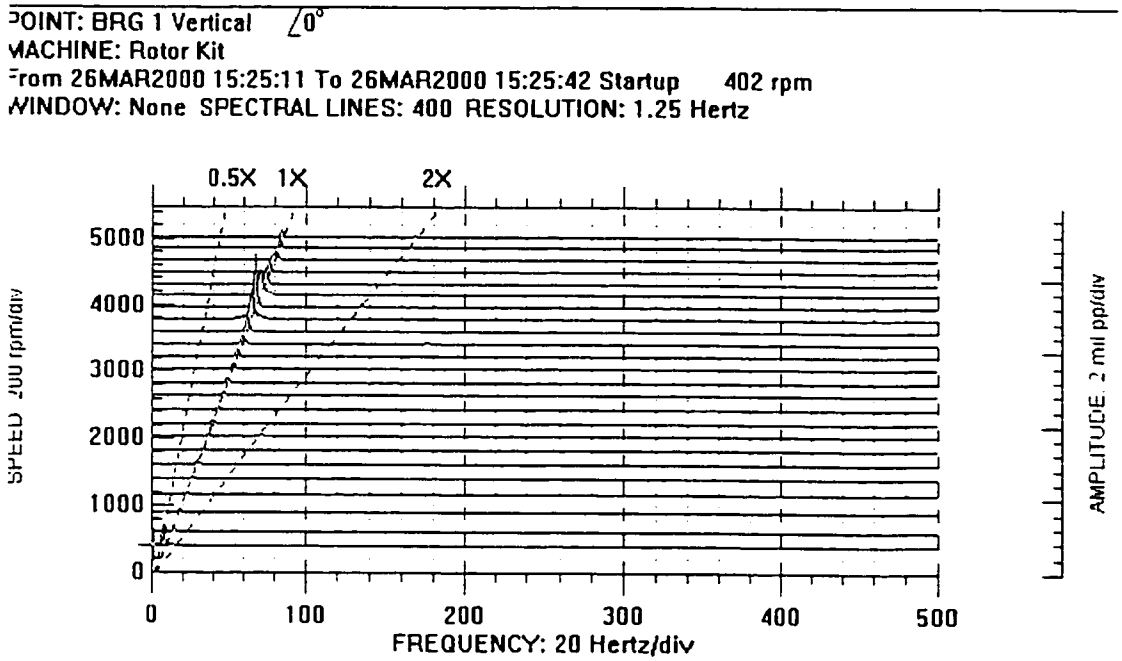

(i) Vertical direction

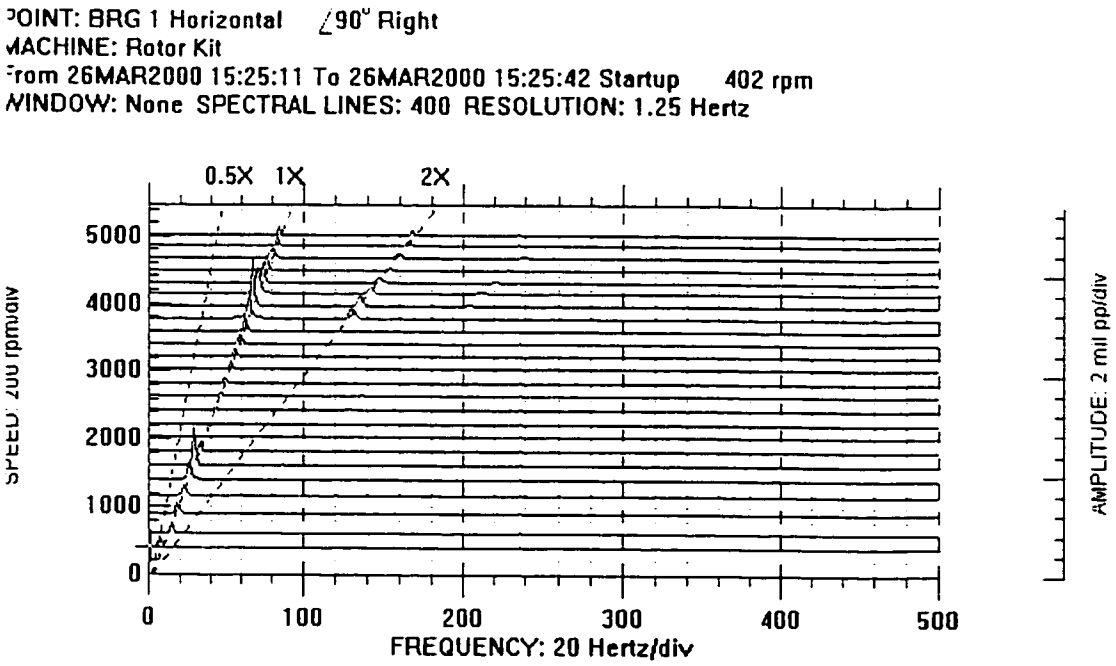

(ii) Horizontal direction

Fig. 5.10 (b). Frequency cascade of startup data for un-cracked shaft with 8 kg hanging side load.

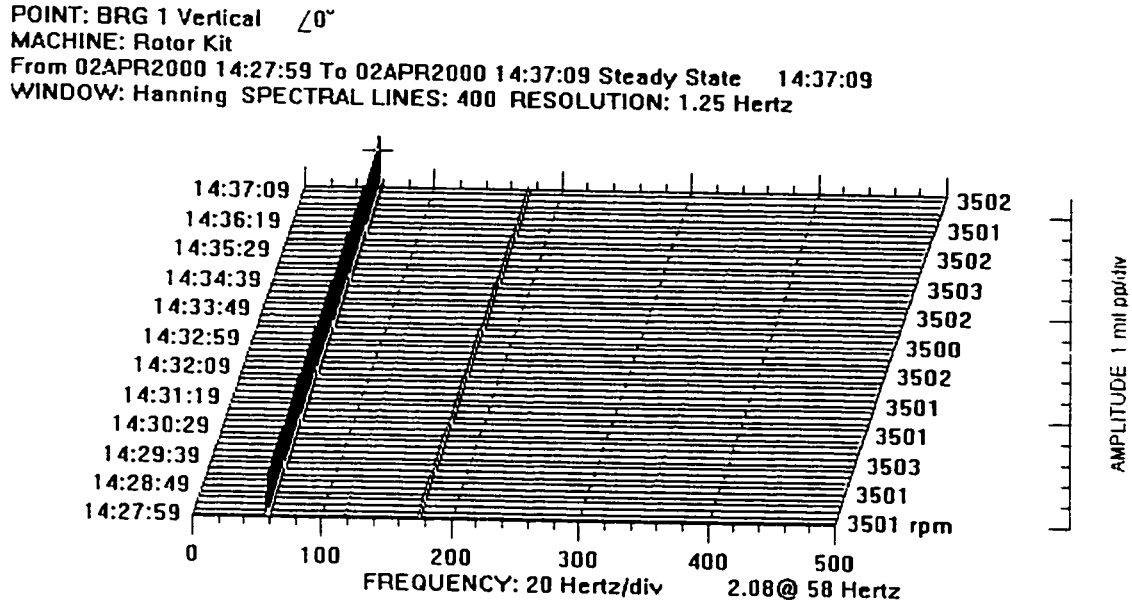

(i) Vertical direction

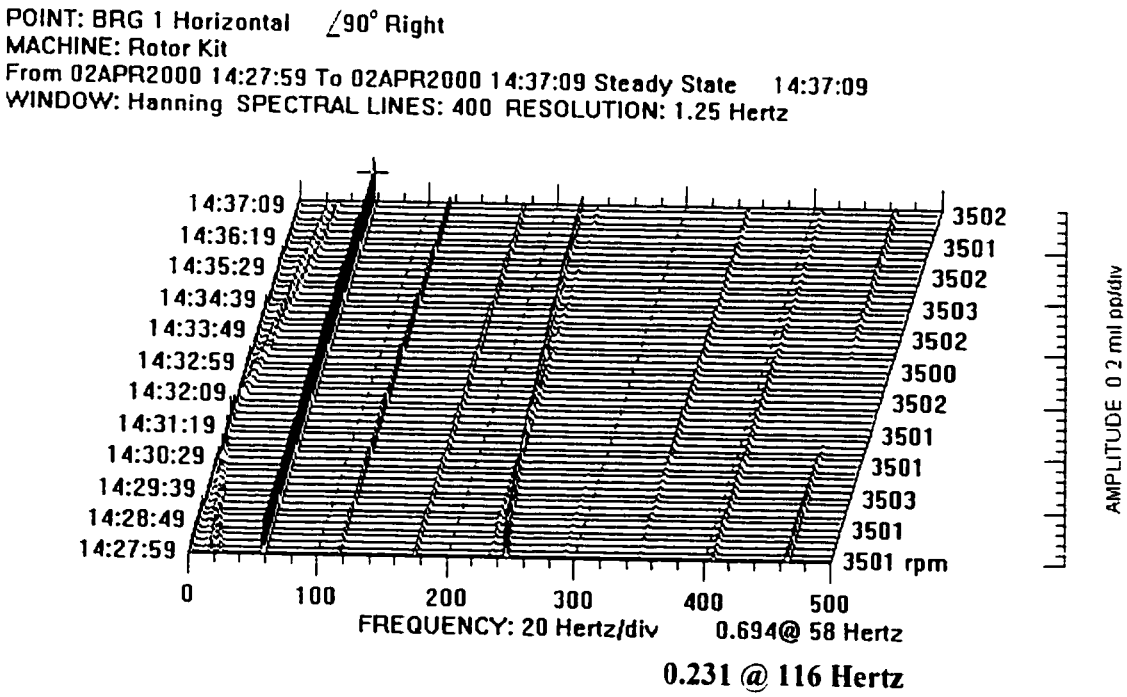

(ii) Horizontal direction

Fig. 5.10 (c). Frequency waterfall of steady state data at 3500 rpm for un-cracked shaft with 8kg hanging side load.

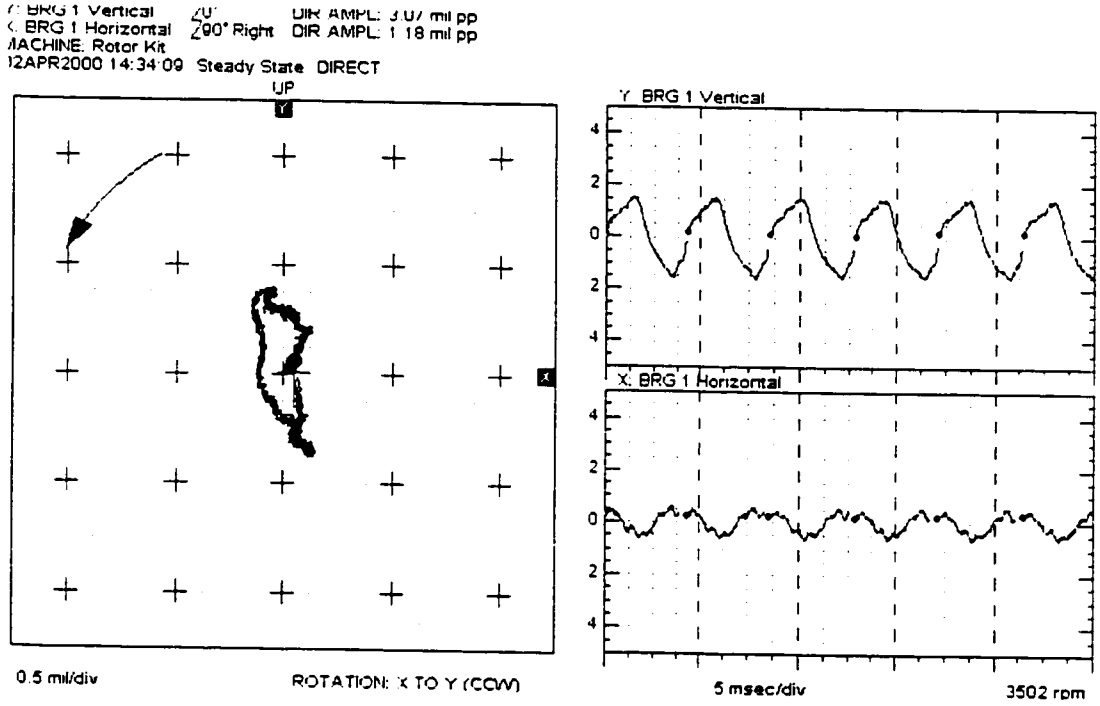

Fig. 5.10 (d) Orbit for un-cracked shaft with 8kg vertical hanging side load

Figure 5.10 Startup and steady state analysis results for un-cracked shaft with 8kg vertical hanging side load.

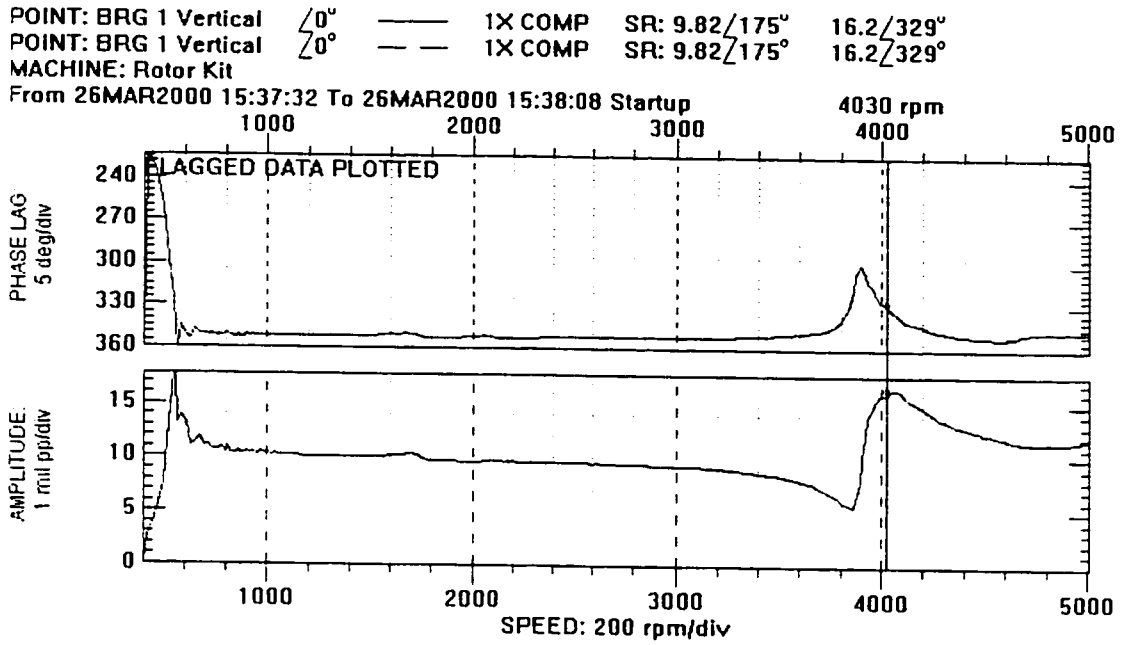

(i) Vertical direction

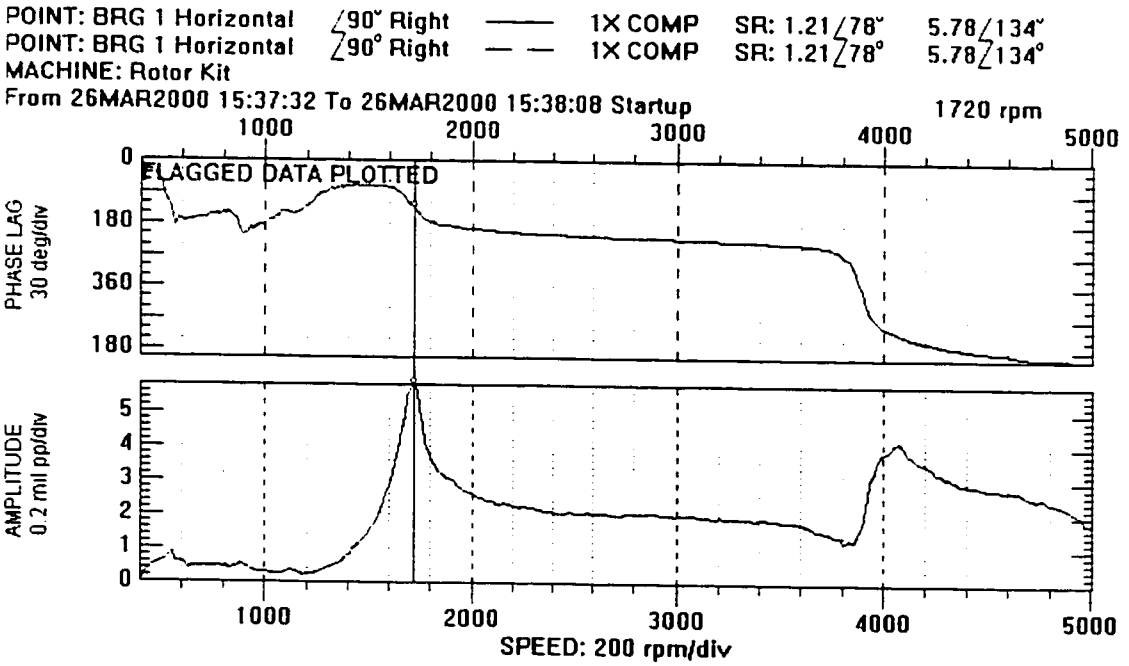

(ii) Horizontal direction

Fig. 5.11(a). Bode plot of startup data for the shaft with 4mm notch crack and 8Kg vertical hanging side load.

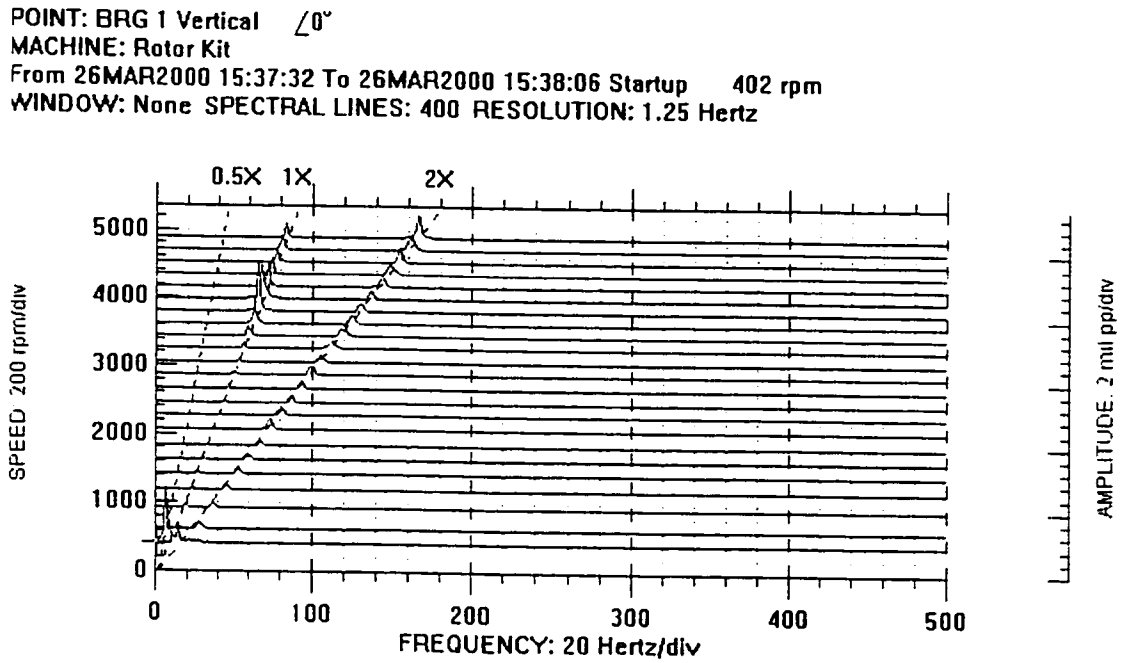

(i) Vertical direction

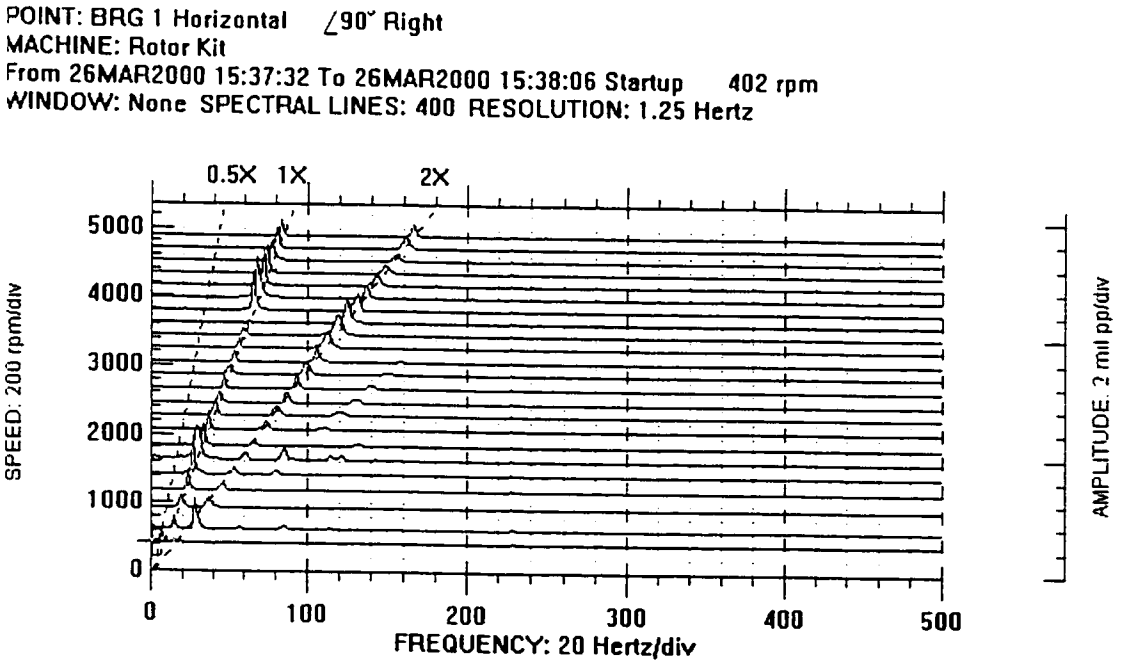

(ii) Horizontal direction

Fig. 5.11(b). Frequency cascade of startup data for the shaft with 4mm notch crack and 8kg vertical hanging side load.

POINT: BRG 1 Vertical ∠0°
MACHINE: Rotor Kit
From 26MAR2000 15:42:56 To 26MAR2000 16:08:46 Steady State 15:43:46
WINDOW: Hanning SPECTRAL LINES: 400 RESOLUTION: 1.25 Hertz

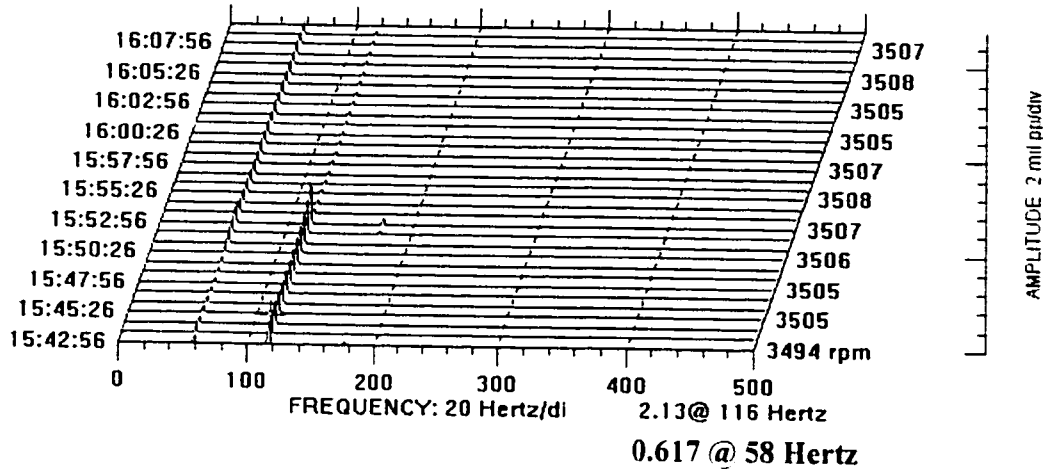

(i) Vertical direction

POINT: BRG 1 Horizontal ∠90° Right
MACHINE: Rotor Kit
From 26MAR2000 15:42:56 To 26MAR2000 16:08:46 Steady State 15:43:46
WINDOW: Hanning SPECTRAL LINES: 400 RESOLUTION: 1.25 Hertz

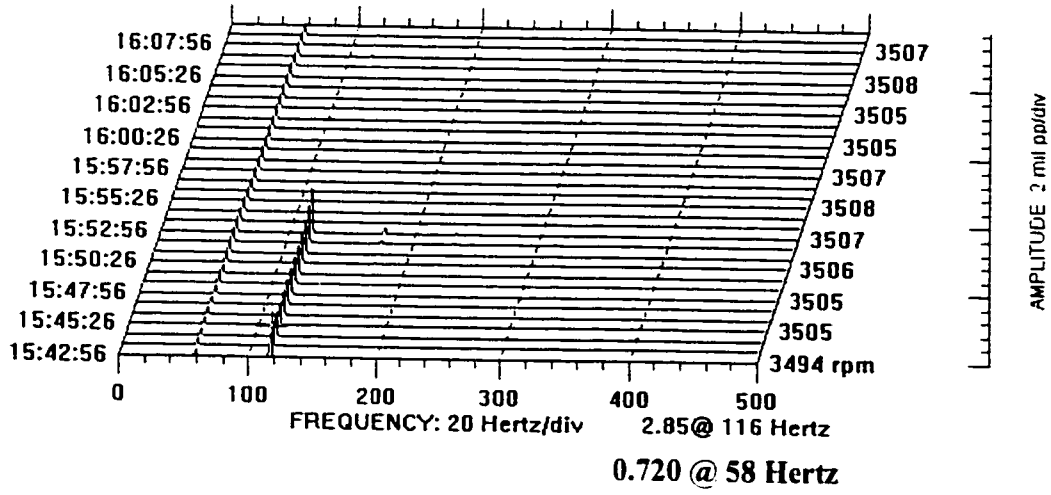

(ii) Horizontal direction

Fig. 5.11(c). Frequency waterfall of steady state data at 3500 rpm for the shaft with 4mm notch crack and 8kg vertical hanging side load.

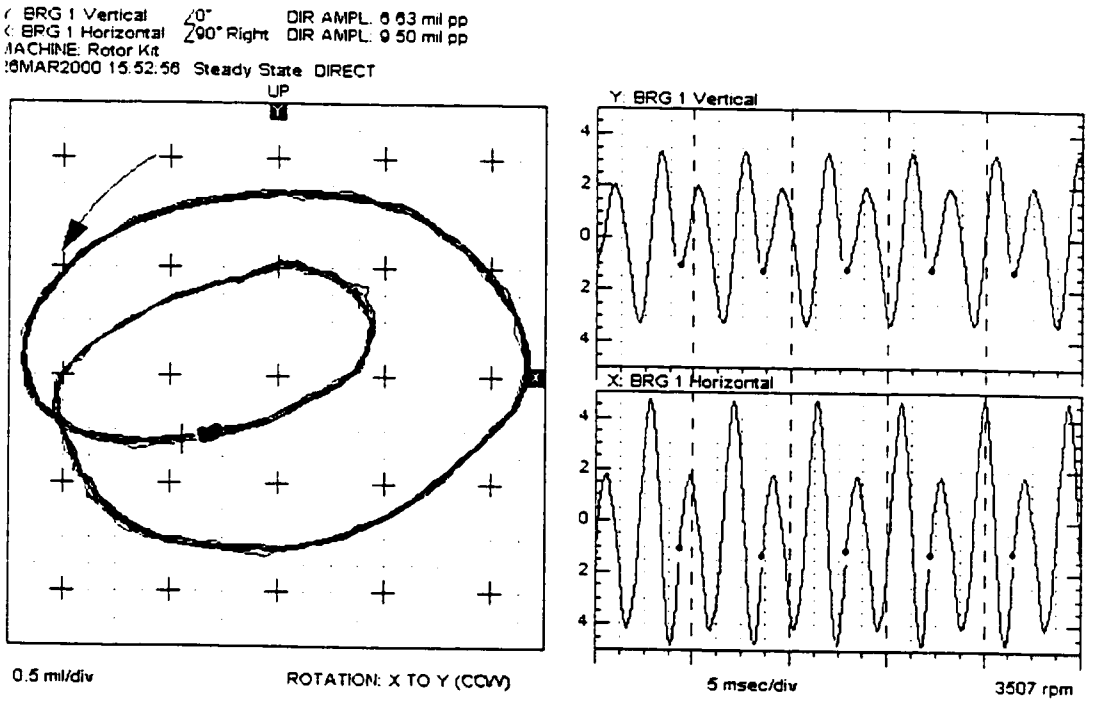

Fig. 5.11(d). Orbit of steady state data at 3500 rpm for the shaft with 4mm notch crack and 8kg vertical hanging side load.

Fig. 5.11. Startup and steady analysis results for the shaft with 4mm notch crack and 8kg vertical hanging side load.

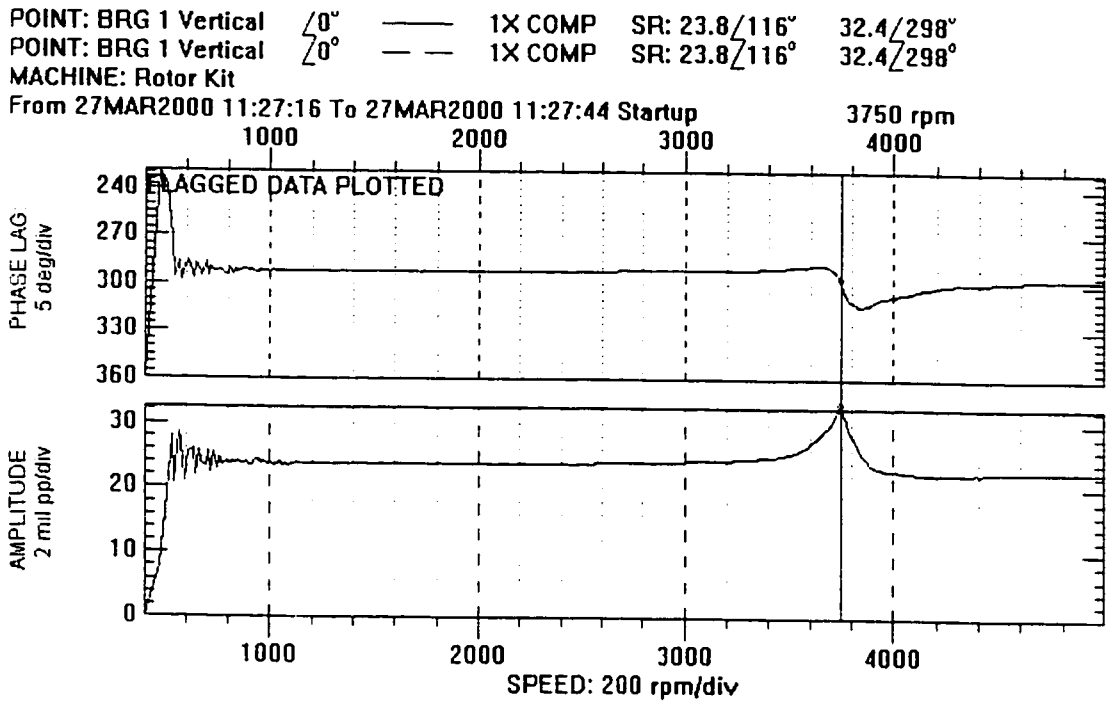

(i) Vertical direction

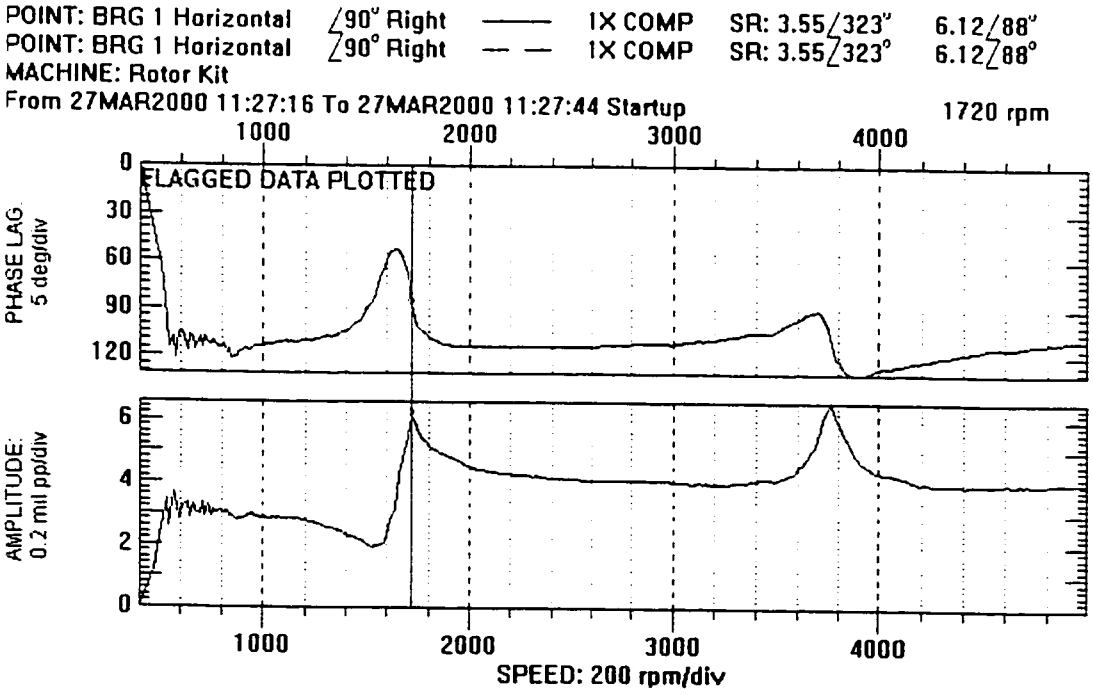

(ii) Horizontal direction

Fig. 5.12 (a). Bode plot of startup data for the 2nd shaft with 4mm notch crack with 8Kg vertical hanging side load.

POINT: BRG 1 Vertical ∠0°
MACHINE: Rotor Kit
From 27MAR2000 11:27:16 To 27MAR2000 11:27:42 Startup 406 rpm
WINDOW: None SPECTRAL LINES: 400 RESOLUTION: 1.25 Hertz

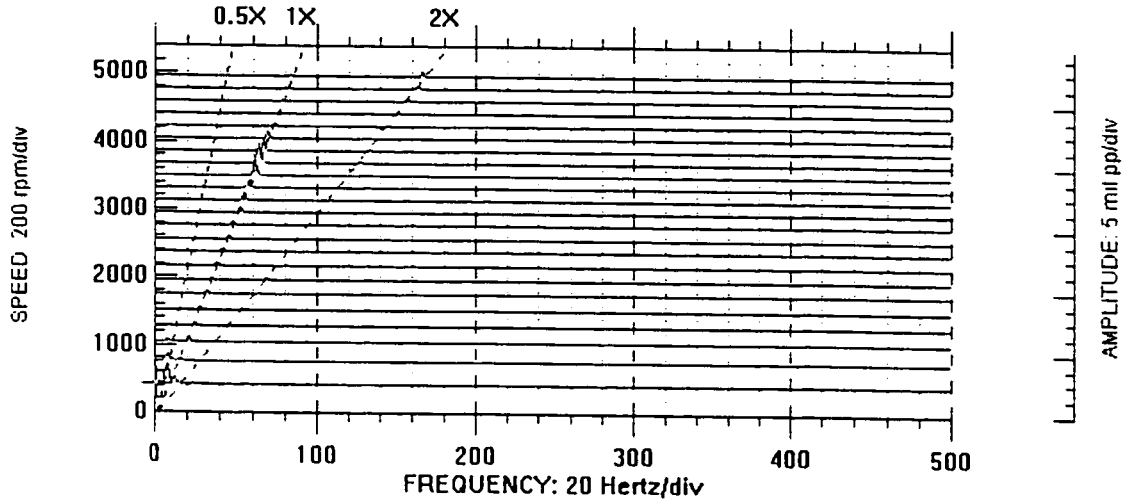

(i) Vertical direction

POINT: BRG 1 Horizontal ∠90° Right
MACHINE: Rotor Kit
From 27MAR2000 11:27:16 To 27MAR2000 11:27:42 Startup 406 rpm
WINDOW: None SPECTRAL LINES: 400 RESOLUTION: 1.25 Hertz

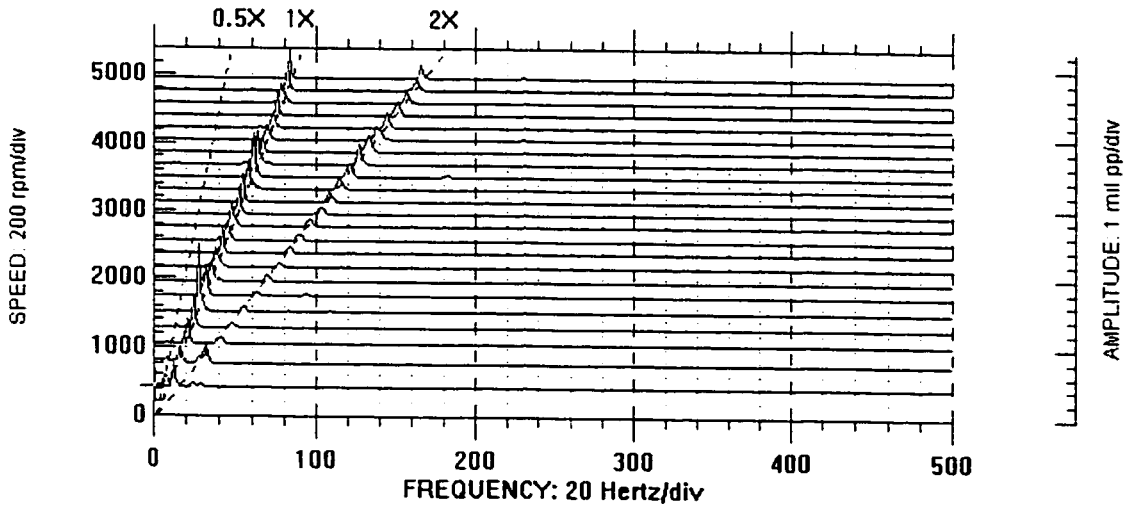

(ii) Horizontal direction

Fig. 5.12(b). Frequency cascade of startup data for the 2nd shaft with 4mm notch crack and 8kg vertical hanging side load.

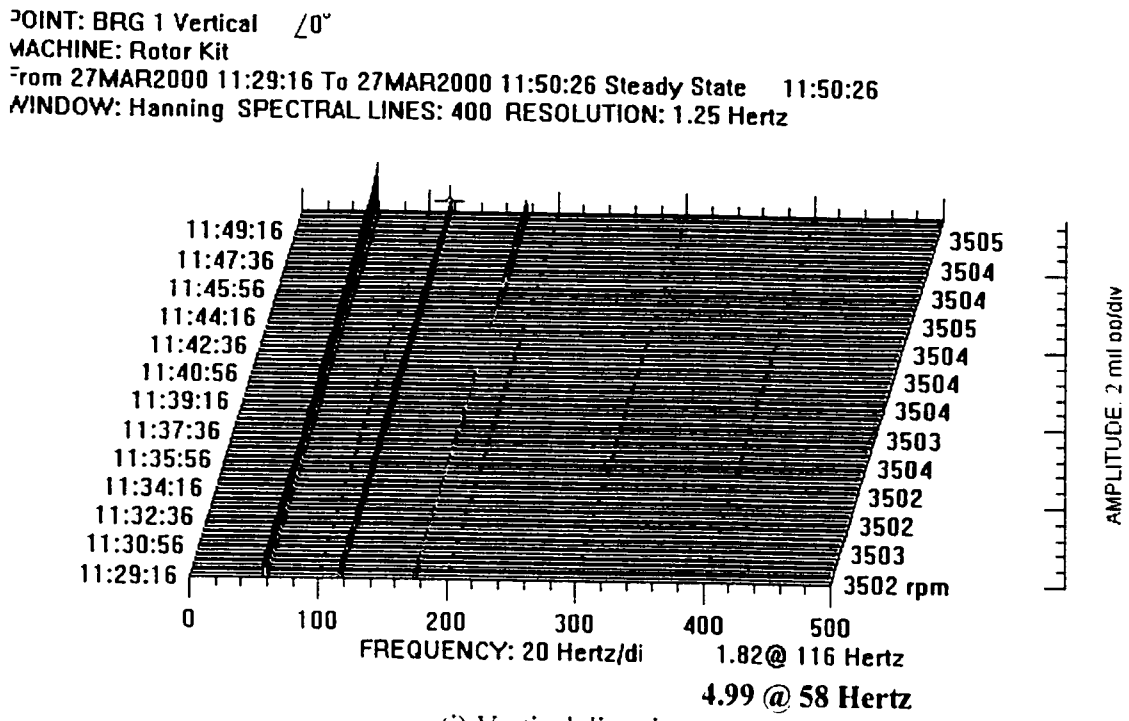

(i) Vertical direction

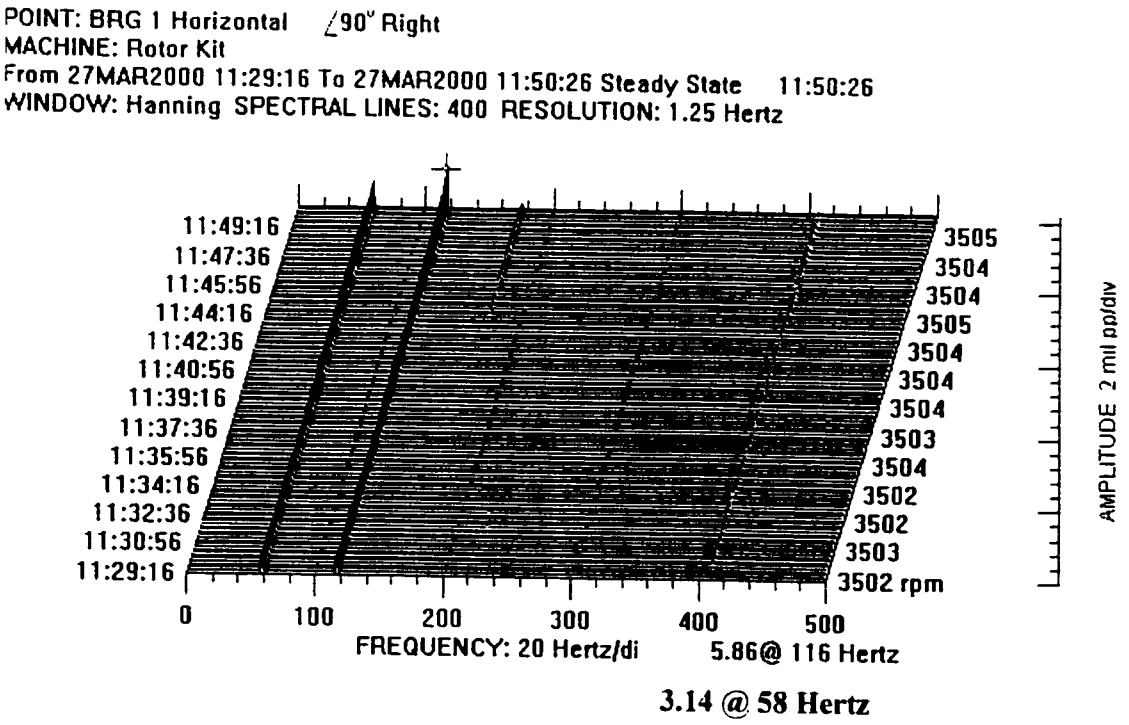

(ii) Horizontal direction

Fig. 5.12(c). Frequency waterfall of steady state data at 3500 rpm for the 2nd shaft with 4mm notch crack with 8kg vertical hanging side load.

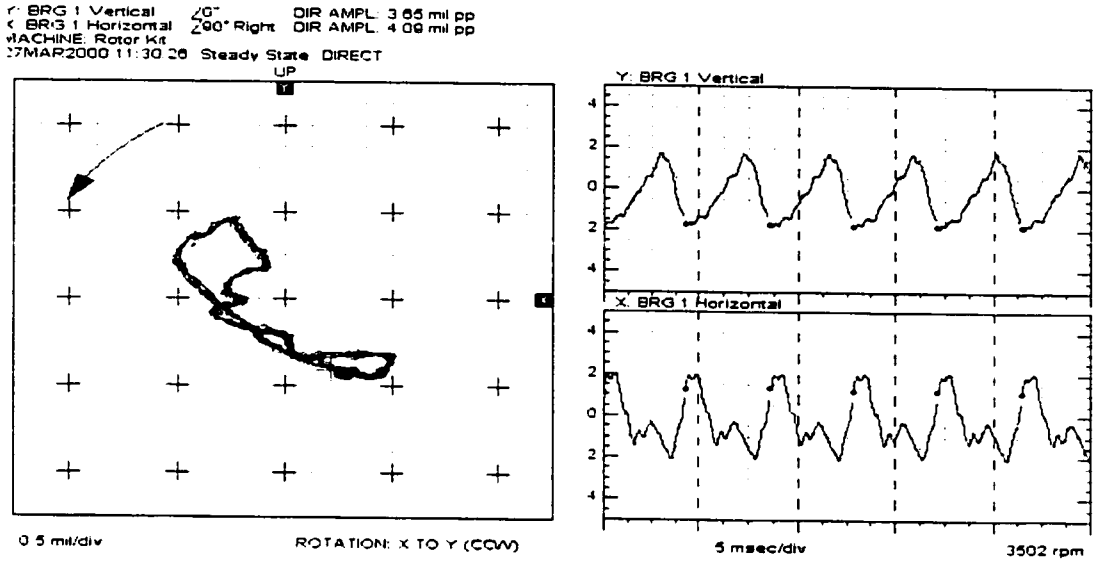

(i) Beginning of crack propagation

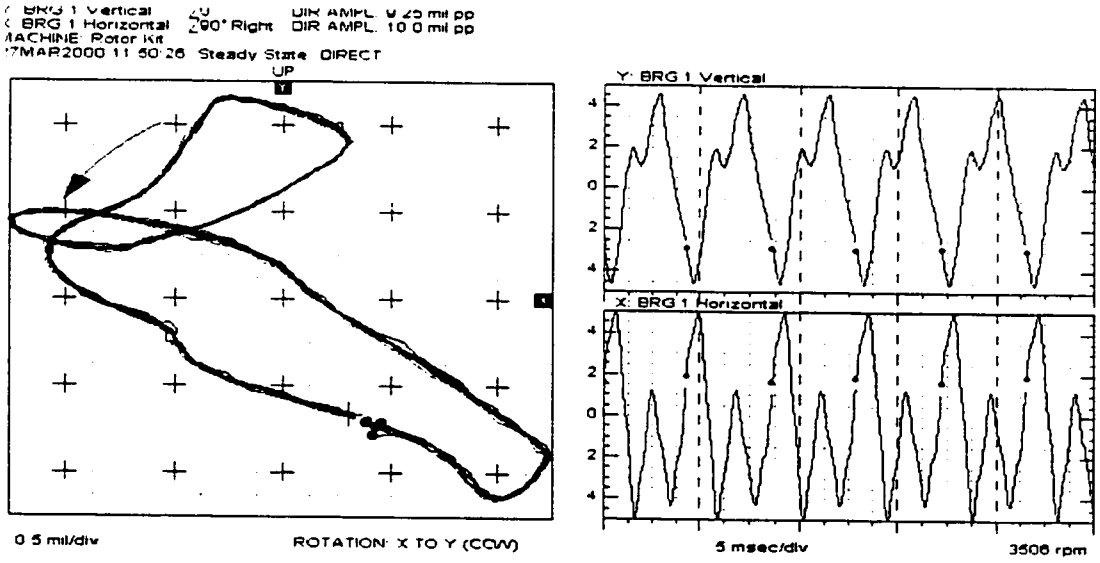

(ii) Just before shaft fracture

Fig. 5.12(d). Orbit of steady state data at 3500 rpm for the 2nd shaft with 4mm notch crack and 8kg vertical hanging side load just before shaft fracture.

Fig. 5.12. Startup and steady analysis results for the 2nd shaft with 4mm notch crack and 8kg vertical hanging side load.

5.3 WAVELET ANALYSIS RESULTS

One of the advantages of wavelet analysis over the Fourier and Spectral analysis is that it can handle both transient and stationary signals. The Discrete Wavelet Transforms (DWT) using Daubechies wavelet (DbN) of both startup and steady state data are presented in this section. The startup waveforms are arranged one after the other to get a single vector of length 1024*n, where n is the number of waveforms. All the waveforms for the steady state could not be used for cases where more than 70 waveforms were taken. For data with less than 70 waveforms, the first 384 points, which correspond to the first three revolutions out of the eight revolutions taken, were arranged consecutively to form the vector that is analyzed. For steady state data with more than 70 waveforms and close to 128 waveforms, the first 384 points of the first, third, fifth, etc. waveforms are arranged in that order to form the vector that is analyzed. This is done to limit the vector length to such that can be analyzed easily by the wavelet transform and to ensure that all the changes that occurred during the span of data acquisition are present in the vector.

5.3.1 First Experimental setup (Simply Supported Shaft)

The results of wavelet transform of vibration signals during startup and steady state measured by vertical and horizontal probes for un-cracked and cracked shafts are presented in this section. The position at which resonance occurred on the scalogram of the discrete wavelet transform of the startup signals is indicated below each graph.

5.3.1.1. Un-cracked shaft

Figures 5.13 and 5.14 show the discrete wavelet transform (DWT) of the startup and the steady state data for un-cracked shaft, respectively. Figure 5.13(a) represents the startup signal. Figures 5.13(b) and 5.14(a) are the scalograms of the DWT (DbN) for the startup and steady state signals, respectively. Figures 5.13(c) and 5.14(b) are the 3-D plot of DWT (DbN) for the startup and steady state data, respectively.

Figures 5.13(b) and 5.13(c) show the transient nature of the startup data and the resonance point. It has been stated in Chapter 3 that dyadic DWT cannot accurately represent frequencies that are not multiples of one another by a factor of two. Therefore, small changes in critical speed cannot be identified along the Level axis. However, changes in critical speed can be identified on the wavelet graphs by considering the time or position of resonance. The speed of the rotor increased with time represented as space on the wavelet scalogram during startup; hence the position of the resonance is proportional to the critical speed.

The main resonance points on Fig. 5. 13(b)(i) and Fig. 5.13(b)(ii) are 4914 and 5486, respectively. This means that the critical speed in the horizontal direction is greater than that in the vertical direction. The reason for the observed discontinuity between 3000 and 3500 in Figures 5.13(b)(i) and 5.13(b)(ii) is because the vibration amplitudes around the region are small; see Figures 5.13(a)(i) and 5.13(a)(ii), compared with other amplitudes. The contour program chooses the color range by default neglecting small values compared with the maximum value. This problem does not happen with the chirp signal presented in Chapter 3 because the amplitude of the signal

is the same throughout the transient period. Fig. 5.14(a) and 5.14(b) are the steady state results and they show the presence of more than two levels corresponding to different frequencies (1X, 2X, 4X) with different amplitudes in the vertical and horizontal directions.

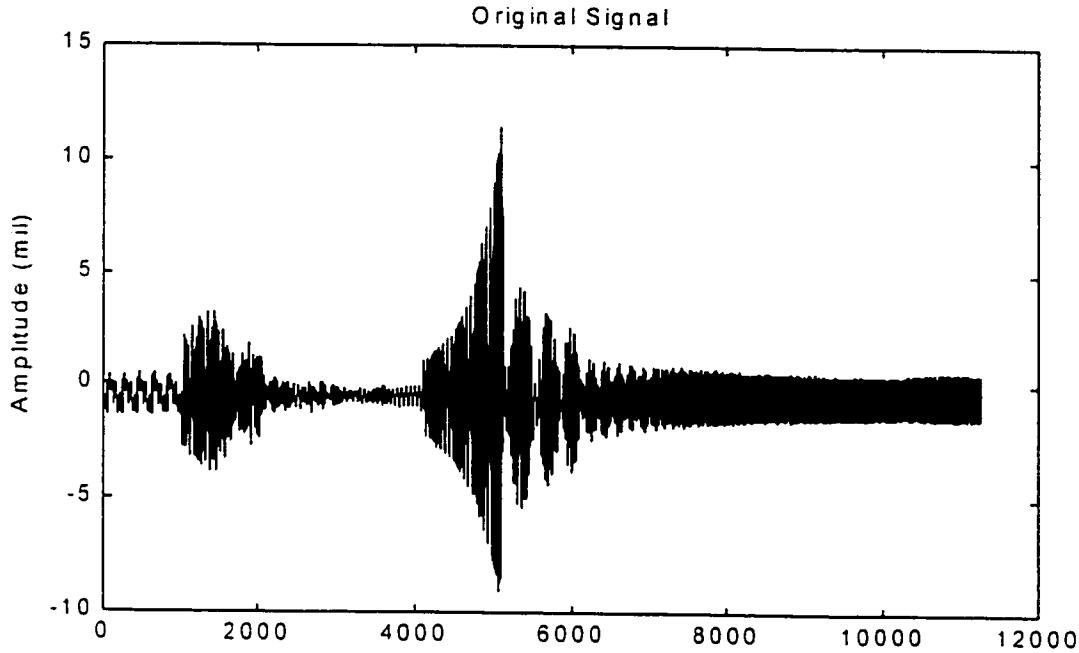

(i) Vertical

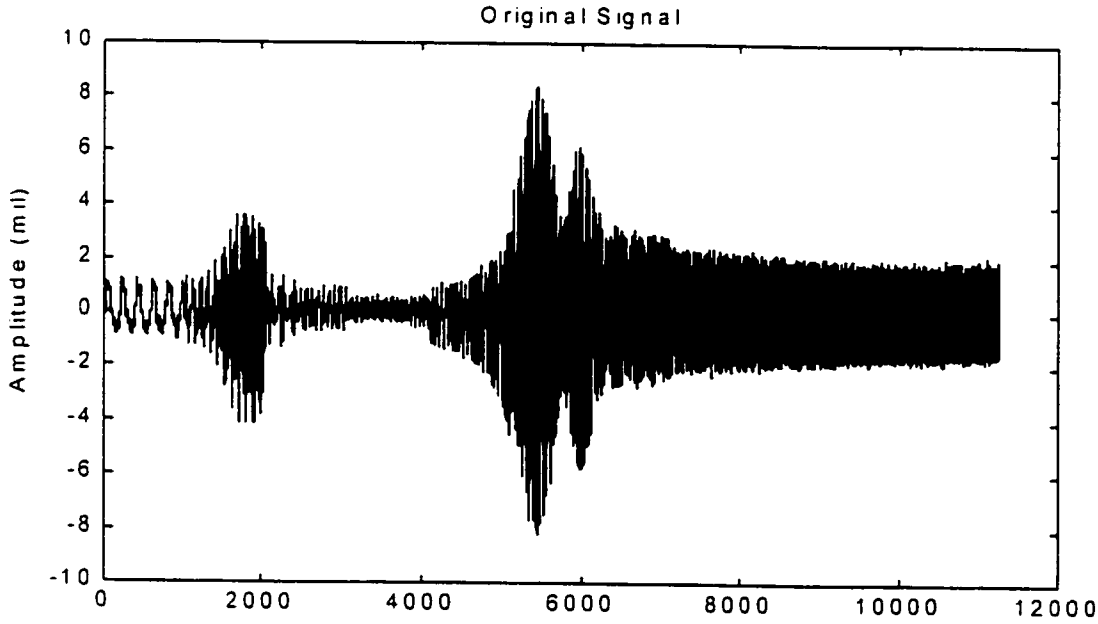

(ii) Horizontal

Fig. 5.13(a). Startup signal for un-cracked shaft

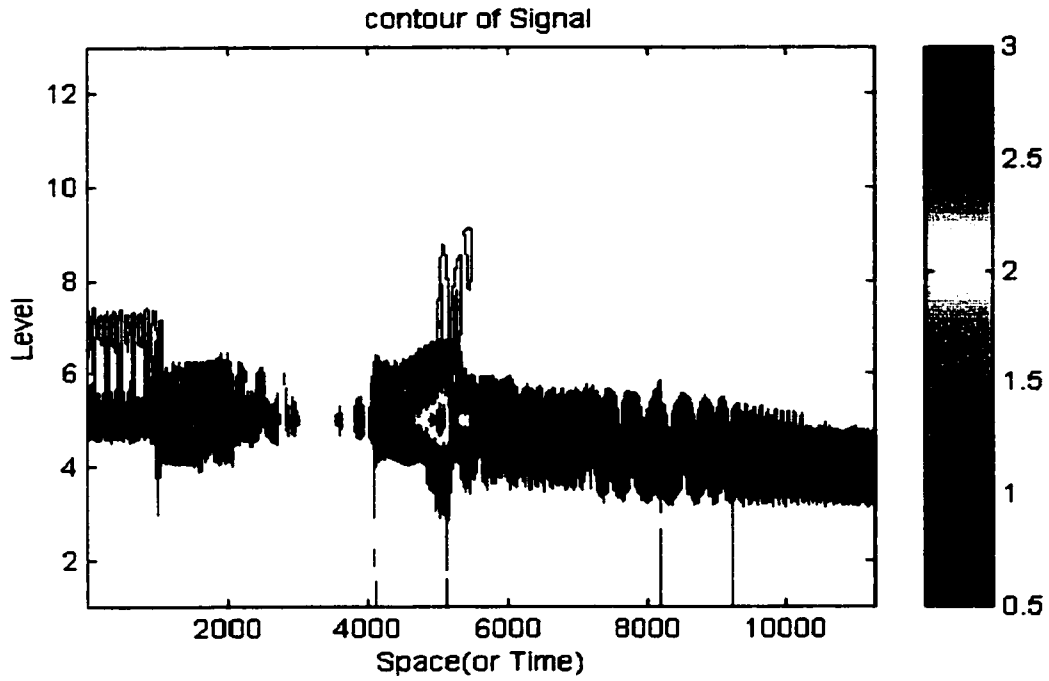

4914

(i) Vertical

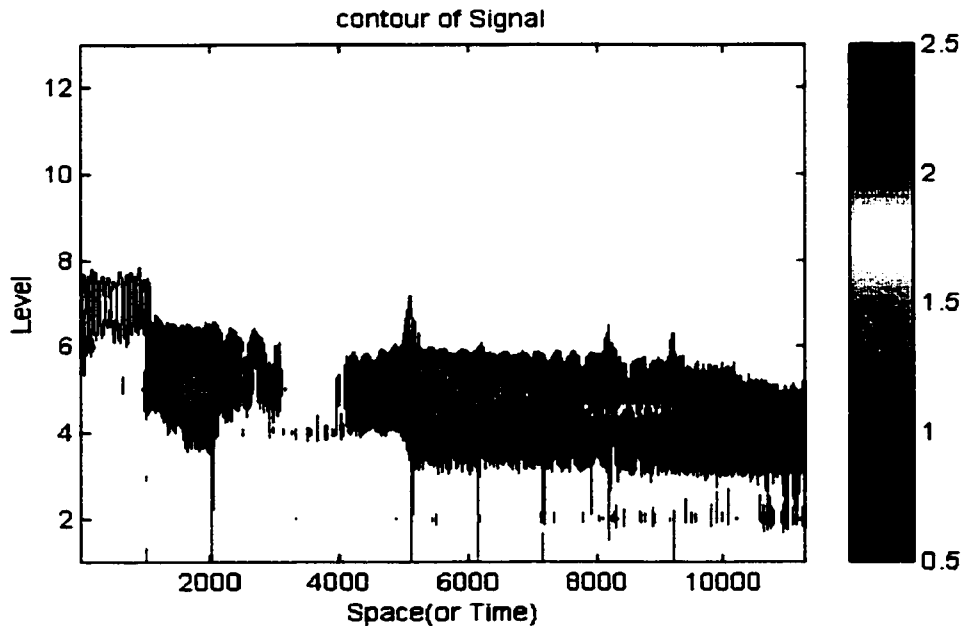

5486

(ii) Horizontal

Fig. 5.13 (b). Scalogram of DWT of startup signal for un-cracked shaft

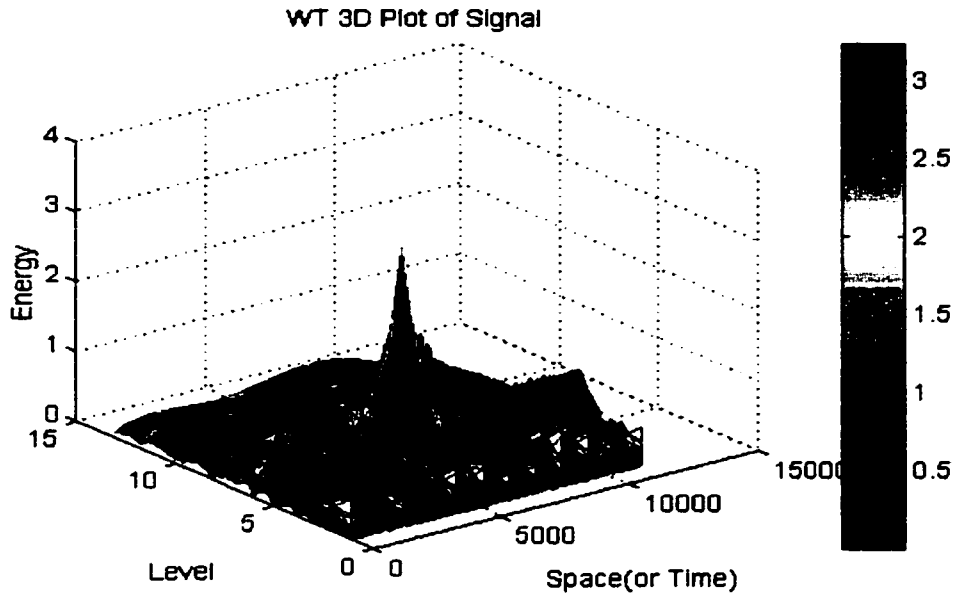

(i) Vertical

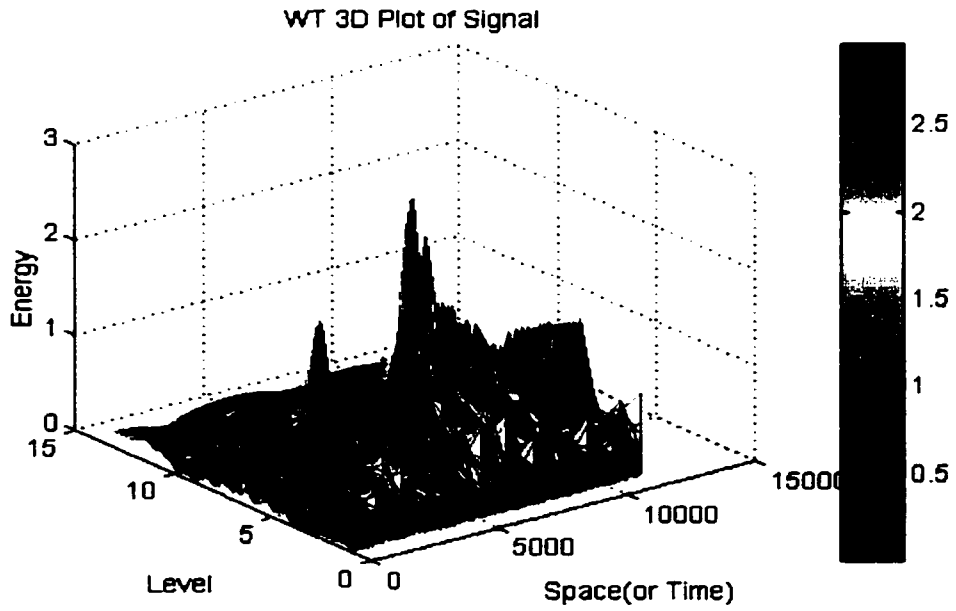

(ii) Horizontal

Fig. 5.13(c). 3-D plot of DWT of startup signal for un-cracked shaft

Figure 5.13 Wavelet analysis of startup data for un-cracked shaft

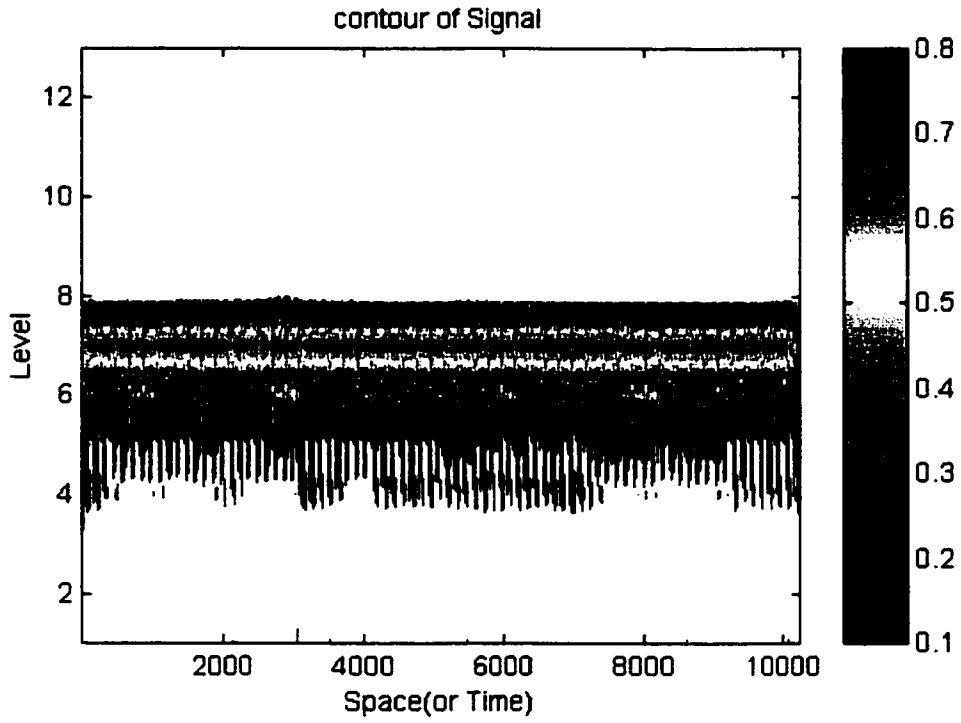

(i) Vertical

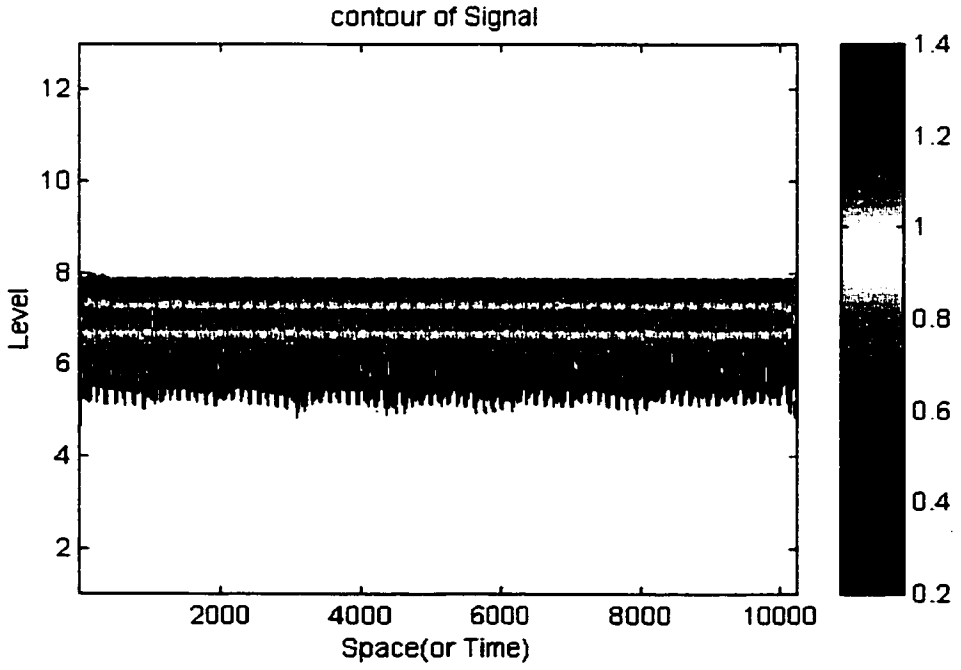

(ii) Horizontal

Fig. 5.14(a). Scalogram of DWT of steady state signal at 3500 rpm for un-cracked shaft

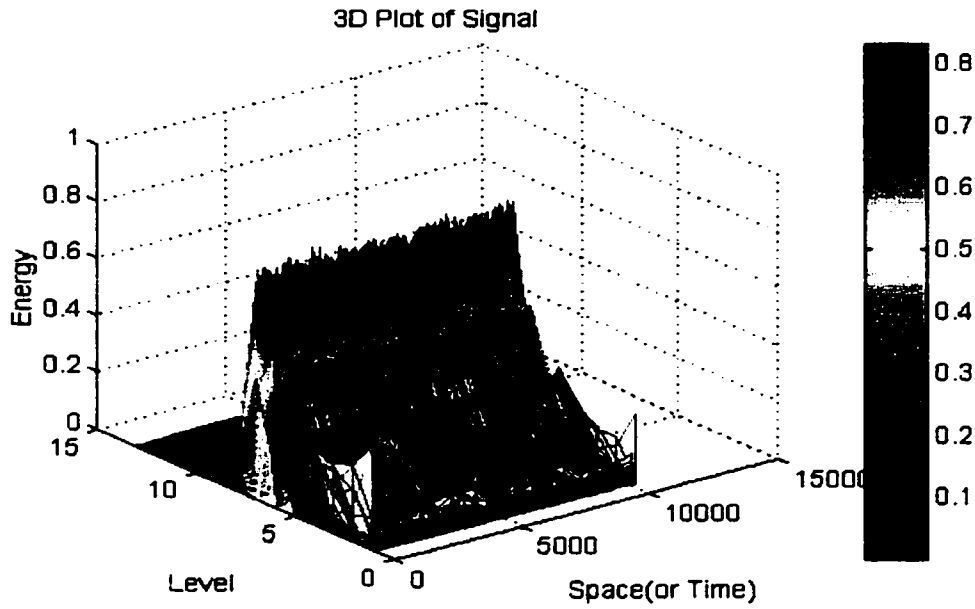

(i) Vertical

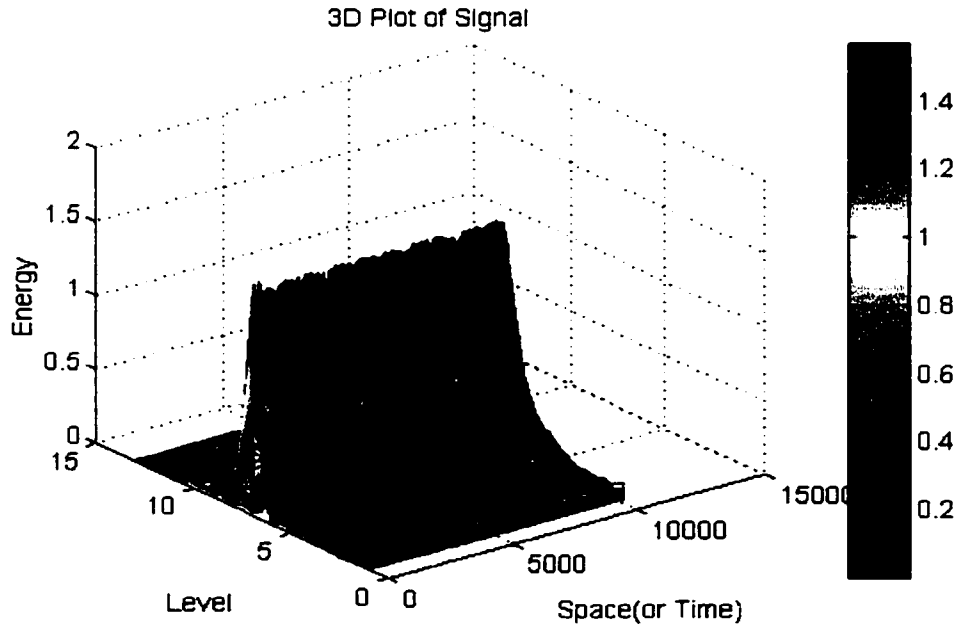

(ii) Horizontal

Figure 5.14 (b) 3-D plot DWT of Steady state data at 3500rpm for un-cracked shaft

Figure 5.14. Wavelet analysis of steady state data at 3500rpm for un-cracked shaft

5.3.1.2 Shaft with Surface Transverse Crack

Figures 5.15 and 5.16 show the discrete wavelet transform (DWT) of the startup and the steady state data for the shaft with 4mm notch crack. Figure 5.15(a) represents the startup signal. Figures 5.15(b) and 5.16(a) are the scalograms of the DWT (DbN) for the startup and steady state signals, respectively. Figures 5.15(c) and 5.16(b) are 3-D plots of DWT (DbN) for the startup and steady state data, respectively.

Figures 5.15(b) and 5.15(c) show the transient nature of the startup data and the resonance point with split resonance, which has been attributed to rotor system anisotropy. The main resonance points on Fig. 5. 15(b)(i) and Fig. 5.15(b)(ii) are 4421 and 4421, respectively. This means that the presence of crack has reduced the critical speed of the system and affects the asymmetry in stiffness of the shaft. Crack also introduced additional features at higher levels during startup that are not present in the startup signature of the un-cracked shaft. Fig. 5.16(a) and 5.16(b) are the steady state results and they show the presence of prominent two levels corresponding to 1X and 2X vibrations with higher amplitudes.

Figure 5.17 represents the results of DWT of the startup signal for the shaft with 4mm notch crack and 4.3 kg vertical tension. Fig. 5.17(b) shows that the critical speed increased compared with Fig. 5.16(b) that represents the effect of crack alone. The critical speed is the same in the vertical and horizontal directions. The split resonance spots caused by anisotropy in shaft system observed in Figures 5.13(b) and 5.15(b) disappeared but the resonance bandwidth increased. The combined effect of crack and side load also introduced a strange signal of low frequency in the horizontal direction (Fig. 5.17(b)).

It should be noted that the resonance spot of the startup data in both directions so far occurred at level 5 despite the fact that there are variations in the critical speeds. The reason for this has been explained at the beginning of the section. Figure 5.18 represents the steady state results for a shaft with 4mm notch crack and 4.3 kg side load. Figures 5.18(a) and 5.18(b) show the presence of two levels corresponding to 1X and 2X vibration.

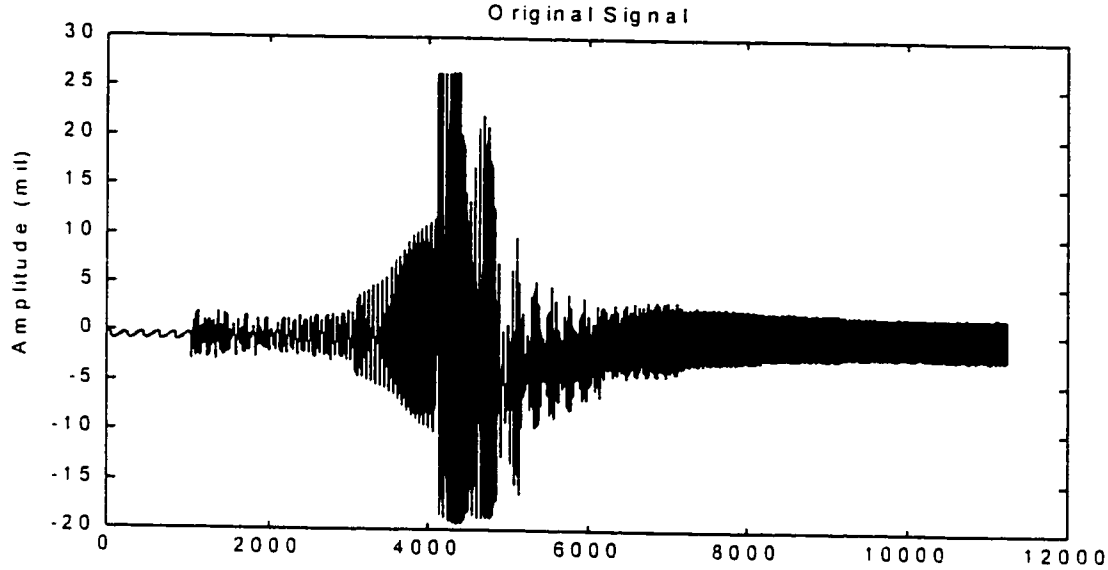

(i) Vertical

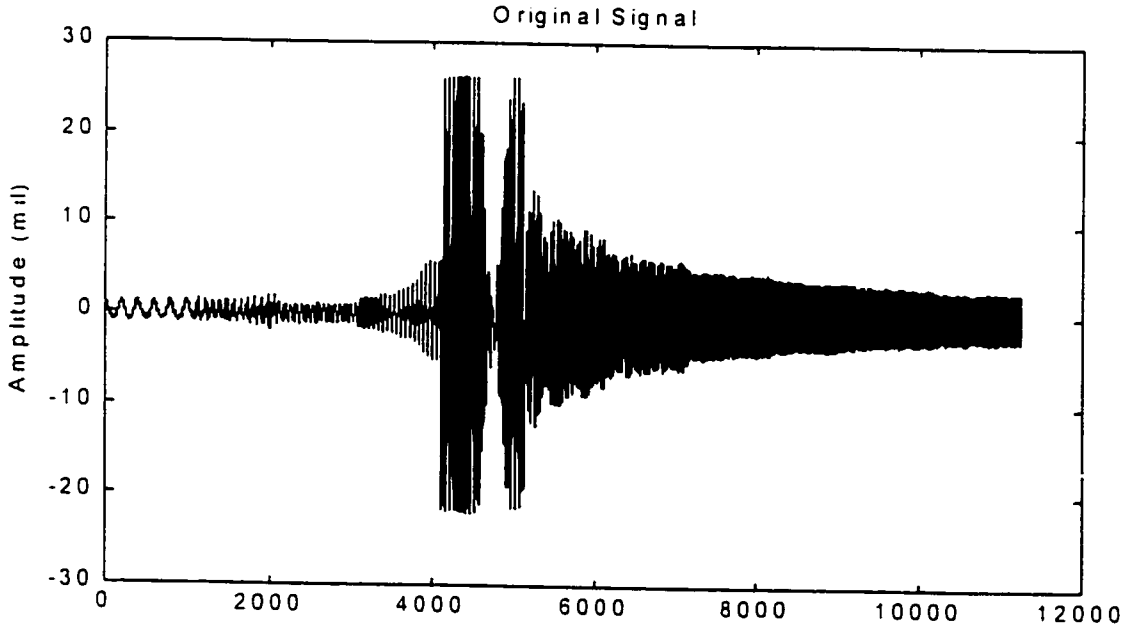

(ii) Horizontal

Fig. 5.15 (a). Startup signal for shaft with 4mm notch crack

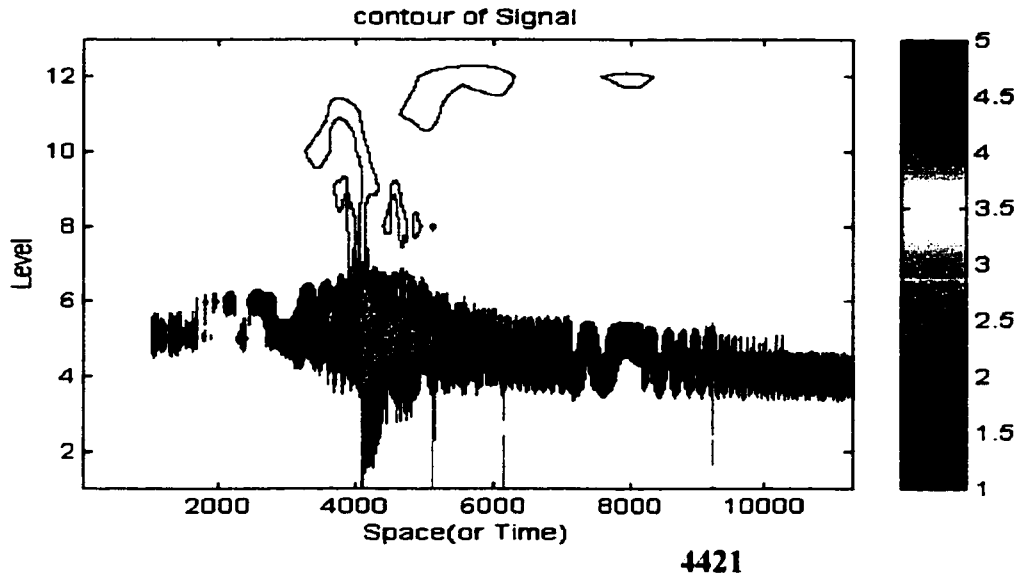

(i) Vertical

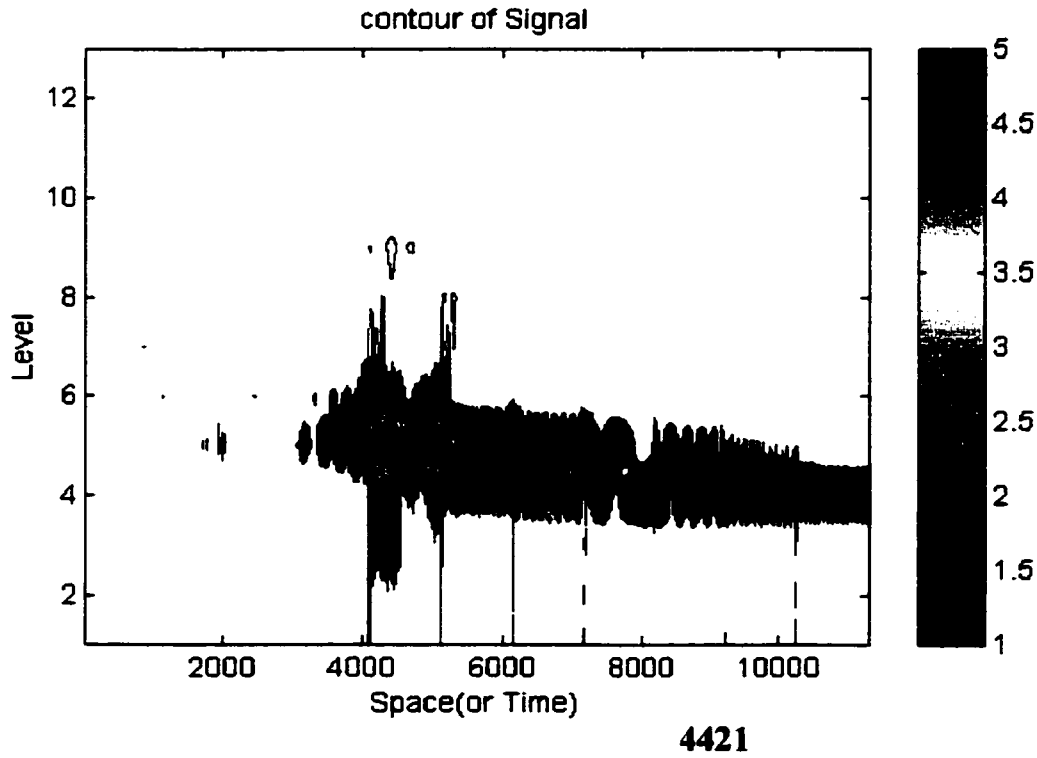

(ii) Horizontal

Fig. 5.15 (b). Scalogram of DWT of startup signal for shaft with 4mm notch crack

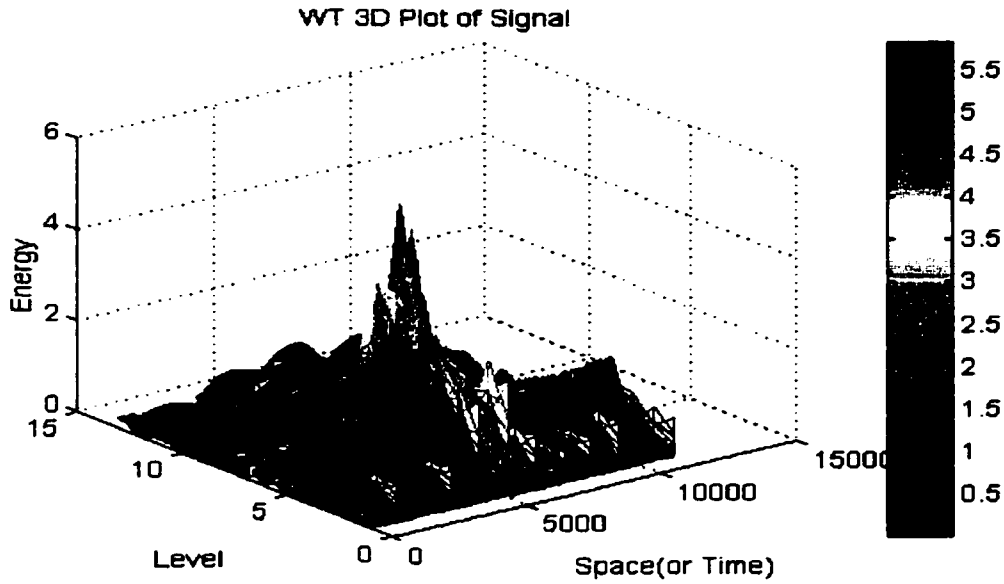

(i) Vertical

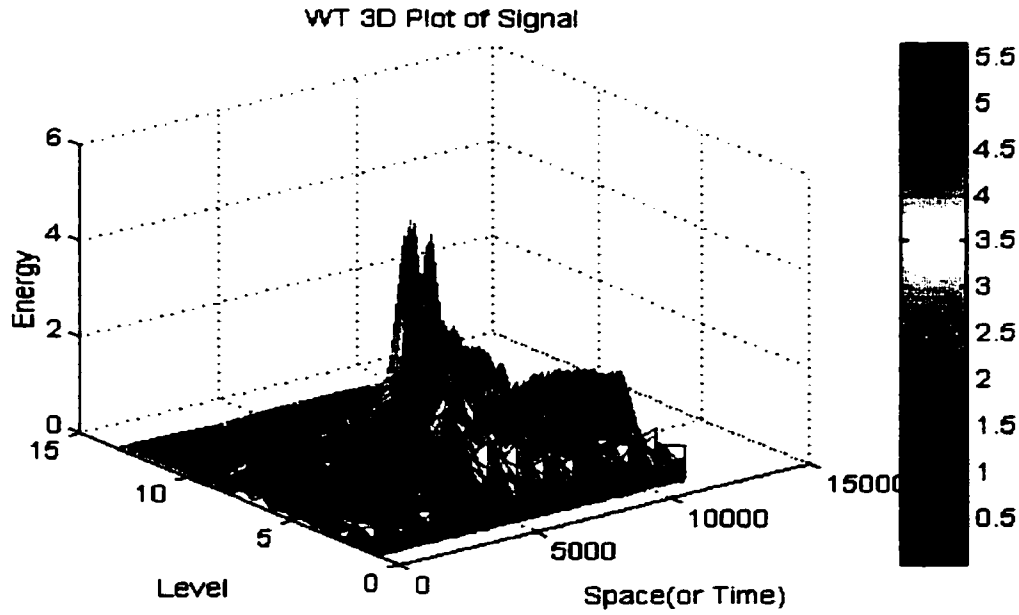

(ii) Horizontal

Fig. 5.15 (c). 3-D plot of DWT of startup signal for shaft with 4mm notch crack

Figure 5.15 Wavelet analysis of startup data for shaft with 4mm notch crack

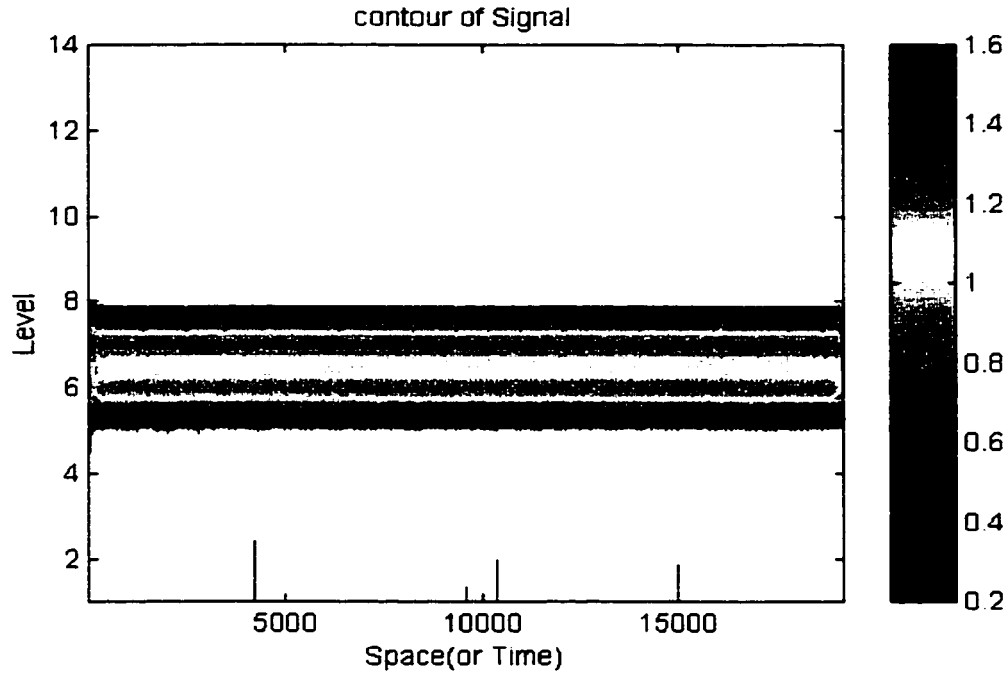

(i) Vertical

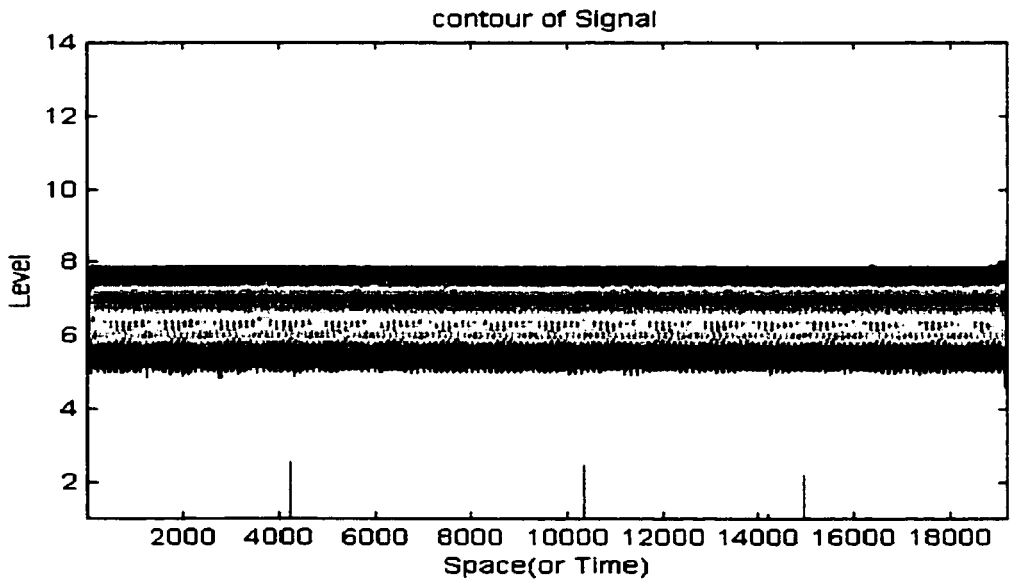

(ii) Horizontal

Fig. 5.16 (a) Scalogram of DWT of steady state signal at 3500 rpm for shaft with 4mm notch crack

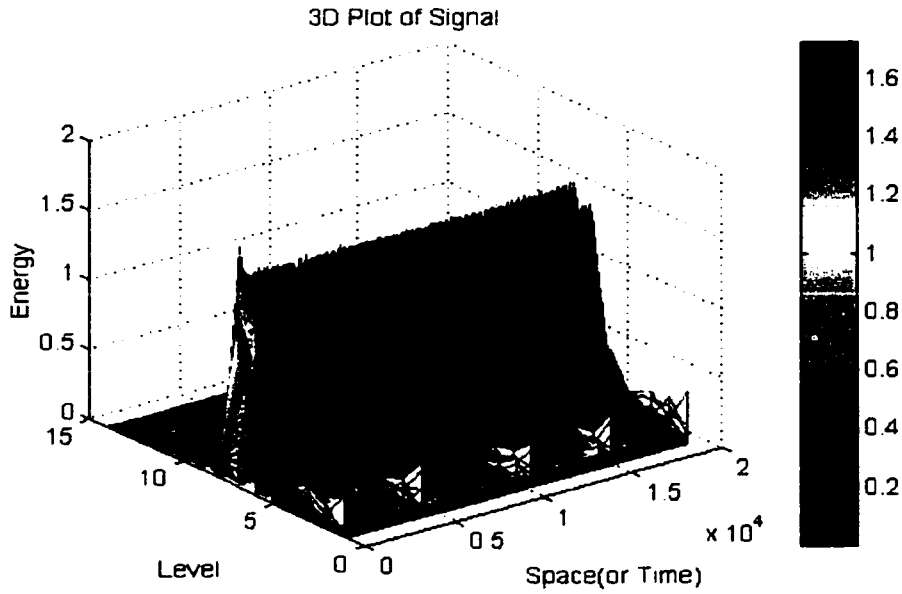

(i) Vertical

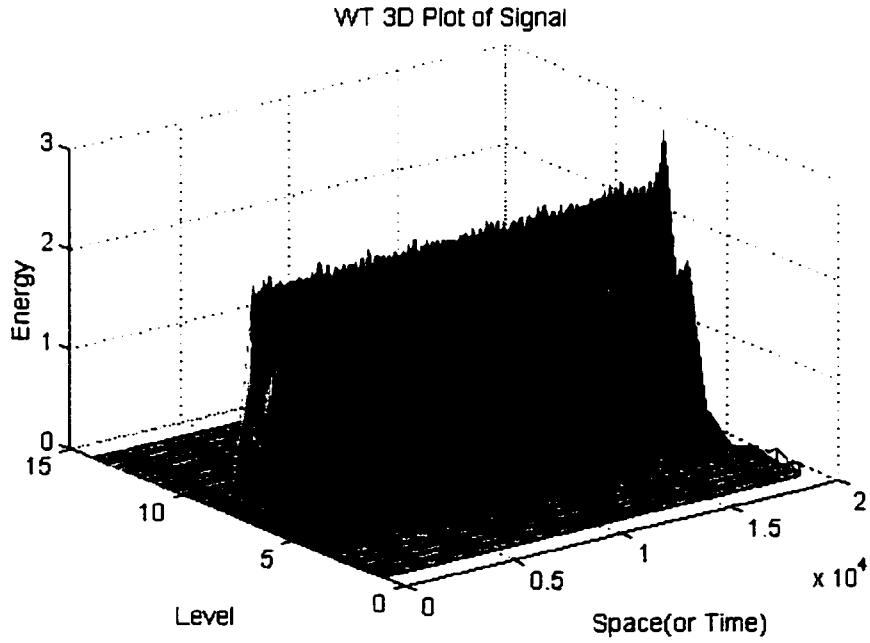

(ii) Horizontal

Fig. 5.16 (b). 3-D plot of DWT of steady state signal at 3500 rpm for signal of shaft with 4mm notch crack .

Figure 5.16 Wavelet analysis of Steady state data at 3500rpm for shaft with 4mm notch crack

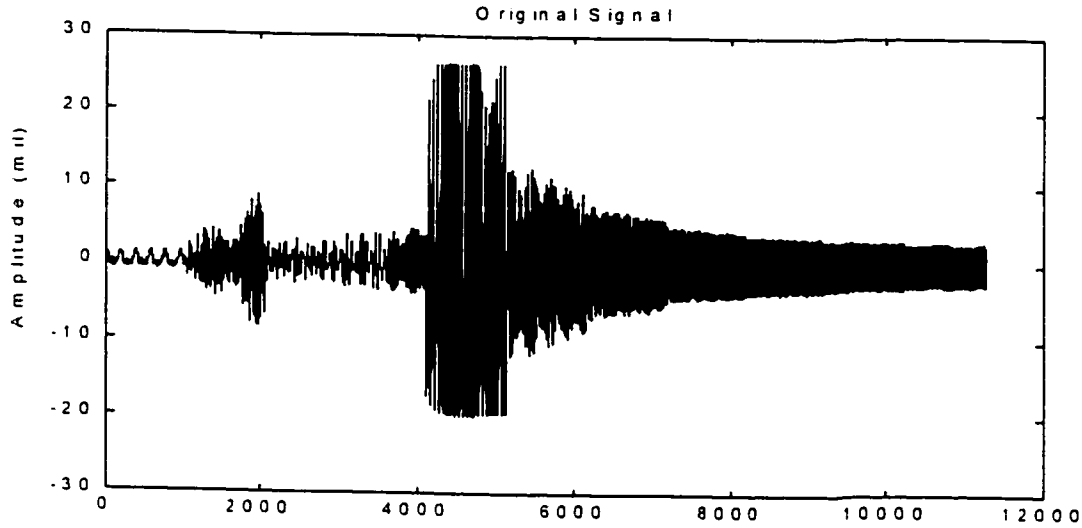

(i) Vertical

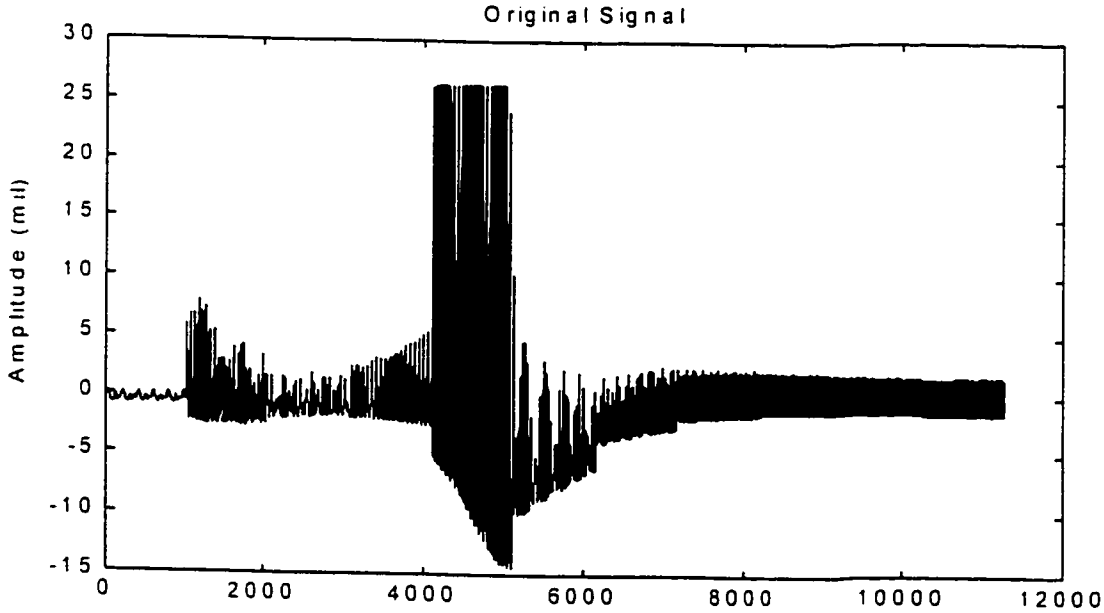

(ii) Horizontal

Fig. 5.17(a). Startup signal for the shaft with 4mm notch crack and 4.3 kg vertical tension

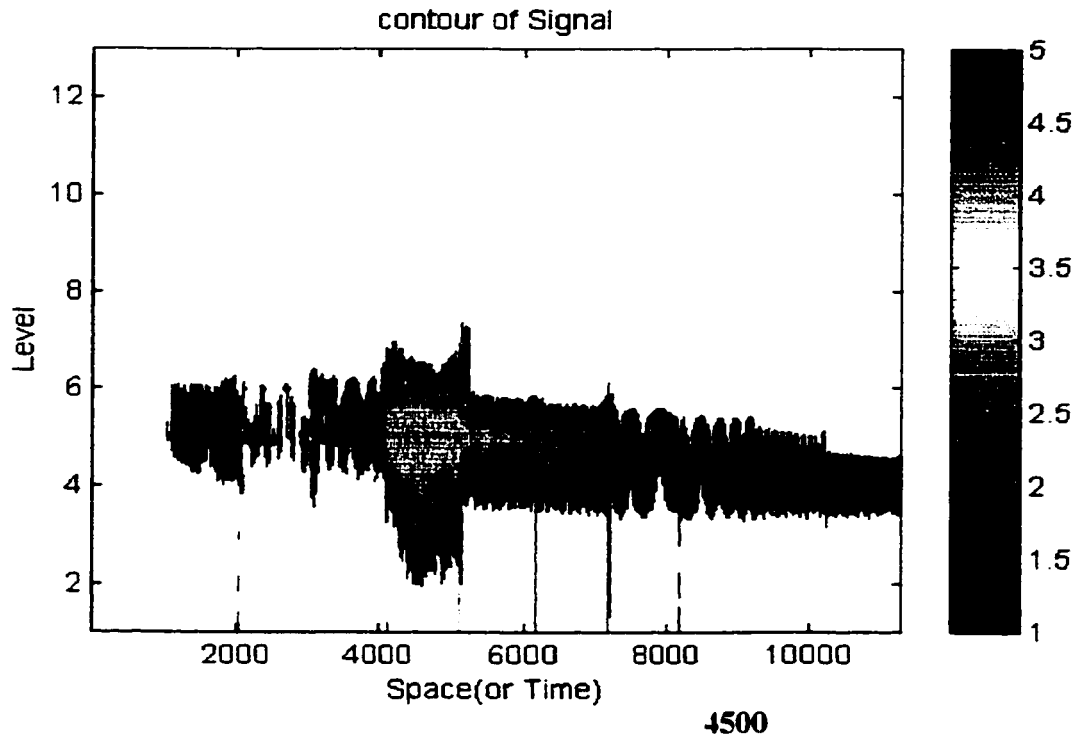

(i) Vertical

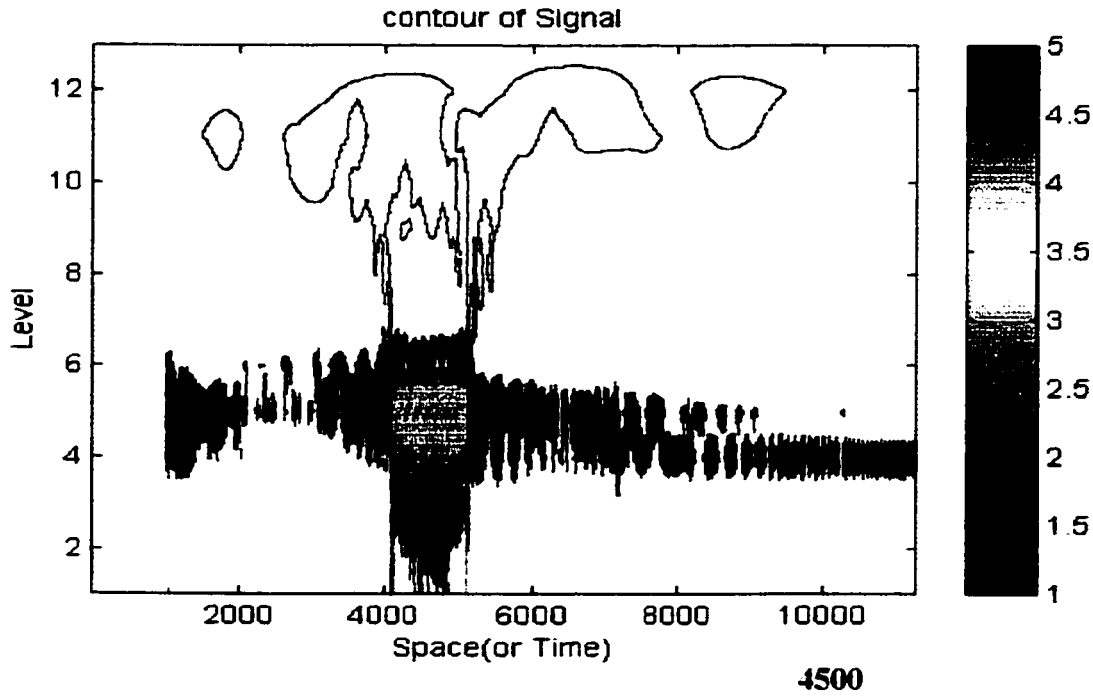

(ii) Horizontal

Fig. 5.17(b) Scalogram of DWT of startup signal for the shaft with 4mm notch crack and 4.3 kg vertical tension

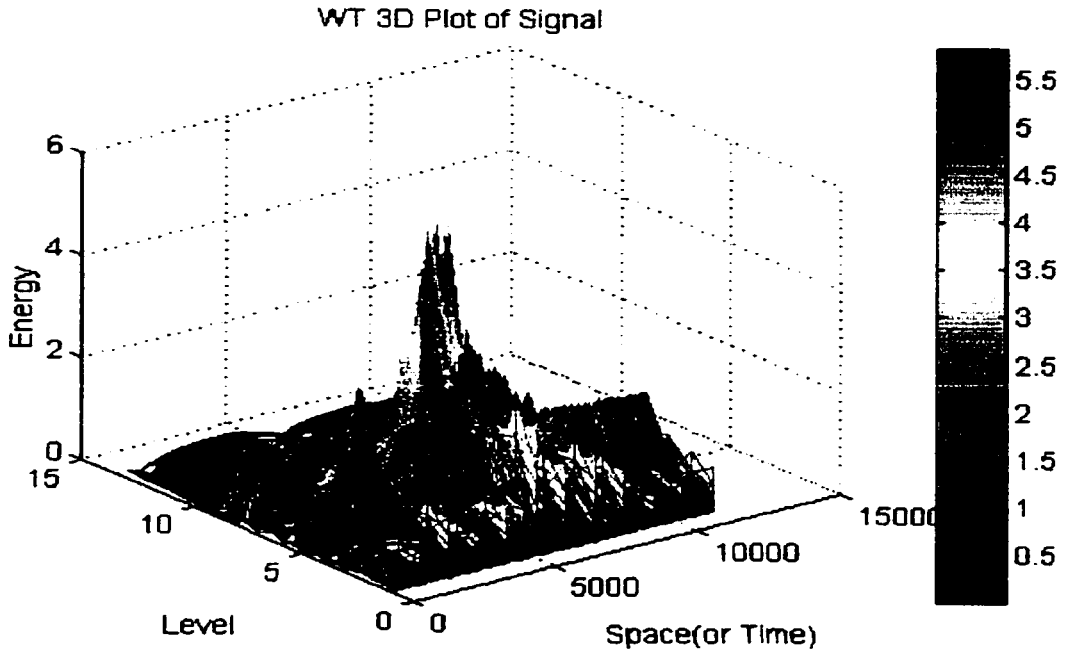

(i) Vertical

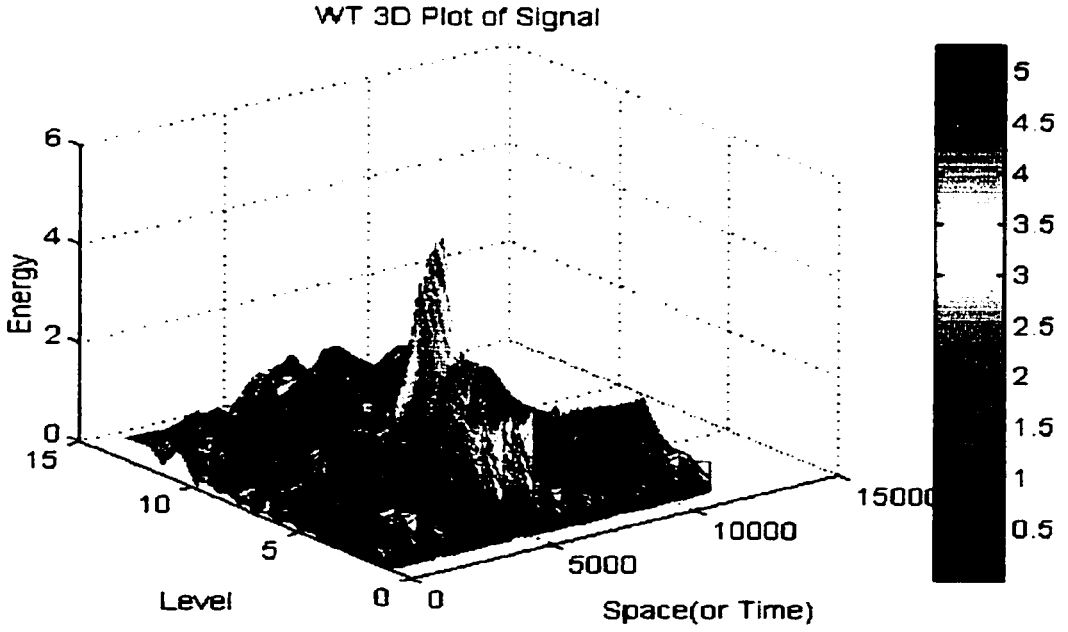

(ii) Horizontal

Fig. 5.17(c) 3-D plot of DWT of startup signal for the shaft with 4mm notch crack and 4.3 kg vertical tension

Figure 5.17 Wavelet analysis of startup data for shaft with 4mm notch crack and 4.3 kg vertical tension.

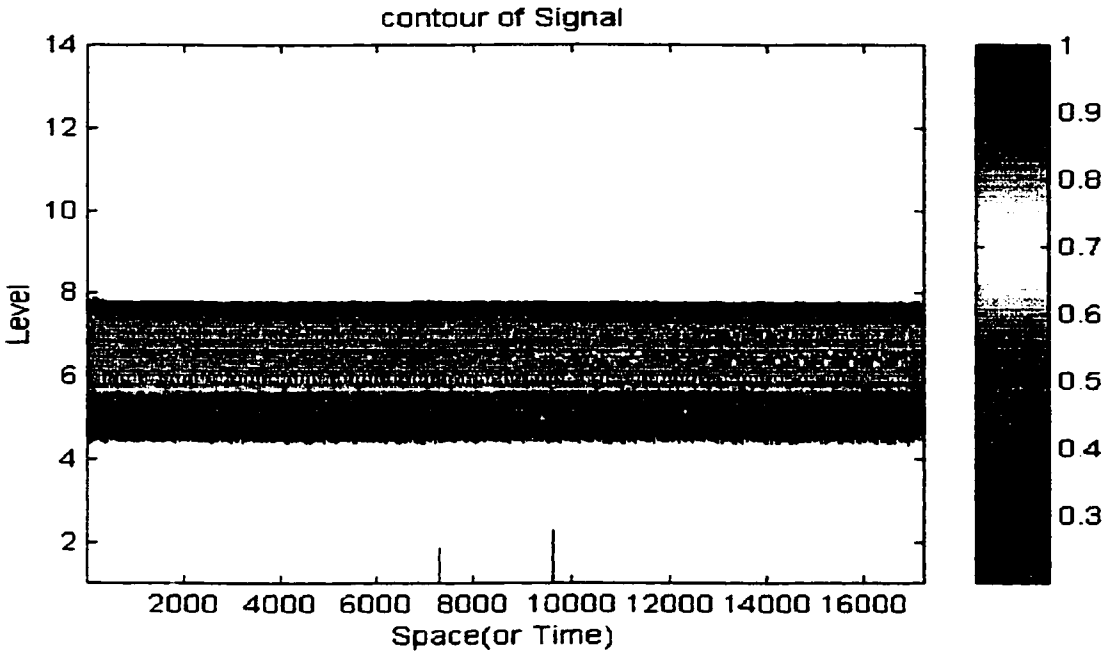

(i) Vertical

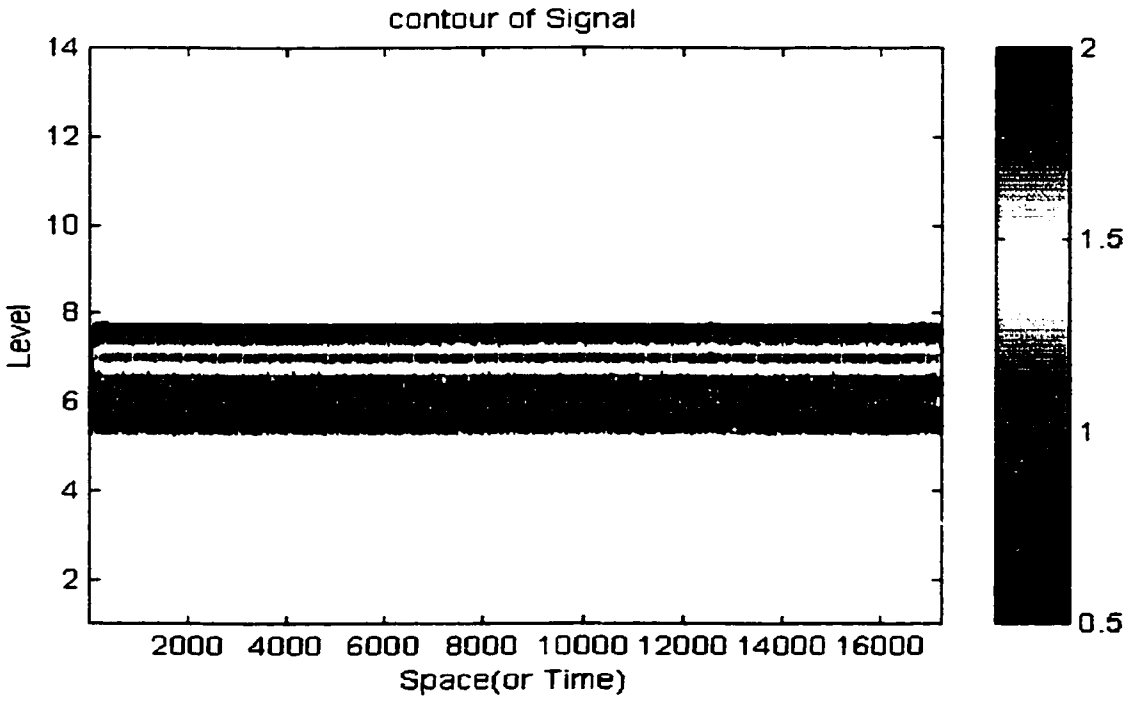

(ii) Horizontal

Fig. 5.18 (a). Scalogram of DWT of steady state signal at 3500 rpm for shaft with 4mm notch crack and 4.3 kg vertical side tension. .

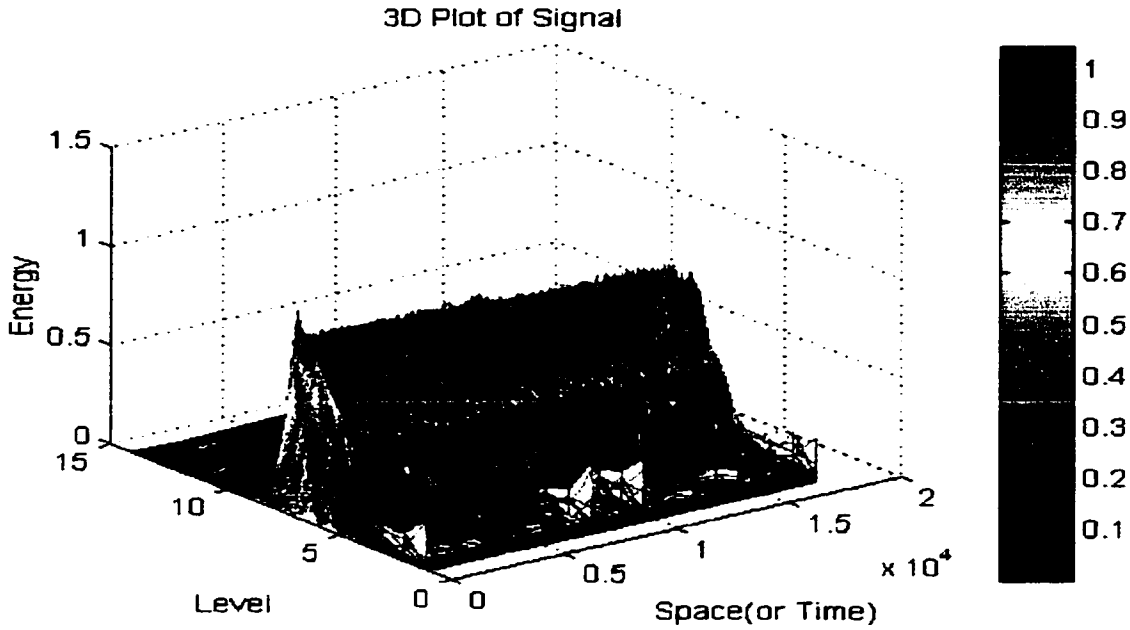

(i) Vertical

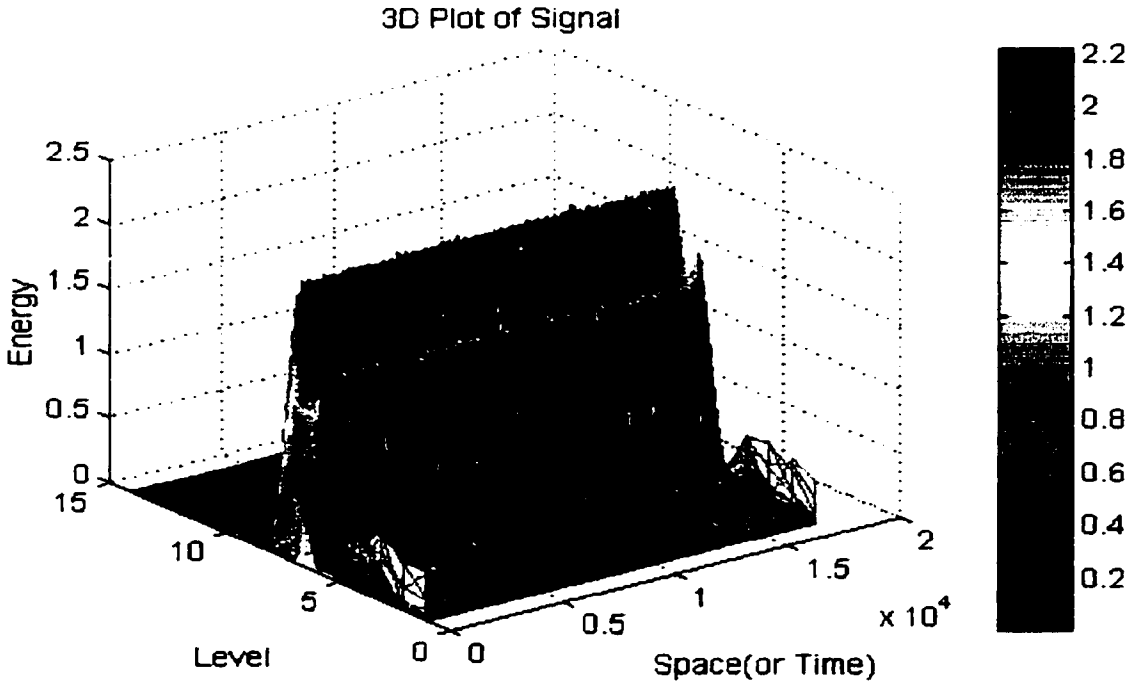

(ii) Horizontal

Fig. 5.18 (b). 3-D plot of DWT of steady state signal at 3500 rpm for shaft with 4mm notch crack and 4.3 kg vertical side tension

Figure 5.18 Wavelet analysis of Steady state data at 3500rpm for shaft with 4mm notch crack and 4.3 kg vertical side tension.

5.3.2 Second Experimental Setup (Overhang Shaft)

The purpose of this setup is to study the effect of crack propagation on the dynamic response of rotating shaft system. A hanging 8 kg side load is attached to the shaft in order to increase the bending stress on the crack, which is located close to the bearing support. The hanging side load and the string used in attaching it to the roller bearing on the shaft introduced another degree of freedom as explained in section 5.2.2. the effect of this will not be considered in the discussion.

5.3.2.1 Un-cracked shaft

Figure 5.19 presents the startup results for an un-cracked shaft with 8kg vertical hanging side load while Figure 5.20 show the steady state results for the same shaft arrangement. Introduction of the side load increased the stiffness and hence the critical speed of the shaft in the vertical direction to approximately twice the critical speed in the horizontal direction. Consequently, the resonance spot in the vertical and horizontal directions occurred at level 4 and Level 5, respectively. It is interesting to note that there is a difference in the stiffness asymmetry produced by an external load and anisotropy of shaft system. Stiffness asymmetry produced by anisotropy of shaft system is accompanied with split resonance as indicated in the Figures in section 5.3.1. Whereas, Figures in this section show that asymmetry produced by external load does not have split resonance. The resonance bandwidth in the vertical direction is wider than that in the horizontal direction.

The steady state results, Figure 5.20, show the presence of two frequency levels in the vertical direction and only one frequency level in the horizontal direction.

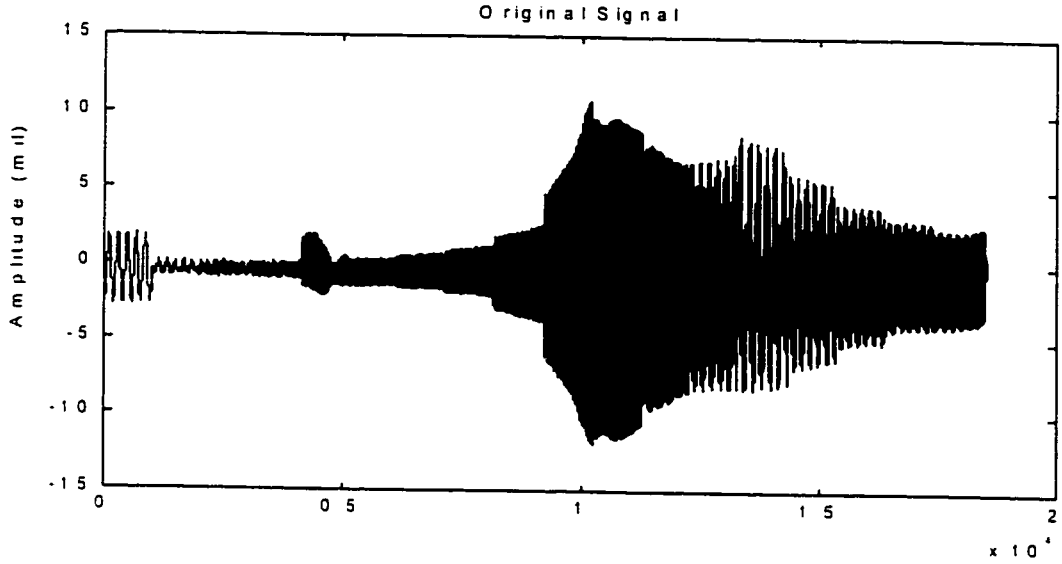

(i) Vertical

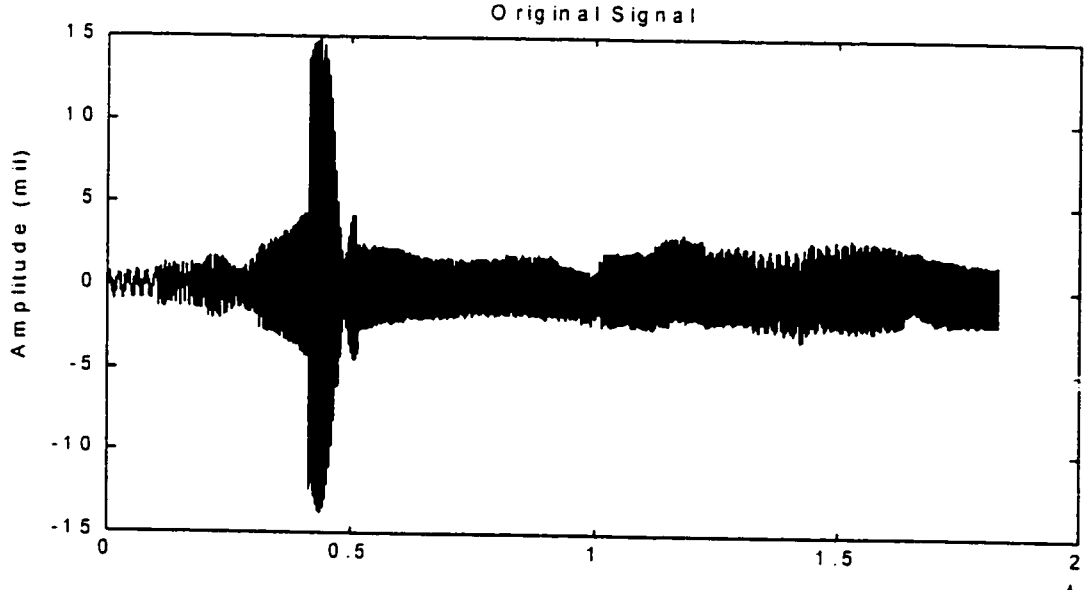

(ii) Horizontal

Fig. 5.19(a). Startup signal for un-cracked shaft with hanging side load of 8kg.

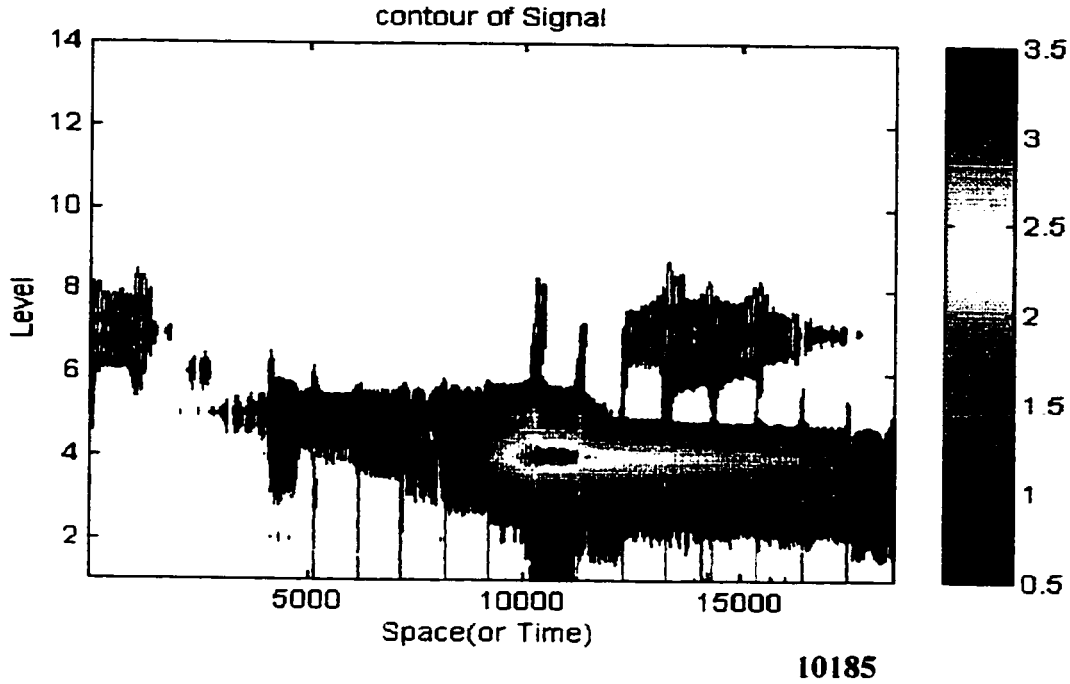

(i) Vertical

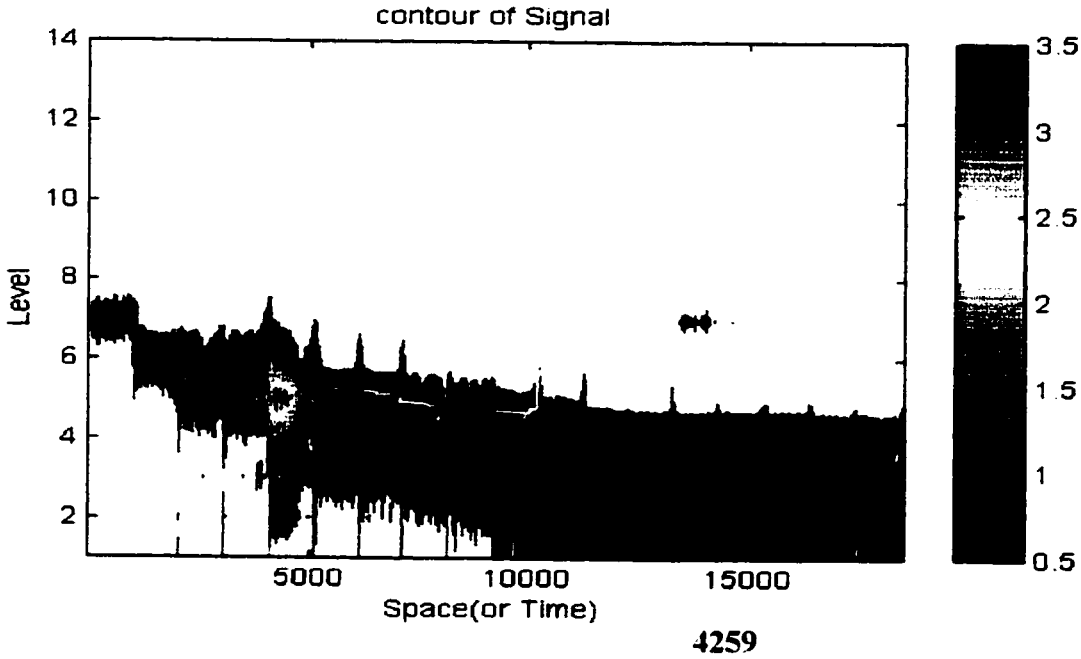

(ii) Horizontal

Fig. 5.19 (b). Scalogram of DWT of the startup data for un-cracked shaft with 8kg side load

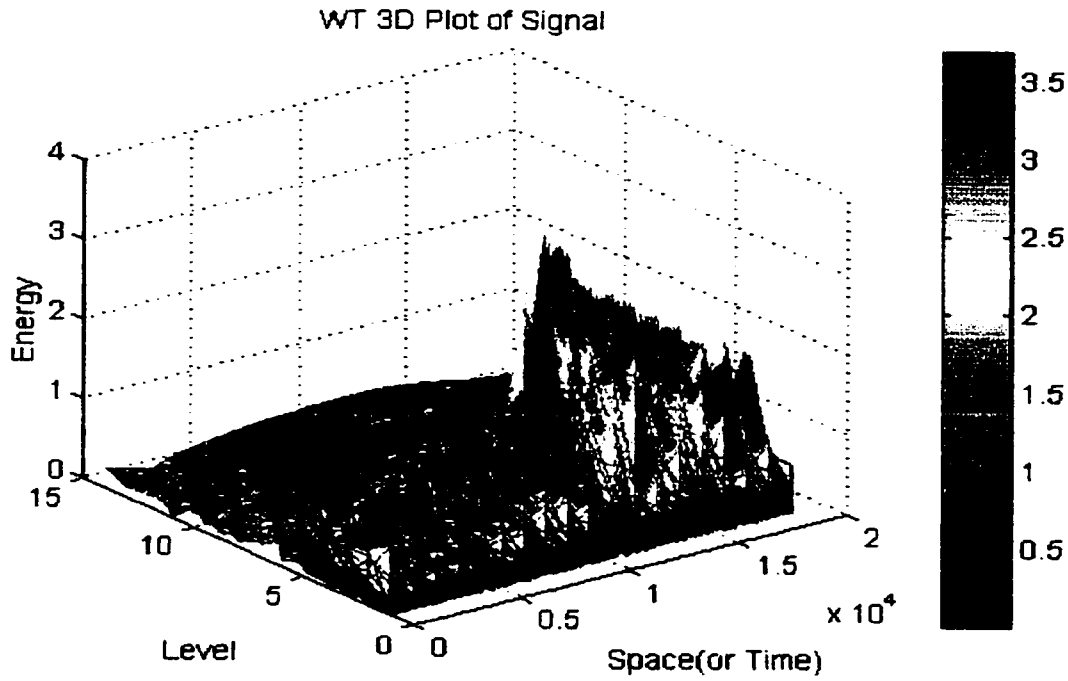

(i) Vertical

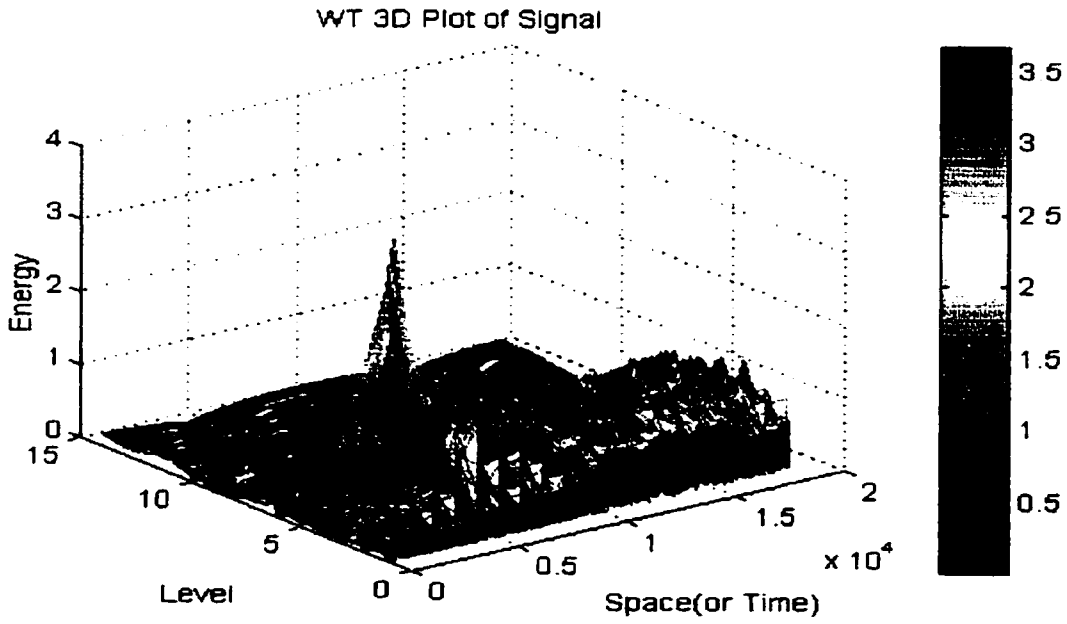

(ii) Horizontal

Fig. 5.19 (c). 3-D plot of DWT of the startup data for un-cracked shaft with 8kg side load.

Figure 5.19 Wavelet analysis for the startup data for un-cracked shaft with 8kg side load.

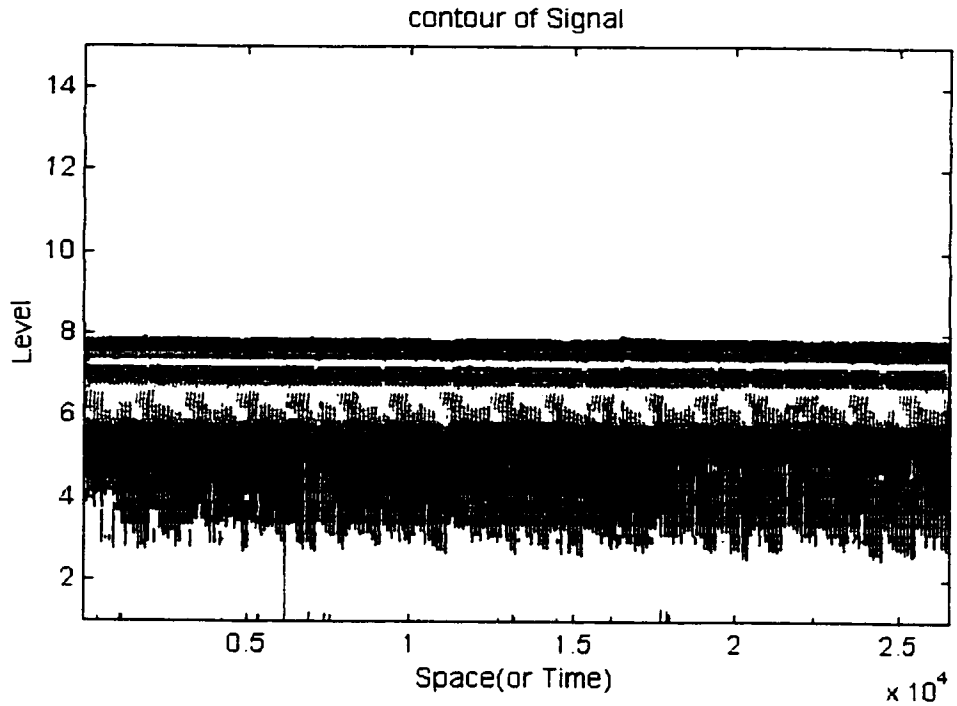

(i) Vertical

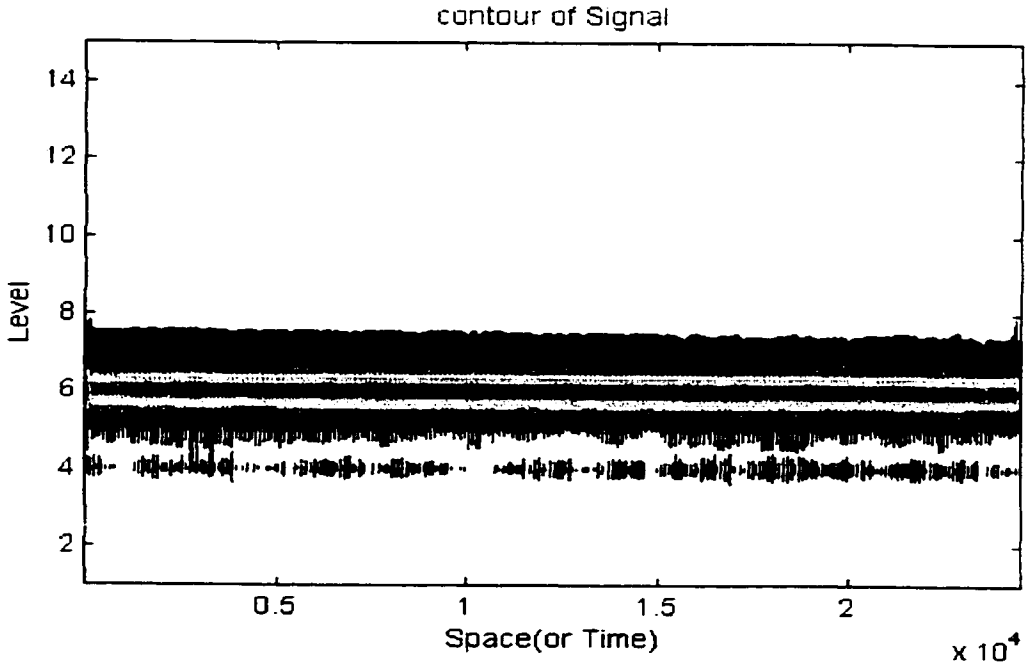

(ii) Horizontal

Fig. 5.20(a). Scalogram of DWT of the steady state data at 2000 rpm for un-cracked shaft with 8kg side load

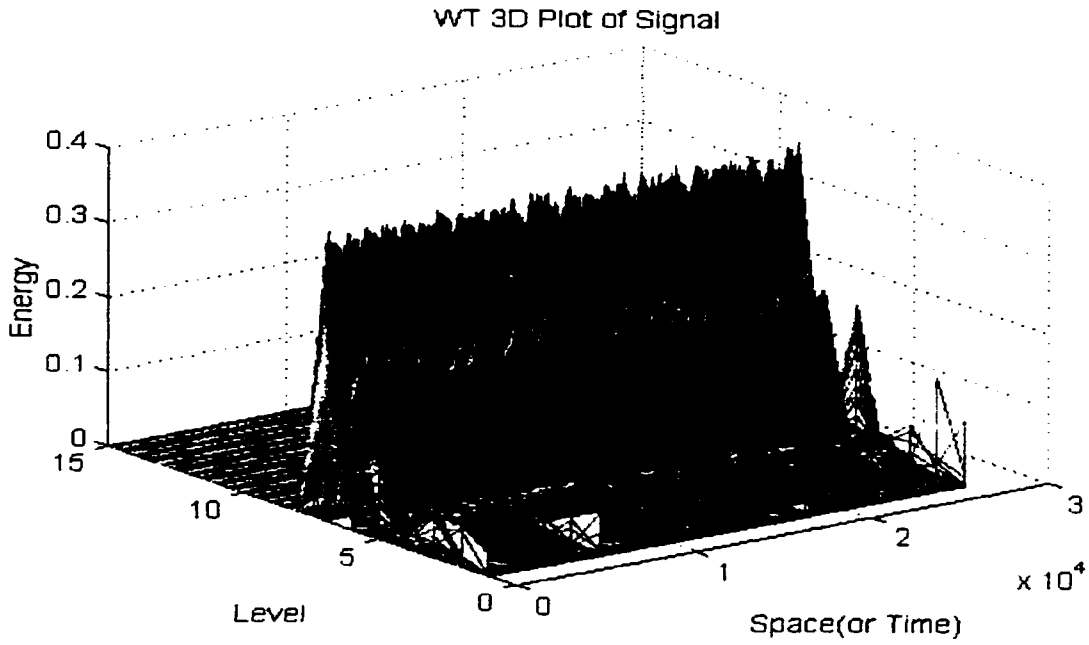

(i) Vertical

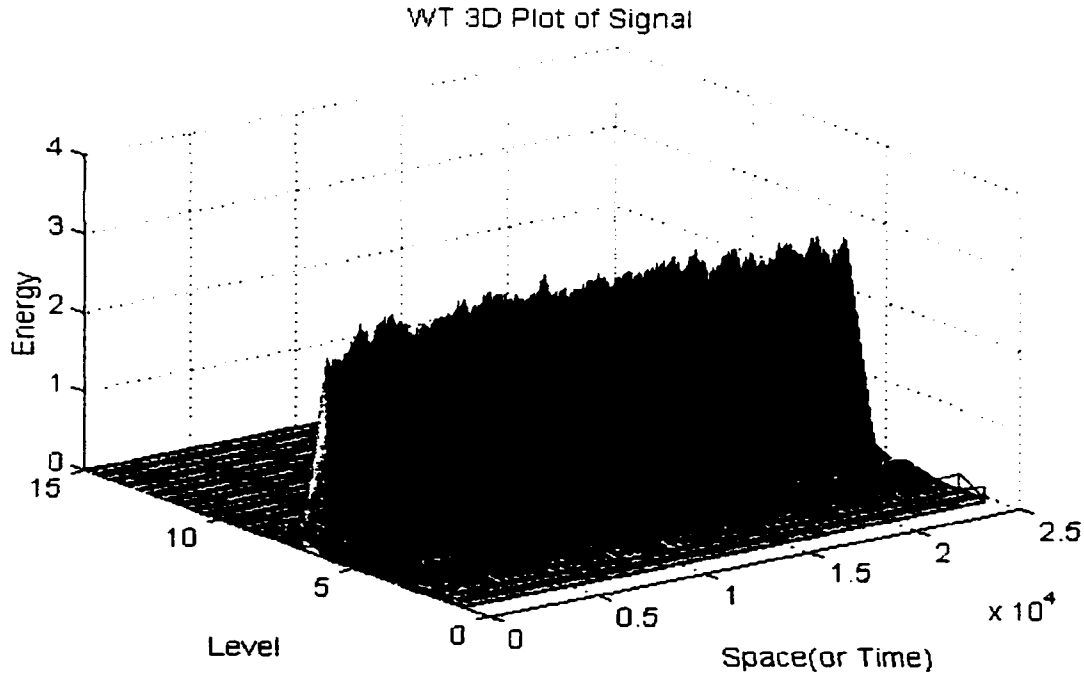

(ii) Horizontal

Fig. 5.20(b). Scalogram of CWT of the steady state data at 2000 rpm for un-cracked shaft with 8kg side load

Figure 5.20 Wavelet analysis for the steady state data at 2000 rpm for un-cracked shaft with 8kg side load

5.3.2.2 Shaft with Surface Transverse Crack

Figure 5.21 represents the startup results for the shaft with 3mm notch crack and 8 kg hanging side load at the beginning of crack propagation. In Fig. 5.21(b), there is an increase in the critical speed in both directions. This is a strange observation since we have seen in the pervious results that crack caused a decrease in the critical speed of shaft by decreasing its stiffness. Possible explanation for the observation may be related to the fact that the shaft is under the combined effects of crack and strain/plastic hardening.

Firstly, it has been reported in the literature that the influence of a crack on the stiffness of a shaft depends on both the crack depth and its location [1, 14]. The crack depth was 3 mm and it was located close to the bearing support. The effect of this arrangement on shaft stiffness may be less compared with the effect of strain hardening.

Secondly, plastic deformation must occur before crack can propagate. During plastic deformation, there is a change in the strength of the material via plastic hardening due to the presence of residual stress in the plastic region. The toughness depends on the strain; therefore, an increase in the strain due to crack propagation will increase the toughness of the material, which may increase the stiffness of the shaft as observed.

In Fig. 5.23(b), startup results for the shaft with 3mm notch crack and 8kg hanging side load before fracture, critical speed increased in the vertical direction but it decreased in the horizontal direction. The inconsistency in the critical speed changes due to crack for the 3mm v-notch cracked shaft may be due to competing factors such as the side load effect, gyroscopic effect, material strain hardening and some non-linearity in

the process of crack breathing. This requires more deep study into the mechanics of crack propagation and other factors, which are beyond the scope of the present work.

Fig. 5.22 shows the steady state results for the shaft with 3mm notch crack and 8kg side load at the beginning of crack propagation. Fig. 5.24 shows the steady state results for the same shaft arrangement just before the fracture of the shaft. Two levels of almost the same amplitude are present in Fig. 5.22(a)(i) and Fig. 5.22(b)(i) while one level is more prominent in Fig. 5.22(a)(ii) and Fig. 5.22(b)(ii). Figure 5.24 represents the steady state results for 3 mm cracked shaft with 8 kg hanging side load just before fracture. In Fig. 5.24(a)(i) and Fig. 5.24(b)(i), three levels (1X, 2X and 4X) are present and their amplitudes increased as crack propagated. However, in Fig. 5.24(ii) and Fig. 5.24(b)(ii), there is a decrease in the amplitude of level 7 (1X) and an increase in the amplitude of Level 6 (2X) as the crack propagated.

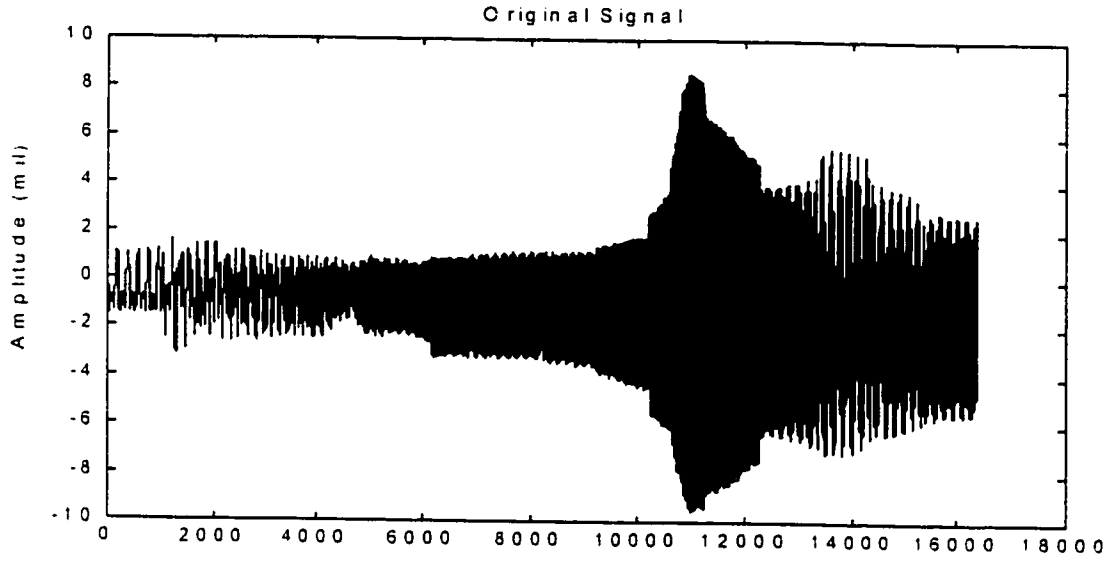

(i) Vertical

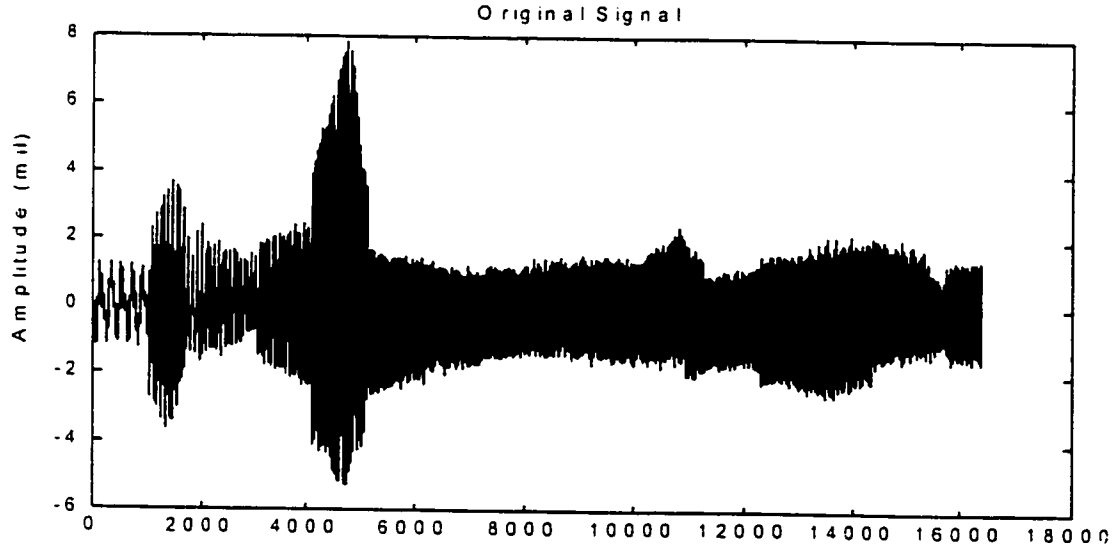

(ii) Horizontal

Fig. 5.21(a). Startup signal for shaft with 3mm notch and 8kg hanging load at the beginning of crack propagation.

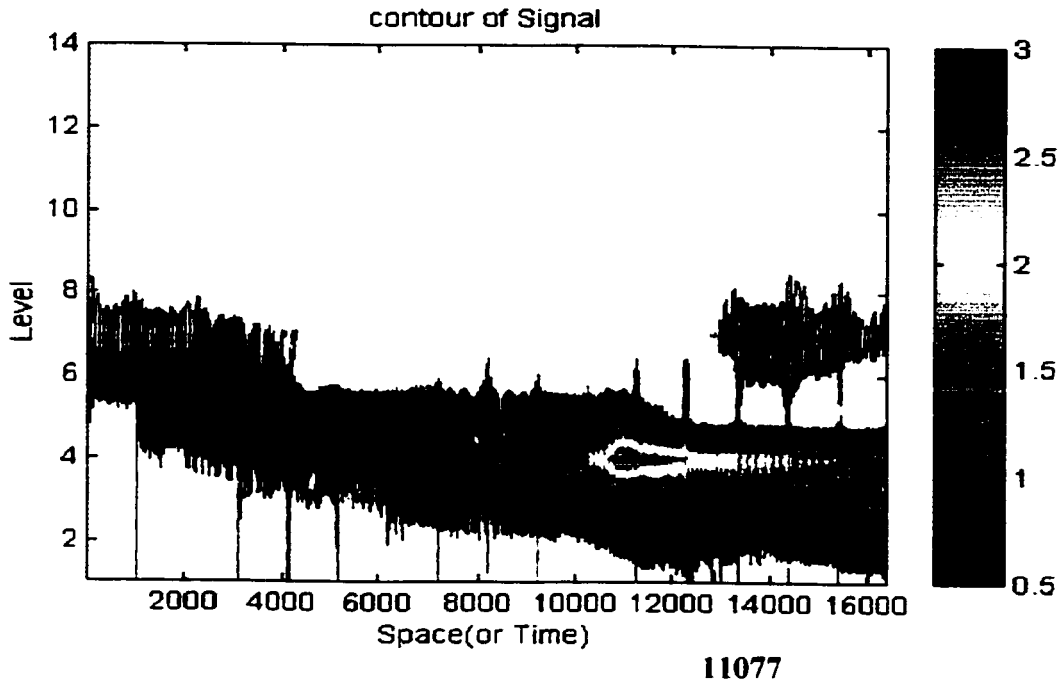

(i) Vertical

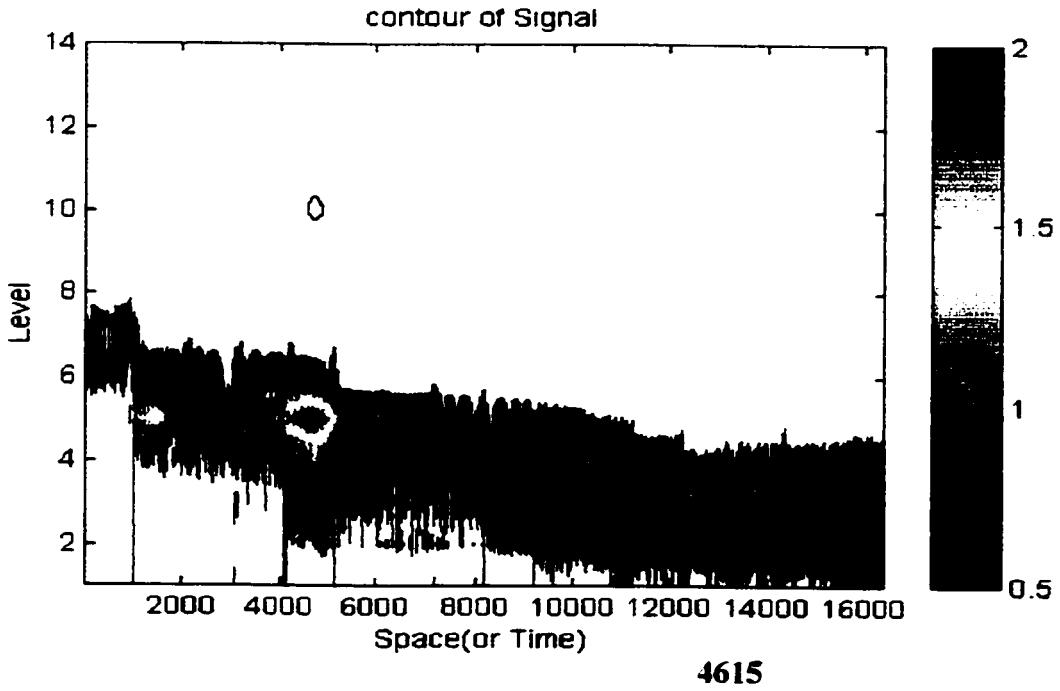

(ii) Horizontal

Fig. 5.21 (b) Scalogram of the DWT of the startup for shaft with 3mm notch and 8kg hanging load at the beginning of crack propagation.

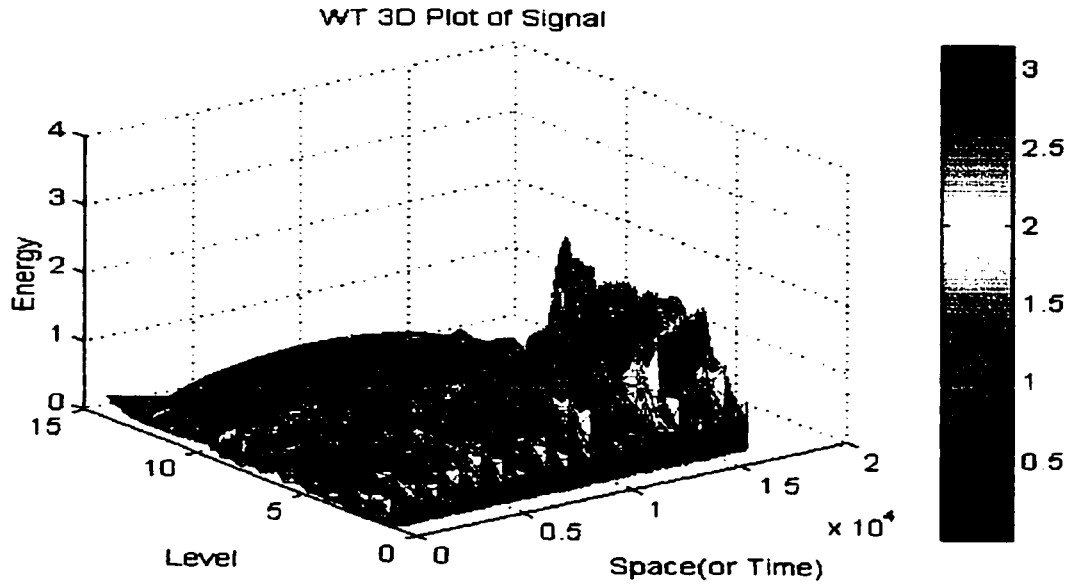

(i) Vertical

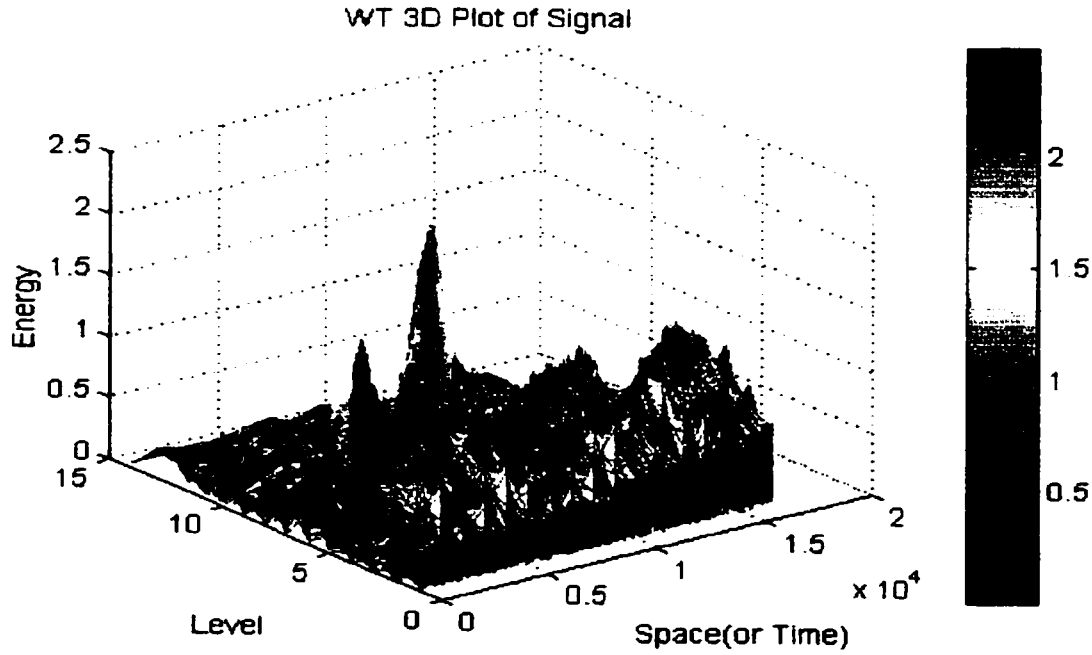

(ii) Horizontal

Fig. 5.21(c). 3-D plot for DWT of startup data for shaft with 3mm notch and 8kg hanging load at the beginning of crack propagation.

Figure 5.21. Wavelet analysis of Startup data for shaft with 3mm notch at the beginning of crack propagation

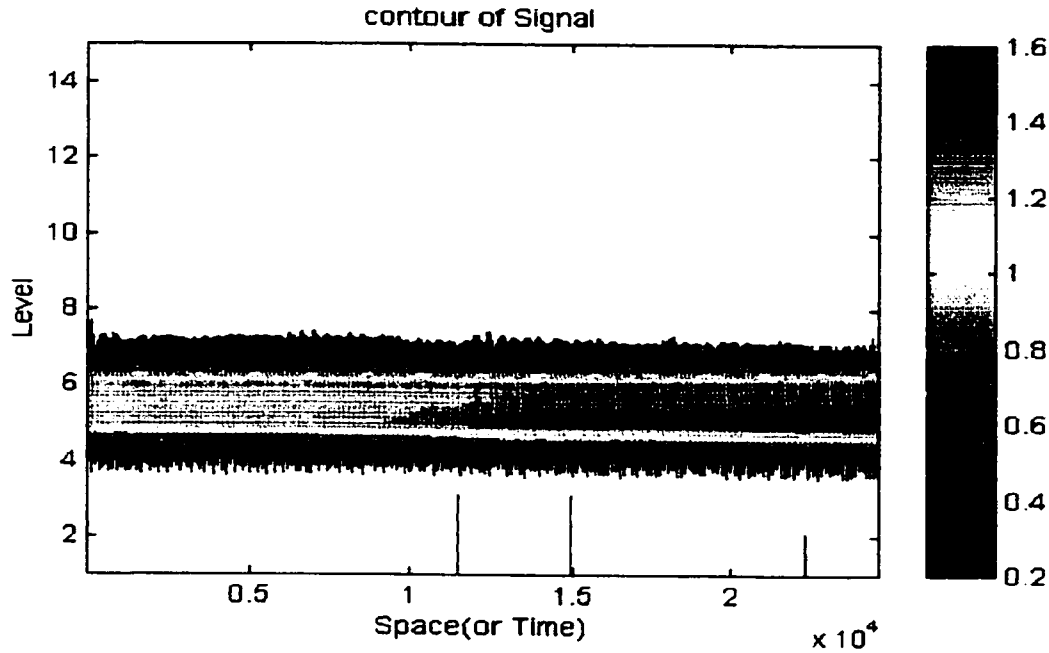

(i) Vertical

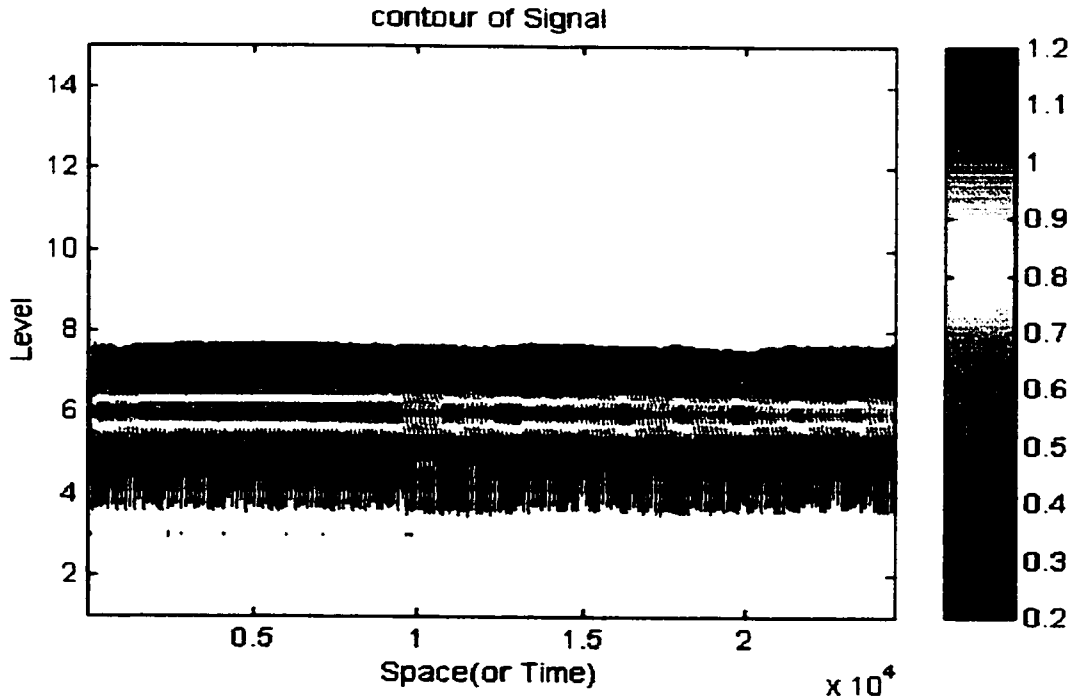

(ii) Horizontal

Fig. 5.22(a). Scalogram for DWT of steady state signal at 2000 rpm for shaft with 3mm notch at the beginning of crack propagation

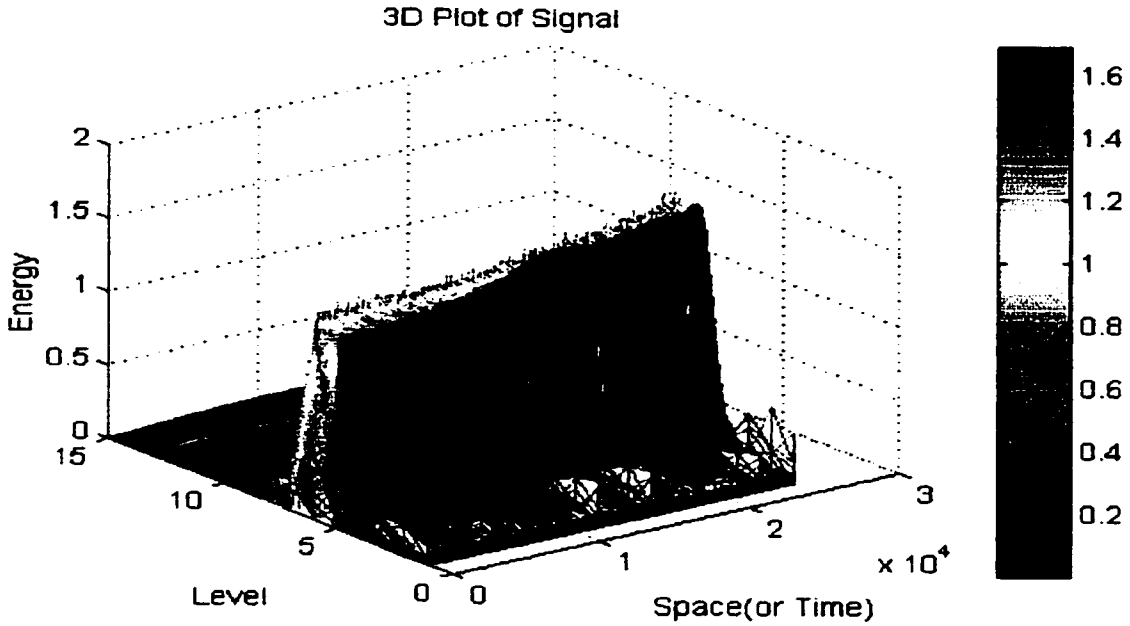

(i) Vertical

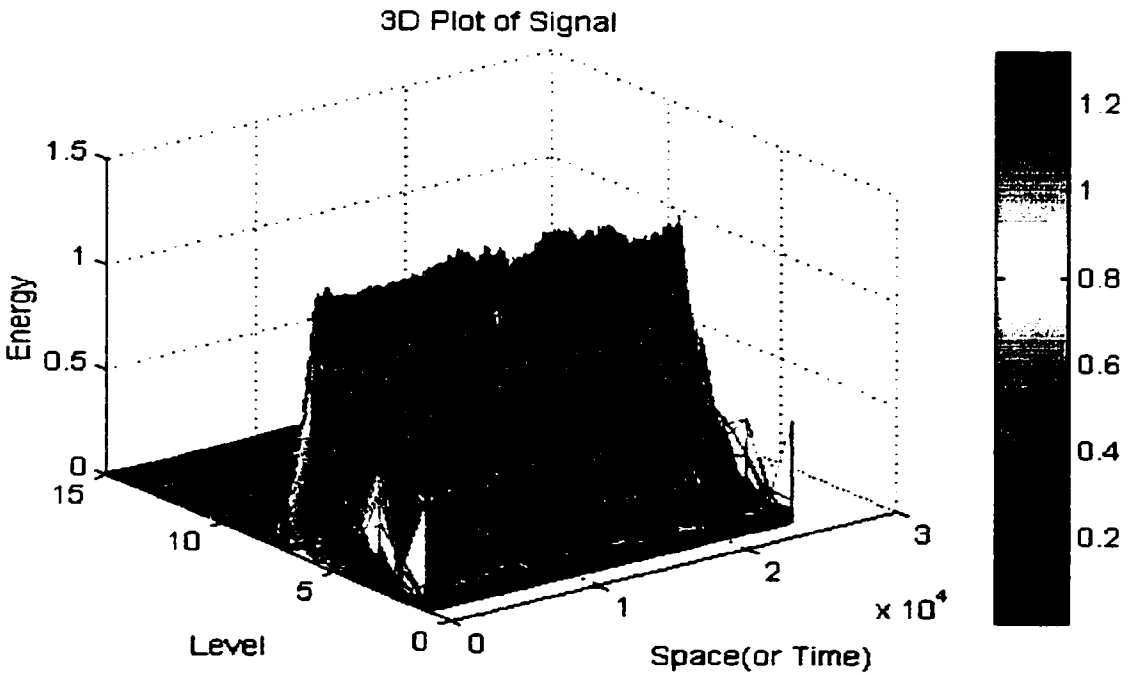

(ii) Horizontal

Fig. 5.22 (b). 3-D plot for DWT of steady state horizontal signal at 2000 rpm for shaft with 3mm notch at the beginning of crack propagation

Figure 5.22. Wavelet analysis of steady state data for shaft with 3mm notch at the beginning of crack propagation

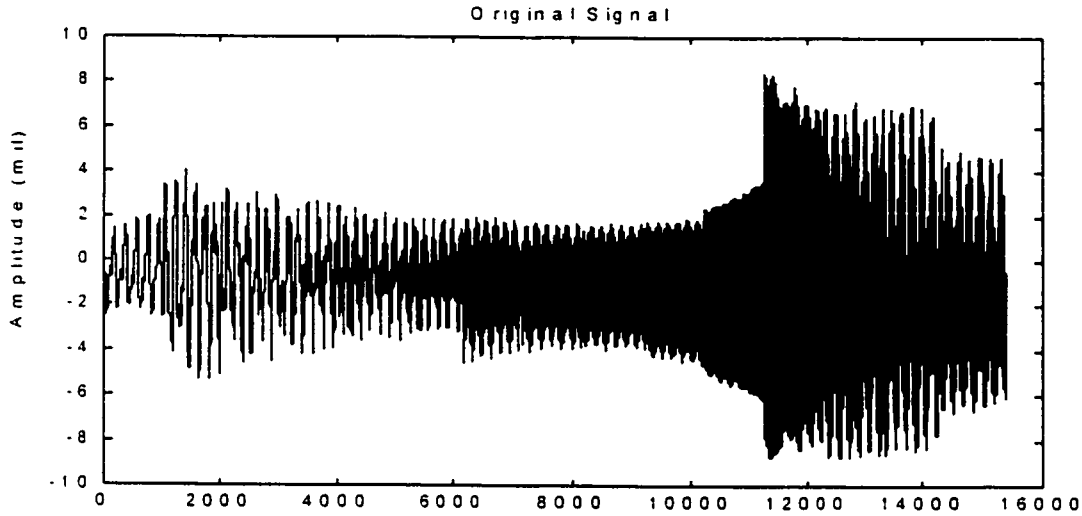

(i) Vertical

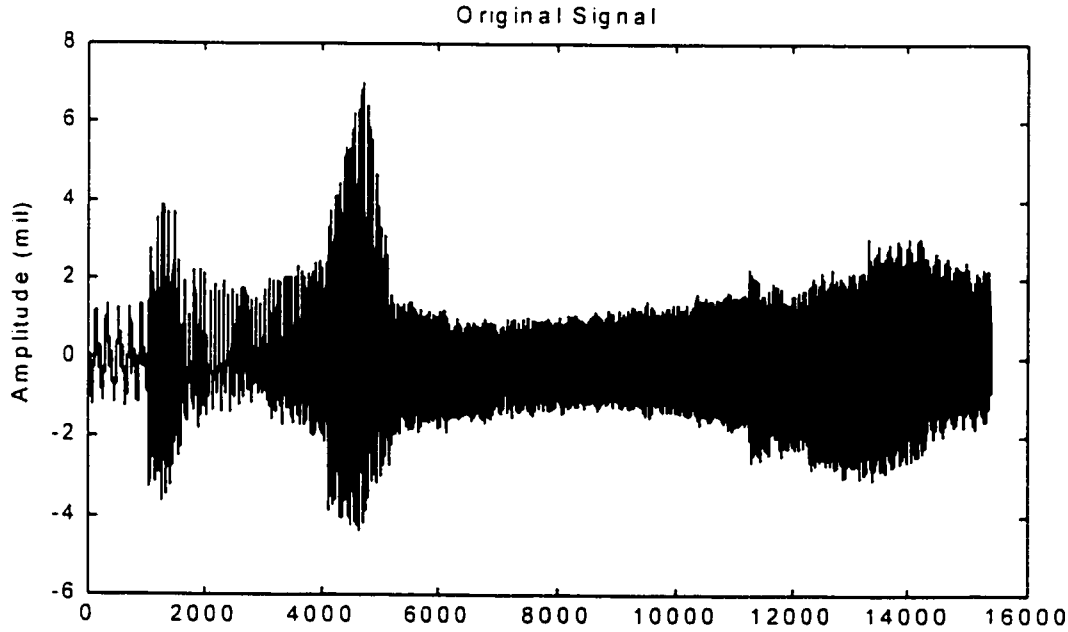

(ii) Horizontal

Fig. 5.23(a). Startup signal for shaft with 3mm notch and 8kg hanging side load and 8kg hanging load just before shaft fracture.

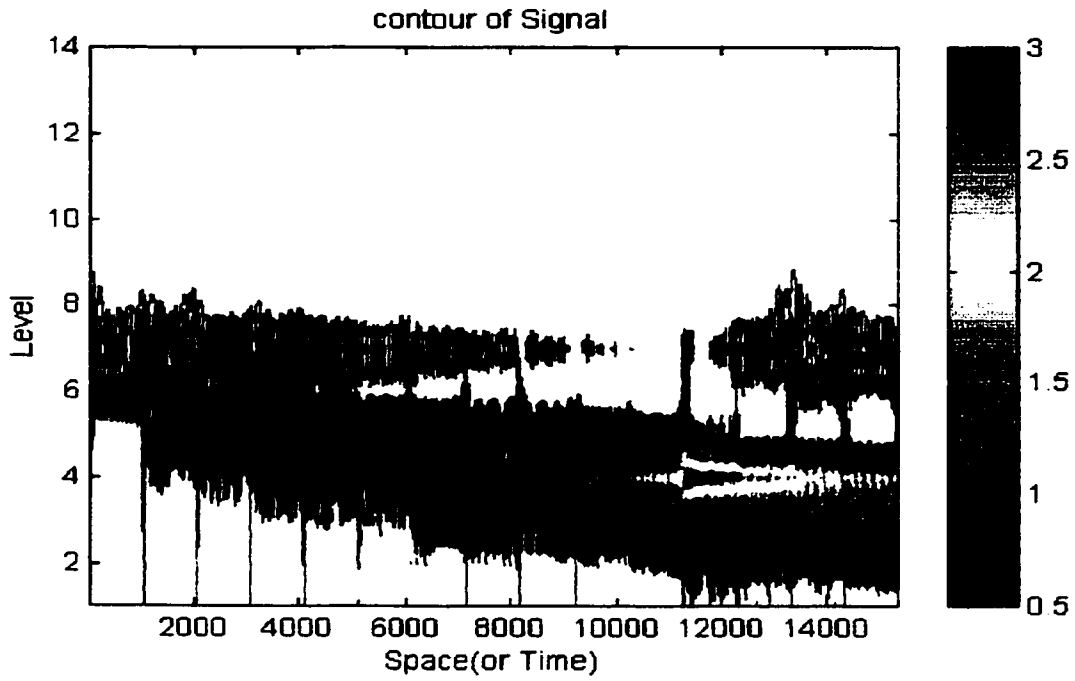

11733

(i) Vertical

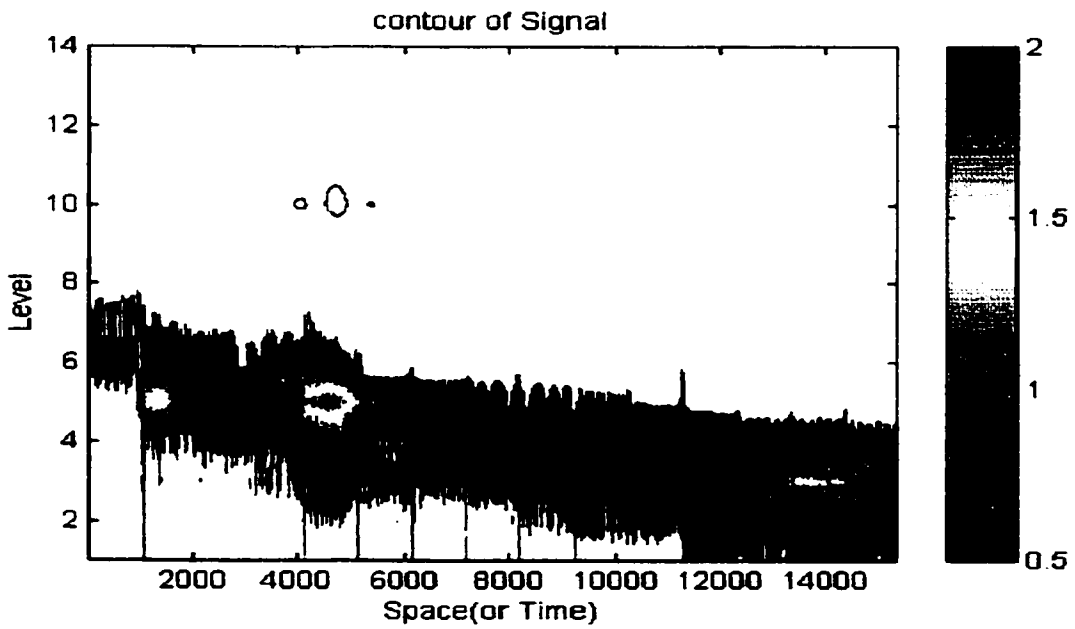

4400

(ii) Horizontal

Fig. 5.23 (b). Scalogram of the DWT of the startup for shaft with 3mm notch and 8kg hanging side load and 8kg hanging load just before shaft fracture.

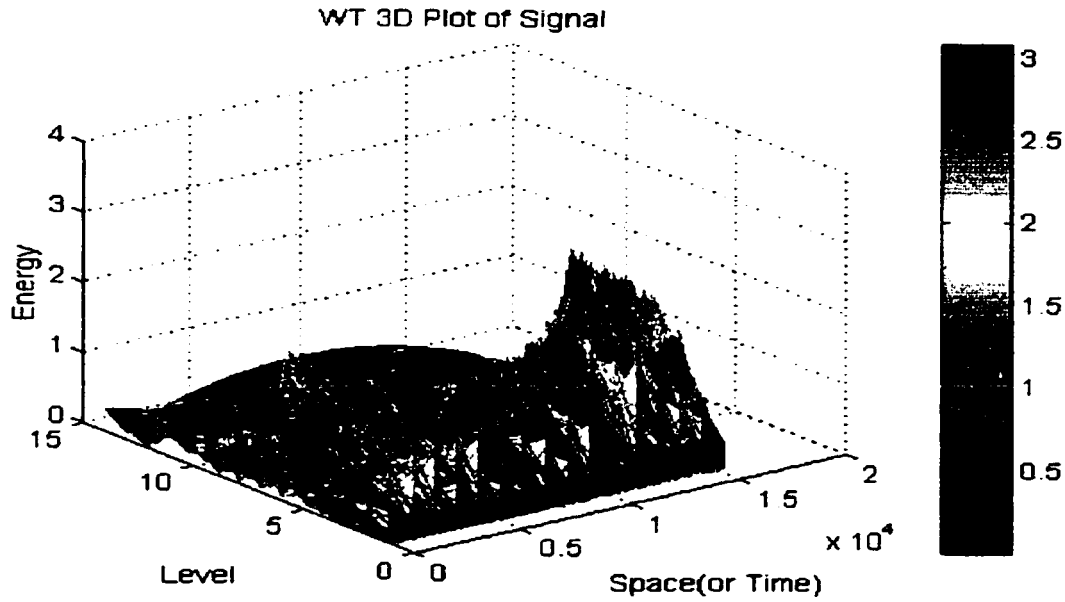

(i) Vertical

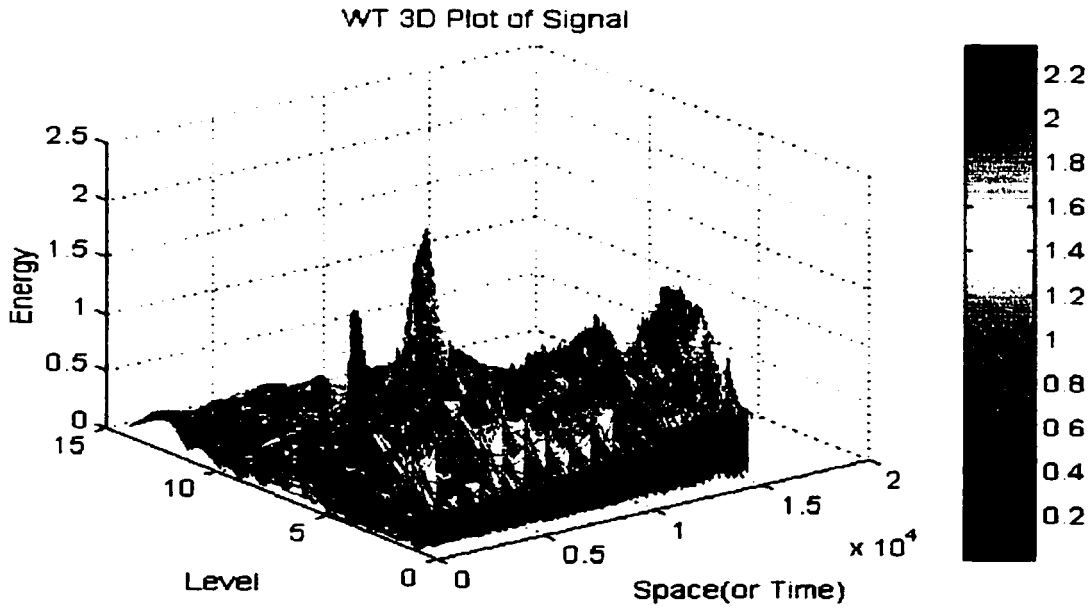

(ii) Horizontal

Fig. 5.23(c). 3-D plot of the DWT of the startup for shaft with 3mm notch and 8kg hanging side load and 8kg hanging load just before shaft fracture.

Figure 5.23. Wavelet analysis of Startup data for shaft with 3mm notch and 8 kg hanging side load just before shaft fracture

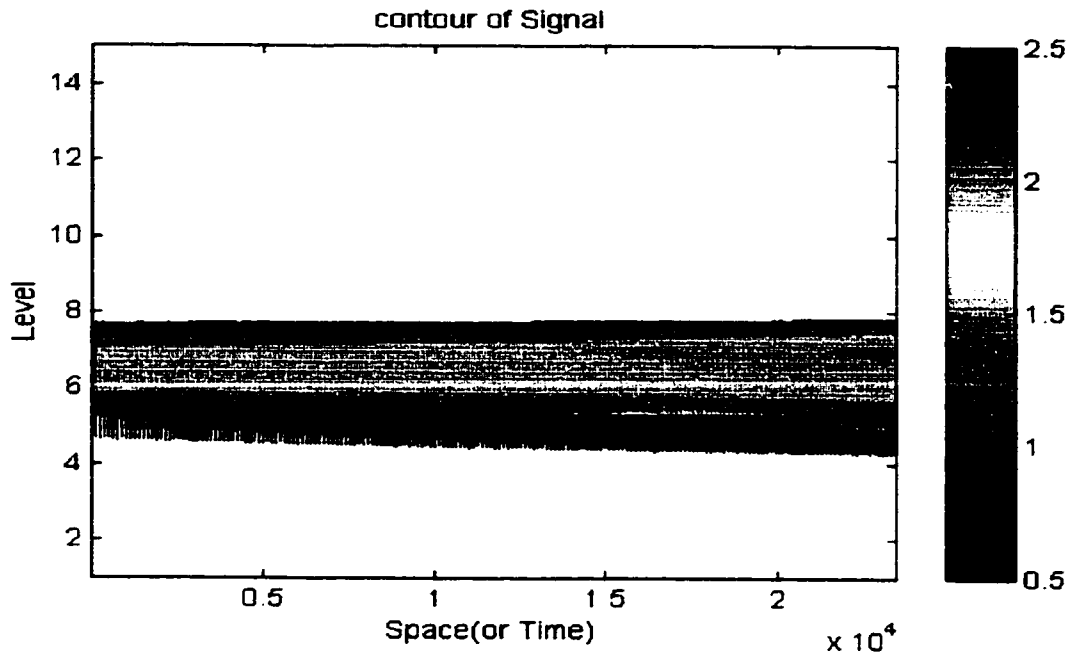

(i) Vertical

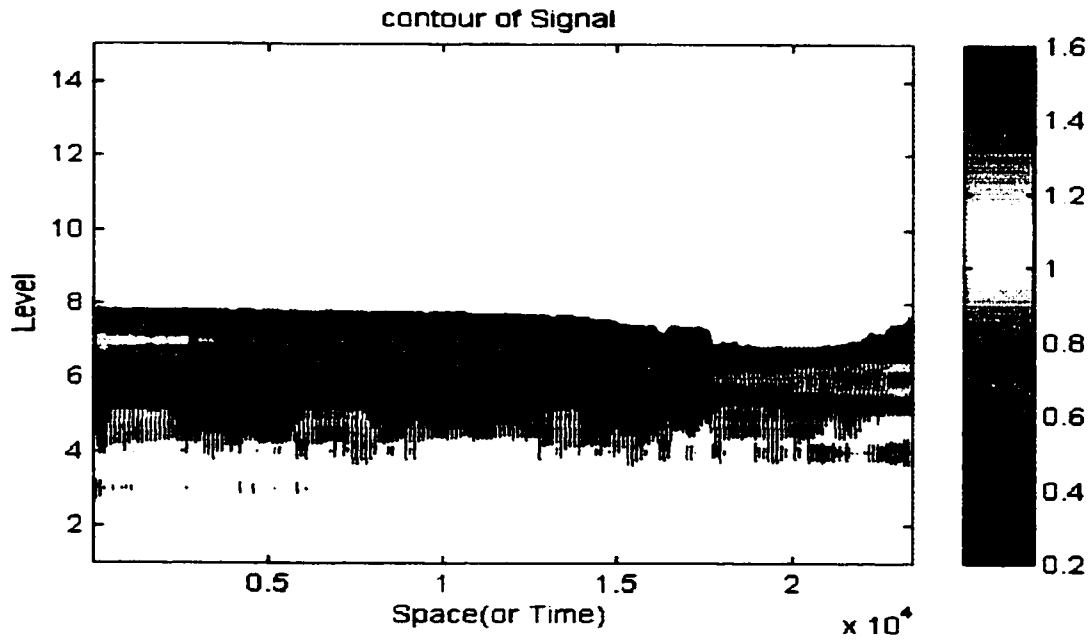

(ii) Horizontal

Fig. 5.24(a). Scalogram of DWT for steady state signal at 2000 rpm for shaft with 3mm notch and 8kg hanging side load just before shaft fracture

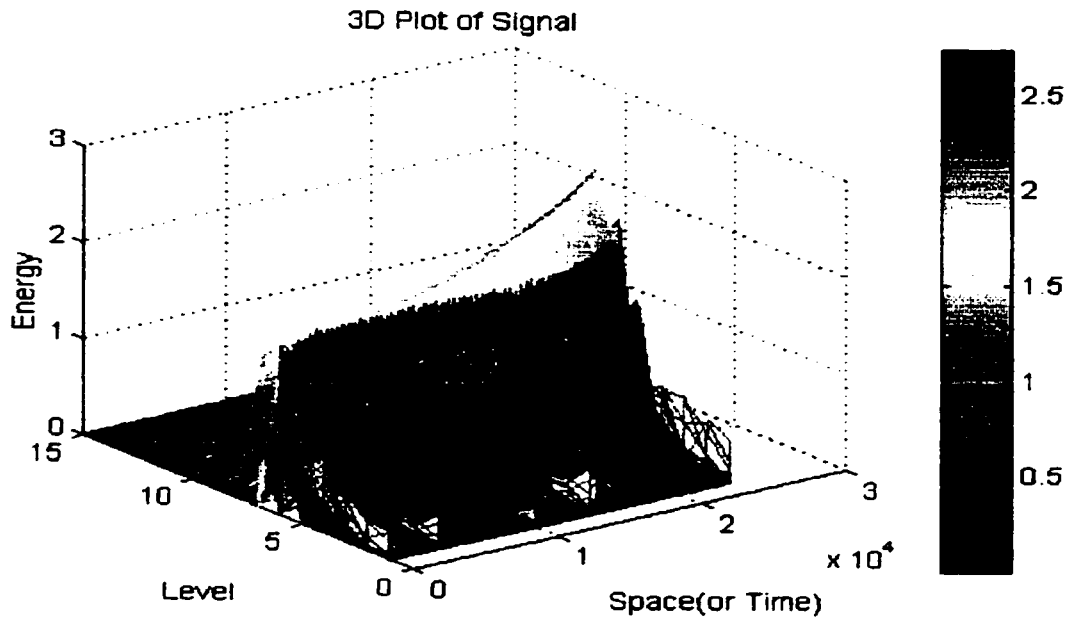

(i) Vertical

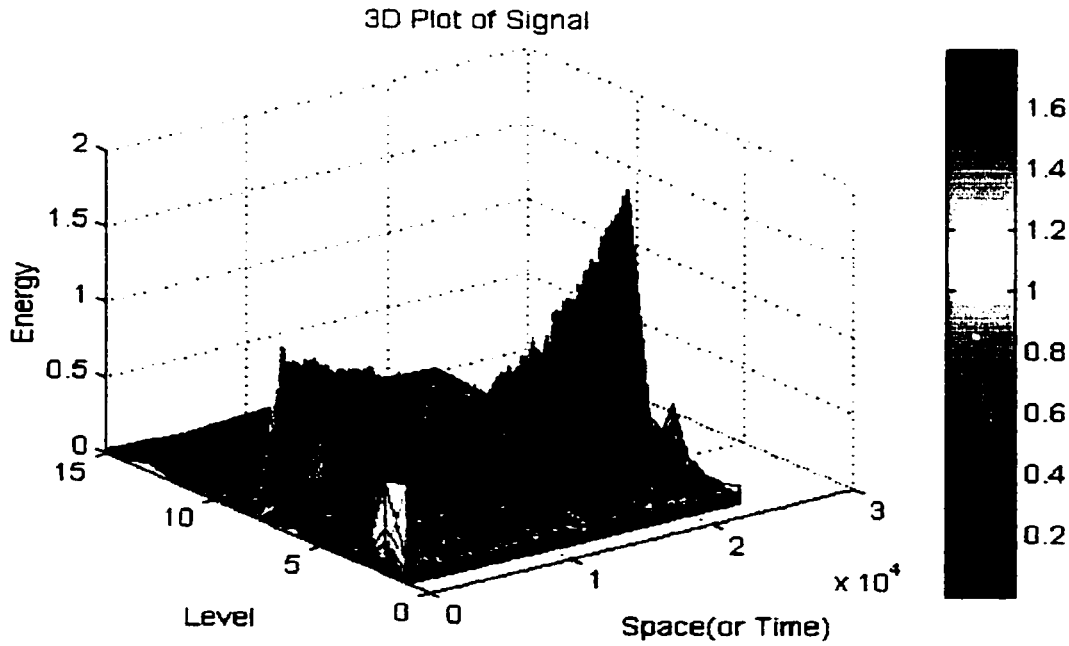

(ii) Horizontal

Fig. 5.24 (b) 3-D plot of DWT for steady state signal at 2000 rpm for shaft with 3mm notch and 8kg hanging side load just before shaft fracture

Figure 5.24 Wavelet analysis of steady state signal for shaft with 3mm notch and 8kg hanging side load just before shaft fracture.

The overhang experimental setup was repeated but with a shaft that has 4mm notch crack rotated at a higher steady state speed of 3500 rpm. The results are presented in Figures 5.25 through 5.28. Figure 5.25 represents the startup wavelet analysis results for un-cracked shaft with 8 kg hanging side load. The critical speeds occurred at positions (corresponding to time) 18542 and 5833 in the vertical and horizontal directions, respectively as shown in Fig. 5.25(a) and 5.25(b). Figure 5.26 shows the steady state results for the same setup. There are more than two levels in the vertical and horizontal directions. Levels 7 and 6 (1X and 2X) are very prominent in the vertical direction while Level 6 is the only prominent level in the horizontal direction. The result is similar to that of Fig. 5.20 except that the changes in amplitude in the horizontal direction is higher in Fig 5.26 and there is the presence of other levels unlike the presence of only one level in Fig. 5.20(b)(ii). The observed variation in amplitude with time may be due to the effect of un-steady vibrations of the overhang mass.

Figure 5.27 presents the startup results for the shaft with 4mm notch crack and 8kg hanging side load. The figure shows a decrease in the critical speeds in both the vertical and horizontal directions. Figure 5.28 represents the steady state results for the 4mm cracked shaft with 8kg hanging side load. Two levels, 6 and 5, corresponding to 1X and 2X, respectively are prominent. The amplitude of both levels increased till fracture occurred; after fracture, Level 5 (2X) disappeared while the amplitude of Level 6 is reduced. The results of this experiment compared with the results for overhang shaft with 3mm notch crack show that the depth of the crack and crack location are important factors that determine the influence of the crack on the stiffness of rotor systems.

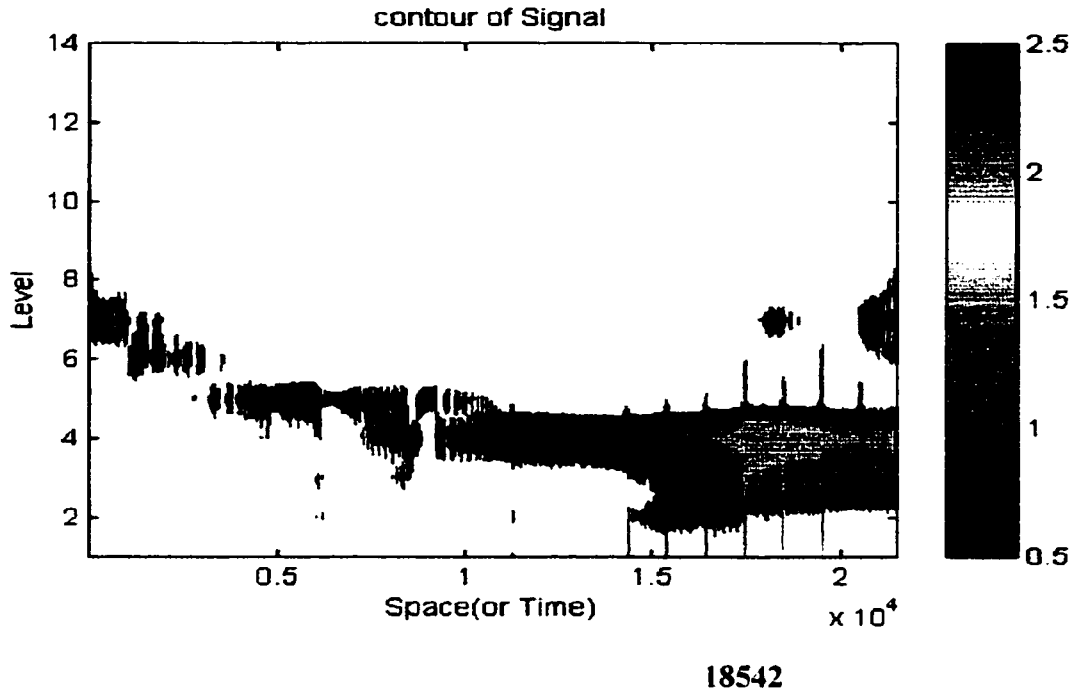

(i) Vertical

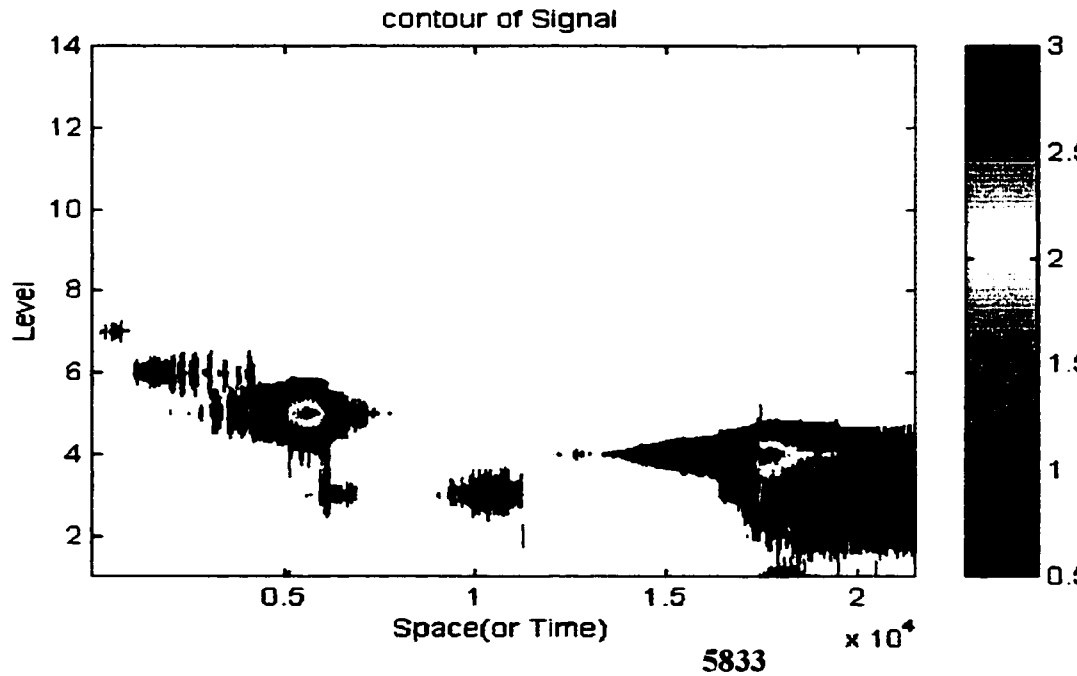

(ii) Horizontal

Figure 5.25(a). Wavelet analysis of startup signal for un-cracked shaft with 8kg hanging side load.

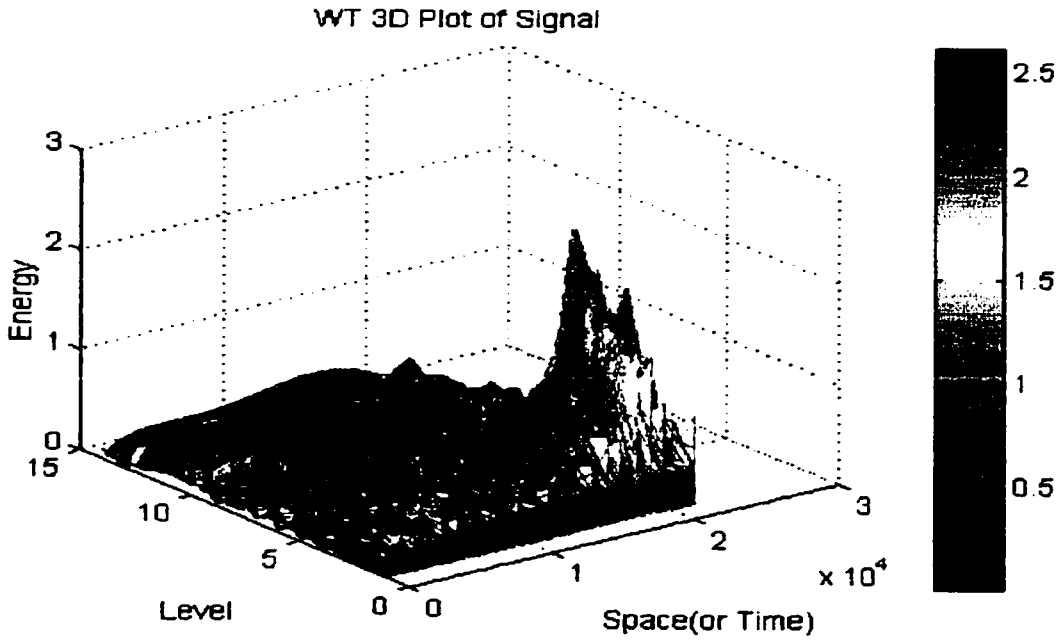

(i) Vertical

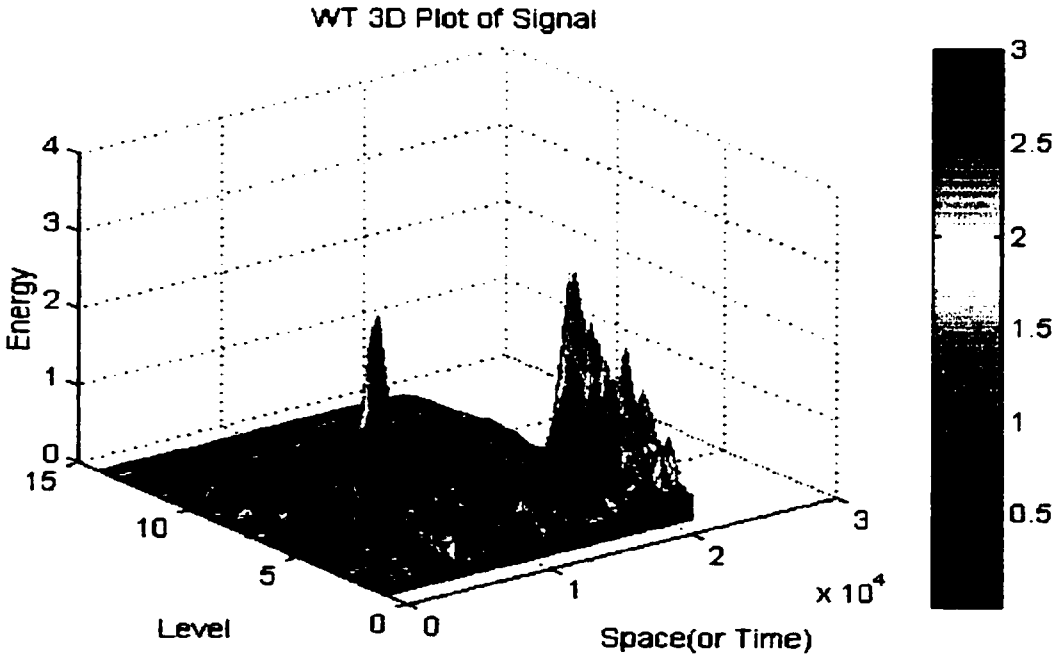

(ii) Horizontal

Figure 5.25(b). 3-D plot of DWT of startup signal for un-cracked shaft with 8kg hanging side load.

Figure 5.25. Wavelet analysis for startup signal for un-cracked shaft with 8kg hanging side load.

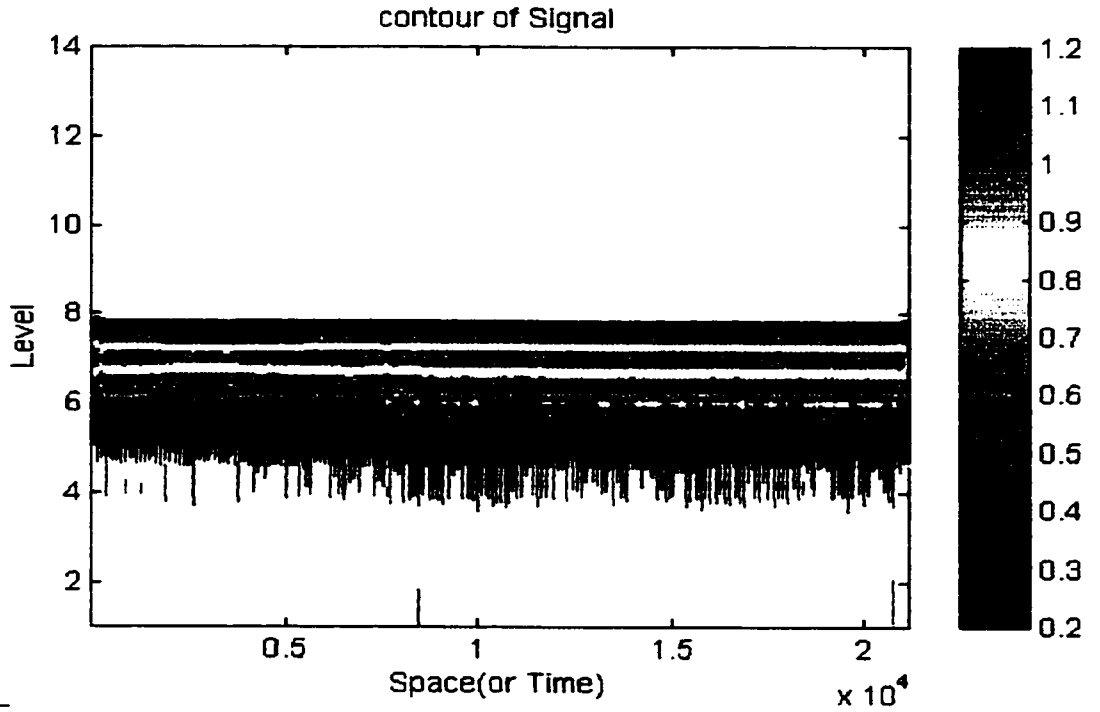

(i) Vertical

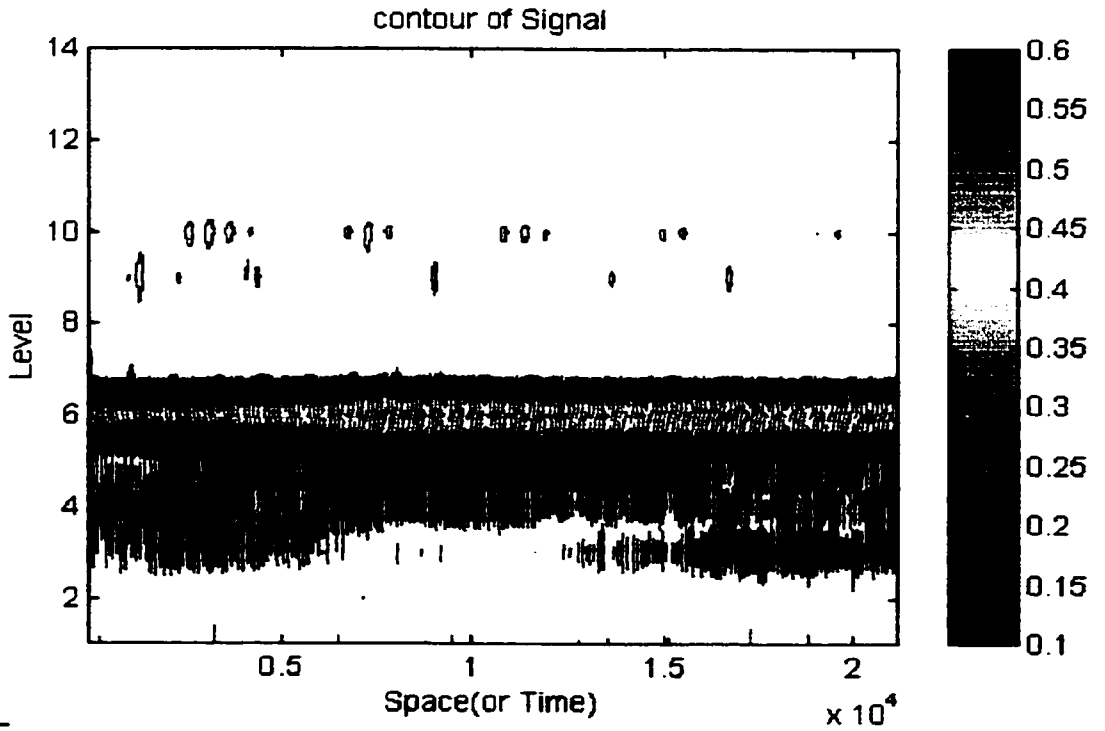

(ii) Horizontal

Figure 5.26(a). Scalogram of DWT of steady state signal for un-cracked shaft with 8kg hanging side load.

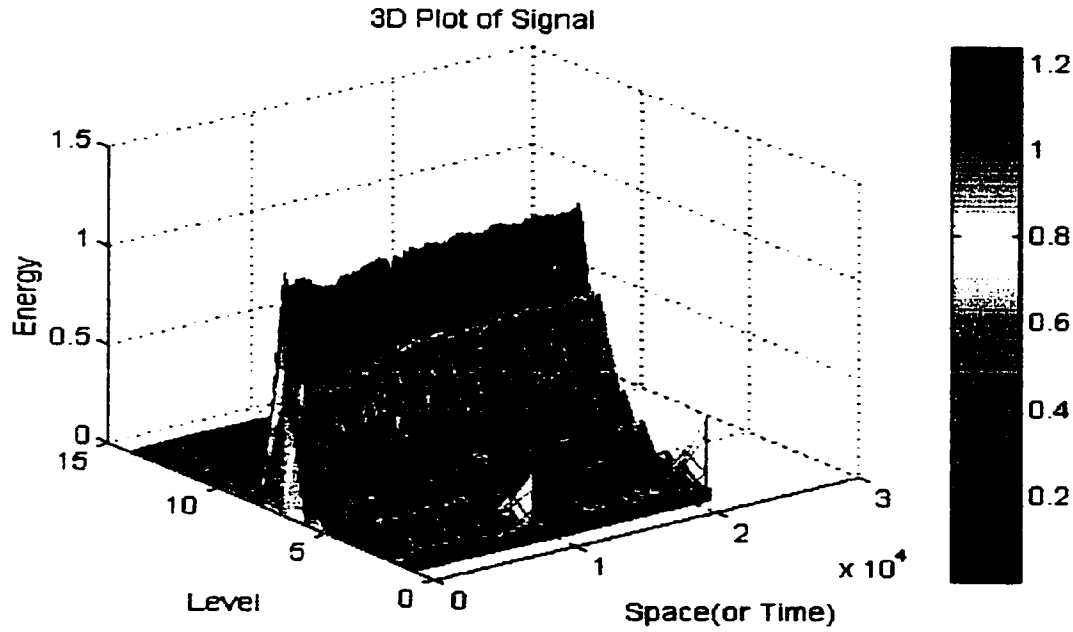

(i) Vertical

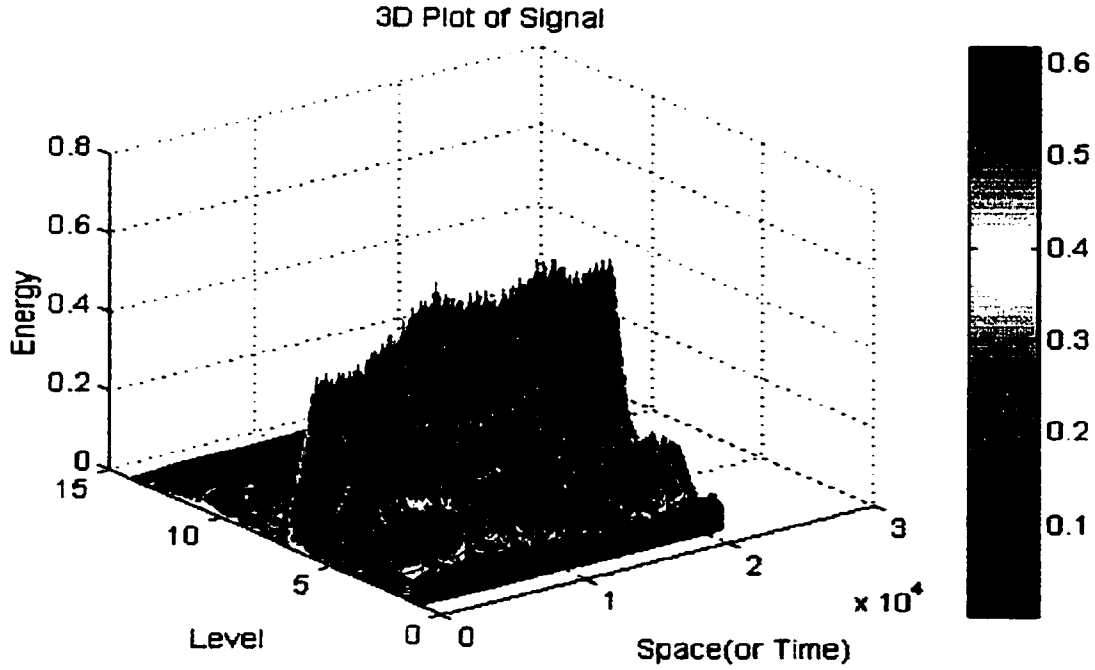

(ii) Horizontal

Figure 5.26(b). 3-D plot of DWT of steady state signal for un-cracked shaft with 8kg hanging side load.

Figure 5.26 Wavelet analysis for steady state signal for un-cracked shaft with 8kg hanging side load.

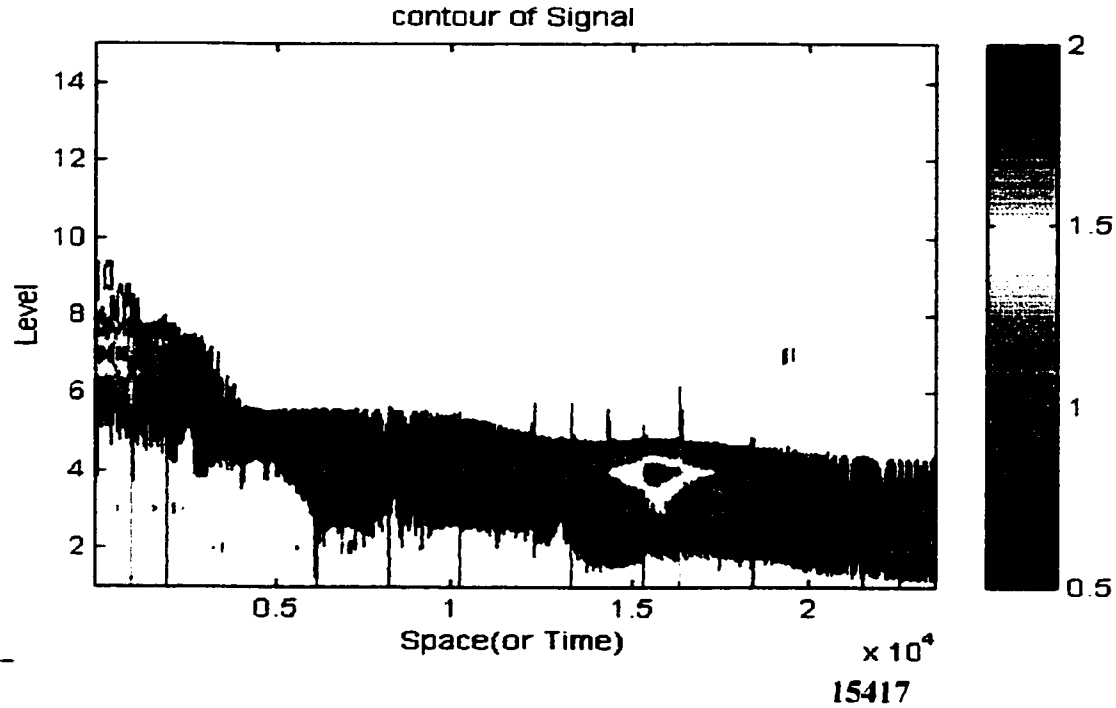

(i) Vertical

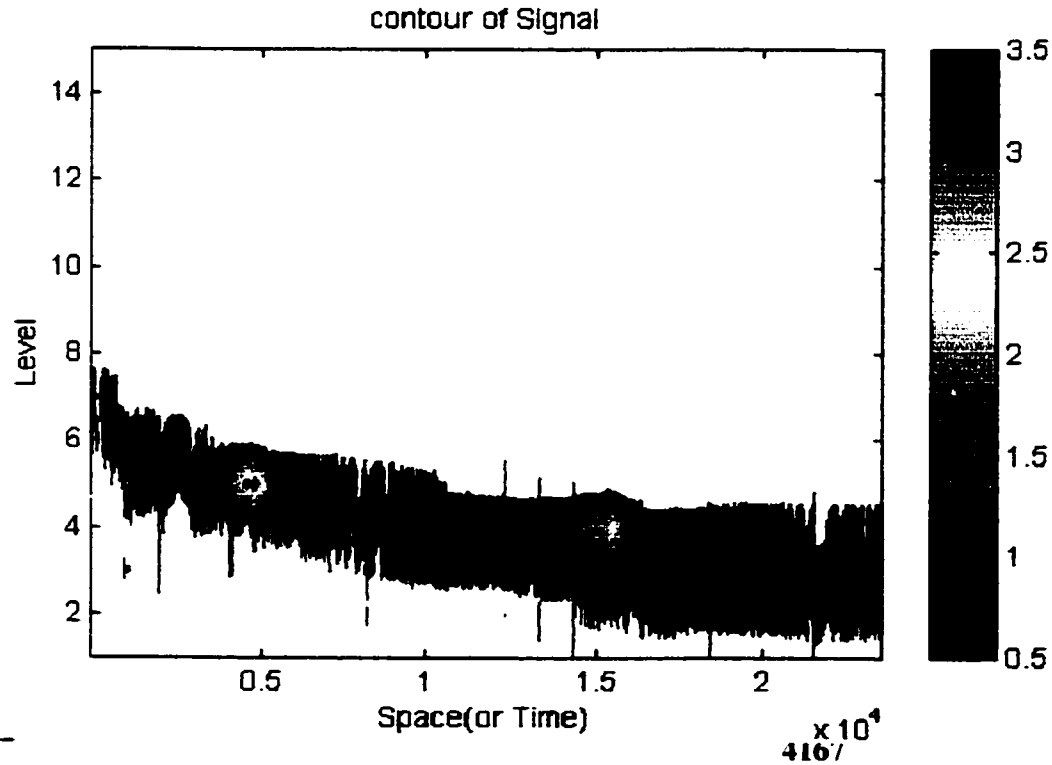

(ii) Horizontal

Figure 5.27(a). Scalogram of DWT of startup signal for shaft with 4 mm notch crack and 8kg hanging side load.

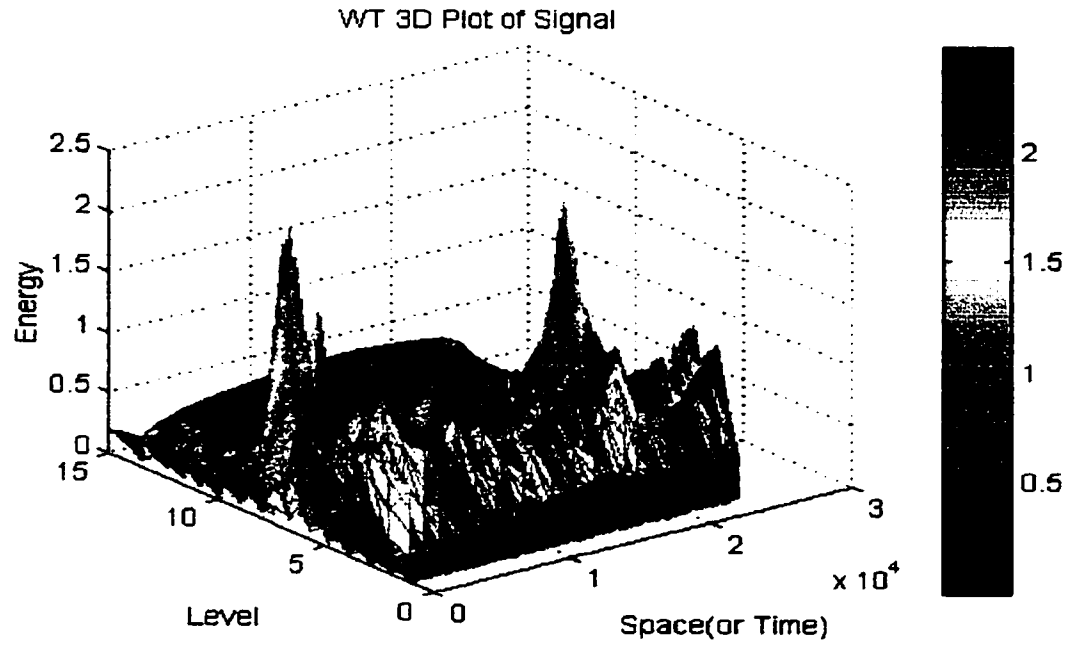

(i) Vertical

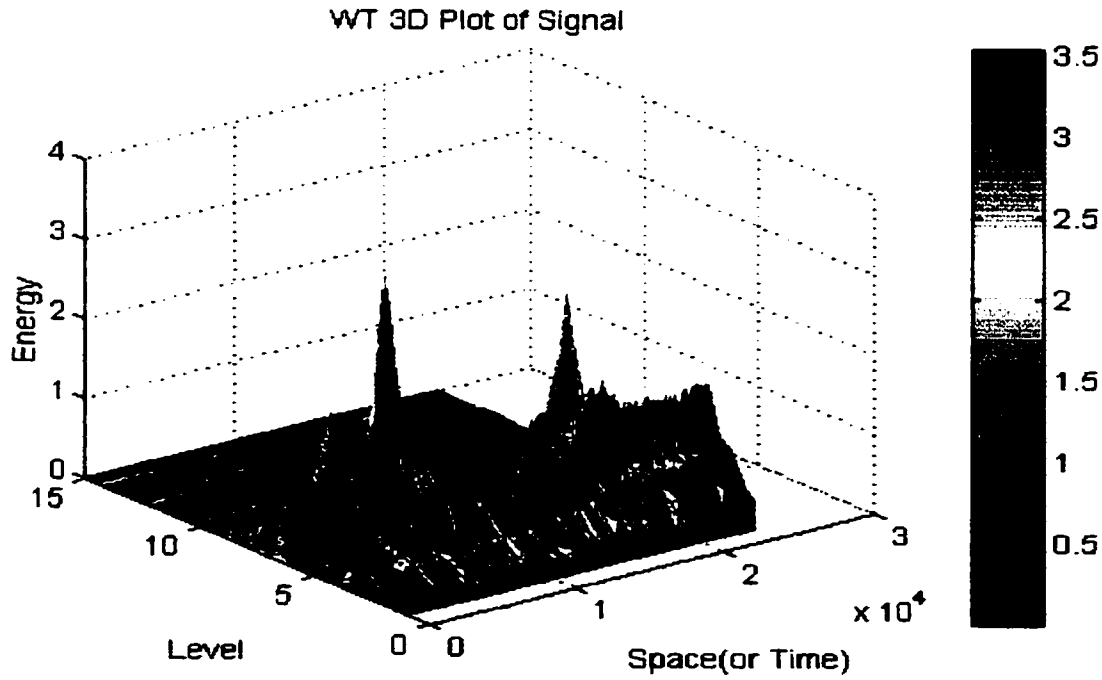

(ii) Horizontal

Figure 5.27(b). 3-D plot of DWT of startup signal for shaft with 4 mm notch crack and 8kg hanging side load.

Figure 5.27. Wavelet analysis of startup signal for shaft with 4 mm notch crack and 8kg hanging side load.

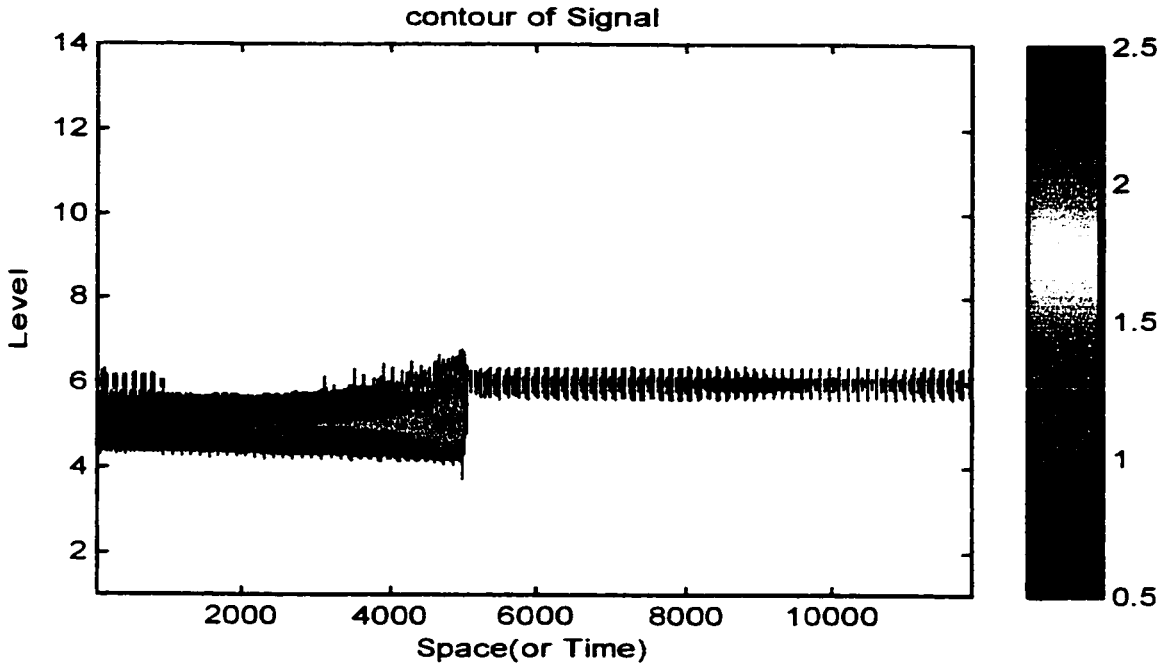

(i) Vertical

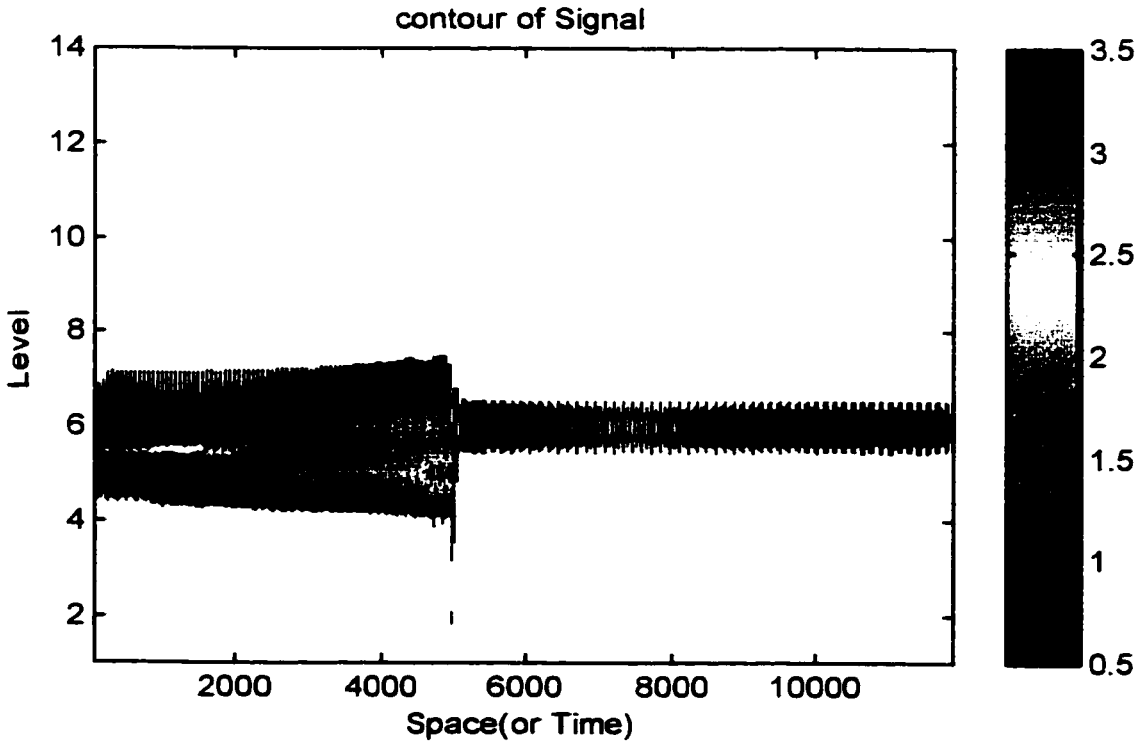

(ii) Horizontal

Figure 5.28(a). Scalogram of DWT of the steady state data at 3500 rpm for shaft with 4mm notch crack and 8 kg hanging side load.

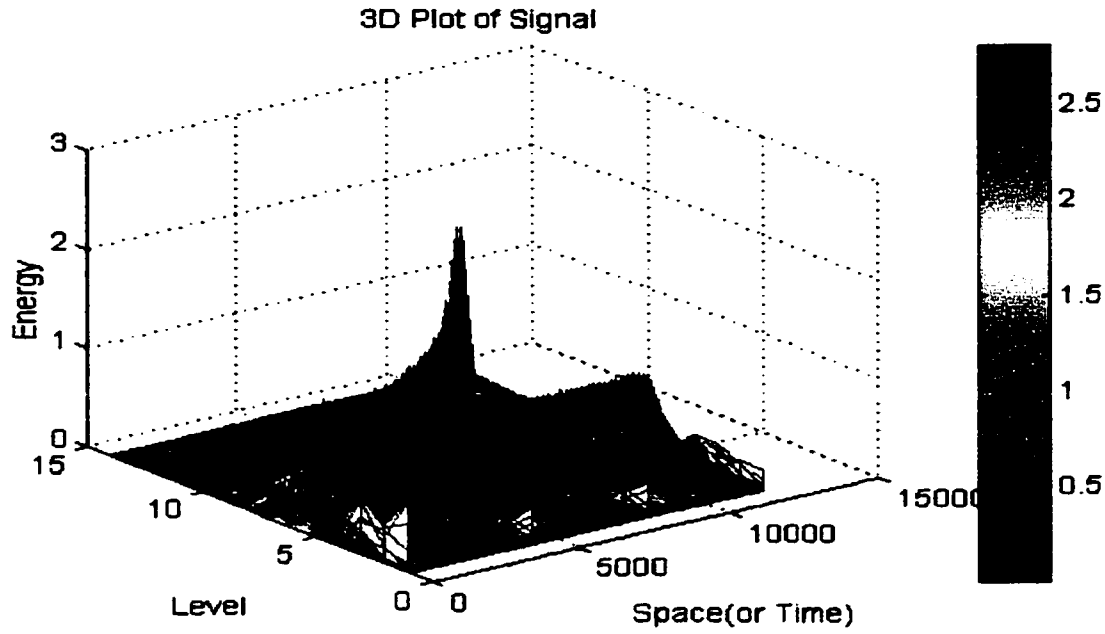

(i) Vertical

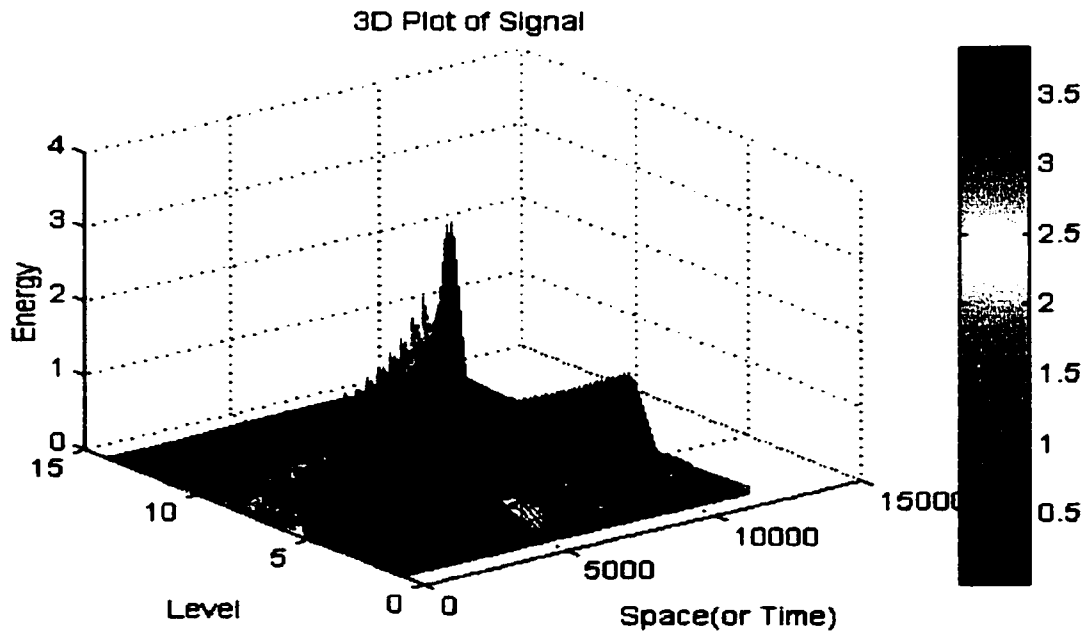

(ii) Horizontal

(ii) Horizontal

Figure 5.28(b). Scalogram of DWT of the steady state data at 3500 rpm for shaft with 4mm notch crack and 8 kg hanging side load.

Figure 5.28. Wavelet analysis for steady state data for shaft with 4mm notch crack and 8 kg hanging side load.

CHAPTER 6

CONCLUSIONS AND RECOMMEDATIONS

6.1 INTRODUCTION

Conclusions drawn from the results and discussions in the previous Chapter are presented according to the way the results were presented and discussed. These conclusions are useful information that can help in detecting the presence of a crack at the point of initiation and propagation. It is important to mention that machine history (previous record of machine performance and vibrations) is very important in fault diagnosis since the results of this work have shown that a change in vibration characteristics is an indication of problem. The arrangement of rotor-bearing system is another factor that can give a clue on the dynamic response of a machine. The results of this study showed that the dynamic response of a simply supported shaft is different from that of an overhang shaft.

6.2 CONVENTIONAL ANALYSIS RESULTS

These are the results of startup and steady state vibration signals using Orbits, Bode plots and the Fast Fourier Transform to get frequency spectra, which are cascaded to give information about variations in frequency contents of the vibration signals with time.

6.2.1 Simply Supported Shaft

The influences of a 4mm depth non-propagating surface crack and 4.3 kg side tension on the dynamic response of a simply supported shaft were studied. The startup data were presented in form of Bode plots and Frequency cascades while the steady state data were presented in form of Frequency Waterfalls and Orbits. The results showed that the vibration signals in the vertical and horizontal directions are different and the summary of the results is as follows

Startup results showed that:

* Crack increased the vibration amplitude at resonance, decreased the critical/resonance speed by decreasing shaft stiffness and increased resonance bandwidth.

* Vertical side load increased the resonance speed and reduced vibration amplitude, does not affect the resonance bandwidth and excites 2X vibration in the startup signal at half the running speed.

The combined effect of crack and side load introduced higher harmonics in the startup vibration signals. The critical speed increased above that critical speed of cracked shaft but it is lower than the critical speed for un-cracked shaft.

Steady state results showed that:

* Crack increased 1X and 2X vibration amplitudes, introduced a small transient signal in the horizontal direction and affected the shape of orbit. This indicates that attention should be paid to the change in orbit shape as this may be due to the presence of a crack.

* Side load decreased 1X and 2X amplitudes and does not affect the shape of orbit.

* The combined effect of crack and side load increased 1X and 2X vibration amplitudes and affected the shape of orbit. The percentage increase in vibration amplitudes in greater than that due to crack alone.

6.2.2 Overhang Shaft

The dynamic response of the overhang shaft arrangement is different from that for the simply supported shaft. This arrangement aided crack propagation and the results are summarized below

Startup results showed that:

* The critical speed of the 3mm notch cracked shaft increased compared with un-racked shaft before and during crack propagation while the critical speed for the 4mm notch cracked shaft decreased before and during crack propagation. Crack introduced split resonance and it did not increase the resonance bandwidth. Also, the presence of

crack excited 2X vibration at half the critical speed of the shaft system; this observation was caused by side tension in the simply supported shaft experiment.

* Side load increased the resonance bandwidth in the vertical direction only and it removed split resonance observed in the Bode plot of cracked and un-cracked shafts without side load. In the simply supported setup, crack caused an increase in the resonance bandwidth in the vertical and horizontal directions.

* The combined effect of crack and side load excited both 1X and 2X vibrations in the startup data, the 2X vibration was not limited to half the critical speed of the shaft system but it also occurred at speeds above the critical speed of the shaft system.

Steady state results showed that:

* For the 3mm notch crack without crack propagation, 1X and 2X vibration amplitudes decreased while 1X amplitude decreased and 2X amplitude increased for 4mm notch cracked shaft. Crack affected the shape of the orbit but no distinct two-loop orbit was formed before crack propagation.

* Hanging side load excited 1X, 2X, 3X and 4X harmonics in the vertical direction but 2X harmonic was absence in the horizontal direction. The amplitudes of these harmonics are less compared with the amplitudes of un-cracked shaft without side load. Side load did not really affect the orbit shape; it caused the orbit to shrink in the direction of the applied side load.

* The combined effect of crack and side load for both 3mm and 4mm notch crack shafts resulted in crack propagation. 1X and 2X vibration amplitudes increased continuously as the crack propagated. The change in the 2X amplitude is greater than the

change in 1X amplitude. The orbit shape changed from distorted one-loop orbit to a two-loop or a distorted two-loop orbit during crack propagation.

6.3 WAVELET ANALYSIS RESULTS

The focus of the wavelet analysis was on finding the differences between the dynamic response of an un-cracked shaft and a cracked shaft with side load.

6.3.1 Simply Supported Shaft

Startup results showed that:

* Crack reduced the critical speed, did not affect the split resonance and introduced additional feature at higher levels that were not present in the vibration signature of the un-cracked shaft.

* The combined effect of 4mm notch crack and 4.3 kg vertical side tension increased the critical speed relative to the shaft with crack alone but the critical speed was lower than the critical speed of the un-cracked shaft. Split resonance disappeared and the critical speed in the vertical and horizontal directions is the same. The resonance bandwidth increased and additional signal at higher levels not present in the signature of un-cracked shaft appeared.

Steady state results showed that:

* The vibration signature of cracked shaft showed the presence of two prominent levels corresponding to 1X and 2X. The amplitudes of the two levels are higher than

those for the un-cracked shaft. Level 7 (1X) amplitude is higher than Level 6 (2X) amplitude.

* The combined effect of crack and side load produced three levels (7,6 and 5) corresponding to 1X, 2X and 4X in the vertical direction. Levels 7 and 6 have almost the same amplitude, which is greater that the amplitude of Level 5. Only two levels (7 and 6) were prominent in the horizontal direction and the amplitude of Level 7 (1X) is greater than that of Level 6 (2X).

6.3.2 Overhang Shaft.

* The results are similar to those reported using the conventional analysis in section 6.2.2. The presence of crack, and crack with side load increased the critical speed of the 3mm notch cracked shaft located close to the bearing support while the critical speed decreased, as expected, for the 4mm notch cracked shaft located close to the bearing support before and during crack propagation. Further investigation is needed to find the cause of increase in the critical of 3mm notch cracked overhang shaft.

* The presence of crack can easily be detected during its propagation as the amplitudes of Level 7 and Level 6 corresponding to 1X and 2X vibrations changed tremendously during crack propagation.

Summary

Below is the summary of some unique features that can be used to detect the presence and possible location of crack. The features that differentiate side load effects on the dynamic response of the rotor from those due to crack are also mentioned.

From the experimental results, the effect of crack on the startup signal are include a decrease in the critical speed of the shaft for a simply supported shaft arrangement. However, it was also observed that crack increased the critical speed of the overhang shaft arrangement for crack depth of 30% of the shaft diameter; further investigation is needed to study the factors responsible for this observation. Crack increased resonance bandwidth and excited 2X vibration in the startup signal. Side load can also excites 2X vibration during startup but this occurred at a speed about half the critical speed of the shaft system. 2X excitation due to crack occurred at all speed but was more prominent above the first critical speed of the system.

Effects of crack on the steady state vibration signals include changes in amplitudes of 1X and 2X vibrations. If the increase in 1X amplitude is greater than 2X, the location of the crack is around midway of the span for a simply supported shaft. If the 2X amplitude is greater, then the crack location is close to the bearing support. Crack also changed the shape orbits for steady state signals before and during crack propagation. During crack propagation, a two-loop orbit or a distorted two-loop orbit will be formed; the two-loop may not be formed before crack propagation but the orbit shape will be different from that for the un-cracked shaft. Side load alone that may be due to weight and misalignment will affect 2X and higher harmonics with little effect on 1X amplitude. Side load usually decreases vibration amplitude in the direction of the applied side load and the orbit shape may not change significantly but will shrink or reduce in size if the load is applied in-between two bearing supports. For hanging side load, the orbit shape may be elongated in the direction of the applied load.

6.4. RECOMMENDATIONS

Mathematical modeling of an overhang shaft with crack located close to the bearing support is recommended to study the effect of crack depth on the stiffness of this arrangement and the cause of an increase in shaft critical speed before and during crack propagation for a crack depth of 30% of the shaft diameter.

Experiment on the measurement of crack depth during crack propagation is recommended

Experimental study of a cracked rotor with oil-lubricated journal bearings, roller bearings, rubbing and other possible machine-working environments is recommended.

A study on how to estimate the period of time that a rotor with a crack can be operated safely before causing severe damage to the machine using vibration signals will be very useful in rotating machine maintenance and diagnosis.

BIBLIOGRAPHY

1. R. Gasch. "A Survey of the Dynamic Behavior of a Simple Rotating Shaft with a Transverse Crack". *Journal of Sound and Vibration*, **160**(2), 1993: pg. 313-332.
2. B. Grabowski. "The Vibrational Behavior of a Turbine Rotor Containing a Transverse Crack". *Transactions of the ASME*, **102,** 1980: pg. 141-146
3. Andrew D. Dimarogonas and Stephen A. Paipetis. *Analytical Methods in Rotor Dynamics*. Applied Science Publishers, London. 1983.
4. Imam, S.H. Azzaro, R. J. Bankert and J. Scheibel. "Development of an On-Line Rotor Crack Detection and Monitoring System". *Journal of Vibration, Acoustics, Stress, and Reliability in Design*, **111,** 1989: pg. 241-250
5. T. Inagaki, H. Kanki and S. Shiraki. "Transverse Vibrations of a General Cracked Rotor Bearing System". *Journal of Mechanical Design*, **104,** 1982: pg. 345-355
6. B. O. Dirr and B. K. Schmalhorst. "Crack Depth Analysis of A Rotating Shaft by Vibration Measurements". *11th ASME Conference on Mechanical Vibration and Noise*. Boston, 1987: pg. 607-614.
7. I. W. Mayes and W. G. R. Davies. "Analysis of the Response of a Multi-Rotor-Bearing System Containing a Transverse Crack in a Rotor". *Journal of Vibration, Acoustics, Stress, and Reliability in Design*, **106,** 1984: pg.139-145
8. D. E. Bently and R. F. Bosmans. "Case Study of Shaft Crack Failure". *Orbit*, 1989.

9. Jorg Wauer. "On the Dynamics of Cracked Rotors: A Literature Survey". *Applied Mechanics Review*, **43**(1), 1990: pg. 13-17.

10. Jorg Wauer. "Modeling and Formulation of Equations of Motion for Cracked rotating Shafts". *International Journal of Solids Structures*, **26**(8), 1990: pg. 901-914.

11. K. R. Collins, R. H. Plaut, Charles E. Via and J. Wauer. "Detection of Cracks in Rotating Timoshenko Shafts using Axial Impulses". *Transactions of the ASME*, **113**, 1991: pg. 74-78.

12. G. Diana, N. Bachschmid and F. Angeli. "An On-Line Crack Detection Method for Turbogenerator Rotors". *Proceedings of International Conference on Rotordynamics, Tokyo*, 1986: pg. 385-390.

13. A. D. Damarogonas and C. A. Papadopoulas. "Vibration of Cracked Shaft in Bending". *Journal of Sound and Vibration*. **91**, 1983: pg. 583-593.

14. G. Meng and E. J. Hahn. "Dynamic Response of a Cracked Rotor With Some Comments on Crack Detection". *Journal of Engineering for Gas Turbine*, **119**, 1997: pg. 447-455.

15. Ming-Chuan Wu and Shyh-Shin Huang. "In-Plane Vibration and Crack Detection of a Rotating Shaft-Disk Containing a Transverse Crack". *Journal of Vibration and Acoustics*. **120**, 1998: pg. 551-555.

16. G. T. Zheng. " Vibration of a Rotor System with a Switching Crack and Detection of the Crack". *Journal of Engineering for Gas Turbine*, **120**, 1998: pg. 149-154

17. Michel Misiti, Yves Misiti, Georges Oppenheim and Jean-Michel Poggi. *Wavelet Toolbox for Use with MATLAB*. The Mathworks Inc. 1996.

18. C. Doubrava. "A New Algorithm for DSP Applications: Better JTFA". *DSP Applications* 1992: pg. 1-7

19. D. E. Newland. "Wavelet Analysis of Vibration, Part 1: Theory". *Journal of Vibration and Acoustics*, **116,** 1994: pg. 409-416

20. D. E. Newland. "Wavelet Analysis of Vibration, Part 2: Wavelet Maps". *Journal of Vibration and Acoustics* . **116,** 1994: pg. 417-425.

21. Taner Onsay and Alan G. Haddow. "Wavelet Transform Analysis of Transient Wave Propagation in a Dispersive Medium" *Journal of the Acoustical Society of America*, **95**(3), 1994: pg. 1441-1449.

22. Kikuo Kishimoto, Hirotsugu Inoue, Makoto Hamada and Toshikazu Shibuya. "Time-Frequency Analysis of Dispersive Waves by Means of Wavelet Transform". *Journal of Applied Mechanics*, **62**, 1995: pg. 841-846

23. M. N. Hamdan, B. A. Jubran, N. H. Shabaneh and M. Abu-Samak. "Comparison of Various Basic Wavelets for the Analysis of Flow Induced Vibration of a Cylinder in Cross Flow". *Journal of Fluids and Structures*, **10,** 1996: pg. 1-19.

24. D. E. Newland. "Application of Harmonic Wavelets to Time-Frequency Mapping". *Fifth International Congress on Sound and Vibration*, 1997.

25. N. Aretakis and K. Mathioudakis. "Wavelet Analysis for Gas Turbine Fault Diagnostics". *Transaction of the ASME*, **119,** 1997: pg. 870-876

26. T. L. Anderson. *Fracture Mechanics: Fundamentals & Applications*. CRC Press, USA. 1991.

27. K. J. Marsh, R. A. Smith and R. O. Ritchie. *Fatigue Crack Measurement: Techniques and Applications*. Engineering Material Advisory Services Limited, UK. 1991.

28. J. Petit, D. L. Davidson, S. Suresh and P. Rabbe. *Fatigue Crack Growth under Variable Amplitude Loading.* Elsevier Applied Science, England. 1988.

29. Shie Qian and Dapang Chen. *Joint Time-Frequency Analysis: Methods and Applications*. Prentice Hall PTR, New Jersey, USA. 1996

30. C. Sidney Burrus, Ramesh A. Gopinath and Haitao Guo. *Introduction to Wavelets and Wavelet Transforms: A primer*. Prentice Hall PTR, New Jersey, USA. 1998

31. A. Grossmann, R. Kronland-Martinet and J. Morlet. "Reading and Understanding Continuous Wavelet Transforms", *Proceedings of International Conference on Wavelets: Time-Frequency Methods and Phase Space*, France, 1987.

32. D. E. Newland. *An Introduction to Random Vibrations, Spectral and Wavelet Analysis.* Third Edition, Longman, Singapore, 1993.

33. Nabeel H. A. Sabaneh, "Wavelet Analysis of Dynamic Response: Flow Induced Vibration of A Single Cylinder in a Cross Flow". *M.Sc. Thesis*, University of Jordan, Amman, Jordan. 1995.

34. K. Gram-Hansen and C. Dorize. "Wavelet and Application: On the Choice of Parameters for Time Frequency Analysis". *Proceedings of International Conference*. Paris, Masson, Y. Meyer edition, May, 1992.

35. W. G. R. Davies and I. W. Mayes. "The Vibrational Behavior of a Multi-Shaft, Multi-Bearing System in the Presence of a Propagating Transverse Crack". *Journal of Vibration, Acoustics, Stress, and Reliability in Design.* **106,** 1984: pg. 146-153

36. Stephen Del Marco and John Weiss. "M-band Wavepacket-based Transient Signal Detector Using a Translation-Invariant Wavelet Transform". *Optical Engineering*. **33**(7), 1994: pg. 2175-2182.

37. Stephane G. Mallat. "A theory for Multiresolution Signal Decomposition: The Wavelet Representation". *IEEE Transactions on Parttern Analysis and Machine Intelligence*. **11**(7), 19989: pg. 674-693.

38. A. Tewfik, D. Sinha and P. Jorgensen. "On the Optimal Choice of A Wavelet for Signal Representation". *IEEE Transactions on Information Theory*, **38**(2), 1992: pg. 747-765.

39. W. Christopher Lang and Kyle Forinash. "Time-Frequency Analysis with the Continuous Wavelet Transform". *American Association of Physics Teachers*, **66**(9), 1998: pg. 794-797

40. L. Satish. "Short-Time Fourier and Wavelet Transforms for Fault Detection in Power Transformers During Impulse Tests". *IEEE Proc. in Sci. Meas. Technol.*, **145**(2), 1998: pg. 77-84.

41. W. H. Prosser, Michael D. Seale and Barry T. Smith. "Time-Frequency Analysis of the Dispersion of Lamb Modes". *Journal of Acoustical Society of America*. **105**(5), 1999: pg. 2669-2675.

42. Osama A. Ahmad. "New Joint Time-Frequency Transforms with Improved Properties". *Ph.D. Dissertation*, King Fahd University of Petroleum and Minerals, Saudi Arabia. 1998

43. Milton G. Bassin, Stanley M. Brodsky and Harold Wolkoff. *Static and Strength of Materials*. McGraw-Hill, USA, 1979.

44. Stefan Pittner and Sagar V. Kamarchi. "Feature Extraction From Wavelet Coefficients for Pattern Recognition Tasks". *IEEE Transaction on Pattern and Machine Intelligence*. **21**(1), 1999: pg. 83-88.

45. B. A. Jubran, M. N. Hamdan and N. H. Shabaneh. "Wavelet and Chaos Analysis of Flow Induced Vibration of a Single Cylinder in Cross-Flow". *International Journal of Engineering Science*, 1998: pg. 1-22

46. L. R. K. Nilson. "On the Vibration Behavior of A Cracked Rotor". *IFToMM Rotordynamics Problems in Power Plants Conference Proceedings*, Rome Sept 1982: pp. 512-524

47. M. A. Mohiuddin. "Finite Element Dynamic Analysis of Multibody Rotor-Bearing System With Cracked Shaft". *Ph.D. Dissertation*, King Fahd University of Petroleum and Minerals, Saudi Arabia, 1997

APPENDIX A

Table A1 Startup data for 1st experimental setup (Simply Supported Shaft)

DESCRIPTION	CRITICAL SPEED (RPM)		
	TRIAL #	Y	X
Un-cracked shaft	1	1690	1730
	2	1660	1710
	3	1650	1690
	4	1570	1680
	5	1560	1660
Average value		**1626**	**1694**
Un-cracked Shaft with Vertical Side tension of 4.3Kg	1	1680	1730
	2	1680	1710
	3	1680	1710
Average value		**1680**	**1717**
Un-cracked Shaft with Horizontall Side tension of 4.3Kg	1	1680	1680
	2	1600	1680
	3	1600	1680
Average value		**1627**	**1680**
Cracked Shaft with 4mm notch	1	1590	1630
	2	1560	1620
	3	1550	1630
Average value		**1567**	**1627**
Cracked Shaft with 4mm notch and 4.3 Kg Vertical Tension	1	1650	1650
	2	1630	1650
	3	1630	1650
Average value		**1637**	**1650**
Cracked Shaft with 4mm notch and 4.3 Kg Horizontal Tension	1	1610	1660
	2	1600	1670
	3	1600	1670
Average value		**1603**	**1670**

Table A2 Steady State data for 1st experimental Setup (Simply Supported shaft)

1st Setup (Simply Supported) Steady State data)					
		Y PROBE		X PROBE	
DESCRIPTION	TRIAL #	1X	2X	1X	2X
Un-cracked shaft	1	1.520	0.206	2.360	0.334
	2	1.460	0.206	2.290	0.334
	3	1.460	0.206	2.290	0.334
	4	1.440	0.206	2.240	0.334
Average value		**1.470**	**0.206**	**2.295**	**0.334**
Un-cracked Shaft with Vertical Side tension of 4.3Kg	1	1.260	0.154	2.240	0.360
	2	1.210	0.154	2.260	0.334
Average value		**1.235**	**0.154**	**2.250**	**0.347**
Un-cracked Shaft with Horizontal Side tension of 4.3Kg	1	1.590	0.206	2.000	0.257
	2	1.640	0.180	2.000	0.257
	3	1.570	0.180	1.930	0.257
Average value		**1.600**	**0.189**	**1.977**	**0.257**
Cracked Shaft with 4mm notch	1	2.540	0.257	3.010	0.231
	2	2.470	0.231	2.960	0.231
	3	2.420	0.231	3.470	0.206
Average value		**2.477**	**0.240**	**3.147**	**0.223**
Cracked Shaft with 4mm notch and 4.3 Kg Vertical Tension	1	2.000	0.411	3.500	0.437
	2	1.980	0.385	3.420	0.411
	3	1.850	0.360	3.320	0.385
Average value		**1.943**	**0.385**	**3.413**	**0.411**
Cracked Shaft with 4mm notch and 4.3 Kg Horizontal Tension	1	2.720	0.360	2.470	0.385
	2	2.520	0.308	2.360	0.385
	3	2.470	0.308	2.420	0.360
Average value		**2.570**	**0.325**	**2.417**	**0.377**

APPENDIX B

Table B. Startup data for 2nd experimental setup (Overhang shaft)

2nd setup startup data (Overhang shaft)

		CRITICAL SPEED (RPM)	
DESCRIPTION	**TRIAL #**	**Y**	**X**
Un-cracked shaft with 8 kg hanging side load	1	3910	1780
	2	4090	1800
	3	4050	1780
	4	4050	1780
Average value		**4025**	**1785**
Cracked Shaft with 8 kg hanging side load	1	3910	1740
	2	3999	1730
	3	4050	1720
	4	4080	1720
Average value		**4010**	**1728**

Vita

- Surajudeen Adedotun Adewusi
- Born on April 3, 1967 in Lagos State, Nigeria
- Obtained B.Sc. in Mechanical Engineering from University of Lagos, Nigeria in August, 1994
- Obtained M.Sc. in Mechanical Engineering (Thermo-Fluids) from University of Lagos, Nigeria in February, 1997
- Obtained M.S. in Mechanical Engineering (Dynamics and Vibrations) from King Fahd University of Petroleum and Minerals, Saudi Arabia in May, 2000
- Worked as Technical Assistant with Federal Ministry of Work and Housing, Lagos, Nigeria; January, 1986 – October, 1988
- Worked as Maintenance Engineer under National Service Program with Nestle Food Nigeria PLC, Nigeria; January, 1995 – November, 1995
- Worked as Field/Service Engineer with Negris Limited, Nigeria; April, 1997-August, 1997.
- Won Afprint & Kewalram Chanrai Foundations Scholarship Award; 1991-1993
- Won University of Lagos Post-Graduate Bursary Award; 1995/1996 Academic Session
- Won Federal Government of Nigeria Post-Graduate Scholarship Award; 1996/1997 Academic Session.